UNIVERSITY OF OKLAHOMA

GRADUATE COLLEGE

INTERBAND CASCADE STRUCTURES FOR INFRARED PHOTODETECTORS AND THERMOPHOTOVOLTAIC DEVICES

A DISSERTATION

SUBMITTED TO THE GRADUATE FACULTY

in partial fulfillment of the requirements for the

Degree of

DOCTOR OF PHILOSOPHY

By

HOSSEIN LOTFI
Norman, Oklahoma
2016

INTERBAND CASCADE STRUCTURES FOR INFRARED PHOTODETECTORS AND THERMOPHOTOVOLTAIC DEVICES

A DISSERTATION APPROVED FOR THE
SCHOOL OF ELECTRICAL AND COMPUTER ENGINEERING

BY

Dr. Rui Q. Yang, Chair

Dr. Matthew B. Johnson

Dr. Zhisheng Shi

Dr. J. R. Cruz

Dr. Ian R. Sellers

To my beloved wife, Samineh, and my parents

Acknowledgements

My biggest debt of gratitude is to my advisor, Prof. *Rui Q. Yang*, for his unparalleled devotion and efforts on shaping my mindset for scientific research. I would like to thank him for his trust and continuing encouragement during the course of my Ph.D. to explore various aspects of interband cascade optoelectronic devices. The two courses I took with him helped me to build my knowledge base for research on quantum engineered devices. Working with him was rewarding and I had a lot of enjoyment and fun. I am also thankful to him for supporting me to attend several conferences to present our research and have fulfilling interactions with the members of the infrared community.

I would like to thank Prof. *Matthew B. Johnson* for his dedication to my research. Many of the works presented in this dissertation would not have been possible without his support, helpful suggestions, and direct efforts. He had a significant impact on my knowledge about the design of experiments, instrumentation, and scientific writing. I would also like to express my gratitude to Prof. *Michael B. Santos* for the MBE growth of many samples presented in this work.

During my Ph.D. studies, I had the privilege to work closely with current and previous members of Quantum Device Laboratory (QDL) at the University of Oklahoma. I worked closely with Dr. *Robert T. Hinkey* during my first year at OU. He helped me to have a quick grasp of the fundamentals of the device theory and related experiments. I would also like to thank Dr. *Lu Li* for the MBE growth and fabrication of many of the samples discussed in this dissertation. He has been very generous to offer his time to explain the device fabrication and growth to me. I express my gratitude to

Dr. *Hao Ye* for MBE growth and material characterization of many of the samples presented in this work. Many thanks to *S. M. Shazzad Rassel*. He has been a good friend to respond in any need whether it was about my research work or life outside academia. I would also like to thank him for his careful proofreading and helpful comments on my dissertation draft. I also worked closely with *Lin Lei* during most of my Ph.D. program. He has made significant contributions to the device experiments presented in different chapters of this dissertation. I am also grateful to Dr. *Yuchao Jiang* for the long discussions I had with him on the physics of interband cascade lasers and band structure modeling. I also acknowledge Dr. *John F. Klem* of Sandia National Laboratories; Dr. *James A. Gupta* of National Research Council of Canada; and Drs. *Yueming Qiu*, *Dmitri Lubyshev*, *Joel M. Fastenau*, and *Amy W. K. Liu* of IQE for the MBE growth of some of the lasers and detectors discussed in this work. I benefited from close collaborations with Dr. *Preston R. Larson* and *Cedric J. Correge* for the research on monolithically integrated interband cascade lasers and detectors. I learned the basics of SEM and FIB from them. I would also like to thank Drs. *Joel C. Keay* and *Tetsuya D. Mishima* for their contributions to the device MBE growth and fabrication. I am thankful to Profs. *Zhisheng Shi*, *J. R. Cruz*, and *Ian R. Sellers* for serving on my Ph.D. committee and their insightful comments and feedback on my general exam and dissertation.

I would like to express my deepest gratitude to my beloved wife, *Samineh*, for her unconditional love, patience, and support. She has been the main source of hope and encouragement in my life and career. Last but not least, I also would like to thank my parents for their unconditional love, prayers, and support throughout my life.

The research presented in this dissertation was supported by funding from DoE EPSCoR program (Award No. DE-SC0004523), C-SPIN, the Oklahoma/Arkansas MRSEC (Award No. DMR- 0520550), AFOSR (Award No. FA9550-12-1-0260), NSF (Award No. ECCS-1202318), AFOSR (Award No. FA9550-15-1- 0067), NSF (Award No. DMR-1229678), and NSF (Award No. DMR-1608224).

Table of Contents

List of Tables

List of Figures

Abstract

Interband cascade (IC) devices are a family of quantum engineered heterostructures that include: IC lasers (ICLs), IC infrared photodetectors (ICIPs) and IC thermophotovoltaic (ICTPV) devices. In these structures, the transport of carriers across different stages is made possible by the type-II broken-gap band alignment between InAs and GaSb. Many shortcomings in conventional single absorber narrow-bandgap devices, such as short carrier lifetime and limited diffusion length (particularly at high temperatures) can be addressed by a multiple-stage architecture. While multiple photons need to be absorbed to output one electron in a multi-stage detector or photovoltaic cell, the multiple-stage architecture has some big benefits, especially at high temperatures and long wavelengths. The multiple excitations (depending on the number of stages) of each electron in an ICIP result in lower noise (higher signal-to-noise) than conventional single-stage detectors with thick absorbers. Furthermore, by keeping individual absorbers shorter than the minority carrier diffusion length most of the photogenerated carriers can be collected. This efficient collection of photogenerated carriers along with the high open-circuit voltages lead to high conversion efficiencies in ICTPV devices. The theoretical and experimental exploration of these properties of ICIPs and ICTPV devices are the main focus of this dissertation.

Design and characterization of ICIPs in different bands including short- through very long-wavelength IR are discussed in detail. It is shown that a multiple-stage detector has superior performance over a single-stage detector at high temperatures.

In contrast to single-stage detectors, in ICIPs high-frequency bandwidths can be achieved with no compromise on the device sensitivity. The high-frequency modeling

and characterization of ICIPs reveal gigahertz bandwidth (~1.3 GHz) with high detectivity (>10^9 cm.Hz$^{1/2}$/W) for three-stage mid-IR ICIPs at 300 K. A comparative study of time domain characteristics (*i.e.*, eye diagrams) of single-stage detectors and ICIPs (with the total absorber thickness equal to that of the single-stage devices) confirmed the higher bandwidth and shorter fall and rise times in ICIPs.

The unidirectional flow of carriers in IC lasers makes their structure feasible for infrared detection. Therefore, it is possible to realize monolithically integrated lasers and detectors on a single chip. Since the detector section is edge-illuminated in these bi-functional devices, detectivities higher than 10^{10} cm·Hz$^{1/2}$/W were estimated for these detectors at room temperature (RT). High-detectivity and high-speed ICIPs along with low power consumption ICLs make monolithically integrated IC lasers and detectors a practical choice for compact spectrometers and lab-on-a-chip devices.

Two sets of ICTPV devices ($E_g < 0.5$ eV) were investigated to understand the influence of number of stages/absorber thickness on the TPV cells performance. Efficiencies up to ~10% were achieved in three-stage ICTPVs with 0.41 eV bandgap. Also, narrow-bandgap ICTPV devices ($E_g < 0.25$ eV) were demonstrated at RT and above with a high open-circuit voltage (~0.65 V at 300 K). These results validate the benefits of a multiple stage architecture with thin individual absorbers for efficient conversion of long wavelength radiant photons from relatively low-temperature heat sources into electricity. Additionally, an effective characterization method for extracting series and shunt resistances has been developed for high-concentration TPV cells.

Chapter 1: Introduction

1.1 Infrared radiation

Infrared (IR) radiation is part of the electromagnetic spectrum that spans wavelengths from about 700 nm to 1 mm. As its name suggests, the IR photons have energies lower than red light and are invisible to human eyes. Every object with an absolute temperature higher than 0 K emits electromagnetic radiation. For a blackbody object with the absolute temperature of T, the spectral radiance follows Planck's law:

$$B_\nu(\nu, T) = \frac{2h\nu^3}{c^2}\frac{1}{exp\left(\frac{h\nu}{k_B T}\right)-1}, \tag{1-1}$$

where h, k_B, c, and v are Planck's constant, refractive index, Boltzmann constant, the speed of light in the vacuum, and frequency, respectively. From Equation 1-1, it is evident that the fraction of the total radiation that falls in the IR region increases by reducing the object's temperature. For example, for a 1000 ºC (1273 K) heat source, which is of particular interest for heaters used in thermophotovoltaic (TPV) systems, 99.98% of total radiation falls in IR band, whereas only 46% of the total radiation from the sun (T=5800 K) falls in this band. As such, silicon (E_g= 1.12 eV) is a viable choice for solar cells but narrower bandgap semiconductors such as GaSb (E_g=0.72 eV), InAs (E_g= 0.36 eV) and their alloys are used in TPV cells and IR photon detectors. Figure 1-1 illustrates the spectral radiance of blackbody objects with selected temperatures for solar cells, TPV devices, and IR photon detectors. As shown in this figure, at higher blackbody temperatures the overall spectral radiance is higher at any wavelength and the peak emission wavelength shifts to shorter wavelengths. Thermal imaging is based on this simple phenomenon in hot objects. Typically, target objects for thermal imaging have a temperature that is close to ambient temperature. This implies that most of their radiation falls in mid-, long-, and very long IR wavelengths, therefore narrow bandgap semiconductors (E_g<0.4 eV) are used in IR photon detectors for detection of objects near the ambient temperature.

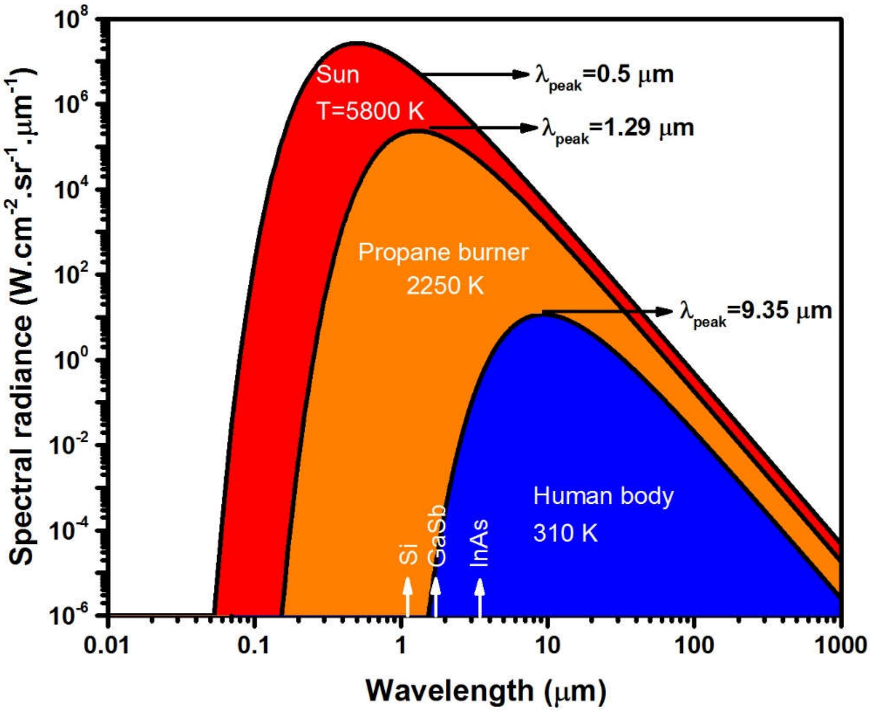

Figure 1-1: Spectral radiance for selected blackbody temperatures. At higher temperatures, the spectral radiance is larger at all wavelengths and the peak emission wavelength shifts to shorter wavelengths. Values on each curve denote the peak emission wavelength at each temperature. The room-temperature bandgap for Si, GaSb and InAs are also shown in this figure.

1.2 Infrared terrestrial bands

In detector community, the IR spectrum is categorized into near IR (NIR) (0.7-1 µm), short-wavelength IR (SWIR) (1-3 µm), mid-wavelength IR (MWIR) (3-5 µm), long-wavelength IR (LWIR) (5-14 µm), very long-wavelength IR (VLWIR) (14-30 µm), and far IR (FIR) (30-100 µm) bands [1]. Figure 1-2 shows different terrestrial IR bands (up to VLWIR) and the corresponding atmospheric transmission at different wavelengths. As a result of strong molecular absorptions in air at certain IR wavelengths, some portions of the IR spectrum are not feasible for applications such as thermal imaging and free space optical (FSO) communications. For instance, the presence of moisture (water vapor) causes strong absorptions in 5.6-7 μm and 14-16 μm wavelength ranges.

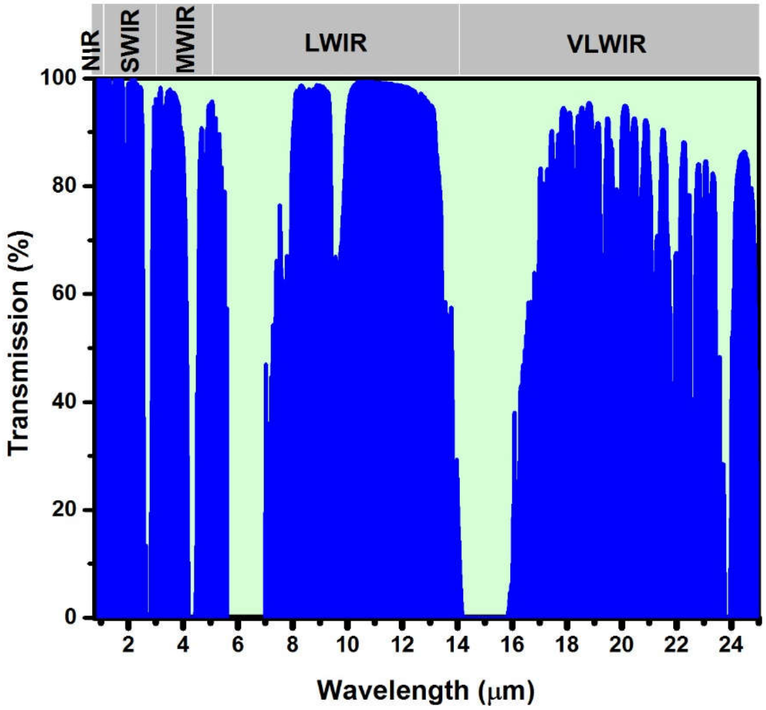

Figure 1-2: Atmospheric transmission of IR radiation at different wavelengths. Transmission data were taken from Gemini observatory website [2].

1.3 Infrared photodetectors

In addition to thermal imaging, IR detectors are one of the key elements in optoelectronic systems used in spectroscopy and FSO communications. Although NIR optoelectronic systems have been extensively investigated for these applications, MWIR and LWIR bands have fundamental advantages over NIR. For instance, as shown in Figure 1-3, many molecules and trace gases have strong absorption lines in these IR bands. Owing to their significantly stronger absorption in MWIR and LWIR bands, the detection limit for these molecules is orders of magnitude lower in these bands over NIR (see Table 1-1) [3]. One prominent example is the detection limit for CO_2 which is more than four orders of magnitude lower in MWIR (λ=4.23 μm) over SWIR band (λ=1.55 μm). Furthermore, the transmission losses associated with Rayleigh (proportional to λ^{-4} and the dominant scattering mechanism for particles smaller than λ/10) and Mie scatterings (not strongly dependent on wavelength and the dominant scattering mechanism for particles larger than λ) are higher at shorter wavelengths, thus FSO links at longer wavelengths are less susceptible to bad weather condition such as fog and smoke [5].

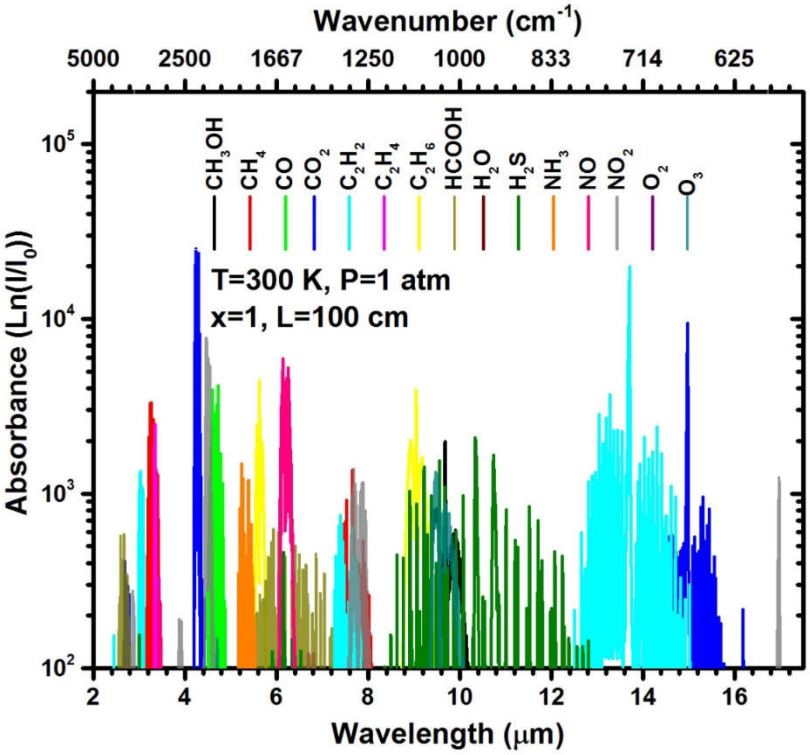

Figure 1-3: Absorbance of different molecules in MWIR and LWIR bands. HITRAN data [4] were acquired from http://www.spectraplot.com

These benefits for MWIR-LWIR over NIR-SWIR bands were known for decades, but the rapid developments of NIR optoelectronic devices and systems due to the telecommunication industry boom in the 1990s resulted in less research on other IR bands. Nevertheless, the recent advances in MWIR and LWIR lasers made of quantum structures namely, quantum cascade lasers (QCLs) [6] and interband cascade lasers (ICLs) [7] with room temperature continuous-wave (cw) operation [8, 9] greatly increased the research and development efforts on optoelectronic devices and systems in these bands.

III-V MWIR and LWIR lasers based on quantum structures have shown compelling performance and experienced a rapid commercialization in recent years. However, III-V photodetectors are not as mature as $Hg_{1-x}Cd_xTe$ detectors[10]. Even high-performance $Hg_{1-x}Cd_xTe$ photodetectors require cryogenic cooling and have some drawbacks associated with irregular substrates, and the complexity of materials growth and fabrication. Since an uncooled photodetector has lower cost, is less bulky and has lower power consumption compared to cryogenically cooled IR detectors, there has

Table 1-1: Comparison of the detection limit for certain molecules in NIR-SWIR and MWIR-LWIR bands. Data from [3].

Molecule	Detection limit			
	MWIR-LWIR		NIR-SWIR	
	ppb	Wavelength (µm)	ppb	Wavelength (µm)
H_2O	2.0	5.94	60	1.38
CO_2	0.13	4.23	4000	1.55
CO	0.75	4.60	3000	1.55
NO_2	3.0	6.14	6000	0.68
CH_4	1.7	3.26	600	1.65
HCl	0.83	3.40	20	1.21
NH_3	0.80	10.30	1000	1.50

been a strong technological drive to achieve MWIR and LWIR photodetectors with room temperature operation. Uncooled lasers and photodetectors made of the same material system are the key components to realize low cost, power efficient and compact, even on-chip integrated, IR optoelectronic systems.

1.3.1 Figures of merit for infrared detectors

1.3.1.1 Responsivity

Responsivity of a photodetector is defined as the amount of the photocurrent or photovoltage generated by the incident optical power:

$$R_i = \frac{I_{ph}}{P_{inc}} \text{ or } R_V = \frac{V_{ph}}{P_{inc}}, \tag{1-2}$$

where R_i, R_v, I_{ph}, V_{ph}, and P_{inc} are the device current response, voltage response, photocurrent, photovoltage, and incident power, respectively. The responsivity spectrum of an IR photodetector is measured with a spectrometer (*e.g.*, an FTIR). In these measurements a broadband IR source is used to obtain the device relative response:

$$R_{relative} = \frac{S_{Measured}}{S_{Source}}, \tag{1-3}$$

where $R_{relative}$, $S_{measured}$ and S_{source} are the device relative response, device raw response spectrum (to the IR source radiation), and the IR source spectrum, respectively. Because the IR source spectrum is usually measured by a spectrally flat thermal detector (*e.g.*, a DTGS detector), the collected spectrum needs to be corrected for the limited frequency response of thermal detectors (see section 1.3.2.1). Typically, after the acquisition of the device relative response, a blackbody source is used to calculate the device absolute response spectrum at different wavelengths.

1.3.1.2 Quantum efficiency

Quantum efficiency is the measure of the device ability to convert the incident photons into electron and hole pairs that are eventually collected at the device contacts. The device quantum efficiency spectrum can be derived from its responsivity spectrum as follows:

$$QE = \frac{1.24\,R_i}{\lambda}, \tag{1-4}$$

where QE, R_i, and λ (in microns) are the quantum efficiency, photocurrent response and wavelength, respectively.

1.3.1.3 Noise

Different sources of noise may be present in photodetectors, some of which like Johnson and shot noise are white noise (are not frequency dependent) and others such as $1/f$ noise and generation and recombination noise are frequency dependent. A short overview of different noise mechanisms in IR photodetectors is provided below.

- Johnson noise (also called thermal noise) is related to the random thermal motion of electronic changes and is defined by:

  $$\langle i^2_{Jonhson-noise}\rangle = \frac{4k_BT}{R}.\Delta f\ , \tag{1-5}$$

  where k_B, T, R and Δf are Boltzmann constant, absolute temperature, device resistance, and measurement bandwidth, respectively.

- The other noise mechanism in photodetectors is shot noise. This type of noise is related to the quantization of electronic charge and photons. Shot noise is described by the following equation:

$$\langle i_{Shotnoise}^{2} \rangle = 2qI\Delta f \,, \qquad (1\text{-}6)$$

  where q and I are the electronic charge and the device current, respectively.

- Another source of noise in detectors is *1/f noise.* As its name suggests, this type of noise is frequency dependent and is inversely proportional to the frequency. $1/f$ noise is the dominant noise factor at low frequencies. While different theories have been developed to explain and model $1/f$ noise in different type of photodetectors [11], the origins of $1/f$ noise is not fully understood yet.

- Generation and recombination (g-r) noise is associated with the random generation and recombination of electron and holes. The g-r noise is frequency dependent ($\propto 1/f^2$). In a nearly intrinsic semiconductor g-r noise is described by [12]:

$$V_{gr} = \frac{2V_b}{(lwt)^{1/2}} \frac{1+\left(\frac{\mu_e}{\mu_h}\right)}{\left(\frac{\mu_e}{\mu_h}\right)n+p} \left(\frac{np}{n+p}\right)^{1/2} \left(\frac{\tau\Delta f}{1+(2\pi f)^2\tau^2}\right)^{1/2} \,, \qquad (1\text{-}7)$$

  where V_b, l, w, t, μ_e, μ_h, n, p, τ, and f are the applied bias, device length, width, thickness, electron mobility, hole mobility, electron concentration, hole concentration, and frequency, respectively.

1.3.1.4 Detectivity

To evaluate a detector's sensitivity, the ratio of the detector signal (*i.e.*, responsivity) and its noise is used. Detectivity is defined as the inverse of the device noise equivalent power (NEP). NEP is the amount of signal power that is equal to the device noise power. Since the measurement bandwidth and the device size affect the device detectivity, a modified term called specific detectivity (D^*) which normalizes the device detectivity to its area and bandwidth was proposed by Jones [13]:

$$D^* = \frac{\sqrt{A.\Delta f}}{NEP}, \tag{1-8}$$

here A denotes the device area. The specific detectivity can be used to make a fair comparison between different types of photodetectors. A more versatile form of the above equation that only includes the Johnson and shot noise terms ($\Delta f = 1\ Hz$) is as follows:

$$D^* = \frac{Ri}{\sqrt{\frac{4k_BT}{RA}+2qJ}}, \tag{1-9}$$

where R_i, RA, and J are the device responsivity, resistance and area product, and current density, respectively.

1.3.1.5 Frequency response

The frequency response of a detector quantifies that how fast it can respond to the incident photons variation in time. The 3-dB bandwidth of a detector is the frequency at which the detector output power decreases to half of its low frequency value. The detector frequency response could be limited either by its packaging (*e.g.*, parasitic capacitance and inductance) or by the fundamental transport time, diffusion or drift process, within the detector structure.

1.3.2 Different types of infrared detectors

A common method to classify IR detectors is based on their cutoff wavelength. For each terrestrial IR band, different types of IR detectors exist within different material systems that can cover single or multiple bands. Aside from their cutoff wavelength, IR detectors are categorized into thermal and photon detectors. Thermal detectors have no wavelength selectivity whereas photon detectors are selective and only respond to IR radiation with energies higher than their bandgap. A brief overview of different types of IR detectors and their operation principles is provided in the next subsections. Detailed reviews of different types of IR detectors and the history of IR detection can be found in [11, 14, 15].

1.3.2.1 Thermal detectors

Thermal detectors have been extensively investigated for IR detection owing to their room temperature operation, low cost, simplicity and wide spectral response. Regardless of their material or structure, thermal detectors have a similar working principle: the absorbed IR radiation induces a temperature change and a subsequent alteration in a property of the sensor material such as its resistivity or polarization, which is proportional to the temperature change. Figure 1-4 shows the schematic of a typical thermal detector where the IR sensitive element is mounted on a substrate through a heat insulator leg. The room temperature specific detectivity (D^*) of thermal detectors is in the range of 10^8-10^9 cm.Hz$^{1/2}$/W at low frequencies (~10 Hz) and sharply drops with increasing the frequency [16]. The main disadvantages of thermal detectors are their very low response speed (in the order of milliseconds) and low sensitivity compared to photon detectors. While the overall performance of thermal detectors is well behind that of cooled photon detectors, their low cost and reasonable room temperature performance make them a perfect fit for less demanding applications. Today, their cost of production is reduced to the level that they have been considered for consumer electronics such as smartphones. Companies like FLIR and Seek thermal have introduced thermal cameras based on VO_x microbolometers for smartphones (see Figure 1-5) in \$250-500 price range [17, 18] .

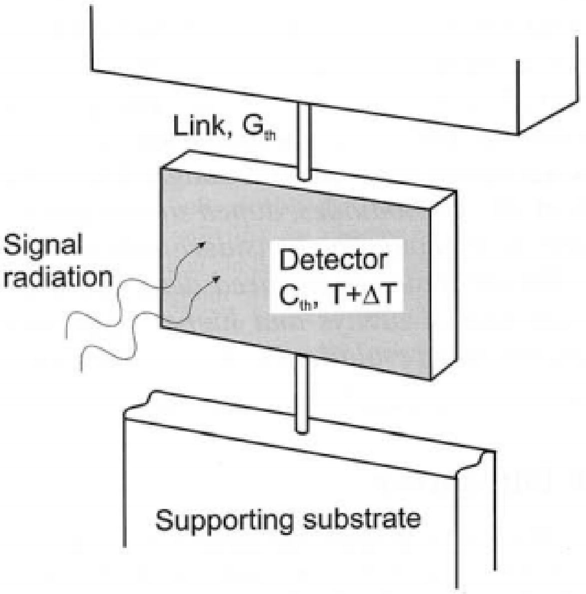

Figure 1-4: Schematic of a typical thermal detector. The absorbed IR radiation induces a temperature change and a subsequent alteration of a property of the sensor material. Image from [19].

1.3.2.1.1 Thermopiles

The operation of thermopiles is based on the Seebeck effect. A thermopile can be made by simply connecting two electrodes made of dissimilar metals or semiconductors. The temperature difference between the two electrodes causes an electric potential that is proportional to the temperature difference between the electrodes. This phenomenon is also employed in thermoelectric devices where an applied electric potential produces a temperature gradient between the two ends of these

Figure 1-5: (a) FLIR One^{TM} and (b) SeeK^{TM} thermal Compactpro^{TM} thermal cameras made of microbolometer arrays for android and iOS smartphones. Images are from [17, 18].

devices. Thermopile detectors can be used with or without a chopper to detect IR radiation. These thermal detectors have low voltage response and their specific detectivity is at the low end of 10^8 cm.Hz$^{1/2}$/W at room temperature [20].

1.3.2.1.2 Bolometers

Bolometer, in essence, is a thermistor in which the device conductivity varies with temperature. The active region of a bolometer is composed of an IR absorber, typically made of metals, certain ceramics or extrinsic semiconductors [16], that under IR radiation its temperature as well as resistance change. If the detector is biased at a constant current, any change in the device resistance results in a potential difference (ΔV) proportional to the temperature change (ΔT). Bolometers have a limited response time, require temperature calibration (a shutter), and their specific detectivity lies on the low to middle end of 10^8 cm.Hz$^{1/2}$/W range at room temperature [11]. However, owing to their simple structure, low manufacturing costs, and small pixel size, with pixel resolutions as large as 3 megapixels [21], microbolometers have the largest market share for uncooled thermal cameras.

1.3.2.1.3 Pyroelectric detectors

In a pyroelectric detector, any change in the device temperature results in an electric polarization of the absorber material and creates a potential difference between the two sides of the detector. Although a large variety of materials have been used for pyroelectric detectors, the most popular materials are PT ($PbTiO_3$), PZT ($Pb(ZrTi)O_3$), BST ($BaSrTiO_3$) and DTGS ($(ND_2CD_2OOD)_3D_2SO_4$). Pyroelectric detectors have better detectivity (~10^9 cm.$Hz^{1/2}$/W at room temperature) compared to bolometers and thermopiles [22]. Since pyroelectric detectors respond to a temperature change rather than the absolute temperature, IR cameras made of pyroelectric detectors usually require a chopper to modulate the IR radiation from a thermal scene.

1.3.2.2 Photon detectors

Amongst different types of photodetectors, photon detectors have the highest theoretical performance limit, fast response and excellent signal to noise ratio (SNR) [11]. Noise in some photon detectors is remarkably low, to the point that noise from the system electronics becomes the limiting factor. However, unlike thermal detectors, photon detectors do not have a flat and wide spectral response and generally require cryogenic cooling.

When IR photons, with energies higher than the detector's bandgap, are incident on a photon detector, they will be absorbed and excite carriers to an excited state in another band or subband. Photon detectors are categorized into two major classes, namely, photoconductors (PC) and photovoltaic (PV) detectors. Photoconductors are typically made of a slab of semiconductor whose conductance changes upon photon absorption. On the other hand, PV detectors employ either a *p*-*n* junction or a heterostructure with selective contacts to separate and collect photo-generated carriers through a photovoltaic process similar to solar cells. Since photon detectors are spectrally selective, different types of semiconductors have been utilized for IR photon detectors for different IR bands. Table 1-2 summarizes some of the most popular semiconductors along with their properties for the different IR bands.

Table 1-2: Summary of main detector technologies for different IR bands.

IR band	Wavelength	Detector technology	Applications
NIR	0.7-1 µm	Si, GaAs, CdTe, InP, InGaAs, CCD, CMOS	Optical data storage
SWIR	1-3 µm	InGaAs, GaSb, Ge, $Hg_{1-x}Cd_xTe$, T2SL	Fiber communications, Spectroscopy, FSO communications, power beaming, LIDAR
MWIR	3-5 µm	InAs, InAsSb, InSb, $Hg_{1-x}Cd_xTe$, T2SL, QWIP, QCD, QDIPs	Thermal imaging, FSO communications, spectroscopy, power beaming
LWIR	5-14 µm	$Hg_{1-x}Cd_xTe$, T2SL, QWIP, QCD, QDIPs	Thermal imaging, FSO communications, spectroscopy
VLWIR	14-30 µm	$Hg_{1-x}Cd_xTe$, T2SL, QWIP, QCD, QDIPs, Si:Mg, Si:Bi, Ge:Au, Ge:Hg	Astronomy, remote sensing, missile detection
FIR	>30 µm	Ge:Cu, Si:Ga, Si:Al, Si:As	Astronomy

1.3.2.2.1 Photoconductors

The simplest form of a photon detector is a slab of semiconductor with certain doping and Ohmic contacts at both ends (see Figure 1-6). The working principle of photoconductors is the change in the resistance of the semiconductor with a change in its carrier concentration. The resistance of a photoconductor can be expressed as:

$$R = \frac{\rho L}{wt} = \frac{L}{q(\mu_e n + \mu_h p)wt} \tag{1-10}$$

where ρ, L, w, t, q, $\mu_{e,h}$, n and p are the resistivity, slab length, width, thickness, electronic charge, electron or hole mobility and electron and hole concentrations, respectively. Since photoconductors have a simple structure, the first photon detector was a photoconductor made of Ti_2S during World War I [23]. Today, photoconductors made of lead salts and $Hg_{1-x}Cd_xTe$ alloys are commercially available in different IR bands, however, most of the research and development on IR detectors is devoted to PV detectors because of their zero-bias operation, larger device resistance, lower noise, and smaller pixel size.

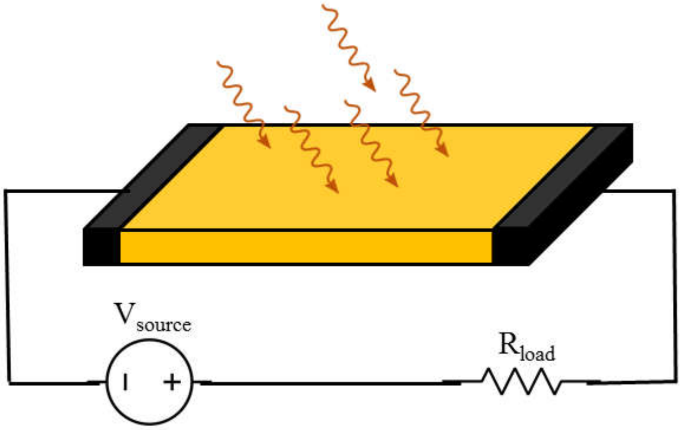

Figure 1-6: Schematic drawing of a PC detector made of a slab of semiconductor.

1.3.2.2.2 Quantum well infrared photodetectors

Quantum well infrared photodetectors, also known as QWIPs, were introduced in 1987 [24]. As shown in Figure 1-7 (a), photon absorption occurs through intersubband transitions within the conduction or valence band of quantum wells (QWs) in QWIPs. These detectors are comprised of multiple quantum wells (MQWs) wherein its simplest form (bound to continuum QWIPs, see Figure 1-7 (b)) carriers are excited by photon absorption from a bound state in each QW to the continuum and are collected by an externally applied electric field. Since QWIPs need to be biased to operate, they are classified under photoconductors. QWIPs have been realized in different material systems including: GaAs/AlGaAs [25], InGaAs/InP [26], GaN/AlN [27], and $Si_{1-x}Ge_x$/Si [28] where GaAs/AlGaAs has been the most investigated material system. These intersubband-based photodetectors can cover a wide range of wavelengths by merely adjusting the well width in QWs. As such, QWIPs are well suited for multi-color applications. Because of the selection rule of intersubband transitions in the conduction band [29-33], n-type QWIPs are not sensitive to TE polarization and require specific device mounting or gratings for normal detection and have a narrow spectral response.

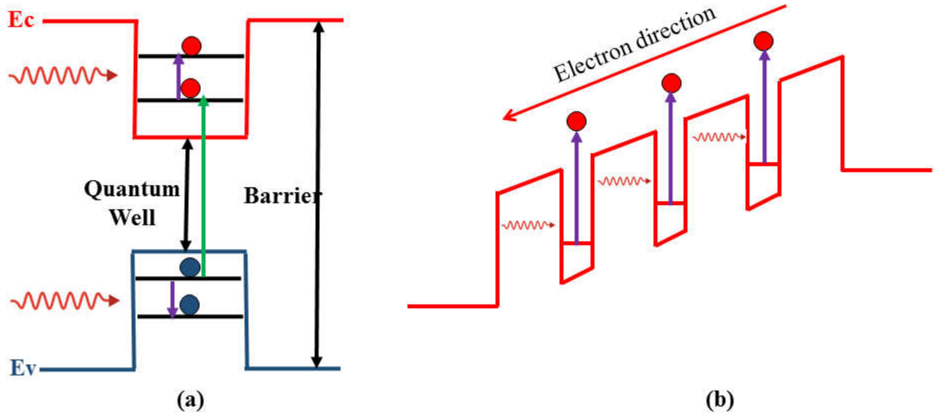

(a) (b)

Figure 1-7: (a) Interband (green arrow) and intersubband absorption (violet arrows) in a type-I QW. (b) Schematic diagram of a bound state to continuum photoconductive QWIP.

1.3.2.2.3 Quantum dot IR photodetectors

Quantum dot IR photodetectors (QDIPs) are a relatively new class of IR detectors where carriers are spatially confined in all three dimensions. Due to this 3-D confinement, QDIPs are projected to have low dark current and be able to operate at high temperatures. The most explored material system for QDIPs is InAs/GaAs [34], where the InAs dots are formed on a GaAs substrate using Stranski-Krastanov crystal growth [35]. In this technique, the compressive strain of epi layer relative to the substrate enables the formation of islands (dots) with certain shape and size. The cutoff wavelength of QDIPs can be tailored by controlling the dot size, shape and material composition, therefore QDIPs can cover different IR bands. Moreover, the absorption selection rules associated with intersubband transitions in n-type QWIPs is not present in QDIPs and they are sensitive to normal illumination. Furthermore, the 3-D confinement of carriers and the phonon bottleneck effect in QDIPs leads to significantly longer carrier lifetimes (up to ns) compared to QWIPs.

The main challenges in the development of QDIPs are the dot size and shape non-uniformities and their low quantum efficiency [34]. Although modified QDIP structures such as quantum dot in a well (QDWELL) [36] has shown some promise to address some of these issues, the research on QDIPs has been received limited attention. It is expected that the increasing interest in QDs for solar cells will stimulate further research on QDIPs in the future.

1.3.2.2.4 Photovoltaic detectors

As stated earlier, photovoltaic (PV) detectors have the highest ultimate performance projections [11, 37] among different types of IR detectors. In this type of detectors, the generated electron and hole pairs are separated by means of an internal electric field. Photodiodes, which are the simplest form of PV detectors, employ a *p-n* junction to separate and collect the photogenerated electron-hole pairs (see Figure 1-8). In brief, the photogenerated carriers in the depletion region of a photodiode are quickly separated by the electric field across the junction and collected. Also, the fraction of photogenerated electrons and holes that are within a diffusion length away from the junction will diffuse to the junction region where they are swept in opposite directions via the junction field and then collected by the device contacts.

A refined version of photodiodes with an enhanced collection efficiency and better response speed, are *pin* photodiodes. In *pin*s, a thick intrinsic layer is inserted between *p-type* and *n-type* regions, so that most of the photon absorption occurs in this intrinsic region. Therefore, photogenerated carriers are mainly collected by the drift process and diffusion, which is a relatively slow process, has a negligible contribution to the carriers transport.

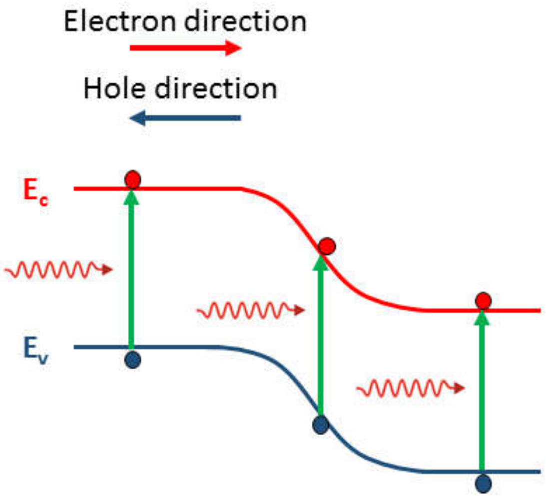

Figure 1-8: Schematic band diagram of a *p-n* photodiode. Photogenerated carriers generated within a diffusion length of the device junction diffuse to the junction region and are collected by the junction's electric field.

1.3.2.2.5 Barrier infrared detectors

The advent of barrier structures in 2007 [38] and the following work [39] led to substantial improvements in the device performance and high-temperature operation of Sb-based detectors. The presence of Shockley-Read-Hall (SRH) centers in narrow bandgap III-V IR detectors (*e.g.*, InSb detectors) inhibited high-temperature operation of these photodiodes for decades.

The Shockley-Read-Hall (SRH) generation-recombination (*g*-*r*) rates have their highest value in the depletion region of a diode [40]. The *g*-*r* currents are the main source of dark current in materials with a large number of SRH centers (*e.g.*, Sb-based materials) where the carrier lifetime is limited by short *g*-*r* lifetimes. This is of particular importance in narrow bandgap semiconductors that suffer from lower material quality.

In a barrier photodetector either the depletion region of *p*-*n* junction is mainly confined to the wider bandgap material (barrier) or the photovoltaic operation is achieved by selective contacts rather than a *p*-*n* junction. Thus, the depletion region is either nearly removed from (or confined to the outside of) the absorber. Figure 1-9 shows the schematics of two types of these detectors, namely nBn [38] and complementary barrier detectors (CBIRDs) [41].

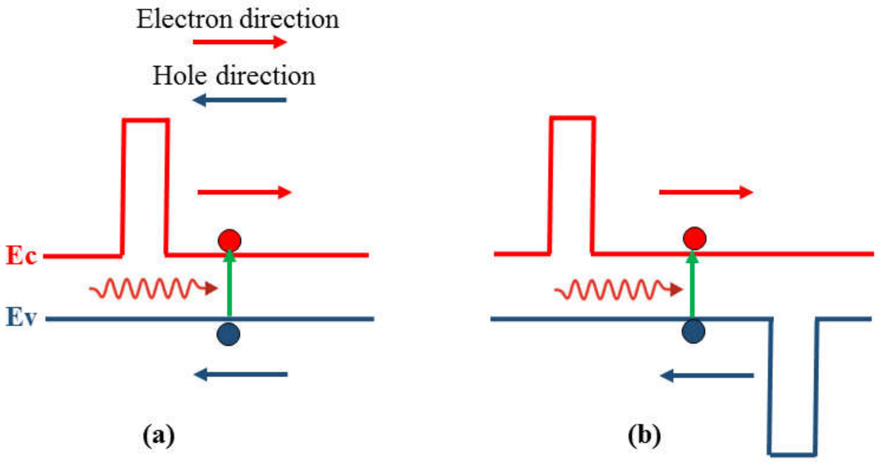

Figure 1-9: Schematic band diagram of (a) an nBn and (b) a complementary barrier photodetector.

1.3.2.2.6 Quantum cascade detectors

The first quantum cascade detector (QCD) was a quantum cascade laser (QCL) used for photon detection [42]. While a QCL operates in forward bias regime for lasing action, the same device can detect photons under zero-bias or reverse-bias condition. To achieve photovoltaic detection, QCDs have an asymmetric structure where the electrons (or holes) are forced to flow in a certain direction. As shown in Figure 1-10, QCDs are bound-to-bound detectors meaning that electrons in the absorption wells are excited from the ground (bound) states to an excited (bound) energy state in the QW. After their excitation electrons tunnel through a thin barrier to a QW in the relaxation region (via resonant tunneling) and experience multiple relaxations through digitally graded QWs and finally tunnel into the ground state of the next absorption QW, where they undergo another excitation process. Similar to QWIPs, QCDs are usually based on intersubband transitions in the conduction band, therefore they are only sensitive to TM polarization and suffer from short intersubband transition lifetime (in the order of ps), which is comparable to the phonon scattering time. However, thin absorbers and short carrier lifetimes make these detectors a perfect candidate for high-speed operation (up to 40 GHz) [43-45]. The main drawbacks of these detectors are their low responsivity, which is further reduced with increasing temperature, and low detectivity (in the range of 10^7 to 10^8 cm.Hz$^{1/2}$/W at room temperature) [46-48]. Further enhancements such as using

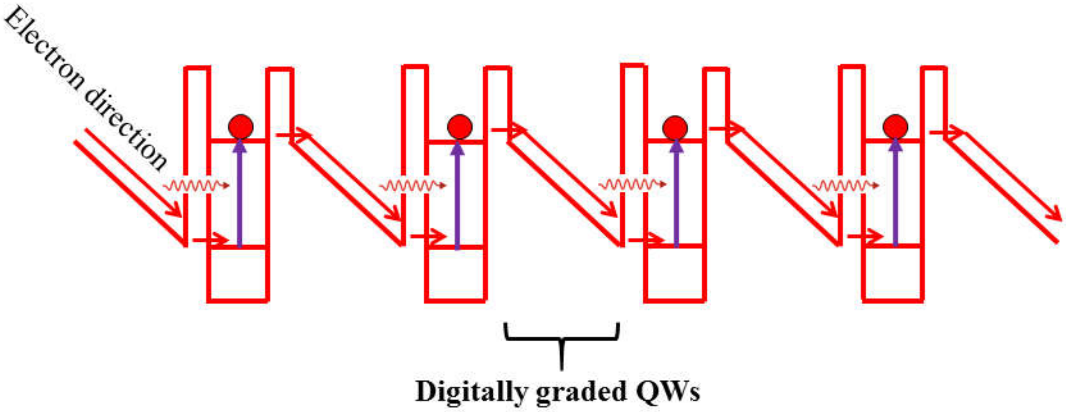

Figure 1-10: Schematic drawing of a QCD. Similar to QWIPs, QCDs are intersubband-based IR photodetectors.

photonic crystal structures has been proposed to increase the device responsivity by 4-6 times [49, 50] in these detectors.

1.3.2.2.7 Multi-junction photodetectors

Multi-junction detectors have a single cutoff wavelength and all of the stages operate simultaneously to contribute to the device voltage and current. These IR detectors should not be confused with multi-color detectors. Although multi-color detectors also have multiple stages/junctions, each stage/junction has different cutoff wavelength and typically different colors (*i.e.*, junctions) do not operate simultaneously. For example, a two-color detector may be designed in such a way that under different bias polarization one of the two colors become operational (is detected) while the other is shunted. Since all the stages are serially connected and should operate simultaneously, Esaki tunnel junctions are incorporated in between the stages in a multi-junction detector in a similar fashion to multi-junction solar cells.

Having similar cutoff wavelengths in different stages may sound counterintuitive, but the current status of narrow bandgap semiconductors is far from ideal and they have limited carrier lifetime and diffusion lengths, particularly at high temperatures. The series connection of different stages results in a higher device resistance, lower noise and more efficient collection of photogenerated carriers compared to a single-stage/junction detector. Additionally, shorter absorbers utilized in multi-stage detectors makes them a viable choice for high-speed applications with almost no compromise on the device sensitivity. The multi-junction IR detectors (Figure 1-11) were first reported in LWIR $Hg_{1-x}Cd_xTe$ detectors in 2003 [51] but did not receive

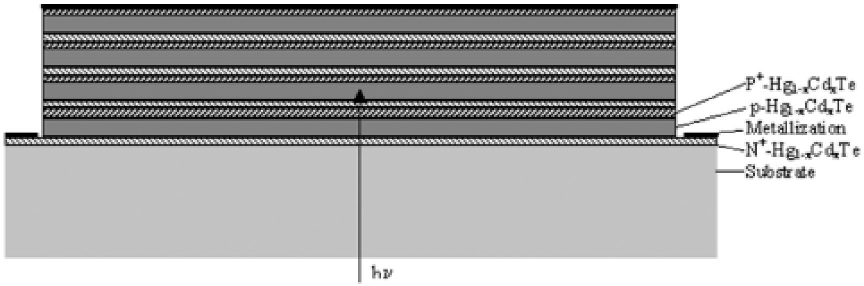

Figure 1-11: Schematic structure of a multi-junction Hg$_{1-x}$Cd$_x$Te photodetector. Image from [51].

much attention. Instead of Esaki tunnel junctions, the unique band alignments in 6.1 Å family of materials (InAs, GaSb, and AlSb) can also be utilized to realize a multi-stage detector. Interband cascade infrared photodetectors (ICIPs) [52] are such multiple-stage detectors. As the bulk of work presented in this dissertation is based on ICIPs, their structure, operation principles and characteristics are discussed in details in Chapter 2.

1.3.2.2.8 Survey of IR photon detectors

From the early efforts on Hg$_{1-x}$Cd$_x$Te photodetectors starting in 1959 [53], different material systems and device architectures have been proposed and investigated to replace or surpass this technology. Although Hg$_{1-x}$Cd$_x$Te has been the most promising technology to achieve the theoretical projections for the high-temperature operation of photon detectors, today, after ~60 years, state-of-the-art IR detectors for MWIR-VLWIR bands still require cryogenic cooling for their operation.

There have been efforts to replace Hg$_{1-x}$Cd$_x$Te with lower cost and more robust material systems, however, technologies such as III-V narrow bandgap materials suffer from low material quality and short carrier lifetime. While there have been some theoretical works that predict superior performance for Auger-limited III-V based type-II superlattice (SL) photodetectors (see section 2.2.2) [54, 55], the material quality for these detectors is not ideal and is limited by the *g*-*r* process. Recent works on barrier structures have shown some promise to overcome the *g*-*r* limitations in III-V detectors, however, $Hg_{1-x}Cd_xTe$ still holds its position as the highest performance technology. Table 1-3 provides a brief overview of the performance of the state-of-the-art IR detectors' technologies for the different IR bands. As can be seen in this table, the performance of type-II SL detectors with barrier structures has become comparable to $Hg_{1-x}Cd_xTe$ at some wavelengths.

Table 1-3: Summary of different IR detector technologies and their performance at different IR bands.

Material	λ_c (µm)	Performance			Comments
		RA ($\Omega.cm^2$)	**Responsivity** (A/W)	D^* ($cm.Hz^{1/2}/W$)	
InGaAs [14]	1.7	-	-	5.0×10^{12}	300 K
HgCdTe [56]	3	-	-	8.0×10^{9}	300K, PV detector
$InAs/InAs_{1-x}Sb_x/AlAs_{1-x}Sb_x$ SL [57]	1.8	285 at -50 mV	0.47 at 0 V	6.45×10^{10}	300 K, *pin* structure
InAs/GaSb/AlSb SL [58]	2.2	15 at 0 V	41.5% (QE), at 0 V	1.7×10^{10}	300 K, M structure
InAs/GaSb/AlInSb/GaSb SL [59]	2.9	4.18 at 0 V	0.37 at 0 V	5.8×10^{9}	300 K, 3-stage ICIP
HgCdTe [56]	4	-	-	4×10^{10}	230 K, PV detector
HgCdTe [56]	4	-	-	4×10^{9}	300 K, PV detector
InAs/GaSb SL [60]	~4	2,470 at 0 V	0.25 at 0 V	1.19×10^{11}	200 K, 5-stage ICIP
InAs/GaSb SL [61]	4.2	5,100 at 0 V	50% (QE), at 0V	1.05×10^{12}	150 K, M structure
InAs/GaSb [62]	4.9	22,000 at -50 mV	2.49 at -50 mV	1.2×10^{12}	150 K, pMp structure
HgCdTe [56]	~8	0.0006	-	5.0×10^{8}	195 K, PV detector
HgCdTe [56]	~8	-	-	8×10^{7}	300 K, PV detector
HgCdTe [56]	~8	-	-	1.2×10^{8}	300 K, multi junction
InAs/GaSb SL [41]	9.9	14,000 at 0 V	1.5 at 200 mV	1.1×10^{11}	78 K, CBIRD
$InAs/InAs_{1-x}Sb_x$ SL [63]	10.0	119 at -90 mV	4.47 at -90 mV	2.8×10^{11}	77 K, nBn structure
InAs/GaSb SL [64]	8.3	1,429 at 0 V	0.14 at 0 V	1.3×10^{11}	78 K, 4-stage ICIP
InAs/GaSb SL [64]	8.7	0.063 at 0 V	0.23 at 0 V	1.7×10^{9}	200 K, 6-stage ICIP
InAs/GaSb SL [64]	10.3	0.01 at 0 V	0.17 at 0 V	1.3×10^{8}	300 K, 8-stage ICIP
$InAs/InAs_{1-x}Sb_x$ [99]	14.6	0.84 at 0 V	4.8 at -300 mV	1.4×10^{10}	77 K, *pin* structure

1.4 Thermophotovoltaic conversion of infrared radiation

1.4.1 Background

Thermophotovoltaic (TPV) devices are the counterpart of solar cells that convert IR radiation from a relatively low-temperature heat source to electrical power. Given that most of the heat source radiation falls in IR band, narrow bandgap semiconductors are typically used in TPV systems.

The earliest efforts on the thermophotovoltaic conversion of energy go back to 1956 [65]. The first reported TPV system utilized a silicon solar cell to convert the radiation from a camping lantern to electric power [66]. While TPV systems were widely explored by the U.S. Army for power generation in the following years, TPV systems did not reach their efficiency and performance expectations after several years of research and development and research on TPVs declined in the 1970s [65]. Later, owing to the significant enhancements in the growth and fabrication of III-V semiconductors, TPVs were reconsidered in 1990s and early 2000s for power generation. However, this line of research went through another period of hibernation as the challenges associated with narrow-bandgap III-V semiconductors namely, low open-circuit voltage and efficiency remained unresolved (see Chapter 7 for further details). Since TPV cells share some roots with IR detectors and are made of similar material as that of III-V IR photodetectors, the recent breakthroughs, and advancements of III-V IR photodetectors (*e.g.*, barrier and quantum engineered structures) could result in another round of extensive research on TPV systems.

TPV systems can be used for electricity generation in different fields including waste heat recovery in the steel and glass industries, off-grid power generation, and portable power systems for battlefields, where quiet and compact power generators are of critical importance. These systems have also been used in hybrid electric car prototypes (*e.g.,* Viking 29) [67] for power generation. Despite their wide range of applications, TPVs have been underutilized compared to solar cells, mainly due to their high production costs associated with their required substrates and growth process. Moreover, narrow bandgap TPV cells made of III-V compounds [68, 69] are far from optimal and suffer from low material quality, non-idealities in device fabrication and passivation, and large non-radiative losses.

1.4.2 Ultimate conversion efficiency in TPV cells

Heat sources with a broad radiation spectral content are the simplest form of heat sources used in TPV systems. However, the broad spectrum of heat radiation is the main loss mechanism in these systems. Since TPV cells have a particular bandgap, the fraction of the source radiation that falls below the device bandgap is not absorbed and is wasted. On the other hand, photons with energies higher than the bandgap will lose part of their energy by thermalization. The seminal work by Shockley and Queisser in 1961 [70] determined that the optimum bandgap for photovoltaic conversion depends on the source temperature and the cell's bandgap with the optimum bandgap being $E_g \approx 2k_B T_{\text{Source}}$ [71]. This means while silicon is a good choice for solar cells ($T_{sun} \approx 5{,}800$ K), for TPV systems with source temperatures well below 5,800 K, narrower bandgap semiconductors are required. The theoretical work by Shockley-Queisser on the evaluation of the ultimate efficiency for single-junction solar cells can be extended to TPV cells with different source temperatures [72, 73]. Since TPV cells are in close proximity to the heat source, the solid angle (Ω) is typically in the range of 1-4π sr (Ω is limited to 6.85×10^{-5} sr in non-concentrated solar cells) [72]. Figure 1-12 shows the ultimate conversion efficiency curves calculated for selected blackbody temperatures based on the Shockley-Queisser detailed balance limit theory (Ω=4π sr). The assumptions made in this theory are listed below:

- All the incoming photons with energies higher or equal to the device bandgap are absorbed. This means the photon reflection at the device top surface is negligible and the absorber is thick enough to absorb all incident photons.
- Each absorbed photon generates an electron-hole pair that is either separated and collected at the device contacts or recombines radiatively. This means the only channel for carrier loss is the radiative recombination.

Based on this theory, for T_{Source}=2,000 K the optimum cell bandgap is 360 meV. This bandgap results in an ultimate conversion efficiency of 34.7%, which is significantly higher than the efficiencies obtained in state-of-the-art TPV systems with spectrally engineered heat sources. As stated earlier, the material quality and related parameters such as carrier lifetime and diffusion length are far from the above assumptions (*e.g.*, infinite diffusion length) made in this theory. Therefore, real device implementations give efficiencies significantly lower than these projections.

In contrast to solar cells, where the radiation source is far away (~1.5×10^{8} km) from the cell, in TPV systems the radiant source is in close proximity (a few microns to several centimeters) to the cell. Being in close proximity to the heat source makes

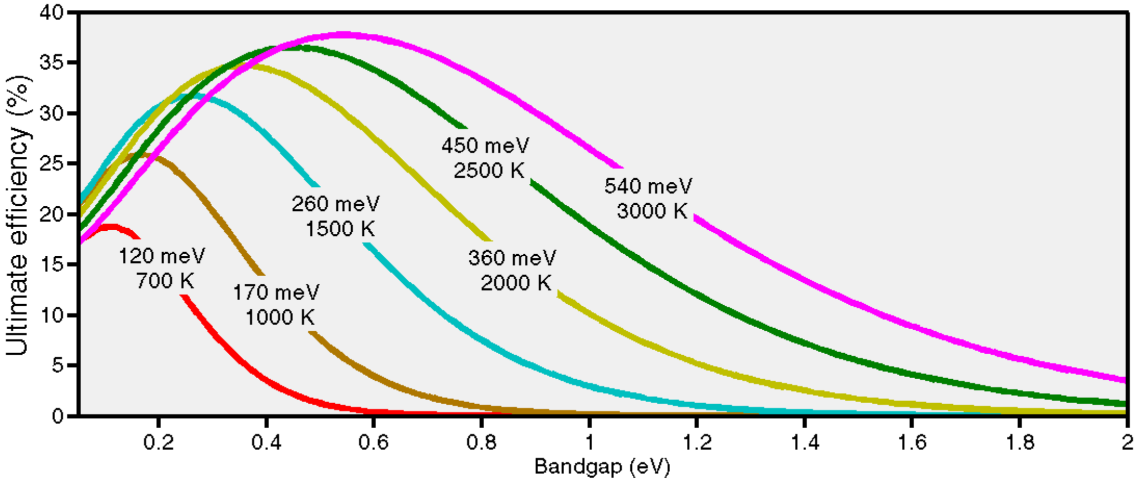

Figure 1-12: The ultimate conversion efficiency based on the theory of detailed balance limit for selected blackbody temperatures. Values on each curve represent the optimum bandgap with the highest efficiency at each temperature.

spectrum shaping a possible route to enhance the system efficiency. Since the below bandgap and thermalization losses are reduced by matching the radiation pattern with the device bandgap, the system efficiency can be significantly improved in TPV systems. Moreover, larger bandgap TPV cells with higher quality and performance can also be used in spectrally engineered TPV systems to further enhance the system efficiency.

1.4.3 Different components of a TPV system

A TPV system that efficiently converts heat radiation into electricity is comprised of three components, namely emitter, and/or filter, TPV cell with a back reflector. Figure 1-13 illustrates the schematic of a typical TPV system. Given that the heat (IR radiation) in a TPV system comes from different sources such as combustion, solar radiation, nuclear reactions, and waste heat, selective emitters, and/or filters are utilized to closely match the spectral content of the heat source to the TPV cell bandgap.

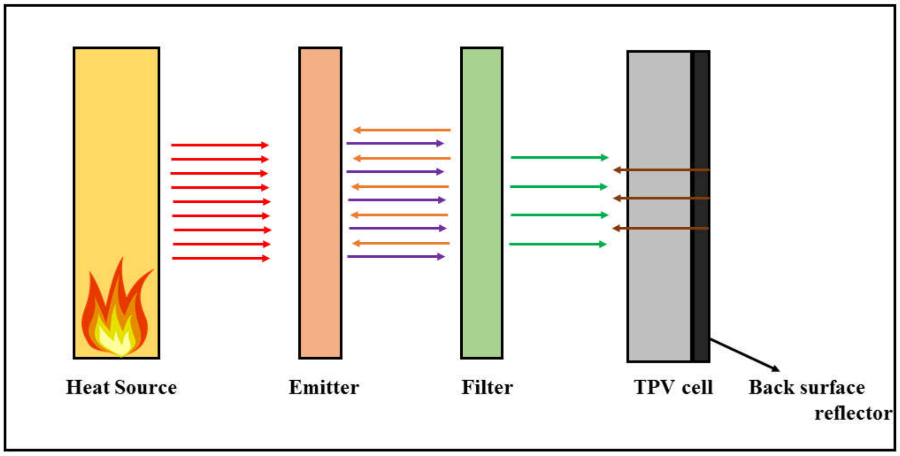

Figure 1-13: Schematic diagram of a TPV system.

A selective emitter absorbs the radiation from a heat source and reradiates the absorbed energy with an altered spectral content that fits the cell's bandgap. Different types of selective emitters made of rare earth oxides [74] have been developed for TPV systems.

More recently, artificial structures, *i.e.*, photonic crystals [75, 76] and metamaterials [77, 78] have been developed to realize efficient selective emitters. One can also enhance the system efficiency by reflecting back the below bandgap photons and high energy photons (as compared to the cell's bandgap) back to the heat source.

The final step to reduce the radiation loss in TPV systems is the use of back surface reflectors (BSRs). BSRs can be as simple as a layer of gold deposited on the back surface of the TPV cell or made of multiples layers such as MgF_2/ SiO_2/Au for enhanced reflection [79, 80].

1.4.4 Survey of thermophotovoltaic cells

As discussed in the previous section, a TPV system is more than just TPV cells, in recent years, the research on other components of TPV systems (*e.g.*, selective emitters and filters) have been more active than the research on TPV cells. For instance, the advent of artificial structures *i.e.*, photonic crystals and metamaterials have resulted in novel structures for selective emitters. Selective emitters and other components of a TPV system are beyond the scope of this dissertation and are not included in this survey.

Research on TPV cells is mainly devoted to cells with bandgaps larger than 0.5 eV. System efficiencies of 19.5-25% [81, 82] have been reported with TPV cells made of InGaAs and InGaAsSb. However, the use of narrower bandgap semiconductors could enhance the system efficiency when the heat source temperature is below 1000 K. TPV cells with bandgaps below 0.5 eV suffer from low open-circuit voltage and fill factor [83-85]. The poor performance of narrow bandgap TPV cells is mainly related to the material quality and could be enhanced by a better understanding of these limiting factors. Table 1-4 provides a brief summary of the performance of TPV cells made of different materials in the last two decades.

Table 1-4: Summary of the device performance for different TPV technologies.

Material	E_g (eV)	J_{sc} (A/cm^2)	V_{oc} (V)	FF	Voltage factor	Comment
GaSb [86]	0.72	3	~0.41	-	0.57	MOVPE
$InGa_{0.53}As_{0.47}$ [87]	0.74	1	0.465	0.64	0.63	
InGaAsSb [88]	0.53	3	0.344	-	0.65	LPE on GaSb
InGaAsSb [89]	0.53	1	0.3	-	0.57	MOVPE and MBE on GaSb
InGaAsSb [90]	0.53	2.9	0.306	0.67	0.58	MOVPE on GaSb
Ge [91]	0.66	10	0.43	-	0.65	
$In_{0.69}Ga_{0.31}As$ [92]	0.6	2.26	0.355	0.665	0.59	MBE on InP
InAsSbP [83]	0.35	3	0.12	-	0.34	LPE on InAs
InAsSbP [83]	0.44	3	0.17	-	0.39	
InAsSbP [93]	0.45	3	0.15	-	0.33	
InGaAs [94]	0.74	0.288	0.405	0.65	0.55	MOVPE on InP
Two-junction InGaAs [95]						MOVPE on InP
J1	0.74	0.303	0.448	0.68	0.61	
J2	0.63	0.461	0.284	0.52	0.45	
Total		0.296	0.724	0.73	-	
$Ga_{0.03}In_{0.97}As_{0.81}P_{0.06}Sb_{0.13}$ [84]	0.34	0.29	0.028	0.33	0.08	LPE on InAs
Two-junction GaSb/GaInAsSb [96]	0.726/0.56	0.7	0.61	0.75	-	LPE on GaSb
InGaSb [97]	0.56	3	0.27	-	0.48	
InGaSb [98]	0.7	0.8	0.38	0.63	0.54	
InAs [85]	0.32	0.89	0.06	0.37	0.19	LPE on InAs

1.5 Dissertation outline

The main focus of this dissertation is on the design and characterization of interband cascade (IC) structures for high-performance IR photodetectors and TPV cells. Chapter 2 provides a detailed historical background and overview of fundamental concepts in IC optoelectronic devices including their unique features. Chapter 3 discusses the design and development of three sets of high-temperature IR photodetectors for LWIR and VLWIR bands. Chapter 4 presents the design and implementation of high-performance SWIR IC detectors along with details on the SL design and limiting factors on the device performance. Chapter 5 details the high-speed and high-temperature operation of MWIR IC optoelectronic systems with IC lasers and detectors. Further discussions on the system design and modeling are also provided in this chapter. Chapter 6 presents our research on monolithically integrated mid-IR lasers and photodetectors. Detailed discussions on the device design, fabrication and characterization along with fabrication issues and challenges are presented. Chapter 7 reports on the room temperature and above performance of two sets of ICTPV devices with cutoff wavelengths of ~3 µm and >5 µm. Details of the device performance and characterization are given in this chapter. Finally, Chapter 8 summarizes the outcomes of this dissertation followed by some concluding remarks on further research and the future of IC optoelectronic devices.

1.6 Bibliography

[1] R. G. Driggers, Encyclopedia of Optical Engineering: Las-Pho, vol. 2, CRC press, 2003.

[2] *Gemini Observatory: Exploring the universe, sharing its wonders*. Available: http://www.gemini.edu/

[3] D. S. Bomse, D. C. Hovde, D. B. Oh, J. A. Silver, and A. C. Stanton, "Diode laser spectroscopy for on-line chemical analysis," in *Proceedings of SPIE, Optically Based Methods for Process Analysis*, vol. 1681, pp. 138-148, 1992.

[4] *The HITRAN Database*. Available: https://www.cfa.harvard.edu/hitran/

[5] A. Soibel, M. W. Wright, W. H. Farr, S. A. Keo, C. J. Hill, R. Q. Yang*, et al.*, "Midinfrared interband cascade laser for free space optical communication," *IEEE Photonics Technology Letters,* vol. 22, pp. 121-123, 2010.

[6] J. Faist, F. Capasso, D. L. Sivco, C. Sirtori, A. L. Hutchinson, and A. Y. Cho, "Quantum cascade laser," *Science,* vol. 264, pp. 553-556, 1994.

[7] R. Q. Yang, "Infrared laser based on intersubband transitions in quantum wells," *Superlattices and Microstructures,* vol. 17, p. 77, 1995.

[8] M. S. Vitiello, G. Scalari, B. Williams, and P. D. Natale, "Quantum cascade lasers : 20 years of challenges," *Optics Express,* vol. 23, pp. 5167-5182, 2015.

[9] I. Vurgaftman, R. Weih, M. Kamp, J. Meyer, C. Canedy, C. Kim*, et al.*, "Interband cascade lasers," *Journal of Physics D: Applied Physics,* vol. 48, p. 123001, 2015.

[10] D. R. Rhiger, "Performance comparison of long-wavelength infrared type II superlattice devices with HgCdTe," *Journal of Electronic Materials,* vol. 40, pp. 1815-1822, 2011.

[11] A. Rogalski, *Infrared detectors*, CRC press, 2010.

[12] D. Long, "Generation-recombination noise limited detectivities of impurity and intrinsic photoconductive 8–14μ infrared detectors," *Infrared Physics,* vol. 7, pp. 121-128, 1967.

[13] R. C. Jones, "A method of describing the detectivity of photoconductive cells," *Review of Scientific Instruments,* vol. 24, pp. 1035-1040, 1953.

[14] A. Rogalski, "HgCdTe infrared detector material: history, status and outlook," *Reports on Progress in Physics,* vol. 68, p. 2267, 2005.

[15] P. Martyniuk, J. Antoszewski, M. Martyniuk, L. Faraone, and A. Rogalski, "New concepts in infrared photodetector designs," *Applied Physics Reviews,* vol. 1, p. 041102, 2014.

[16] J. Caniou, *Passive infrared detection: theory and applications*, Springer Science & Business Media, 2013.

[17] *FLIR ONE Thermal imaging camera attachment for iOS and android*. Available: http://www.flir.com/flirone/ios-android/

[18] *CompactPRO - High-performance thermal imaging for your smartphone*. Available: http://www.thermal.com/products/compactpro/

[19] R. Ciupa and A. Rogalski, "Performance limitations of photon and thermal infrared detectors," *Optoelectronics Review,* pp. 257-266, 1997.

[20] N. Neumann and V. Banta, "P12-Comparison of Pyroelectric and Thermopile Detectors," *Proceedings IRS^2 2013,* pp. 139-143, 2013.

[21] J. Hecht, "Photonic frontiers: Room-temperature IR imaging-microbolometer arrays enable uncooled infrared cameras," *Laser Focus World,* vol. 48, p. 70, 2012.

[22] A. Rogalski, "Infrared detectors: status and trends," *Progress in Quantum Electronics,* vol. 27, pp. 59-210, 2003.

[23] A. Rogalski, "History of infrared detectors," *Optoelectronics Review,* vol. 20, pp. 279-308, 2012.

[24] B. Levine, K. Choi, C. Bethea, J. Walker, and R. Malik, "New 10 μm infrared detector using intersubband absorption in resonant tunneling GaAlAs superlattices," *Applied Physics Letters,* vol. 50, pp. 1092-1094, 1987.

[25] H. L. Schneider, Hui Chun, *Quantum well infrared photodetectors: Physics and applications*, Springer, 2006.

[26] S. Gunapala, B. Levine, D. Ritter, R. Hamm, and M. Panish, "InGaAs/InP long wavelength quantum well infrared photodetectors," *Applied Physics Letters,* vol. 58, pp. 2024-2026, 1991.

[27] D. Hofstetter, S.-S. Schad, H. Wu, W. J. Schaff, and L. F. Eastman, "GaN/AlN-based quantum-well infrared photodetector for 1.55 μm," *Applied Physics Letters,* vol. 83, pp. 572-574, 2003.

[28] R. Karunasiri, J. Park, and K. Wang, "$Si_{1-x}Ge_x$/Si multiple quantum well infrared detector," *Applied Physics Letters,* vol. 59, pp. 2588-2590, 1991.

[29] D. D. Coon and R. P. G. Karunasiri, "New mode of IR detection using quantum wells," *Applied Physics Letters,* vol. 45, pp. 649-651, 1984.

[30] L. C. West and S. J. Eglash, "First observation of an extremely large-dipole infrared transition within the conduction band of a GaAs quantum well," *Applied Physics Letters,* vol. 46, pp. 1156-1158, 1985.

[31] R. Q. Yang, J. Xu, and M. Sweeny, "Selection rules of intersubband transitions in conduction-band quantum wells," *Physical Review B,* vol. 50, p. 7474, 1994.

[32] H. Liu, M. Buchanan, and Z. Wasilewski, "How good is the polarization selection rule for intersubband transitions?," *Applied Physics Letters,* vol. 72, pp. 1682-1684, 1998.

[33] M. Helm, "The basic physics of intersubband transitions," *Semiconductors and Semimetals,* vol. 62, pp. 1-99, 1999.

[34] P. Martyniuk and A. Rogalski, "Quantum-dot infrared photodetectors: Status and outlook," *Progress in Quantum Electronics,* vol. 32, pp. 89-120, 2008.

[35] I. N. Stranski and L. v. Krastanow, "Zur Theorie der orientierten Ausscheidung von Ionenkristallen aufeinander," *Monatshefte für Chemie/Chemical Monthly,* vol. 71, pp. 351-364, 1937.

[36] S. Krishna, "Quantum dots-in-a-well infrared photodetectors," *Infrared Physics & Technology,* vol. 47, pp. 153-163, 2005.

[37] D. Long, "Photovoltaic and photoconductive infrared detectors," in *Optical and infrared detectors*, Springer, pp. 101-147, 1980.

[38] S. Maimon and G. W. Wicks, "nBn detector, an infrared detector with reduced dark current and higher operating temperature," *Applied Physics Letters,* vol. 89, p. 151109, 2006.

[39] P. Martyniuk, M. Kopytko, and A. Rogalski, "Barrier infrared detectors," *Optoelectronics Review,* vol. 22, pp. 127-146, 2014.

[40] J. Nelson, *The physics of solar cells*, World Scientific, 2003.

[41] D. Z.-Y. Ting, C. J. Hill, A. Soibel, S. a. Keo, J. M. Mumolo, J. Nguyen*, et al.*, "A high-performance long wavelength superlattice complementary barrier infrared detector," *Applied Physics Letters,* vol. 95, p. 023508, 2009.

[42] D. Hofstetter, M. Beck, and J. Faist, "Quantum-cascade-laser structures as photodetectors," *Applied Physics Letters,* vol. 81, pp. 2683-2685, 2002.

[43] D. Hofstetter, M. Graf, T. Aellen, J. Faist, L. Hvozdara, and S. Blaser, "23 GHz operation of a room temperature photovoltaic quantum cascade detector at 5.35 µm," *Applied Physic Letters,* vol. 89, pp. 1-3, 2006.

[44] A. Vardi, N. Kheirodin, L. Nevou, H. Machhadani, L. Vivien, P. Crozat*, et al.*, "High-speed operation of GaN/AlGaN quantum cascade detectors at λ=1.55 µm," *Applied Physic Letters,* vol. 93, 2008.

[45] S. Sakr, P. Crozat, D. Gacemi, Y. Kotsar, A. Pesach, P. Quach*, et al.*, "GaN/AlGaN waveguide quantum cascade photodetectors at λ≈ 1.55 µm with enhanced responsivity and~ 40 GHz frequency bandwidth," *Applied Physics Letters,* vol. 102, p. 011135, 2013.

[46] F. R. Giorgetta, E. Baumann, M. Graf, Q. Yang, C. Manz, K. Köhler*, et al.*, "Quantum cascade detectors," *IEEE Journal of Quantum Electronics,* vol. 45, pp. 1039-1052, 2009.

[47] D. Hofstetter, F. R. Giorgetta, E. Baumann, Q. Yang, C. Manz, and K. Köhler, "Mid-infrared quantum cascade detectors for applications in spectroscopy and pyrometry," *Applied Physics B,* vol. 100, pp. 313-320, 2010.

[48] P. Reininger, T. Zederbauer, B. Schwarz, H. Detz, D. MacFarland, A. M. Andrews*, et al.*, "InAs/AlAsSb based quantum cascade detector," *Applied Physics Letters,* vol. 107, p. 081107, 2015.

[49] P. Reininger, B. Schwarz, A. Harrer, T. Zederbauer, H. Detz, A. M. Andrews*, et al.*, "Photonic crystal slab quantum cascade detector," *Applied Physics Letters,* vol. 103, p. 241103, 2013.

[50] A. Harrer, B. Schwarz, R. Gansch, P. Reininger, H. Detz, T. Zederbauer*, et al.*, "Plasmonic lens enhanced mid-infrared quantum cascade detector," *Applied Physics Letters,* vol. 105, p. 171112, 2014.

[51] J. Piotrowski, P. Brzozowski, and K. Jóźwikowski, "Stacked multijunction photodetectors of long-wavelength radiation," *Journal of Electronic Materials,* vol. 32, pp. 672-676, 2003.

[52] J. V. Li, R. Q. Yang, C. J. Hill, and S. L. Chuang, "Interband cascade detectors with room temperature photovoltaic operation," *Applied Physics Letters,* vol. 86, p. 101102, 2005.

[53] W. Lawson, S. Nielsen, E. Putley, and A. Young, "Preparation and properties of HgTe and mixed crystals of HgTe-CdTe," *Journal of Physics and Chemistry of Solids,* vol. 9, pp. 325-329, 1959.

[54] C. H. Grein, P. M. Young, and H. Ehrenreich, "Minority carrier lifetimes in ideal InGaSb/InAs superlattices," *Applied Physics Letters,* vol. 61, p. 2905, 1992.

[55] C. H. Grein, P. M. Young, M. E. Flatté, and H. Ehrenreich, "Long wavelength InAs/InGaSb infrared detectors: Optimization of carrier lifetimes," *Journal of Applied Physics,* vol. 78, pp. 7143-7152, 1995.

[56] Vigo System S.A. catalogue.

[57] A. Haddadi, X. V. Suo, S. Adhikary, P. Dianat, R. Chevallier, A. M. Hoang*, et al.*, "High-performance short-wavelength infrared photodetectors based on type-II $InAs/InAs_{1-x}Sb_x/AlAs_{1-x}Sb_x$ superlattices," *Applied Physics Letters,* vol. 107, p. 141104, 2015.

[58] A. M. Hoang, G. Chen, A. Haddadi, S. Abdollahi Pour, and M. Razeghi, "Demonstration of shortwavelength infrared photodiodes based on type-II

InAs/GaSb/AlSb superlattices," *Applied Physics Letters,* vol. 100, p. 211101, 2012.

[59] H. Lotfi, L. Li, L. Lei, R. Q. Yang, J. F. Klem, and M. B. Johnson, "Short-wavelength interband cascade infrared photodetectors operating above room temperature," *Journal of Applied Physics,* vol. 119, p. 023105, 2016.

[60] Z.-B. Tian and S. Krishna, "Mid-infrared interband cascade photodetectors with different absorber designs," *IEEE Journal of Quantum Electronics,* vol. 51, pp. 1-5, 2015.

[61] S. A. Pour, E. K. Huang, G. Chen, A. Haddadi, B.-M. Nguyen, and M. Razeghi, "High operating temperature midwave infrared photodiodes and focal plane arrays based on type-II InAs/GaSb superlattices," *Applied Physics Letters,* vol. 98, p. 143501, 2011.

[62] G. Chen, A. Haddadi, A.-M. Hoang, R. Chevallier, and M. Razeghi, "Demonstration of type-II superlattice MWIR minority carrier unipolar imager for high operation temperature application," *Optics Letters,* vol. 40, pp. 45-47, 2015.

[63] A. Haddadi, G. Chen, R. Chevallier, A. Hoang, and M. Razeghi, "InAs/$InAs_{1-x}Sb_x$ type-II superlattices for high performance long wavelength infrared detection," *Applied Physics Letters,* vol. 105, p. 121104, 2014.

[64] L. Lei, L. Li, H. Ye, H. Lotfi, R. Q. Yang, M. B. Johnson*, et al.*, "Long wavelength interband cascade infrared photodetectors operating at high temperatures," *Journal of Applied Physics,* vol. 120, p. 193102, 2016.

[65] R. E. Nelson, "A brief history of thermophotovoltaic development," *Semiconductor Science and Technology,* vol. 18, p. S141, 2003.

[66] H. Kolm, "Solar-battery power source," *Quarterly Progress Report,* vol. 13, 1956.

[67] S. Christ and M. Seal, "Viking 29-a thermophotovoltaic hybrid vehicle designed and built at Western Washington University," SAE Technical Paper 0148-7191, 1997.

[68] T. Coutts, "A review of progress in thermophotovoltaic generation of electricity," *Renewable and Sustainable Energy Reviews,* vol. 3, pp. 77-184, 1999.

[69] M. G. Mauk, "Survey of thermophotovoltaic (TPV) devices," in *Mid-infrared Semiconductor Optoelectronics*, Springer, pp. 673-738, 2006.

[70] W. Shockley and H. J. Queisser, "Detailed balance limit of efficiency of p-n junction solar cells," *Journal of Applied Physics,* vol. 32, pp. 510-519, 1961.

[71] D. Chubb, *Fundamentals of thermophotovoltaic energy conversion*, Elsevier, 2007.

[72] G. D. Cody, "Theoretical maximum efficiencies for thermophotovoltaic devices," in *Fourth NREL Conference on Thermophotovoltaic Generation of Electricity*, pp. 58-67, 1999.

[73] J. L. Gray and A. El-Husseini, "A simple parametric study of TPV system efficiency and output power density including a comparison of several TPV materials," *AIP Conference Proceedings,* vol. 358, pp. 3-15, 1996.

[74] B. Bitnar, W. Durisch, J.-C. Mayor, H. Sigg, and H. Tschudi, "Characterisation of rare earth selective emitters for thermophotovoltaic applications," *Solar Energy Materials and Solar Cells,* vol. 73, pp. 221-234, 2002.

[75] P. Nagpal, S. E. Han, A. Stein, and D. J. Norris, "Efficient low-temperature thermophotovoltaic emitters from metallic photonic crystals," *Nano Letters,* vol. 8, pp. 3238-3243, 2008.

[76] M. Pralle, N. Moelders, M. McNeal, I. Puscasu, A. Greenwald, J. Daly*, et al.*, "Photonic crystal enhanced narrow-band infrared emitters," *Applied Physics Letters,* vol. 81, pp. 4685-4687, 2002.

[77] C. Wu, B. Neuner III, J. John, A. Milder, B. Zollars, S. Savoy*, et al.*, "Metamaterial-based integrated plasmonic absorber/emitter for solar thermo-photovoltaic systems," *Journal of Optics,* vol. 14, p. 024005, 2012.

[78] S. Molesky, C. J. Dewalt, and Z. Jacob, "High temperature epsilon-near-zero and epsilon-near-pole metamaterial emitters for thermophotovoltaics," *Optics Express,* vol. 21, pp. A96-A110, 2013.

[79] X. Wu, A. Duda, J. J. Carapella, J. S. Ward, J. D. Webb, and M. W. Wanlass, "A study of contacts and back-surface reflectors for 0.6-eV $Ga_{0.32}In_{0.68}As/InAs_{0.32}P_{0.68}$ thermophotovoltaic monolithically interconnected modules," in *AIP Conference Proceedings*, vol. 460, pp. 517-524, 1999.

[80] M. Mauk and V. Andreev, "GaSb-related materials for TPV cells," *Semiconductor Science and Technology,* vol. 18, p. S191, 2003.

[81] E. Brown, G. Nichols, P. Baldasaro, D. DePoy, S. Burger, L. Danielson*, et al.*, *The Status of Thermophotovoltaic Energy Conversion Technology at Lockheed Martin Corp*, United States, Department of Energy, 2003.

[82] V. L. Teofilo, P. Choong, J. Chang, Y. L. Tseng, and S. Ermer, "Thermophotovoltaic Energy Conversion for Space," *The Journal of Physical Chemistry C,* vol. 112, pp. 7841-7845, 2008.

[83] M. Mauk, O. Sulima, J. Cox, and R. Mueller, "Low-bandgap (0.3 to 0.5 eV) InAsSbP thermophotovoltaics: assessment for open-circuit voltage improvements," in *3rd World Conference on Photovoltaic Energy Conversion, 2003.*

[84] K. Cheetham, P. Carrington, N. Cook, and A. Krier, "Low bandgap GaInAsSbP pentanary thermophotovoltaic diodes," *Solar Energy Materials and Solar Cells,* vol. 95, pp. 534-537, 2011.

[85] A. Krier, M. Yin, A. R. J. Marshall, and S. E. Krier, "Low bandgap InAs-based thermophotovoltaic cells for heat-electricity conversion," *Journal of Electronic Materials,* vol. 45, pp. 2826-2830, 2016.

[86] A. Bett and O. Sulima, "GaSb photovoltaic cells for applications in TPV generators," *Semiconductor Science and Technology,* vol. 18, p. S184, 2003.

[87] L. Karlina, A. Vlasov, M. Kulagina, and N. K. Timoshina, "Thermophotovoltaic cells based on $In_{0.53}Ga_{0.47}As$/InP heterostructures," *Semiconductors,* vol. 40, pp. 346-350, 2006.

[88] O. Sulima, R. Beckert, A. Bett, J. Cox, and M. Mauk, "InGaAsSb photovoltaic cells with enhanced open-circuit voltage," *IEE Proceedings-Optoelectronics,* vol. 147, pp. 199-204, 2000.

[89] H. Choi, C. Wang, G. Turner, M. Manfra, D. Spears, G. Charache*, et al.*, "High-performance GaInAsSb thermophotovoltaic devices with an AlGaAsSb window," *Applied Physics Letters,* vol. 71, 1997.

[90] M. W. Dashiell, J. F. Beausang, H. Ehsani, G. Nichols, D. M. Depoy, L. R. Danielson*, et al.*, "Quaternary InGaAsSb thermophotovoltaic diodes," *IEEE Transactions on Electron Devices,* vol. 53, pp. 2879-2891, 2006.

[91] V. Khvostikov, V. Rumyantsev, O. Khvostikova, M. Shvarts, P. Gazaryan, S. Sorokina*, et al.*, "Thermophotovoltaic cells based on low-bandgap compounds," in *AIP Conference Proceedings*, vol. 738 , pp. 436-444, 2004.

[92] M. K. Hudait, M. Brenner, and S. Ringel, "Metamorphic $In_{0.7}Al_{0.3}As/In_{0.69}Ga_{0.31}As$ thermophotovoltaic devices grown on graded $InAs_yP_{1-y}$ buffers by molecular beam epitaxy," *Solid-State Electronics,* vol. 53, pp. 102-106, 2009.

[93] V. Andreev, V. Khvostikov, O. Khvostikova, E. Oliva, V. Rumyantsev, and M. Shvarts, "Low-bandgap Ge and InAsSbP/InAs-based TPV cells," in *Fifth*

Conference on Thermophotovoltaic Generation of Electricity, pp. 383-391, 2003.

[94] R. Tuley, J. Orr, R. Nicholas, D. Rogers, P. Cannard, and S. Dosanjh, "Lattice-matched InGaAs on InP thermophovoltaic cells," *Semiconductor Science and Technology,* vol. 28, p. 015013, 2012.

[95] D. M. Wilt, R. J. Wehrer, W. F. Maurer, P. P. Jenkins, B. Wernsman, and R. W. Schultz, "Buffer layer effects on tandem InGaAs TPV devices," in *Sixth Conference on Thermophotovoltaic Generation of Electricity*, pp. 453-461, 2004.

[96] V. Andreev, V. Khvostikov, V. Larionov, V. Rumyantsev, S. Sorokina, M. Shvarts*, et al.*, "Tandem GaSb/InGaAsSb thermophotovoltaic cells," in *26th Photovoltaic Specialists Conference*, pp. 935-938, 1997.

[97] P. Dutta, J. Borrego, H. Ehsani, G. Rajagopalan, I. Bhat, R. Gutmann*, et al.*, "GaSb and $Ga_{1-x}In_xSb$ thermophotovoltaic cells using diffused junction technology in bulk substrates," in *Fifth Conference on Thermophotovoltaic Generation of Electricity*, pp. 392-401, 2003.

[98] V. Sundaram, S. Saban, M. Morgan, W. Horne, B. Evans, J. Ketterl*, et al.*, "GaSb based ternary and quaternary diffused junction devices for TPV applications," in *AIP Conference Proceedings*, vol. 401, pp. 105-115, 1997.

[99] A. Haddadi, G. Chen, R. Chevallier, A. M. Hoang, and M. Razeghi, "$InAs/InAs_{1-x}Sb_x$ type-II superlattices for high performance long wavelength infrared detection," *Applied Physics Letter,* vol. 105, p. 121104, 2014.

Chapter 2: Interband cascade structures for infrared optoelectronic devices

2.1 Background

The idea of interband cascade (IC) structures for IR optoelectronic devices goes back to 1994 [1]. IC structures were first proposed to realize efficient lasers in mid- and long-IR bands. At that time, there was a strong demand for mid- and long-IR lasers with cw operation at room temperature and lead-salt lasers were the major player for decades, although their operating temperatures were typically far below room temperature. While lead-salt lasers cover a wide range of wavelengths (3 µm to beyond 20 µm) their cw operation at room temperature has not been achieved even after several decades [2], leading to the advent of quantum engineered lasers (*viz*. quantum cascade lasers (QCLs)[3] and interband cascade lasers (ICLs)[1, 4]). In short, much of the related research and development switched from lead-salt lasers to QCLs and ICLs.

The other two members of the IC devices family: interband cascade infrared photodetector (ICIPs) and interband cascade thermophotovoltaic (ICTPV) devices have similar structures to ICLs. Simply put, the fact that the ICL structure provides a rectifying function for the flow of carriers, they can be used to achieve photovoltaic action. In fact, the first ICIPs reported in 2005 [5] were actually ICL structures. Since the active region in ICLs (absorber in ICIPs) is typically comprised of two InAs/GaInSb QWs, the detector responsivity of such ICL structures was low. In 2010 [6], ICIP structures were refined and InAs/GaSb type-II SL layers with hundreds of nanometers to a few microns thickness were used as absorbers [6, 7].

ICTPVs are a relatively new concept introduced in 2010 [8]. These devices have similar structure and operation principles to that of ICIPs, however, they operate at a forward bias in contrast to zero or reverse bias for detectors. While ICTPV devices with conversion efficiencies up to ~10% (see Chapter 7) have been recently demonstrated, there has been little work on their design, growth and fabrication compared to laser and detector IC devices.

In this chapter, a detailed overview of the theory and operation principles of different types of IC optoelectronic devices along with some discussion on the methods of their growth, fabrication and characterization is provided.

2.2 6.1 Å material system

2.2.1 Material properties and band alignments

Interband cascade devices, no matter being a laser, detector or TPV cell, are made of InAs, GaSb, AlSb and their alloys. The lattice constant of InAs (6.0583 Å), GaSb (6.09593 Å) and AlSb (6.1355 Å) are nearly matched to each other (at 6.1 Å), therefore these materials have significant technological advantages with regards to the growth and strain engineering. Different properties of these compounds are listed in Table 2-1. The heterostructures formed between these materials have unique features that make them well suited for the realizion of IC devices. As shown in Figure 2-1, all three possible band lineups can be realized with these compounds. AlSb/GaSb, AlSb/InAs, and GaSb/InAs QWs have type-I, type-II staggered and type-II broken-gap band alignments, respectively. In contrast to type-I QWs, where the electron and hole wave functions are spatially located in the same layer, the broken-gap band alignment

Table 2-1: Summary of the material properties for the 6.1 Å material family. μ_e, μ_h and ε_s are the electron mobility, hole mobility and static dielectric constant, respectively. All data are for 300 K and taken from [9].

Compound name	E_g(300 K) (eV)	Crystal structure	Lattice constant (Å)	μ_e (cm^2/V.s)	μ_h (cm^2/V.s)	ε_s	Thermal conductivity (W/cm.K)
InAs	0.36	Zinc blende	6.0583	30,000	450	14.3	0.233
GaSb	0.72	Zinc blende	6.09593	12,040	1,624	15.5	0.317
AlSb	1.63	Zinc blende	6.1355	200	420	11.21	0.592

between InAs and GaSb results in the spatial separation of electron and hole wave functions in different layers (see Figure 2-2). As such, the effective bandgap for InAs/GaSb QWs can be adjusted over a wide range of energies to cover the SWIR to VLWIR bands.

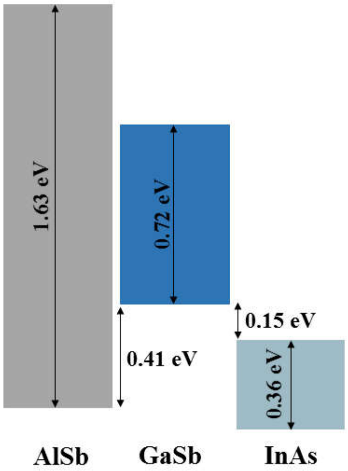

Figure 2-1: Schematic drawing of different band lineups between 6.1 Å material family.

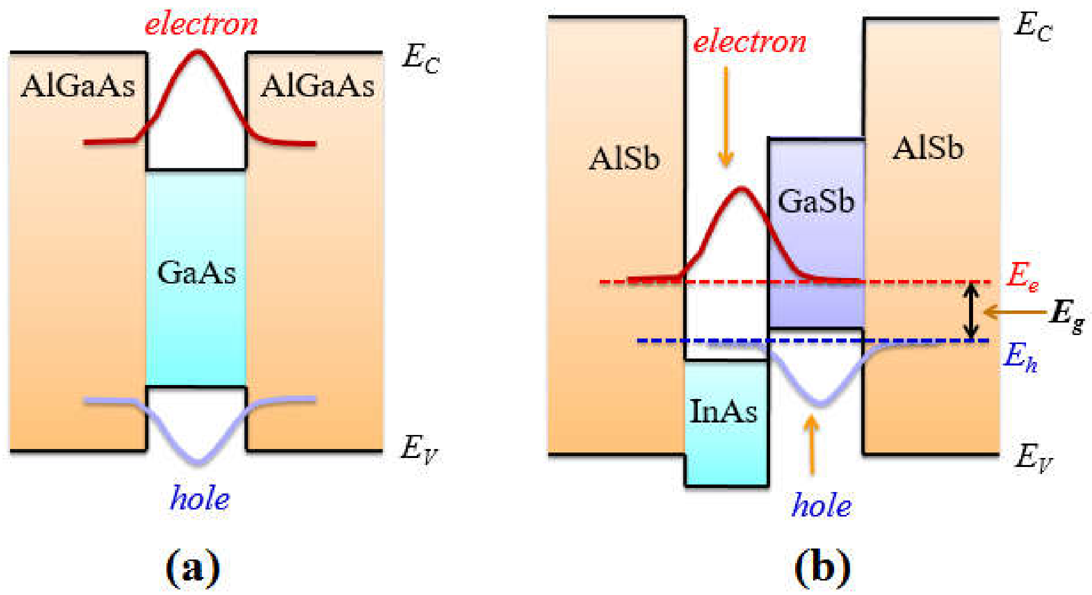

Figure 2-2: Illustrative comparison between (a) type-I and (b) type-II broken-gap QWs. While the electron and hole wave functions are located in the same layer, in a type-I QW, they are spatially separated and located in different layers in a type-II QW [10].

2.2.2 Type-II superlattice

Since their introduction in 1970 [11], superlattice (SL) structures have been broadly used to realize different types of electronic and optoelectronic devices such as transistors, lasers, and detectors. Due to the type-II broken-gap band alignment between InAs and GaSb, SL structures made of these two materials are called type-II superlattices (T2SLs). The broken-gap band alignment between the constituting layers of a T2SL (see Figure 2-3) bring about some unique features for these structures that make them a viable choice for IR detectors in the different IR bands. The T2SL bandgap can be tuned over a wide range of wavelengths from 2.3 to 30 µm by merely changing the layers' thickness. Moreover, large electron effective masses (compared to $Hg_{1-x}Cd_xTe$ with similar bandgap), which are relatively insensitive to the structure bandgap, makes them less susceptible to tunneling dark currents [12]. Moreover, the nearly matched lattice constants of InAs and GaSb makes them a great candidate for multicolor IR detectors [13].

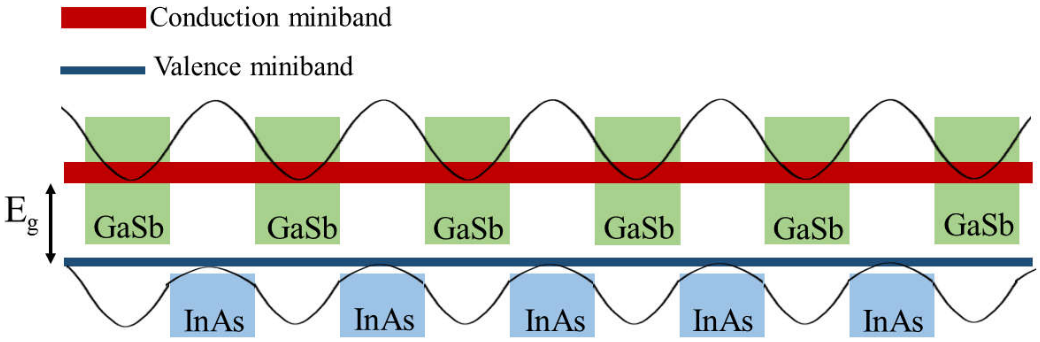

Figure 2-3: Schematic of the conduction and valence minibands in a T2SL structure made of InAs and GaSb layers.

2.3 Interband cascade lasers

ICLs are not the main focus of this dissertation, however, since the original concepts behind the ICIPs and ICTPVs have their roots in ICLs and to provide a self-contained overview of the theory of IC devices, a brief overview of ICLs is provided in the next sub-section.

2.3.1 Operation principles of ICLs

ICLs are hybrid lasers in a sense that both interband transitions that are incorporated in conventional semiconductor lasers and cascade transport utilized in QCLs are employed to achieve lasing action. IC lasers are made of multiple stages that are serially connected. Each stage in an ICL is composed of three regions, namely, active region, electron injector and hole injector. In modern ICLs, the active region is made of InAs/GaInSb/InAs QWs, which is known as W structure [14]. The optical matrix element is larger in an active region with W structure compared to single QW active regions used in early ICLs. The electron injector in an ICL is made of InAs/AlSb

QWs which facilitates the injection of electrons to the conduction band in the active region. Holes are also provided to the valence band by the hole injector, which is made of GaSb/AlSb QWs. The cascade region that includes the multiple stages is sandwiched between the bottom and top cladding layers (see Figure 2-4).

As can be seen in Figure 2-5, electrons that are injected (under forward bias) to the active region are confined in this area to generate population inversion. Because of the device band structure, there is a large chance that electrons radiatively fall into the valence band in the active region. Then these electrons will go through an interband tunneling process and are injected to the conduction band of the next stage, where they make another interband transition and emit an additional photon. This cascade process is repeated as many times as the number of stages and each individual electron emits this number of photons. Due to this electron recycling effect in cascade lasers quantum efficiencies larger than 100% and high output powers are achievable. The series connection of stages results in lower carrier concentrations (lower injection

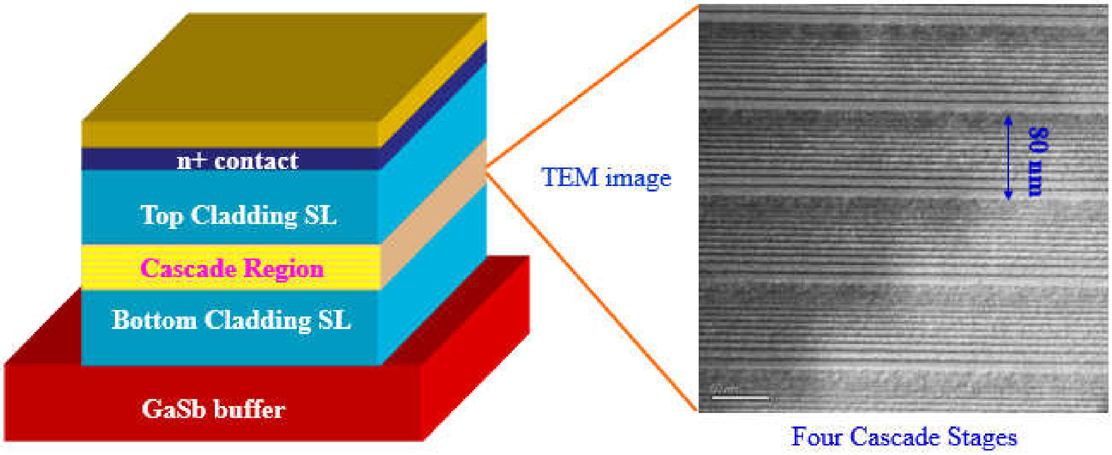

Figure 2-4: The schematic structure of a typical ICL. Right side panel is a TEM image of the cascade region [15].

current) to achieve lasing action and, as a consequence, the Ohmic losses are smaller compared to conventional semiconductor lasers. Also, cascade lasers benefit from a more uniform carrier injection across different stages as compared to MQW lasers [16].

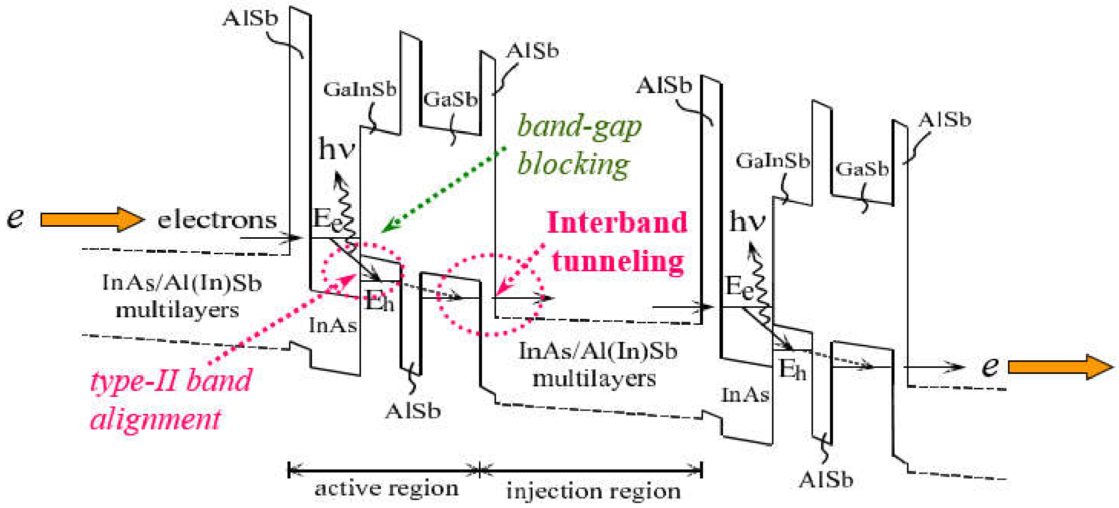

Figure 2-5: Schematic drawing of the band alignments in different regions of an ICL [10].

2.3.2 Current status of technology

Depending on the substrate used, two distinctive technologies have been developed for ICLs. InAs-based ICLs are the technology of choice for long wavelength ICLs (6 µm and beyond), while GaSb-based ICLs have been developed for shorter wavelengths. Currently, the shortest wavelength reported for type-II ICLs is 2.8 µm [17] and the longest wavelength has been 11.2 µm [18]. ICLs with an emission wavelength in 2.8-5.6 µm [17, 19] can operate in cw mode with an output power of ~500 mW at room temperature and above[20].

2.4 Interband cascade infrared photodetectors

2.4.1 Background

While theoretically projected to outperform $Hg_{1-x}Cd_xTe$ photodetectors, especially in the LWIR and VLWIR bands [21-23], real device implementations have not fully realized the benefits of T2SL InAs/GaSb IR detectors [24, 25]. In recent years, IR detector designs utilizing various barrier architectures such as nBn, XBn, and CBIRD configurations have shown promise to reach the ultimate performance predictions for T2SL IR photodetectors [26-28]. Wide bandgap (compared to absorber's bandgap) barriers made of bulk or SL materials reduce the dark current from the Shockley-Read-Hall centers, tunneling and diffusion process in these detectors. Despite being successful in addressing the high levels of dark current and related noise in T2SL IR photodetectors, there are some other performance limiting factors that remain largely unresolved. For instance, the reduced absorption coefficient in T2SL LWIR photodetectors near their bandgap necessitates a thicker absorber to achieve sufficient photon absorption and high quantum efficiency. Nevertheless, increasing the absorber thickness beyond the diffusion length would not enhance the quantum efficiency, while the diffusion length would be shortened at high temperatures as expected from the significantly reduced carrier mobility and lifetime [29-31] in T2SL IR photodetectors at such high operating temperatures. This implies that narrower-bandgap materials will have shorter carrier diffusion lengths $L_{e,h} = \sqrt{D_{e,h}\tau_{e,h}}$ and consequently long absorbers (longer than the diffusion length) will not produce a high quantum efficiency. Therefore, a thick SL absorber does not necessarily enhance the quantum efficiency in a T2SL detector, especially at high temperatures. These issues can be circumvented in a multiple-stage device architecture where each individual absorber is shorter than the minority carrier diffusion length.

2.4.2 Theory of ICIPs

2.4.2.1 Device structure

ICIPs, which are based on the 6.1 Å material system, are a promising structure to address the above-mentioned issues in T2SL IR photodetectors. In these multiple-stage IR photodetectors each individual absorber, typically made of InAs/GaSb T2SL, is sandwiched between hole and electron barriers to form one cascade stage. Note that the absorber could be made of a bulk material given that the required band alignments are satisfied in different regions of each stage. ICIPs with bulk GaInAsSb absorbers have been recently reported by our group [32]. The electron barriers are made of GaSb/AlSb QWs and the hole barriers are composed of InAs/AlSb QWs. The placement of the electron and hole barriers on opposite sides of the absorber ensures that electrons and holes flow in opposite directions. In ICIPs, photo-generated electrons and holes are separated without utilizing a conventional *p*-*n* junction. Consequently, drawbacks of a conventional *p*-*n* junction [33] can be avoided.

The structure of an ICIP and the band lineups in different regions are illustrated in Figure 2-6. The incident photons with energies higher than the SL bandgap are absorbed in the absorber region and generate electron-hole pairs. The generated electrons and holes travel in opposite directions to reach their collection points. The collection point for electrons (holes) is the hole (electron) barrier. Electrons that reach the hole barrier will relax down the energy ladder provided by the digitally graded QWs and will go through an interband tunneling process to recombine with the holes coming from the adjacent stage.

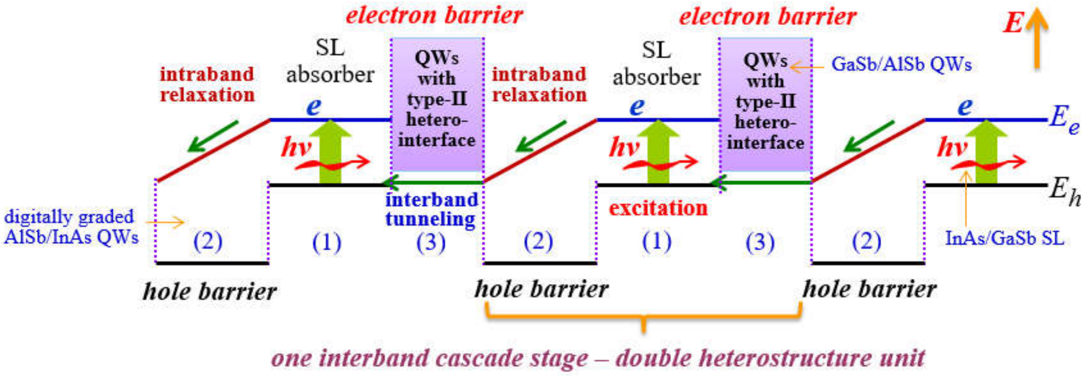

Figure 2-6: Schematic structure of an ICIP. Each stage consists of three regions, known as absorber, electron barrier, and hole barrier. Absorbers are typically made of T2SL; hole and electron barriers are made of InAs/AlSb and GaSb/AlSb multiple QWs, respectively [15].

2.4.2.2 Device configurations

Depending on whether the photons and electrons travel in the same direction or not, ICIPs are divided into two categories: regular and reverse configurations as shown in Figure 2-7 (a) and (b), respectively. In the regular configuration, photogenerated electrons travel in the same direction as the incident photons and consequently most of the photogenerated electrons are farther away from the collecting layer (hole barriers). This means the photo-generated electrons need to travel relatively long distances before reaching the collecting layers. If the diffusion length becomes shorter than the absorber thickness in one or more of the cascade stages, some of the photogenerated electrons will recombine before being collected at the hole barriers. To circumvent this possible problem (which is expected to become more significant at high temperatures and for thick absorbers) the reverse configuration was introduced. In a reverse configuration ICIP, the layering sequence is reversed and the photo-generated electrons travel in the opposite direction to the incident photons, thus most of these electrons will be close to the collection layers (hole barriers). When the minority carrier diffusion length becomes shorter than the absorber thickness, it is expected that the reverse configuration ICIPs have superior collection efficiency compared to regular configuration devices. Note that this is valid only if the minority carriers are electrons and the carrier transport is controlled by minority carriers.

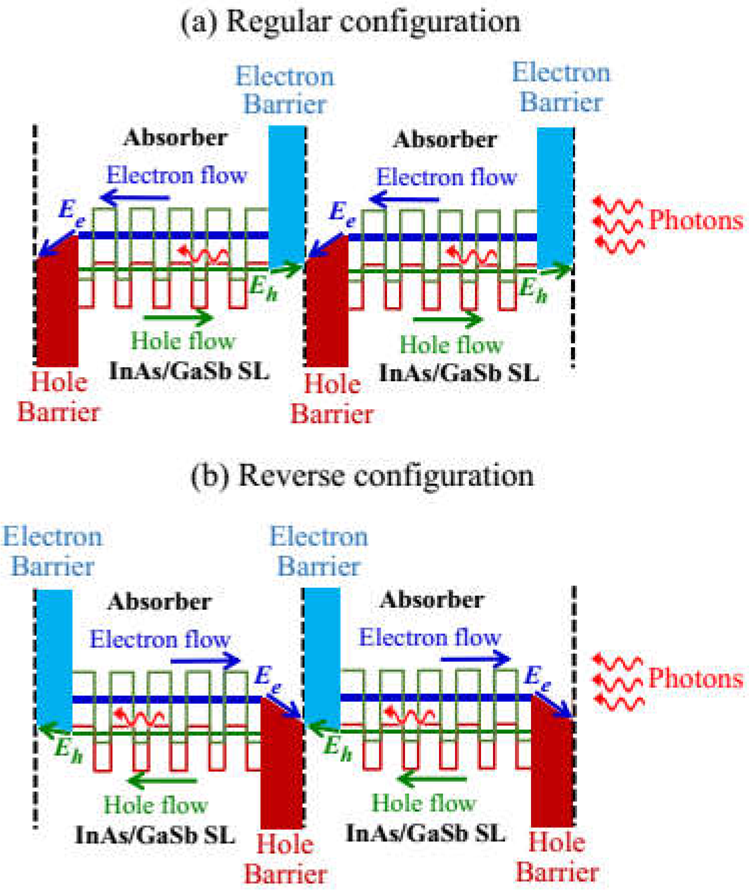

Figure 2-7: Schematic band diagram for (a) two-stage ICIPs with regular and (b) reverse configurations. Note that photons and electrons travel in the same direction in the regular configuration, but in opposite directions in the reverse configuration. The two configurations can be realized by reversing the growth order of layers in one structure without changing the light illumination direction.

2.4.3 Single-single detectors *vs.* ICIPs

2.4.3.1 Device sensitivity

Photocurrent in a single absorber photodetector with a *p*-type absorber with a thickness of *t* and electron diffusion length of L_e can be formulated as:

$$I_{ph} = q\int_0^t g_{ph}(x) f_c(x)\,dx\,, \tag{2-1}$$

$$g_{ph}(x) = \alpha(\lambda)\varphi_0 e^{-\alpha(\lambda)x}\ \text{, and} \tag{2-2}$$

$$f_c(x) = \frac{\cosh({}^{(t-x)}/_{L_e})}{\cosh({}^{t}/_{L_e})}\,, \tag{2-3}$$

where q, α, φ_0, $g_{ph}(x)$ and $f_c(x)$ denote electronic charge, absorption coefficient, photon flux, the generation rate and electrons collection probability, respectively. Note that the surface recombination velocity was assumed to be zero in Equation 2-3. As stated in Equation 2-1, the detector photocurrent and quantum efficiency (QE) are determined by the product of the generation rate and collection probability, therefore a large photon absorption without sufficiently long diffusion length (large $f_c(x)$ across absorber length) does not produce a high photocurrent or QE.

The rule of thumb for the absorber thickness to ensure sufficient photon absorption and QE is to make the absorber thickness equal or longer than the device cutoff wavelength [34].Therefore, a 4 µm-thick absorber suites well for an MWIR detector with a cutoff wavelength near 4 µm. Longer absorbers are required for detectors with longer cutoff wavelengths. Figure 2-8 compares the collection probability ($f_c(x)$) *vs*. the distance from the collection point (x) for a 4 µm-thick hypothetical photodetector, where different values were assumed for the minority carriers diffusion length. As shown in this figure, $f_c(x)$ is quite sensitive to the device diffusion length and sharply decreases for diffusion lengths shorter than the absorber thickness. Therefore, if the absorber thickness becomes longer than the minority carrier diffusion length, thicker absorbers will not result in enhanced QE. To alleviate this problem, a thick absorber can be partitioned into multiple absorbers where each individual absorber is shorter than the minority carrier diffusion length. Although the device external quantum efficiency (EQE) is not higher than the EQE in a single-stage detector with a thick absorber, multiple excitations for each photogenerated carrier before its collection at the device contacts reduce the device noise (through an averaging process) compared to a single-stage detector. Thus, the device overall performance (*e.g.*, signal to noise ratio) is enhanced in a multiple-stage detector. Moreover, because the stages are serially connected in a multiple-stage detector, the device resistance is higher than a single-stage detector. This large device resistance at high temperatures is of significant importance as it can reduce the detector's noise and the complexity of its integration with other system electronics. A detailed theoretical analysis of the ultimate performance of multiple- and single-stage photovoltaic detectors is provided in [35, 36].

Based on the theory of ideal ICIPs, where the carrier transport is controlled by diffusion process, the product of the device zero-bias resistance and area product (R_0A) can be written as [35]:

$$R_0A = \frac{k_BT}{q^2 g_{th} L_e} \sum_m \frac{1}{\tanh\left(\frac{t_m}{L_e}\right)} \tag{2-4}$$

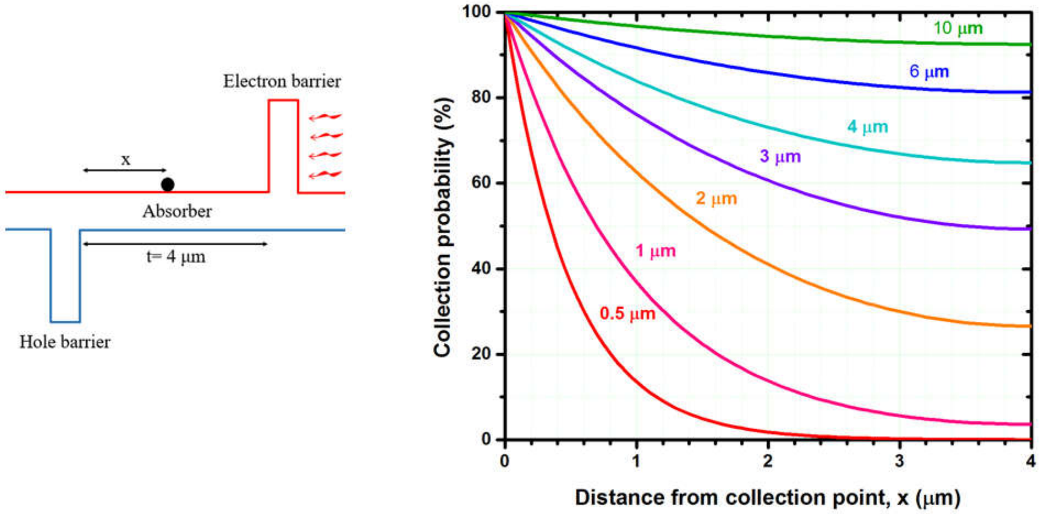

Figure 2-8: Collection probability for minority carriers (*i.e.*, electrons) *vs*. their distance from the collection point (hole barrier) in a hypothetical photodetector with a 4 μm-thick absorber. Provided numbers on each curve denote the assumed minority carrier diffusion lengths. Minority carrier diffusion lengths below 1 μm are realistic assumptions for T2SL photodetectors at high temperatures as discussed in the following chapters. The left side panel shows the simplified structure of one stage in an ICIP.

where k_{B}, T, q, g_{th}, L_{e}, and t_{m} are the Boltzmann constant, absolute temperature, electron charge, thermal generation rate, electron diffusion length and absorber thickens in the m^{th} stage, respectively. From this equation, one can see that the device R_0A increases by reducing the absorber thickness in each stage provided that the diffusion length is longer than its thickness and the Johnson noise term accordingly will reduce. On the other hand, thin absorbers reduce the device responsivity due to limited photon absorption. This means a tradeoff exists between the lower noise and higher responsivity and the device designer should bear in mind an optimum absorber thickness and number of stages based on the system requirements and material parameters. External quantum efficiency (EQE) in an ICIP is expressed as follows [35]:

$$EQE = \left[\frac{\alpha L_e}{1-(\alpha L_e)^2}\right]\left[\frac{Sinh\left({}^{t_1}/_{L_e}\right)+\alpha L_e e^{-\alpha t_1}}{cosh\left({}^{t_1}/_{L_e}\right)} - \alpha L_e\right] \tag{2-5}$$

Since the different stages are assumed to be photocurrent matched, the absorber thickness in the first stage (t_1) is used in the above equation. If the photocurrent matching condition is not satisfied, the stage with the lowest I_{ph} determines the device photocurrent.

The specific detectivity (D^*) which is the most relevant metric to compare different detectors is described by the following equation in ICIPs [35]:

$$D^* = \frac{\lambda}{hc}\frac{EQE}{\sqrt{4g_{th}L_e}}\sqrt{\sum_m \frac{1}{\tanh\left(\frac{t_m}{L_e}\right)}}\,. \tag{2-6}$$

Rather than defining separate terms for shot and Johnson noise, a general noise term based on a stochastic treatment of the thermal generation of carriers is introduced in Equation 2-6. However, in order to directly calculate the device noise based on the device electrical and optical measurements, the device D^* can be written as follows:

$$D^* = \frac{R_\lambda}{\sqrt{\frac{4k_BT}{RA}+\frac{2qJ_b}{N_S}+2qJ_s}}, \tag{2-7}$$

where R_λ, J_b, and J_s are the device responsivity, and the bulk and surface components of the device dark current, respectively. As can be seen in the above equation, two separate terms are considered for the device shot noise. Since the device bulk dark current passes through the cascade region the shot noise term is described by $(2qJ_b)/N_s$. However, the surface currents do not pass through the cascade structure and therefore the surface current shot noise is similar to the shot noise term in conventional single-stage detectors

($2qJ_s$). If the surface leakage term (J_s) is removed, which is a sound assumption in devices with high-quality passivation, the specific detectivity can be written as [6]:

$$D^* = \frac{R_\lambda}{\sqrt{\frac{4k_BT}{RA}+\frac{2qJ_d}{N_S}}}\,. \tag{2-8}$$

From Equation 2-8, one can see that even for the same level of dark current (for the case of negligible surface currents), an ICIP with more stages will have lower shot noise in comparison with a single-stage detector or an ICIP with a fewer number of stages. Indeed, lower shot noise (*cf.* conventional single-stage detectors) has been observed in MWIR ICIPs by direct noise measurements [37].

Figure 2-9 compares the performance of single-stage detectors over that of a multiple-stage detector with photocurrent-matched absorbers. The benefits of a multiple-stage device are observed when the product of absorption coefficient and minority carrier diffusion length ($\alpha.L_e$) falls below 0.5 [35]. To our knowledge, there has been just handful of studies on the minority carrier diffusion length in InAs/GaSb T2SL material system which are limited to low temperatures. However, our studies on the device responsivity and photocurrent in detectors and thermophotovoltaic devices with T2SL absorbers confirm that the minority carriers diffusion length is sharply reduced at high temperatures. Based on our preliminary analysis on the T2SL diffusion length at high temperatures the electrons diffusion length is estimated to be shorter than 1 µm at room temperature (see section 4.3.2). Furthermore, the absorption coefficient for T2SL photodetectors is within 1000-3500 cm^{-1} range depending on the device cutoff wavelength and temperature. This means the absorber thickness should be in the range of 3-10 µm to ensure sufficient photon absorption and high QE. The contour plot

αL_e=0.5 *vs*. the device absorption coefficient and minority carrier diffusion length are provided in Figure 2-10. The shaded area below this curve shows the feasible area wherein a multiple-stage device has superior performance over a single-stage detector. Based on our investigations, some of which are presented in the following chapters, the device absorption coefficient and minority carrier diffusion length for T2SL detectors, particularly at longer wavelengths and high temperatures, falls in this area and a multiple-stage device will result in a more efficient collection of photogenerated carriers and higher D^*.

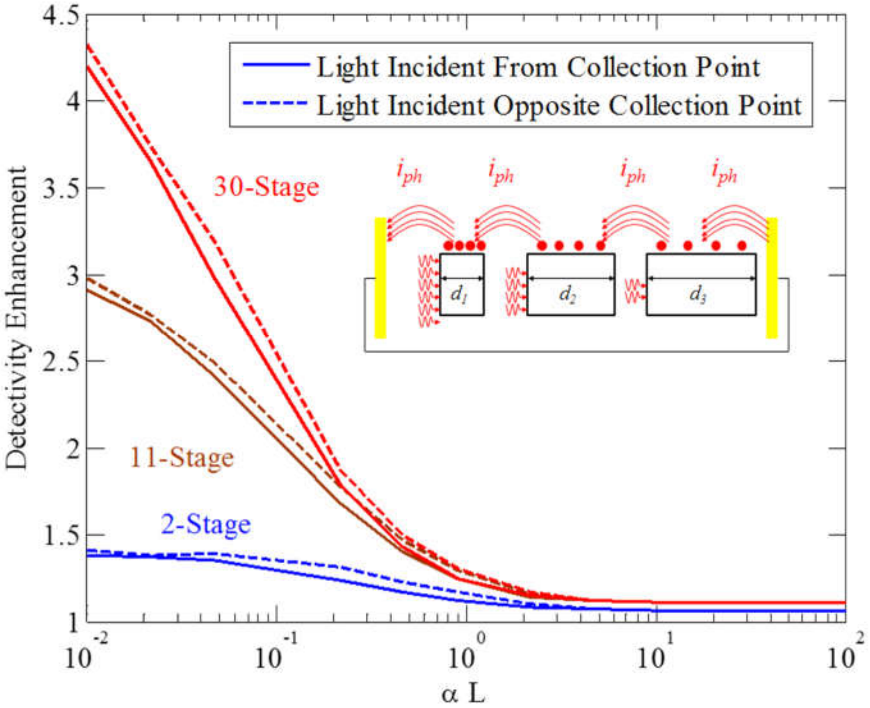

Figure 2-9: Comparison of the device detectivity for a multiple-stage detector (*e.g.*, ICIPs) over a single-stage detector [35].

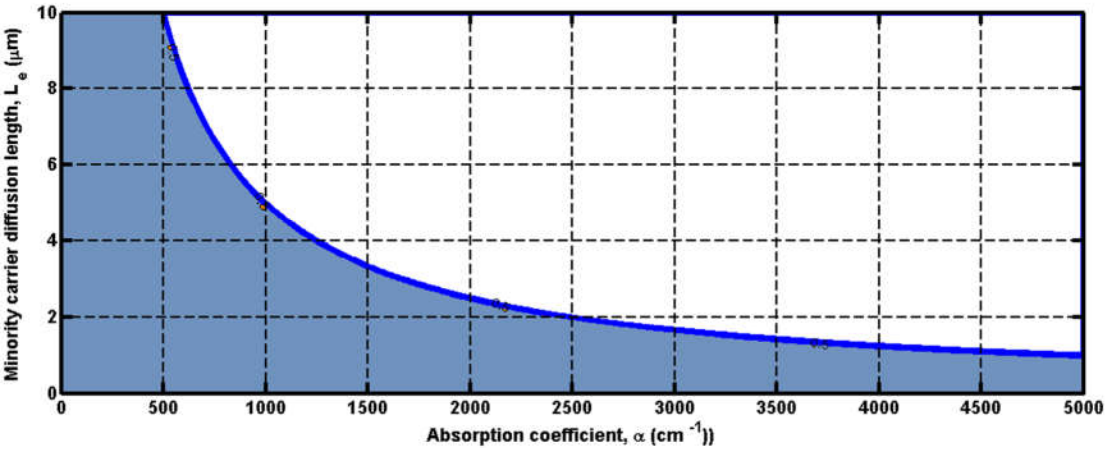

Figure 2-10: Contour plot of αL_e=0.5 for different values of the absorption coefficient and minority carrier diffusion length. Colored area shows the space where a multiple-stage detector has superior performance over a single-stage detector.

2.4.3.2 Device frequency response

The transit time of photogenerated carriers by means of the diffusion and/or drift process reduces as the absorber thickness is shortened in a photodetector. However, in conventional single-stage photodetectors, the higher device speed comes with a price on the device sensitivity. It is well-accepted that the product of the device bandwidth and sensitivity is almost constant in single-stage photodetectors. This issue can be addressed in a multiple-stage architecture where each individual absorber is kept short contingent with the speed requirements. Meanwhile, because of higher device resistance and lower Johnson and shot noise, the device sensitivity is as high as that of a single-stage detector with a thick absorber. Aside from the short transit times, as different stages are serially connected in a multiple-stage detector, the equivalent device capacitance associated with the device structure is lower ($C_{eq}=C_{single\text{-}stage}/N_s$) than that of a single-stage detector with a thin absorber. Therefore, the device capacitance and its influence on the device frequency response is less of a concern in multiple-stage detectors.

2.5 Interband cascade thermophotovoltaic devices

2.5.1 Background

Thermophotovoltaic (TPV) systems are clean, quiet (no moving parts), and compact photovoltaic systems for converting the radiant energy from a heat source into electrical energy. The development of TPV systems has not progressed as quickly as expected, and the efficiency of the TPV cells remains far below the predicted theoretical limits [38-42]. The bulk of research on TPV cell has focused on GaInAsSb/GaSb [43-45] and InGaAsP/InP material systems [38-41, 46] with absorber bandgaps of 0.5 eV and above. Consequently, the below bandgap loss is the dominant source of loss in TPV systems with blackbody-type heat sources. The percentage of total radiated photons with energies lower than 0.5 eV is plotted in Figure 2-11 for various heat source temperatures. As can be seen in this graph, most of the emitted photons (>50%) have energies below 0.5 eV for heat source temperatures below 1650 K. For example, for a 700 K (1000 K) heat source, 97% (83%) of total emitted photons have energies below 0.5 eV. Theoretical studies [47] have shown that in the detailed balance limit, TPV cells with bandgaps in the range of 0.2-0.4 eV are optimal for TPV applications when the emitter temperatures are relatively low. This is meaningful for waste-heat recovery applications because more heat sources are available at low temperatures (700-1,000 K) and such TPV systems can be made simpler. In fact, it is beneficial to hold the emitter at as low a temperature as possible to avoid overheating of the TPV cell when it is placed in close proximity of the emitter. This is especially important for micron-gap configurations [38, 48] that use TPV cells with narrow bandgaps (<0.5 eV), where the

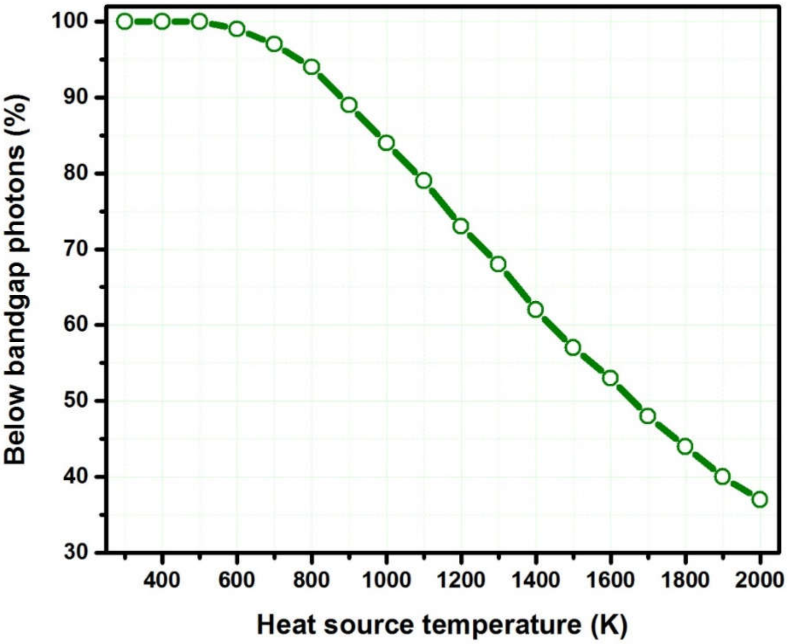

Figure 2-11: Percentage of below-bandgap (E_g=0.5 eV) photons at different heat source temperatures. The heat source is assumed to have a blackbody-type radiation pattern.

enhanced radiative transfer between hot and cold surfaces is achieved by a micron-gap (about the radiation wavelength). Narrow-bandgap TPV cells may also be useful for certain laser power-beaming applications. Most notably, mid-infrared light may be the best choice for remote energy-delivery in bad-weather conditions, since light transferred across other portions of the optical spectrum may be subject to a large amount of absorption and scattering losses.

2.5.2 Theory of ICTPV devices

The interband cascade architecture offers a promising alternative TPV cell design that can mitigate Ohmic losses as well as other issues, such as the low V_{oc} in narrow bandgap cells. ICTPV devices are multiple-stage heterostructures in which each stage is composed of three regions, namely, absorber, electron barrier, and hole barrier (see Figure 2-12). Electron and hole barriers are made of wider bandgap materials to facilitate the separation of photogenerated electrons and holes, making them move in opposite directions. As the absorber layer is made of InAs/GaSb T2SL with broken-gap band alignment, the bandgap of the absorber can be tailored to cover a wide range of the IR spectrum (2.3-30 µm) by merely changing the thickness of each layer in the SL. This feature makes the spectral splitting much easier compared to the conventional approach, which uses different materials. Similar to multi-junction solar cells, absorbers in an ICTPV device could have different bandgaps to efficiently convert photons at different energies. When an ICTPV device is illuminated, the photo-voltages from each individual cascade stage add together, creating a high overall open-circuit voltage. Furthermore, photo-generated carriers can be collected with nearly 100% efficiency in each stage. This is because the carriers travel over only a single cascade stage, designed to be shorter than a typical diffusion length. Since the carrier transport between interband cascade stages are facilitated with the semi-metallic-like type-II heterointerface in contrast to the Esaki tunnel junction that is used in conventional multi-junction tandem solar cells, series resistance between interband cascade stages is negligible. Other advantages of ICPV devices include the elimination of conventional depletion region in *p*-*n* junctions for suppressing Shockley-Read-Hall recombination current; and the flexibility provided by quantum engineering, as discussed more extensively in [49]. With these features, ICTPV devices provide an attractive option for achieving high performance in the long wavelength spectrum. Further details on the theory and ultimate performance of ICTPV devices can be found in [50].

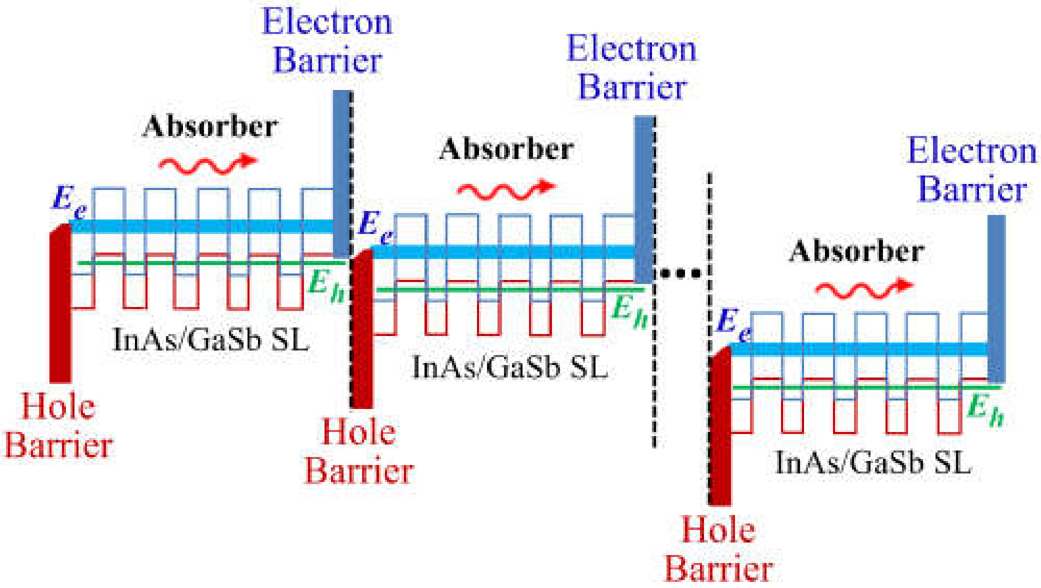

Figure 2-12: Schematic illustration of an ICTPV device with multiple stages. Each stage is composed of a T2SL absorber sandwiched between electron and hole barriers. E_e and E_h denote the energy for electron (light blue) and hole (green) minibands, respectively. The energy difference (E_e-E_h) is the bandgap (E_g) of the T2SL.

2.6 Growth of interband cascade devices

IC optoelectronic devices are made of thousands of layers, some of which are just a few angstroms thick. Therefore, a very high degree of precision and control is required during the epi growth. Molecular beam epitaxy (MBE) is an ultra-high vacuum ($<10^{-9}$ Torr) growth system that can achieve these levels of precision. In order to achieve monolayer accuracy in epitaxial growth, various cells, which are heated by coil heaters, are embedded in an MBE system for growth and doping of epitaxial layers. A shutter that is integrated into each cell along with the cell temperature controls the beam flux in each cell. Typically, valved cracker cells are used for group V materials (Sb and As) to crack Sb_4 and As_4 into Sb_2 and As_2 and to achieve better flux control. During the growth process, the substrate is heated (T_{sub}=400-450 °C) and rotated to ensure a uniform material growth. Further details on the MBE growth of the IC optoelectronic devices is provided in [51].

2.7 Fabrication of interband cascade devices

The device fabrication process flow is similar for all different types of IC optoelectronic devices. The ICL's fabrication has some difference in terms of the mask shape and size compared to ICIPs and ICTPV devices. Figure 2-13 displays the device fabrication process flow for ICIPs and ICTPV devices. Most of the steps depicted in this figure are self-explanatory.

It is worth noting that for the device passivation a two-layer passivant that comprises a SiN_x (typically 200 nm thick) layer followed by a SiO_2 (the typical thickness is same as the SiN_x layer thickness) layer is used. The stack passivation made of SiO_2/SiN_x is widely used in solar cells and exhibited superior performance (lower surface recombination velocity) compared to single-layer passivation in c-Si solar cells [52-54]. Our comparative device performance analysis shows that the device dark current is minimized when SiN_x/SiO_2 with similar thicknesses of 200 nm is used for the device passivation. We speculate that the two-layer passivation improves the overall stress management and also reduces pin holes, which are a prevalent issue in SiN_x layers. Since the thermal conductivity of SiN_x is more than 20 times higher than that of SiO_2, better heat dissipation is expected provided that the SiN_x layer is deposited before the SiO_2 layer.

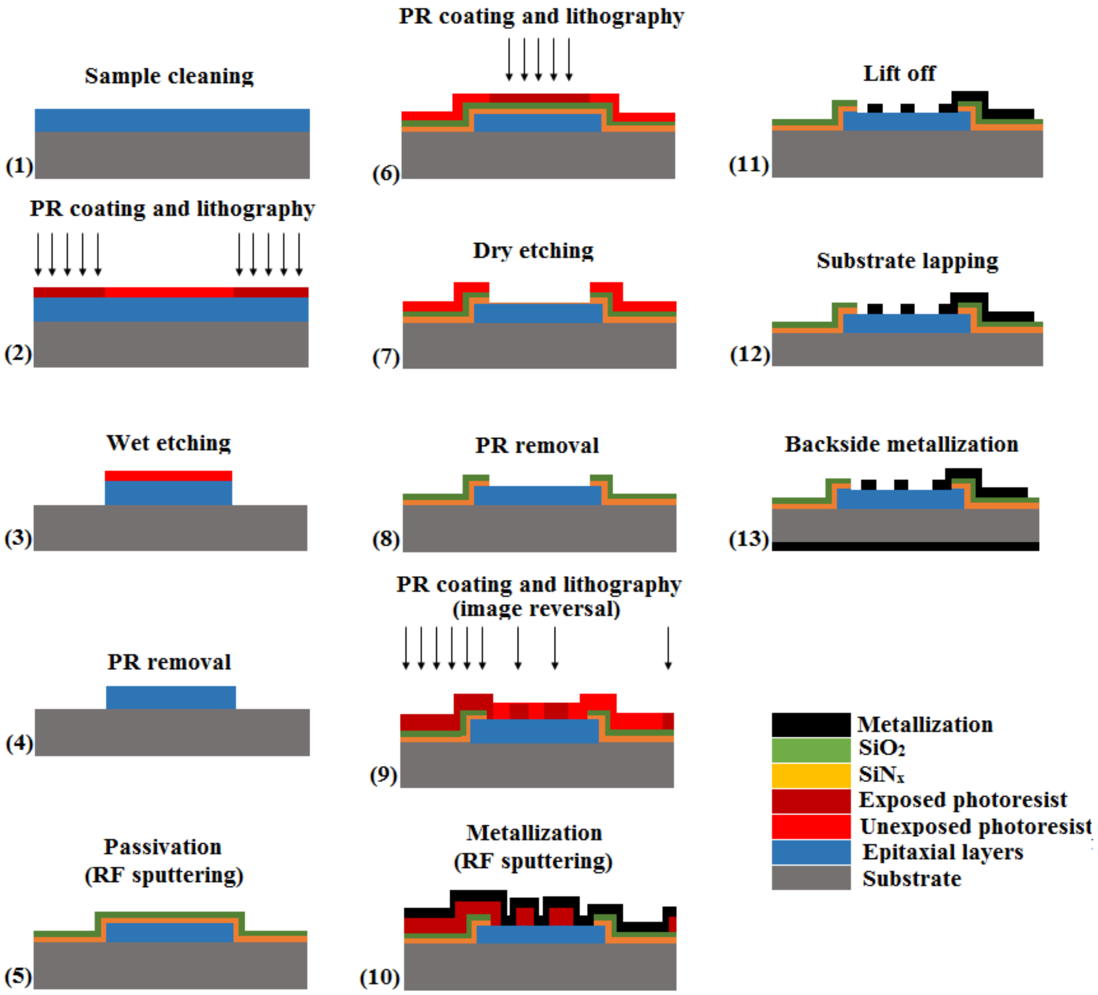

Figure 2-13: Device fabrication flow for ICIPs and ICTPV devices. The overall device fabrication flow for ICLs is similar to that of ICIPs and ICTPVs.

2.8 Bibliography

[1] R. Q. Yang, "Infrared laser based on intersubband transitions in quantum wells," *Superlattices and Microstructures,* vol. 17, p. 77, 1995.

[2] M. Tacke, "Lead–salt lasers," *Philosophical Transactions of the Royal Society of London A: Mathematical, Physical and Engineering Sciences*, vol. 359, pp. 547-566, 2001.

[3] J. Faist, F. Capasso, D. L. Sivco, C. Sirtori, A. L. Hutchinson, and A. Y. Cho, "Quantum cascade laser," *Science,* vol. 264, pp. 553-556, 1994.

[4] C.-H. Lin, R. Q. Yang, D. Zhang, S. Murry, S. Pei, A. Allerman*, et al.*, "Type-II interband quantum cascade laser at 3.8 μm," *Electronics Letters,* vol. 33, pp. 598-599, 1997.

[5] J. V. Li, R. Q. Yang, C. J. Hill, and S. L. Chuang, "Interband cascade detectors with room temperature photovoltaic operation," *Applied Physics Letters,* vol. 86, p. 101102, 2005.

[6] R. Q. Yang, Z. Tian, Z. Cai, J. F. Klem, M. B. Johnson, and H. C. Liu, "Interband-cascade infrared photodetectors with superlattice absorbers," *Journal of Applied Physics,* vol. 107, p. 054514, 2010.

[7] Z. Tian, R. T. Hinkey, R. Q. Yang, D. Lubyshev, Y. Qiu, J. M. Fastenau*, et al.*, "Interband cascade infrared photodetectors with enhanced electron barriers and p-type superlattice absorbers," *Journal of Applied Physics,* vol. 111, p. 024510, 2012.

[8] R. Q. Yang, Z. Tian, J. Klem, T. D. Mishima, M. B. Santos, and M. B. Johnson, "Interband cascade photovoltaic devices," *Applied Physics Letters,* vol. 96, p. 063504, 2010.

[9] S. Adachi, *Properties of semiconductor alloys: group-IV, III-V and II-VI semiconductors*, John Wiley & Sons, 2009.

[10] R. Q. Yang, L. Li, Y. Jiang, "Interband cascade lasers: from original concept to practical devices," *Progress in Physics*, vol. 34, pp.169-190, 2014, (in Chinese).

[11] L. Esaki and R. Tsu, "Superlattice and negative differential conductivity in semiconductors," *IBM Journal of Research and Development,* vol. 14, pp. 61-65, 1970.

[12] M. Razeghi, *Technology of Quantum Devices*, Springer, 2010.

[13] A. M. Hoang, A. Dehzangi, S. Adhikary, and M. Razeghi, "High performance bias-selectable three-color short-wave/mid-wave/long-wave infrared photodetectors based on type-II InAs/GaSb/AlSb superlattices," *Scientific Reports,* vol. 6, p. 24144, 2016.

[14] I. Vurgaftman, J. R. Meyer, and L. R. Ram-Mohan, "Mid-IR vertical-cavity surface-emitting lasers," *IEEE Journal of Quantum Electronics,* vol. 34, pp. 147-156, 1998.

[15] R. Q. Yang, Course handout for "Quantum structrues and devices", Spring 2013.

[16] R. Q. Yang and S. Pei, "Novel type-II quantum cascade lasers," *Journal of Applied Physics,* vol. 79, pp. 8197-8203, 1996.

[17] J. Scheuermann, R. Weih, M. von Edlinger, L. Nähle, M. Fischer, J. Koeth*, et al.*, "Single-mode interband cascade lasers emitting below 2.8 μm," *Applied Physics Letters,* vol. 106, p. 161103, 2015.

[18] L. Li, H. Ye, Y. Jiang, R. Q. Yang, J. C. Keay, T. D. Mishima*, et al.*, "MBE-grown long-wavelength interband cascade lasers on InAs substrates," *Journal of Crystal Growth*, vol. 425, pp. 369-372, 2015.

[19] W. W. Bewley, C. L. Canedy, C. S. Kim, M. Kim, C. D. Merritt, J. Abell*, et al.*, "Continuous-wave interband cascade lasers operating above room temperature at λ = 4.7-5.6 μm," *Optics Express,* vol. 20, pp. 3235-3240, 2012.

[20] I. Vurgaftman, R. Weih, M. Kamp, J. Meyer, C. Canedy, C. Kim*, et al.*, "Interband cascade lasers," *Journal of Physics D: Applied Physics,* vol. 48, p. 123001, 2015.

[21] C. H. Grein, P. M. Young, and H. Ehrenreich, "Minority carrier lifetimes in ideal InGaSb/InAs superlattices," *Applied Physics Letters,* vol. 61, p. 2905, 1992.

[22] C. H. Grein, P. M. Young, M. E. Flatté, and H. Ehrenreich, "Long wavelength InAs/InGaSb infrared detectors: Optimization of carrier lifetimes," *Journal of Applied Physics,* vol. 78, pp. 7143-7152, 1995.

[23] D. L. Smith and C. Mailhiot, "Proposal for strained type II superlattice infrared detectors," *Journal of Applied Physics,* vol. 62, pp. 2545-2548, 1987.

[24] W. E. Tennant, "“Rule 07” Revisited: Still a Good Heuristic Predictor of p/n HgCdTe Photodiode Performance?," *Journal of Electronic Materials,* vol. 39, pp. 1030-1035, 2010.

[25] D. R. Rhiger, "Performance Comparison of Long-Wavelength Infrared Type II Superlattice Devices with HgCdTe," *Journal of Electronic Materials,* vol. 40, pp. 1815-1822, 2011.

[26] S. Maimon and G. W. Wicks, "nBn detector, an infrared detector with reduced dark current and higher operating temperature," *Applied Physics Letters,* vol. 89, p. 151109, 2006.

[27] P. Klipstein, ""XBn" barrier photodetectors for high sensitivity and high operating temperature infrared sensors," in *Proceedings of SPIE, Infrared Technology and Applications XXXIV*, vol. 6940, p. 69402U, 2008.

[28] D. Z.-Y. Ting, C. J. Hill, A. Soibel, S. a. Keo, J. M. Mumolo, J. Nguyen*, et al.*, "A high-performance long wavelength superlattice complementary barrier infrared detector," *Applied Physics Letters,* vol. 95, p. 023508, 2009.

[29] B. C. Connelly, G. D. Metcalfe, H. Shen, and M. Wraback, "Direct minority carrier lifetime measurements and recombination mechanisms in long-wave infrared type II superlattices using time-resolved photoluminescence," *Applied Physics Letters,* vol. 97, p. 251117, 2010.

[30] D. Wang, D. Donetsky, S. Jung, and G. Belenky, "Carrier lifetime measurements in long-wave infrared InAs/GaSb superlattices under low excitation conditions," *Journal of Electronic Materials,* vol. 41, pp. 3027-3030, 2012.

[31] Y. Peter and M. Cardona, *Fundamentals of semiconductors: physics and materials properties*: Springer Science & Business Media, 2010.

[32] L. Lei, L. Li, H. Lotfi, Y. Jiang, R. Q. Yang, M. B. Johnson*, et al.*, "Mid-wave interband cascade infrared photodetectors based on GaInAsSb absorbers," *Semiconductor Science and Technology,* vol. 31, p. 105014, 2016.

[33] P. Martyniuk, M. Kopytko, and A. Rogalski, "Barrier infrared detectors," *Optoelectronics Review,* vol. 22, pp. 127-146, 2014.

[34] J. W. Beletic, R. Blank, D. Gulbransen, D. Lee, M. Loose, E. C. Piquette*, et al.*, "Teledyne Imaging Sensors: infrared imaging technologies for astronomy and civil space," in *Proceedings of SPIE High Energy, Optical, and Infrared Detectors for Astronomy III,* vol. 7021, pp. 70210H-70210H-14, 2008.

[35] R. T. Hinkey and R. Q. Yang, "Theory of multiple-stage interband photovoltaic devices and ultimate performance limit comparison of multiple-stage and single-stage interband infrared detectors," *Journal of Applied Physics,* vol. 114, p. 104506, 2013.

[36] R. T. Hinkey and R. Q. Yang, "Comparison of ultimate limits of interband cascade infrared photodetectors and single-absorber detectors," *in Proceedings of SPIE, Infrared Sensors, Devices, and Applications III,* vol. 8868, p. 886804, 2013.

[37] L. A. Treider, V. M. Cowan, C. P. Morath, Z. Tian, and S. Krishna, "Noise spectrum measurements of a midwave, interband cascade infrared photodetector with 33 nm wide electron barrier," in *Proceedings of SPIE, Nanophotonics and Macrophotonics for Space Environments VII*, vol. 8876, p. 88760B, 2013.

[38] M. G. Mauk, "Survey of thermophotovoltaic (TPV) devices," in *Mid-infrared Semiconductor Optoelectronics*, Springer, pp. 673-738, 2006.

[39] T. Bauer, *Thermophotovoltaics: basic principles and critical aspects of system design*, Springer Science & Business Media, 2011.

[40] A. Datas and C. Algora, "Global optimization of solar thermophotovoltaic systems," *Progress in Photovoltaics: Research and Applications,* vol. 21, pp. 1040-1055, 2013.

[41] T. Coutts, "A review of progress in thermophotovoltaic generation of electricity," *Renewable and Sustainable Energy Reviews,* vol. 3, pp. 77-184, 1999.

[42] N.-P. Harder and P. Würfel, "Theoretical limits of thermophotovoltaic solar energy conversion," *Semiconductor Science and Technology,* vol. 18, p. S151, 2003.

[43] C. Wang, H. Choi, S. Ransom, G. Charache, L. Danielson, and D. DePoy, "High-quantum-efficiency 0.5 eV GaInAsSb/GaSb thermophotovoltaic devices," *Applied Physics Letters,* vol. 75, pp. 1305-1307, 1999.

[44] C. Wang, R. Huang, D. Shiau, M. Connors, P. Murphy, P. O'BRIEN*, et al.*, "Monolithically series-interconnected GalnAsSb/AlGaAsSb/GaSb thermophotovoltaic devices with an internal backsurface reflector formed by wafer bonding," *Applied Physics Letters,* vol. 83, pp. 1286-1288, 2003.

[45] R. K. Huang, R. J. Ram, M. J. Manfra, M. K. Connors, L. J. Missaggia, and G. W. Turner, "Heterojunction thermophotovoltaic devices with high voltage factor," *Journal of Applied Physics,* vol. 101, p. 6102, 2007.

[46] R. Tuley and R. Nicholas, "Band gap dependent thermophotovoltaic device performance using the InGaAs and InGaAsP material system," *Journal of Applied Physics,* vol. 108, p. 084516, 2010.

[47] T. J. Coutts and J. S. Ward, "Thermophotovoltaic and photovoltaic conversion at high-flux densities," *IEEE Transactions on Electron Devices,* vol. 46, pp. 2145-2153, 1999.

[48] W. R. Chan, P. Bermel, R. C. Pilawa-Podgurski, C. H. Marton, K. F. Jensen, J. J. Senkevich*, et al.*, "Toward high-energy-density, high-efficiency, and moderate-temperature chip-scale thermophotovoltaics," *Proceedings of the National Academy of Sciences USA,* vol. 110, pp. 5309-5314, 2013.

[49] R. T. Hinkey, Z.-B. Tian, S. S. S. Rassel, R. Q. Yang, J. F. Klem, and M. B. Johnson, "Interband cascade photovoltaic devices for conversion of mid-IR radiation," *IEEE Journal of Photovoltaics,* vol. 3, pp. 745-752, 2013.

[50] R. T. Hinkey and R. Q. Yang, “Theoretical comparison of performance limits of single- and multiple-stage photovoltaic devices”, *Semiconductor Science and Technology*, vol. 30, p.015013, 2015.

[51] H. Ye, *Molecular beam epitaxy of InAs, GaSb, AlSb structures for interband cascade devices*, Ph.D. dissertation, University of Oklahoma, 2016.

[52] J. Schmidt, M. Kerr, and A. Cuevas, "Surface passivation of silicon solar cells using plasma-enhanced chemical-vapour-deposited SiN films and thin thermal SiO_2/plasma SiN stacks," *Semiconductor Science and Technology,* vol. 16, p. 164, 2001.

[53] M. Hofmann, S. Kambor, C. Schmidt, D. Grambole, J. Rentsch, S. W. Glunz, *et al.*, "PECVD-ONO: A new deposited firing stable rear surface passivation layer system for crystalline silicon solar cells," *Advances in Optoelectronics*, vol. 2008, 2008.

[54] S. Keipert-Colberg, N. Barkmann, C. Streich, A. Schütt, D. Suwito, P. Schäfer*, et al.*, "Investigation of a PECVD silicon oxide/silicon nitride passivation system concerning process influences," in *Proceedings of 26th European PV Solar Energy Conference and Exhibition*, pp. 5-9¸ 2011.

Chapter 3: Long- and very long-wavelength interband cascade infrared photodetectors

3.1 Background and motivation

LWIR and VLWIR detectors have a wide range of civilian, defense and security applications. These detectors are extensively investigated for thermal imaging, medical diagnostics, remote sensing and failure detection and analysis in electronic and electric systems. High-performance LWIR and VLWIR photon detectors require cryogenic cooling for their operation. The narrow bandgap semiconductors used in these detectors are far from ideal and have complicated growth and fabrication process.

While $Hg_{1-x}Cd_xTe$ detectors are yet the main player in LWIR and VLWIR market after several decades, T2SL-based detectors with some encouraging performance have received the most attention in recent years. Nevertheless, along with its prominent benefits over $Hg_{1-x}Cd_xTe$, T2SL has its own shortcomings that require careful considerations and remedies before their adoption by commercial markets.

The absorption coefficient near the band-edge is reduced as the cutoff wavelength of T2SL IR detectors is made longer. Thus, in order to achieve a high absorption quantum efficiency in an LWIR detector, the absorber must be thicker than those typically used for MWIR detectors. Additionally, the carrier lifetime is expected to be lower for narrower-bandgap materials. This implies that these materials will have shorter carrier diffusion lengths and consequently the attainable quantum efficiency will be lower. This effect could become more detrimental at high temperatures as the diffusion length is further reduced, as suggested by data from the literature[1, 2].

Therefore, a thick SL absorber may not necessarily enhance the external quantum efficiency in a T2SL detector, especially at high temperatures.

The discrete multiple absorber architecture used in ICIPs can circumvent these issues and will enhance the collection efficiency of photogenerated carriers while the detector noise is reduced. Experimental investigations of ICIPs in the MWIR band have shown that these detectors can operate at very high temperatures with high performance[3, 4]. It is expected that the interband cascade approach will have prominent advantages for LWIR and VLWIR detectors, especially for high-operating-temperature (HOT) applications. In this chapter, we report on the first demonstration of LWIR and VLWIR ICIPs. Our preliminary investigations reveal great prospects for HOT LWIR and VLWIR ICIPs.

3.2 High-operating-temperature ICIPs with ~8 μm cutoff wavelength

3.2.1 Device design, growth and material characterization

3.2.1.1 Device design, growth, and fabrication

The three ICIPs presented in this section were grown at IQE Inc. by MBE on GaSb substrates. They were designed with identical unipolar barriers and absorber's SL period (see Figure 3-1) to investigate the effects of different number of stages and illumination direction on their electrical and optical properties. Two of these wafers were two-stage detectors with reverse (Rev.-2S) and regular (Reg.-2S) illumination configurations, while the three-stage detector had the regular illumination configuration (Reg.-3S). A detailed discussion on different configurations for ICIPs is provided in section 2.4.2.2. Each SL period in the absorbers was designed to be 59 Å thick and composed of InAs (33.5 Å), GaSb (21.9 Å) and a thin InSb (3.6 Å) layer. The thin InSb layer was inserted in each SL period to compensate for the tensile strain from the InAs layers. The SL absorber thicknesses from the top to the bottom were 590 nm (absorber #1), 713.9 nm (absorber #2) and 914.5 nm (absorber #3), where the optically deeper absorbers were made thicker to achieve photocurrent matching. The absorbers were partially *p*-doped (the half of the absorber thickness close to the electron barriers) to 3.5×10^{16} cm^{-3}. The partial doping was, in part, to compensate the possible band bending close to the electron barriers as suggested by device simulations [5]. The electron barrier comprised of three GaSb/AlSb QWs with 32, 43 and 58 Å thick wells, respectively. The hole barrier was composed of seven InAs/AlSb QWs forming an

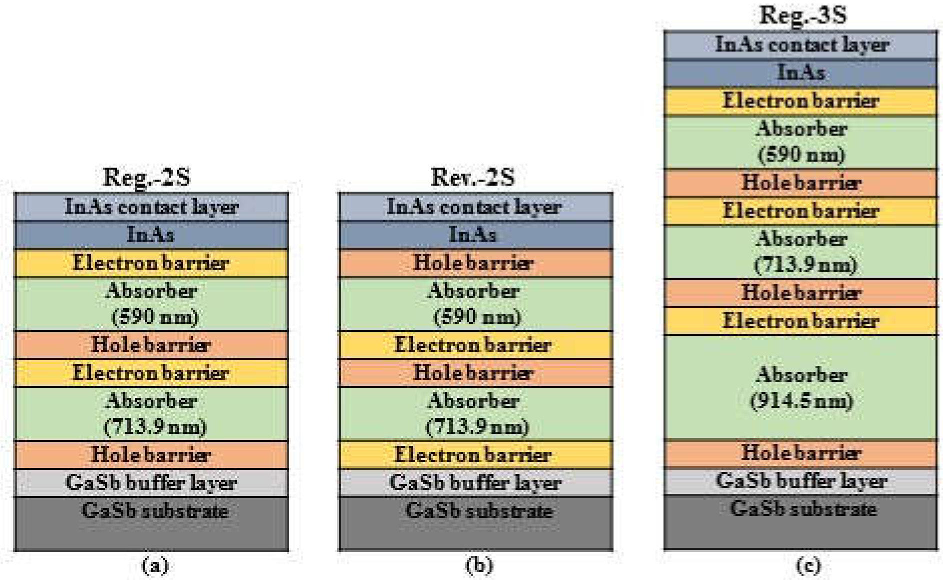

Figure 3-1: Device structure for the ICIPs: (a) regular-illumination configured two-stage (Reg.-2S), (b) reversed-illumination configured two-stage (Rev.-2S); and (c) regular-illumination configured three-stage (Reg.-3S). Device illumination was from the top in all of these detectors.

energy ladder to allow photo-generated electrons in the absorber region to quickly move to the adjacent electron barrier or contact layers.

After the MBE growth, square mesas with edge sizes ranging from 200 to 1000 μm were fabricated using our conventional contact photolithography and chemical wet etching. Further details on the device fabrication can be found in section 2.7. The passivation layer for these detectors consisted of a 156 nm Si_3N_4 layer followed by a 140 nm SiO_2 layer. Both of these layers were deposited by RF-magnetron sputtering. Finally, top and bottom contacts made of Ti (30 nm)/Au (300 nm) were deposited and the devices were wire bonded for characterization.

3.2.1.2 X-ray diffraction (XRD)

The crystalline quality of the wafers was investigated by high-resolution XRD (HRXRD). The (004) HRXRD ω-2θ scans and simulations spectra for the three wafers are shown in Figure 3-2. From XRD measurements, the SL period is estimated as 59.34, 59.41 and 59.25 Å for Reg.-2S, Reg.-3S, and Rev.-2S, respectively, which are only slightly (0.4 -0.7%) larger than the designed SL period of 59 Å. The measured XRD spectra are in good agreement with the simulations. From the XRD measurements, all these ICIP structures had small tensile strain relative to the GaSb substrate, as shown in Table 3-1, along with the full width at half maximum (FWHM) of the 0th order peak of the SL. These XRD measurements indicate that the interface and material quality was similar in the three wafers.

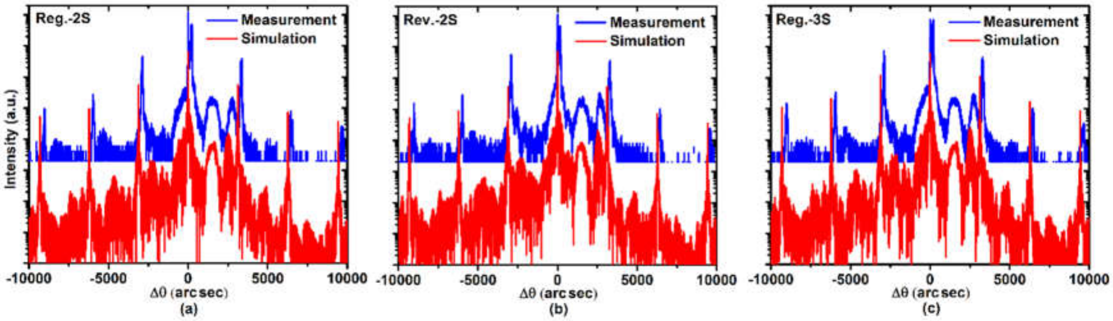

Figure 3-2: High resolution X-ray diffraction measurements (blue) and simulations (red) for (a) Reg.-2S, (b) Rev.-2S and (c) Reg.-3S wafers. XRD data reveal similar interface and material qualities for the three wafers.

Table 3-1: Summary of the parameters extracted from HRXRD measurements.

Wafer	**SL period (Å)**	***Δa/a* (%)**	**Strain type**	**SL 0th order peak FWHM (arc sec)**
Reg.-2S	59.34	0.197	tensile	24.94
Reg.-3S	59.41	0.164	tensile	32.90
Rev.-2S	59.25	0.128	tensile	30.32

3.2.1.3 Electroluminescence measurements

Similar to photoluminescence (PL) measurements, which have been extensively used for characterization of semiconductor materials, electroluminescence (EL) spectra can be used to evaluate ICIP structures. The FWHM of the EL spectrum and its peak intensity are good indicators of the material quality and its optical properties. EL measurements were carried out on ICIPs with the same size (500×500 μm^2) at equal injection currents (100 mA). Except for growth order, wafers Reg.-2S and Rev.-2S had the same cascade structure with the total absorber thicknesses of ~1.3 μm, so that their EL can be meaningfully compared. As shown in Figure 3-3, EL from both wafers had similar shape and peaks at the same wavelength (5.59 μm at 78 K), with higher peak intensity from Reg.-2S. This suggests that the two wafers have similar structural and interface quality, while wafer Reg.-2S may have somewhat better quality in terms of optical properties. This observation is qualitatively in agreement with our device electrical measurements described later. The EL spectra for Reg.-2S at T=78-300 K are illustrated in Figure 3-3(b). The EL peak positions are well matched to the device 50% photo-response cutoff wavelength (shown later). The photon energy corresponding to the EL peak position was approximately equal to the sum of the SL bandgap and the thermal energy ($k_B T$) at each temperature. From the EL peak position, the device bandgap was 214 meV (5.8 μm) at 78 K and 157 meV (7.9 μm) at T=300 K.

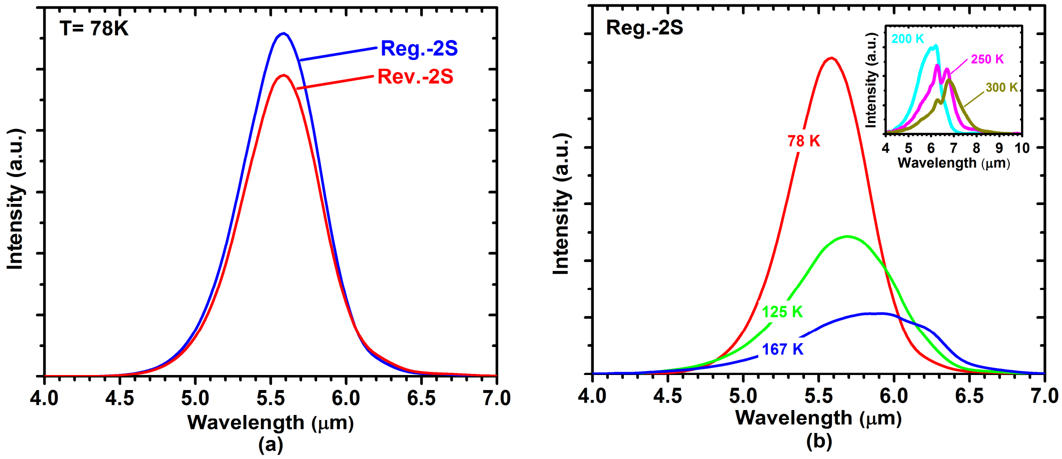

(a) (b)

Figure 3-3: (a) EL spectra at 78 K for Reg.-2S and Rev.-2S wafers, (b) EL spectra for a device from Reg.-2S at different temperatures.

3.2.2 Device characterization and discussion

3.2.2.1 Electrical measurements

3.2.2.1.1 Dark current

Detectors from the three wafers were mounted in a shielded cryostat and the device dark current (I_d) was measured at temperatures from 78 to 300 K. Dark current density (J_d) *vs*. bias voltage (V) for the three detectors (made from three wafers, respectively) are shown in Figure 3-4. For the reversed structure (Rev.-2S), shown in Figure 3-4(b), the applied bias had opposite polarity compared to the other two structures. At T=78 K the dark current densities were 5.65×10^{-7} (Reg.-2S), 1.20×10^{-6} (Reg.-3S), 7.63×10^{-5} (Rev.-2S) A/cm^2 at a reverse bias of 50 mV. We noticed that the measured dark currents at this bias did not follow the theory of ideal ICIPs (with diffusion limited dark current) [6]. For example, because the thermal generation of carriers is uniform through the absorbers, similar dark currents were expected in Reg.-2S and Rev.-2S. Also, based on the theory of ideal ICIPs, Reg.-3S was expected to have the lowest dark current among these detectors. By inspecting the J_d-V curves in reverse bias region we found that none of these detectors had diffusion limited dark current at 78 K (flattened dark current was not observed for $V>>k_\mathrm{B}T/q$ in the reverse bias region). Hence, the dark currents at this low temperature could not be described by the theory of ideal ICIPs. Nevertheless, with similar material quality and fabrication, the Reg.-2S and Rev.-2S detectors should exhibit similar electrical characteristics. The significantly higher dark current (more than two orders of magnitude) in Rev.-2S in comparison with Reg.-2S at 78 K implied that the material growth and/or device fabrication had some

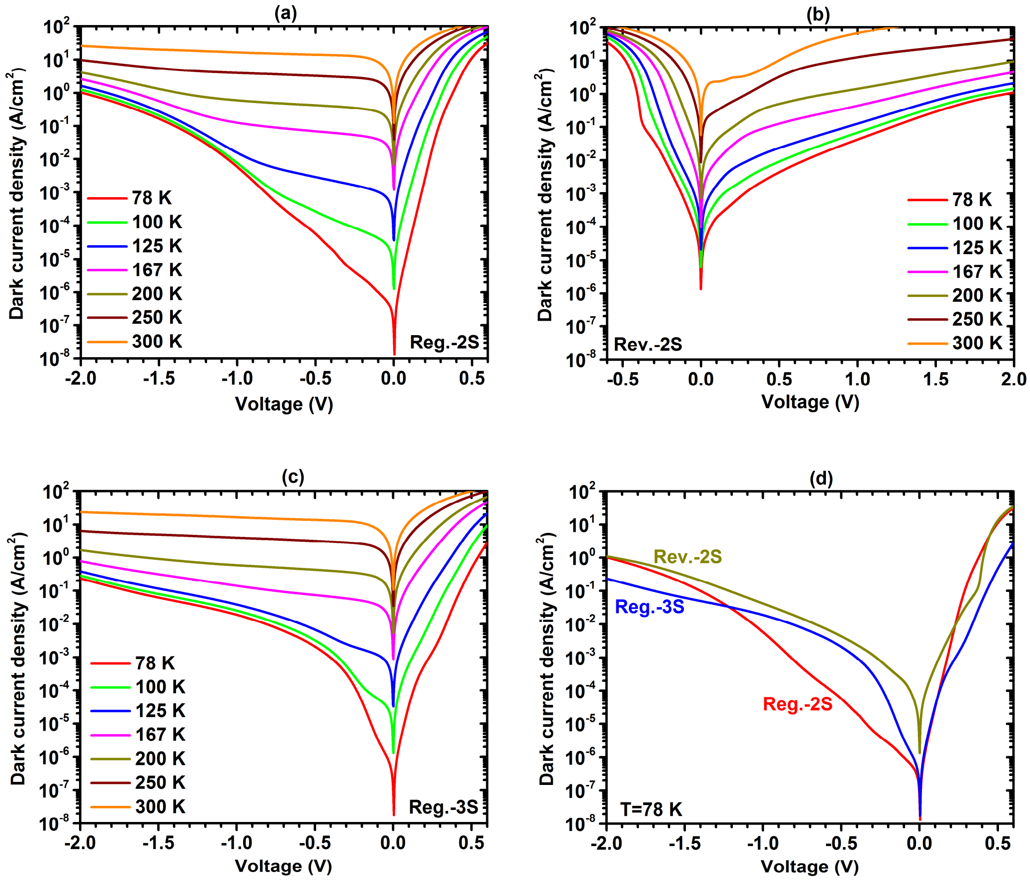

Figure 3-4: Dark current densities *vs*. voltage for: (a) Reg.-2S (regular two-stage), (b) Rev.-2S (reversed two-stage) and (c) Reg.-3S (regular three-stage), at different temperatures. (d) Dark current densities at T=78 K for representative devices from the three wafers.

variations from one wafer to another. Figure 3-4(d) compares the J_d-V curves for representative detectors from the three wafers at 78 K. We note that the bias polarity of J_d-V curve for Rev.-2S was reversed in this figure to make clear comparisons among different detectors. Apparently, Reg.-2S had the lowest dark current density at 78 K for a large range of reverse bias (beyond -1 V). The dark current densities for Reg.-2S and Rev.-2S converged at ~-2 V. At this high level of reverse bias, the dark current in both detectors could be dominated by the tunneling current that was mostly related to the device structure and less affected by the quality of the device material and fabrication. Properly designed ICIPs operate near zero-bias, where the tunneling has a negligible contribution to the device dark current and does not affect the normal operation of devices.

A linear plot of the dark current density *vs*. voltage for Reg.-2S and Rev.2S at 78 K is provided in Figure 3-5. A near-linear relationship between voltage and current for Rev.-2S is exhibited over several times the thermal energy voltage (k_BT/q) around zero bias in contrast with the more ideal-diode-like asymmetric characteristics of Reg.-2S. This suggests that Rev.-2S was limited by shunt leakage at low reverse bias. In general, such shunt behavior can be identified by inspecting the detector's *I-V* characteristics under low reverse and forward bias looking for the Ohmic behavior expected for a shunt channel. As shown in Figure 3-5, Rev.-2S had significant shunt leakage comparing to Reg.-2S, which was responsible for its much lower R_0A (620 Ω.cm^2) comparing to Reg.-2S (5.5×10^4 Ω.cm^2) (where R_0A is the zero-bias resistance device area product used to unravel leakage mechanisms). We also found that the diffusion dark current was smaller in Rev.-2S when the forward bias became higher than 228 mV. By increasing

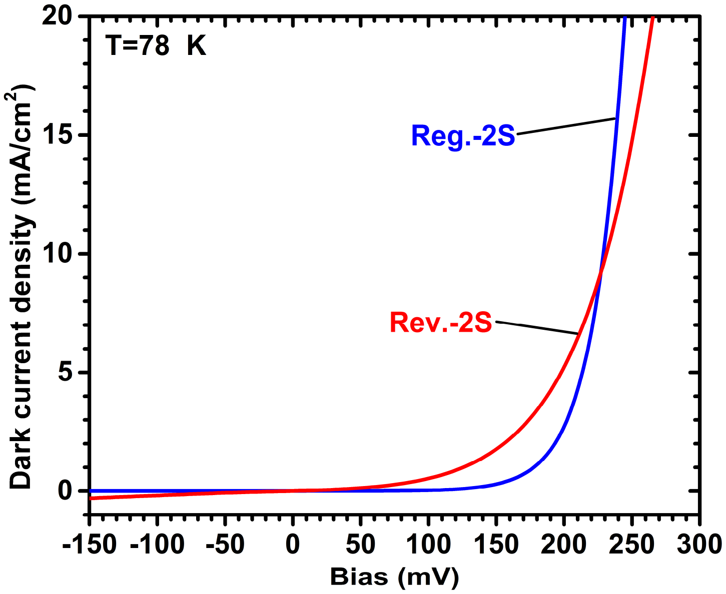

Figure 3-5: Linear plot of *J-V* for Reg.-2S and Rev.-2S detectors at 78 K. Shunt leakage was clearly observed in Rev.-2S wafer at low injection current.

the forward bias, the shunt effect became negligible as the diffusion dark current exponentially increased with bias. The lower *J* in this large bias range in Rev.-2S could be attributed to either a lower J_0 (saturation dark current density) or a larger *n* (ideality factor) for Rev.-2S. The larger *n* suggests lower material quality for Rev.-2S, which is in contradiction to the other possibility (lower J_0) that suggests higher material quality for this wafer. Based on the dark current characteristics of the two detectors and EL spectra, a larger ideality factor is likely responsible for all the observed behaviors.

3.2.2.1.2 Activation energy

To further investigate the device electrical performance, the activation energy was extracted by fitting an Arrhenius plot of dark current densities. Fitting results are tabulated in Table 3-2. We were able to appropriately fit the dark currents with a single activation energy over a wide temperature range for Reg.-2S (78-250 K) and Reg.-3S (91-250 K) but not Rev.-2S. The activation energy for Rev.-2S in a reduced temperature range (78-100 K) was 37 meV, which was significantly lower than the device bandgap and half the bandgap. The Rev.-2S activation energy increased to 71 meV at higher temperatures. These low activation energies confirmed that the device dark current was essentially controlled by a leakage mechanism (*e.g.*, surface leakage) that was relatively insensitive to temperature over this temperature range (78-167 K). We also found that the estimated activation energies decreased by increasing the reverse bias and could be fitted with similar activation energies for all the three devices over a smaller range of temperatures.

Table 3-2: Summary of activation energies obtained for the three wafers at different reverse bias voltages. Numbers in the parenthesis show the temperature range for which the activation energies are applicable.

Wafer name	Device config.	# of stages	Activation energy for different reverse bias (meV)				
			11 mV	50 mV	200 mV	500 mV	1000 mV
Reg.-2S	Regular	2	141 (78-250 K)	144 (78-250 K)	146 (91-250 K)	144 (111-250 K)	136 (143-250 K)
Reg.-3S	Regular	3	142 (91-250 K)	145 (91-250 K)	142 (100-250 K)	151 (143-250 K)	145 (167-250 K)
Rev.-2S	Reverse	2	37 (78-100 K) 71 (111-167 K)	31 (78-100 K) 69 (111-167 K)	29 (78-100 K) 64 (100-167 K)	22 (78-100 K) 62 (100-167 K)	15 (78-100 K) 45 (111-167 K)

This supports the idea that the dominant source of dark current transitions from a more temperature sensitive mechanism (*e.g.*, diffusion or *g*-*r*) to a less temperature sensitive mechanism (*e.g.*, tunneling) by increasing the reverse bias in these detectors. The extracted activation energy (at -11 mV) was ~140 meV for Reg.-2S and ~142 meV for Reg.-3S, which is smaller than the device bandgap. Activation energies obtained for these two detectors indicate that the dark current is not limited by diffusion in these two detectors and the *g*-*r* current has a substantial contribution among different factors.

Values of R_0A for representative devices at different temperatures are shown in Figure 3-6. At T=125 K and higher temperatures, the R_0A for a device made from wafer Rev.-2S is larger than the other two devices made from wafers Reg.-2S and Ref.-3S. As discussed below, this abnormal behavior probably resulted from an undesirable electrostatic barrier in the Rev.-2S structure, which blocked *both* dark current and photocurrent. The very low zero-bias photo-response observed in Rev.-2S confirms the

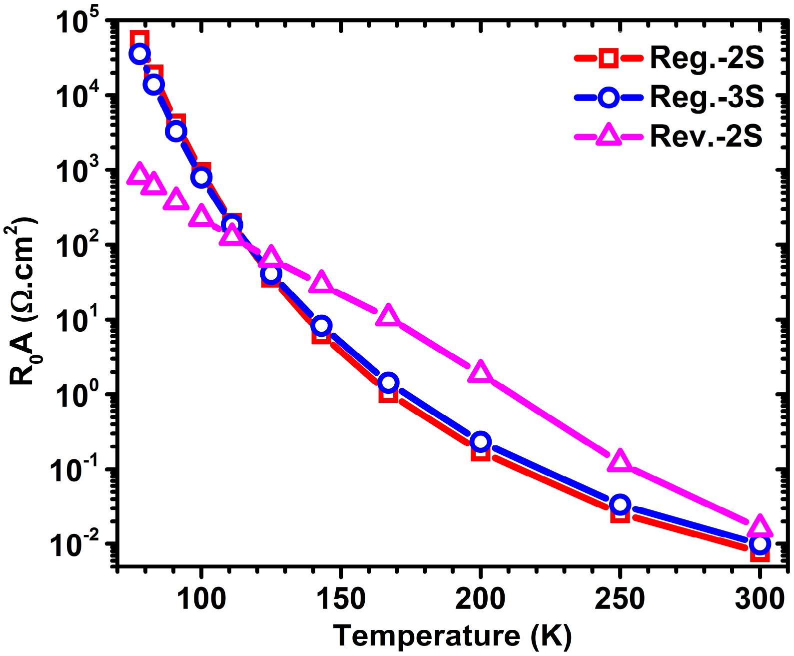

Figure 3-6: R_0A *vs*. temperature for: Reg.-2S (squares), Rev.-2S (triangles) and Reg.-3S (circles).

the existence of this electrostatic barrier. In other words, the higher value of R_0A for Rev.-2S (at $T \geq 125$ K) came at the expense of decreased photocurrent and does not necessarily imply a better performance for detector Rev.-2S compared to the other two detectors at these temperatures.

At temperatures of 125 K and above, Reg.-3S had higher R_0A than Reg.-2S. In contrast to Rev.-2S, the undesirable electrostatic barrier was not observed in Reg.-2S and Reg.-3S structures. Consequently, the higher value of R_0A observed in Reg.-3S was attributed to the extra stage in its structure. These two observations suggest that at relatively high temperatures, the imperfections associated with the device growth and fabrication was less influential on the device performance and diffusion currents may start to dominate the device dark current.

As discussed in Chapter 2, the R_0A for photocurrent-matched ICIPs with diffusion-limited dark current can be expressed by Equation 2-4. From this equation, a higher R_0A is expected in detectors with more stages. Assuming that the minority carrier diffusion length is larger than the absorber thickness in all of the device stages (*i.e.* $L_{e,h} >> d_m$), which is a reasonable assumption for ICIPs at certain temperature ranges. For the two- and three-stage detectors we have:

$$\frac{R_0A_{3-stage}}{R_0A_{2-stage}} = \frac{d_1d_2+d_1d_3+d_2d_3}{(d_1+d_2)d_3} \tag{3-1}$$

where d_1, d_2, and d_3 denote the absorber thicknesses in different stages. The above ratio is equal to 1.35 for detectors presented in this work. The extracted ratios between measured R_0A values for the Reg.-2S and Reg.-3S devices (two- and three-stage regular, respectively) are 1.13, 1.31, 1.37,1.35 and 1.31 at T=125, 143, 167, 200 and 250 K, respectively. These values agree very well with the theory for ICIPs [6]. We expect that by improving the material quality and the device fabrication theoretically predicted performance will be obtained at lower device temperatures.

3.2.2.2 Optical measurements

3.2.2.2.1 Responsivity

Response spectra were obtained using our established setup for response characterization (see section 1.3.1.1) and a 600 K blackbody source. Figure 3-7 shows the zero-bias responsivity spectra for devices made from wafers Reg.-2S and Reg.-3S at T=78-300 K. These regular two- and three-stage ICIPs had responsivities of 0.38 and 0.34 A/W at 78 K for λ=5 μm, respectively, which indicates an effective implementation of photocurrent matching between different stages in these two detectors. As can be seen in this figure, the responsivity mismatch (~10% at 5 μm) between the two- and three-stage ICIPs increased at shorter wavelengths. Considering the stronger absorption at the shorter wavelengths and specific requirements for particular applications, better photocurrent matching can be achieved by increasing the absorber thickness for optically deeper stages. The two detectors were able to sustain full photo-response at zero bias (the photo-response did not increase with a reverse bias) at temperatures up to 200 K, which means that the photo-generated carriers were efficiently collected up to this temperature. At *T*=250 K the photo-response started to decrease in both detectors. Because of decreased diffusion length and carrier lifetime, the carriers transport and collection become less efficient at high temperatures. Since ICIPs are multiple stage detectors with flexible absorber thicknesses and number of stages, the collection of photo-generated carriers and the device performance at room temperature (and above) can be improved by carefully adjusting the structure parameters. The inset to Figure 3- 7(b) shows relative photoresponse spectra (without calibration) for devices at temperatures up to 340 K. Despite being somewhat noisy at these temperatures, we were able to operate a three-stage ICIP with decent response spectra up to 340 K where the 100% cutoff wavelength was longer than 8 μm. At *T*=

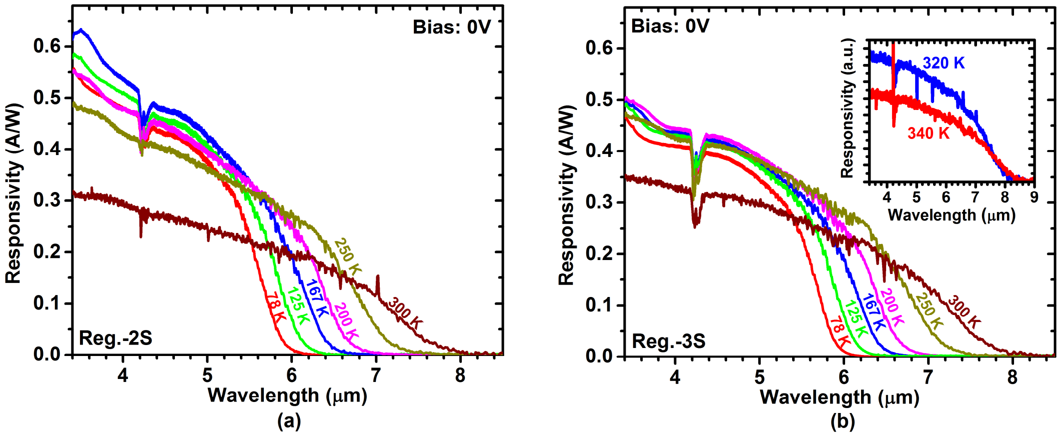

Figure 3-7: Zero-bias response for (a) Reg.-2S and (b) Reg.-3S at different device temperatures. The responsivity increased for temperatures up to 200 K in Reg.-3S detector. Inset in (b) shows the response spectra at 320 and 340 K.

300 K the response for the three-stage detector was higher than the response of the two-stage ICIP, which was contrary to our observations at lower temperatures. This discrepancy may be attributed to the uncertainty and inaccuracy in our measurements due to a very low resistance (*e.g.,* <10 Ω) for devices especially with two-stage structures at high temperature. In such scenarios, the series resistance from contact and external wire connections could be comparable to or even higher than the internal device resistance, presenting a difficulty in extracting an accurate value of intrinsic photocurrent in devices at high temperatures. Hence, the responsivity could be underestimated for devices at high temperatures, which might be more significant for the two-stage devices (since the device resistance was lower in two-stage devices compared to three-stage devices). For ICIPs with more stages, this difficulty is alleviated because the internal device resistance increases with the number of cascade stages. This is another advantage of multi-stage ICIPs over a single-stage detector for high-temperature operation.

In addition to the relatively poor electrical performance (especially up to 125 K), the optical characteristics of Rev.-2S were also not as good as the other two wafers. At zero-bias, a typical Rev.-2S detector had a low responsivity (*e.g.,* 25 mA/W at 78 K for λ=5 μm), which was about 15 times smaller than the response for Reg.-2S detectors. Figure 3-8 shows the responsivity *vs*. reverse bias for Rev.-2S detectors. As can be seen in this figure, a relatively high reverse bias was required in order to reach the maximum photoresponse in this detector. Ideally, Rev.-2S and Reg.-2S should exhibit similar response characteristics at any bias. The unexpected photo-response observed in Rev.-2S may have two explanations:

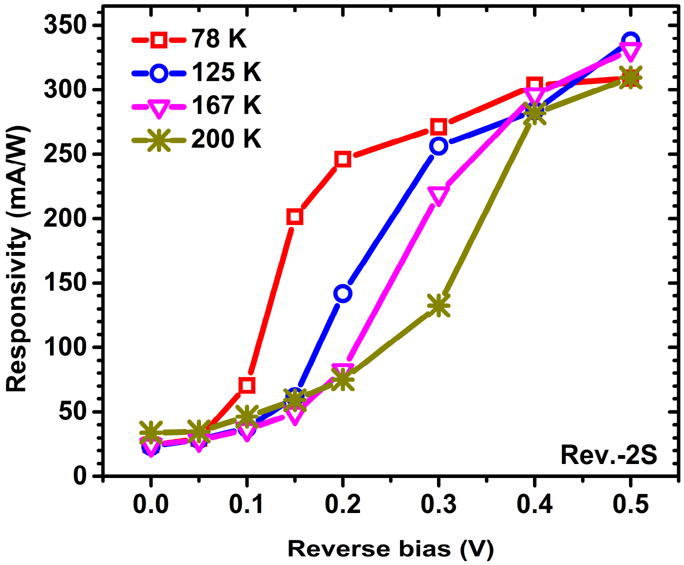

Figure 3-8: Responsivity *vs*. reverse bias (at λ=5 μm) for Rev.-2S at temperatures up to 200 K. By increasing the device temperature, higher levels of reverse bias were required to reach the same response level.

(1) The existence of an undesirable electrostatic barrier between the absorber and the hole (or electron) barrier that inhibited the transport of electrons (and/or holes).

(2) Although SL absorbers were partially *p*-doped, the minority carriers could be holes (rather than electrons) at certain temperatures and/or the transport in the SL may become limited by intrinsic carriers and ambipolar diffusion at high temperatures.

If **(1)** is true, then at higher temperatures as carriers gain more thermal energy, the electrostatic barrier will become less effective in blocking the photo-generated carriers. This was in agreement with our observations for the zero-bias response in Rev.-2S. However, it cannot explain why a relatively high reverse bias is still required to reach similar response values at higher temperatures. For detectors with narrow bandgaps, the intrinsic carrier concentration increases rapidly with temperature and may become comparable to the absorber doping level at certain temperatures. This is likely in a T2SL because of its narrow bandgap and the *n*-type (background) doping expected for InAs layers grown by MBE. Because holes have a considerably lower diffusion length comparing to that of electrons, if the transport of carriers was largely affected by holes, then the reverse illumination configuration (Rev.-2S), in which most of the photogenerated holes were away from the collection layer (the electron barriers), would be less effective to collect the photo-generated carriers. In this case, a certain reverse bias is required to facilitate the holes' transport. As the diffusion length and carrier lifetime decrease at high temperatures, a relatively larger reverse bias is then required to reach significant response levels by increasing the device temperature.

3.2.2.2.2 Detectivity

For detectors made from wafers Reg.-2S and Reg.-3S we were able to achieve the maximum response under zero bias for temperatures up to 200 K, and the Johnson-noise-limited detectivity (D^*) was used to evaluate the device sensitivity. Figure 3-9(a) shows the Johnson-noise-limited D^* at 5 μm for devices made from the three wafers. At temperatures up to 125 K, the calculated D^* for Reg.-2S was larger than the corresponding values for Reg.-3S. This difference was in disagreement with theoretical predictions and is attributed to the lower responsivity (probably due to mismatch of the photocurrent with the third stage absorber) and lower R_0A in the Reg.-3S device at temperatures lower than 125 K. At temperatures above 125 K, D^* in Reg.-3S was higher, in qualitative agreement with the theory. Compared to Rev.-2S, Reg.-2S and Reg.-3S had higher D^* at 78 K (~2 orders of magnitude), which is related to their much lower dark current and their higher photocurrent under zero-bias operation.

For Rev.-2S, the detector's response was bias dependent at all the temperatures so the shot noise term related to the device dark current needs to be considered in the evaluation of D^* (Equation 2-8). Note that the shot noise in ICIPs is inversely proportional to the number of stages (N_s) [7]. This implies that the shot noise is reduced in ICIPs with more stages. In other words, at equal dark currents, the overall noise is lower in a multiple stage ICIP compared to a single stage detector. Specific detectivity as a function of the reverse bias for Rev.-2S at T=78-200 K is shown in Figure 3-9(b). The D^* increased in the Rev.-2S device by adding the reverse bias to a certain level and then it started to decline at higher reverse biases. The observed bias dependent behavior for D^* suggests that the increase in the device signal (photocurrent) for a reverse bias was more significant than the dark current increase up to some levels of reverse bias, resulting in increased D^* with reverse bias.

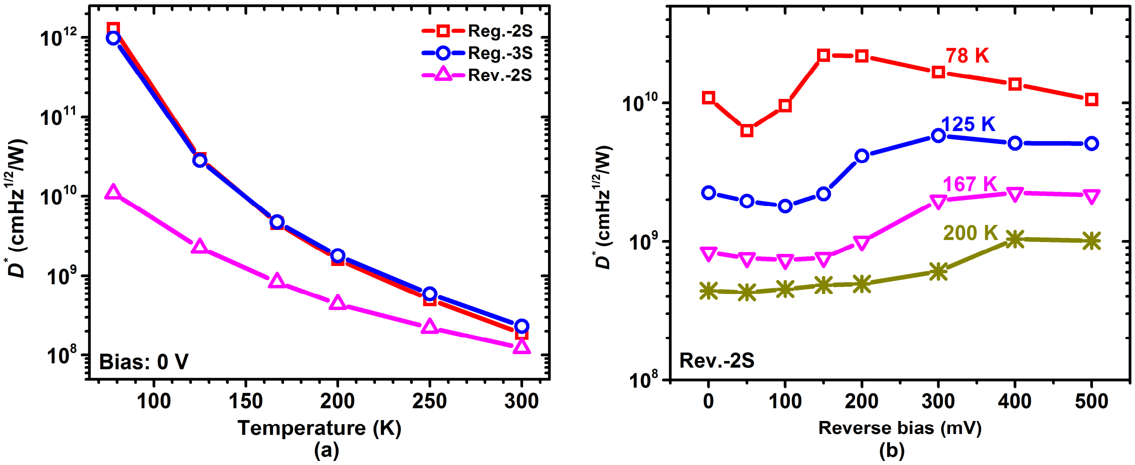

Figure 3-9: (a) Zero-bias specific detectivity (at λ=5 μm) for the three wafers up to room temperature. (b) D^* for Rev.-2S *vs*. reverse bias for temperatures up to 200 K.

3.3 Long wavelength ICIPs with cutoff wavelength of ~9 μm

3.3.1 Device structure, growth, and fabrication

Two LWIR ICIPs with two stages and with reverse configuration (wafers R120 and R121) were designed to investigate the performance of ICIPs in this band. The layering sequence was nearly identical in both detectors, aside from their InSb strain-balancing layers. The absorber layers had thicknesses of 620.0 nm and 756.4 nm, with each SL period composed of 36.3 Å of InAs and 21.9 Å of GaSb. In each SL period of R120, a 1.9-Å-thick InSb layer was intentionally inserted into both the InAs-on-GaSb and the GaSb-on-InAs layers as the interface layer. However, in R121, the InSb layer (3.8 Å) is only inserted into the GaSb-on-InAs layers. Figure 3-10 shows the schematic drawing of these two structures. The device fabrication process followed the process flow described in section 2.7 with a 170 nm of Si_3N_4 followed by 137 nm of SiO_2 for device passivation.

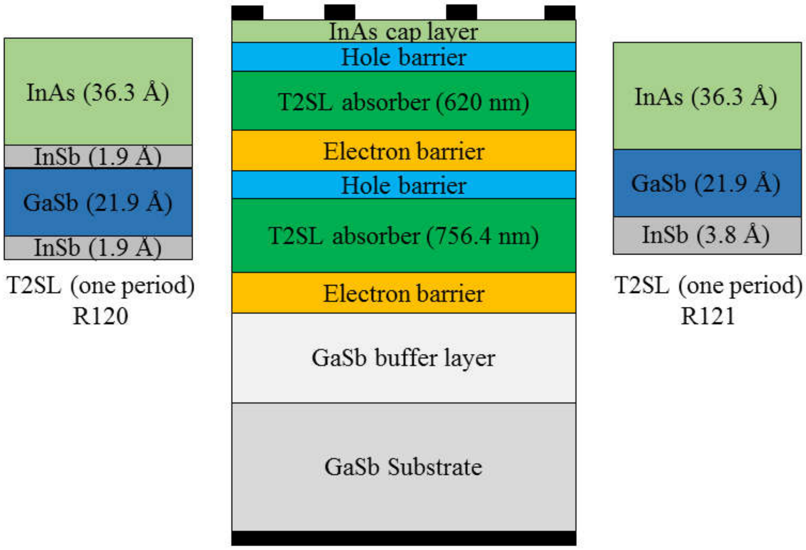

Figure 3-10: Schematic drawing of the device structure for R120 and R121 wafers. The only difference between the two wafers was the InSb strain-balancing layers used in each period of T2SL absorbers.

3.3.2 Electrical performance

For dark current measurements, the devices were mounted in a cryostat with a cold shield. Many devices made from these two wafers were characterized. At 78K, the average R_0A for the R121 wafer (16 detectors) was 58.3 Ω.cm^2. This value was noticeably higher than the average value (32.7 Ω.cm^2) for devices (17 detectors) made from the R120 wafer. Comparing the best performing devices from both wafers (see Figure 3-11), the dark current density at 50 mV was 3.0×10^{-4} (3.5×10^{-4}) A/cm^2 for R121 (R120) with corresponding R_0A of 150 (115) Ω.cm^2 at 78 K. The electrical characteristics of devices made from these two wafers did not exhibit any enhancement (lower dark current) by using two InSb interface (R120) over one InSb interface detectors (R121), which is in agreement with our material characterizations (X-ray diffraction and optical microscopy) [8]. This suggested that wafers R120 and R121 had comparable material quality.

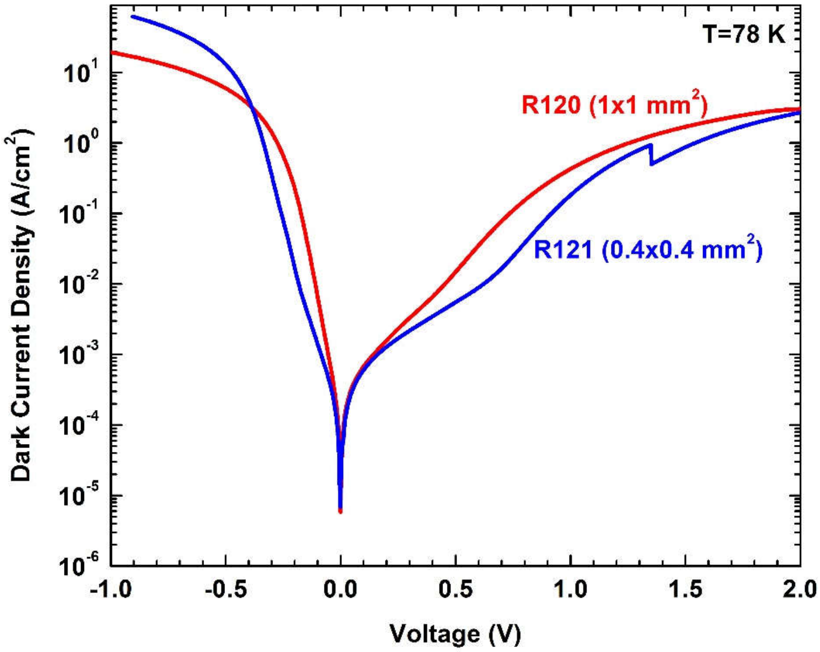

Figure 3-11: Dark current density (J_d) *vs.* voltage (V) at 78 K for two devices made from R120 and R121 wafers.

J_d-V curves at different operating temperatures for a representative photodetector from the R120 wafer are shown in Figure 3-12. In order to identify the dominant dark current mechanism, an Arrhenius plot of the device dark current (at 50 mV bias) across the 100-250 K temperature range was fitted to the following equation:

$$J_d = Ce^{-\frac{E_a}{k_B T}}, \tag{3-2}$$

where E_a is the activation energy. As shown in the inset to Figure 3-12, the activation energy is estimated to be 102 meV. The activation energy (not shown in the figure) for devices from wafer R121 is 126 meV. At 78 K the corresponding bandgap energy at the 100% cutoff wavelength for photoresponse was 131 and 135 meV for wafers R121 and R120, respectively. The fitted activation energy was closer to the device 100% bandgap energy at 78 K for wafer R121. These activation energies imply that the detectors are neither diffusion limited nor dominated by the *g*-*r* process (activation energy is larger than $E_g/2$) for this temperature range. The deviation from the diffusion limit is probably related to the non-uniform doping that is applied to the absorber regions, which may result in an electric field that could affect the Shockley-Read-Hall generation-recombination in the absorber layers. Further investigations are required to quantify different elements of dark current in ICIPs.

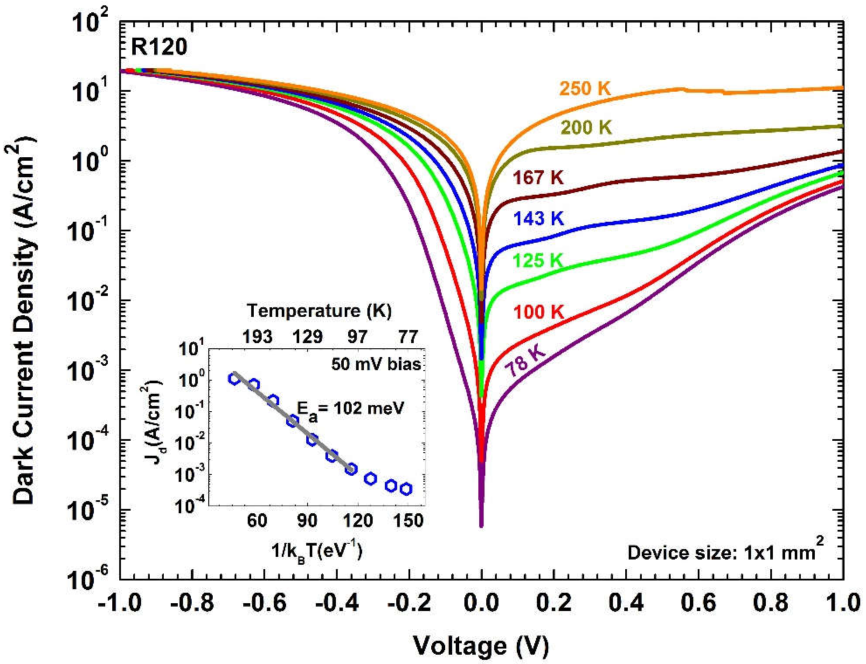

Figure 3-12: Dark current density *vs*. bias at different temperatures for an LWIR detector from R120 wafer. The inset shows the fitted activation energy for the Arrhenius plot of the device dark current.

3.3.3 Optical performance

3.3.3.1 Responsivity

The optical response characterization of the devices was performed using a 600 K blackbody source with a 0.76 cm aperture size positioned 30 cm away from the device under test (DUT). The device 100% cutoff wavelength was ~9.2 μm at 78 K and extended to ~11.4 μm at 220 K. For devices from the R120 wafer, the device response increased by raising the device temperature and was not bias-dependent up to 167 K. However, at higher temperatures (as shown in Figure 3-13), the maximum response was achieved under some level of reverse bias. Notice that a somewhat higher reverse bias was required to reach maximum response at higher device temperature. The zero-bias response spectra at temperatures of 240 and 250 K are also shown in the inset to Figure

3-13. For these temperatures, we were not able to sufficiently bias these detectors, because the dark current overloaded the current amplifier. While some uncertainty exists in the accuracy of the calibrated photoresponse at elevated temperatures, it is clear that the device photoresponse sharply decreases at high temperatures (the calibrated response at 240 K was more than 4 times lower than the response at 125 K), which is indicative of significantly shorter diffusion length at elevated temperatures. Therefore, the absorbers thicknesses in each stage should be further reduced to achieve full response under zero-bias condition.

The bias dependency of the response at high temperatures is an indicator of inefficiencies in the carrier transport process, which could be ascribed to the decreased diffusion length. Switching of the residual doping from *p*-type to *n*-type for InAs/GaSb SL material has been reported in [9-11]. Studies of mid-wave infrared InAs/GaSb SLs confirm that the material becomes *n*-type for temperatures higher than 120 K [11].

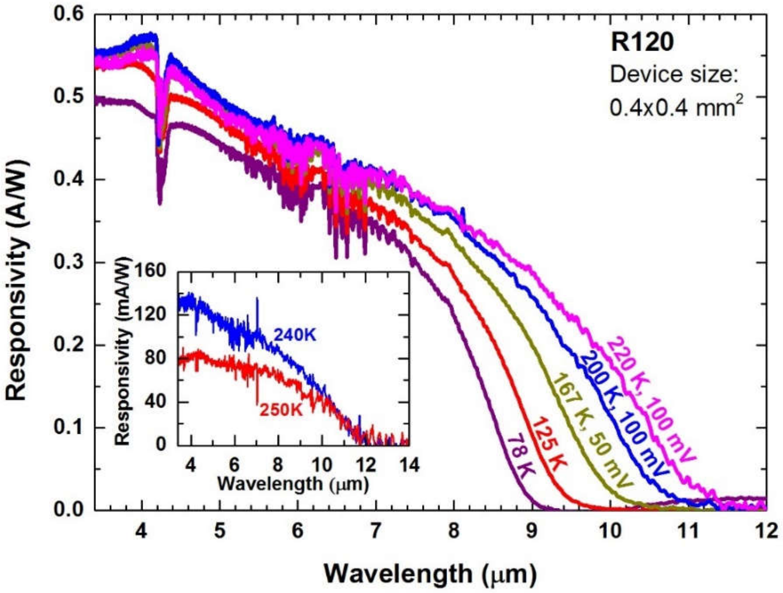

Figure 3-13: Responsivity spectra of a photodetector from R120 wafer at temperatures up to 220 K. Inset shows its zero-bias responsivity spectra at 240 and 250 K.

There is a strong possibility for a carrier-type alteration to occur at lower temperatures for LWIR photodetectors due to thicker layers of InAs that are included in each SL period. The resulting lower diffusion length of holes and the revered designed utilized in these photodetectors could negate the carrier collection.

3.3.3.2 Detectivity

The detectivity for a representative device from R120 wafer is displayed in Figure 3-14 at different temperatures. At 78 K, the highest D^* for R120 and R121 wafers at $\lambda = 8.0$ µm under zero-bias operation was 3.7×10^{10} cm.Hz$^{1/2}$/W. In contrast to the response curves that have their maximum at relatively large reverse bias, particularly at high temperatures, D^* did not increase with reverse bias. We also note that although the device resistance was higher at a small reverse bias compared to the zero-bias resistance (lower Johnson noise), the increased dark current under a reverse bias (larger shot noise) had a more significant influence on the device signal to noise ratio, resulting in a reduced value of D^*.

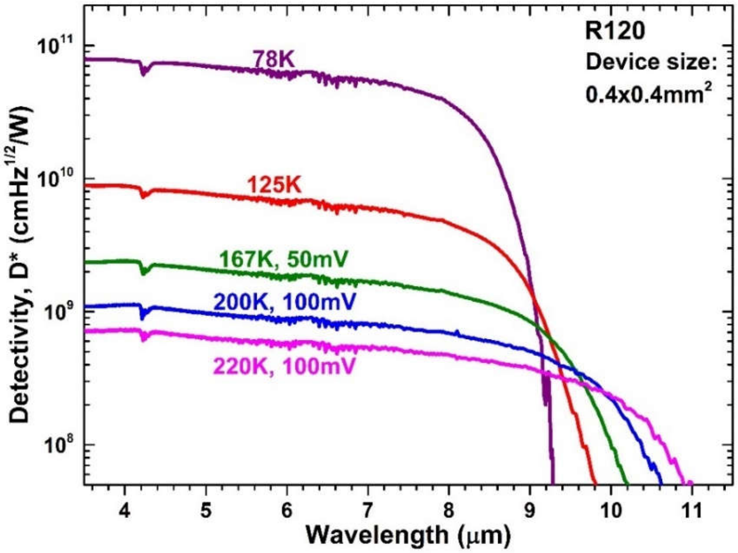

Figure 3-14: Detectivity D^* for a detector made from R120 wafer at temperatures up to 220 K.

3.4 Very long-wavelength ICIPs

3.4.1 Device design, growth, and fabrication

A set of three photo-current matched ICIP structures was designed to target the VLWIR region. For this set, each SL period was composed of 45-Å-thick InAs and 21.2-Å-thick GaSb layers, with a thin InSb (4.8 Å) layer inserted into the GaSb-on-InAs layers as an interface to compensate the tensile strain introduced by the relatively thick InAs layers. The two- and three-stage devices had 568-nm and 639-nm-thick absorbers. The three-stage detectors had an additional stage with a 752.6–nm- thick absorber. To compare the performance of ICIPs with that of single-stage detectors, the third structure was a one-stage device with the absorber thickness of 1.96 μm, equal to the total thickness of the absorbers in the three-stage device. The schematic structure for these ICIPs is shown in Figure 3-15. In order to make electrons the minority carriers, half of the GaSb layers in the SL absorbers were *p*-doped with a doping density of 3.9×10^{16} cm^{-3}. The electron and hole barriers in each of these devices had identical designs and all the ICIPs were grown by MBE on non-intentionally doped GaSb substrates at OU. After growth, square mesa devices with edge lengths ranging from 200 to 1000 μm were fabricated using conventional contact UV lithography and chemical wet etching. A 228-nm- thick Si_3N_4 layer was used as the passivation layer for these detectors and the top and bottom contacts consisted of sputtered 30-nm-thick Ti and 300-nm-thick Au layers (no contact annealing was performed).

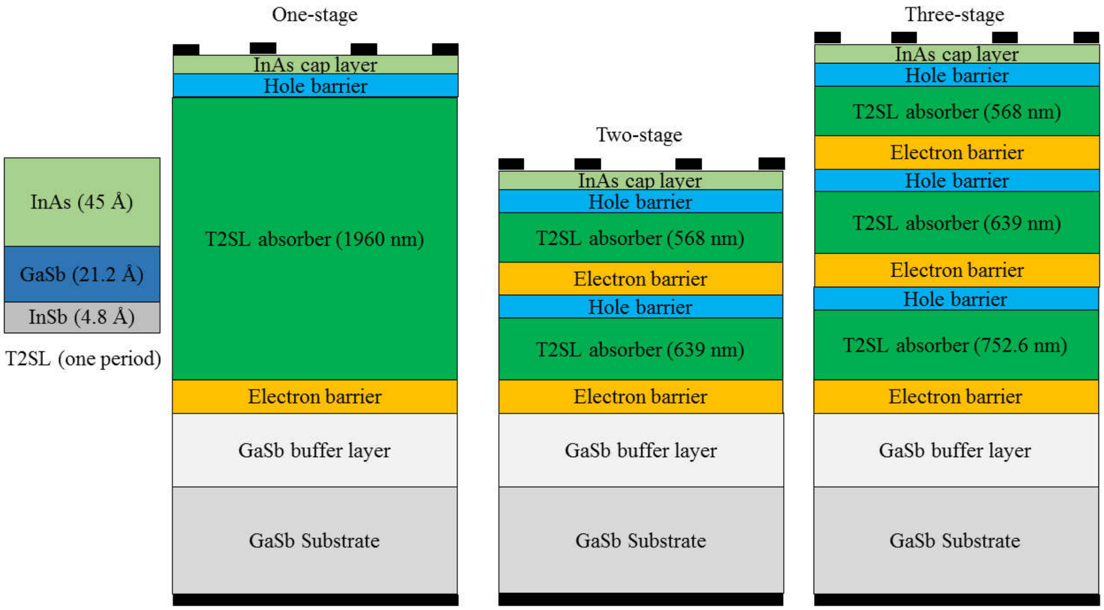

Figure 3-15: Schematic structure of the three VLWIR detectors.

3.4.2 Electrical performance

As shown in Figure 3-15, the VLWIR ICIPs had a reverse configuration. Since the hole barrier is at the top of each stage, the device is under reverse bias when a positive voltage is applied to the top contact. Dark current density (J_d) *vs*. bias voltage (V) for representative one-, two- and three-stage devices at various temperatures is shown in Figure 3-16. As displayed in this figure, the dark current density at 78 K for a one-stage device (*e.g.*, 0.1 A/cm^2 at 50 mV) was the highest among all the three detectors. This was expected based on the theory for ideal diffusion-limited detectors. However, the dark current data for some two- and three-stage devices, especially at low temperatures, did not follow what was expected from theoretical predictions [6, 7]. This was likely due to variations in material uniformity and device fabrication. For devices shown in Figure 3-15, at 50 mV and at 78 K, the dark current density was 25 mA/cm^2 for a three-stage device, which was comparable to the corresponding value of 24 mA/cm^2 for a two-stage detector. For a multiple stage detector with diffusion limited dark current, the product of device resistance at zero bias (R_0) and device area (A) is expressed by Equation 2-4. One can see that R_0A is proportional to the sum of $1/\tanh(d_m/L_e)$ and will be higher for detectors with more stages, and is lower for detectors with longer absorbers. Applying Equation 2-4 to VLWIR detectors at 78 K and assuming that the minority carrier diffusion length is much longer than the absorber thickness (*i.e.*, d_m/L_e <<1), the R_0A for two- and three–stage detectors should be 6.5 and 9.1 times larger than the corresponding value for the one-stage detectors, respectively. The experimentally extracted values of the R_0A for the two- and three-stage detectors were 2.4 Ω.cm^2 and 2.3 Ω.cm^2, which are about 4 times higher than that of the one-stage device (0.56 Ω.cm^2). Hence, R_0A for multiple-stage devices was not as high as expected from Equation 2-4 in the d_m/L_e <<1 limit. This discrepancy indicates that the dark current in these detectors deviated from a diffusion-limited behavior, as mentioned

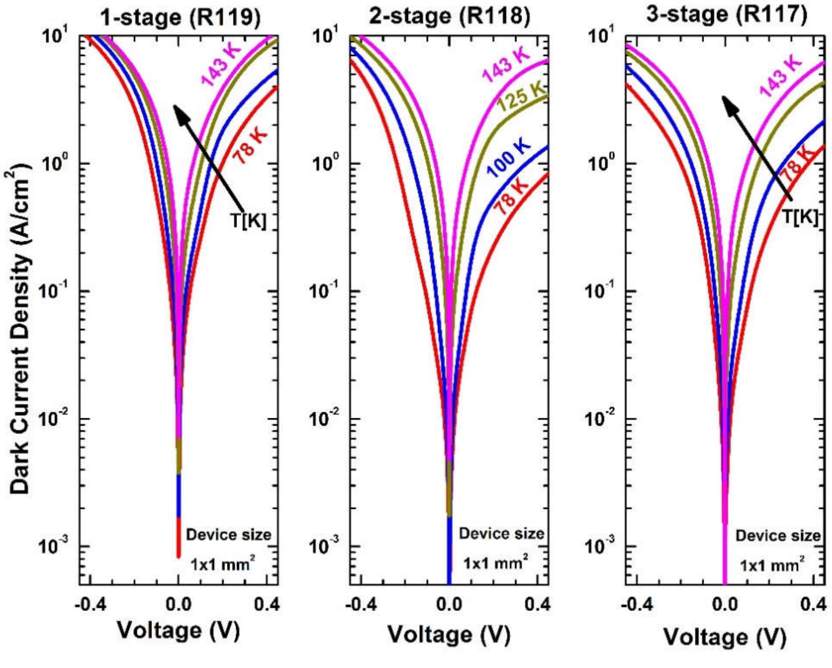

Figure 3-16: Dark current density *vs*. bias voltage for one-, two- and three-stage VLWIR ICIPs for 78-143 K.

above, and that the carrier transport is primarily mediated by other processes that cause the minority carrier diffusion length to be shorter than the absorber thickness. If the diffusion length is much shorter than the absorber thicknesses (*i.e.* $d_m/L_e >> 1$), the R_0A for the two- and three-stage detectors would be smaller according to Equation 2-4 and is only two and three times larger than the one-stage detector, respectively. However, the measured values were higher than the theoretical projection in the limit of $d_m/L_e >> 1$. This suggests that the dark current may not be dominated by the diffusion process and/or the absorber thicknesses–to-diffusion length ratio was somewhere between these two extreme cases (*i.e.*, $d_m/L_e << 1$ and $d_m/L_e >> 1$).

At temperatures above 100 K, the dark current density was lower for the three-stage detector than for the two-stage device, which is qualitatively more consistent with what is implied in Equation 2-4. The irregular behavior at low temperatures suggests that additional factors (such as variations in the material and fabrication quality) influence the device dark current. For all devices from the three wafers, the dark current was sensitive to the bias voltage across the entire range of applied reverse bias and did not saturate. Note that the dark current densities in VLWIR detectors are intrinsically high due to the very narrow bandgaps. Additionally, crystalline defects (surface defect density of $5\text{-}10\times10^5$ cm^{-2}) and defect-assisted tunneling open additional channels that increase the dark current in these devices.

3.4.3 Optical characteristics

3.4.3.1 Responsivity

Optical response measurements were performed following the procedure described in section 1.3.1.1. Notice that the blackbody source was placed at a distance of 9.5 cm from the device under test (DUT) to enhance the signal to noise ratio during photocurrent measurements. Unlike most of our ICIPs, which have a large photo-response under the zero-bias condition, the device photocurrent was strongly bias dependent and substantially increased under reverse bias in these ICIPs. This behavior is indicative of some non-idealities in the carrier transport. One possible situation is the existence of an unintentional electrostatic barrier between the absorber and the hole barrier, which impeded the collection of the photo-generated electrons. Meanwhile, the SL absorber is InAs rich (there is about twice as much InAs as GaSb in the SL for the VLWIR detectors) and the background doping of MBE-grown InAs is *n*-type, therefore chances are that the SL absorber may have become *n*-type, despite the intentional *p*-doping of the absorber in GaSb layers. Furthermore, due to the very narrow bandgap of these detectors (at 78 K), it is likely that the intrinsic carrier concentration (n_i) becomes higher than the doping concentration. Thus, even with intentional *p*-doping of the absorber (in GaSb layers), the SL absorber may be *n*-type in VLWIR detectors, even at low temperatures [9]. This implies that the diffusion length could be shorter than expected due to the low vertical hole mobility in InAs/GaSb SLs. Consequently, the collection of photogenerated carriers would be less efficient, particularly in the reverse configuration ICIPs, where most of the holes are generated far from the collection point. In this case, the applied reverse bias would accelerate holes towards the electron barrier, *i.e*. the collection point and facilitates the carriers transport.

The responsivity spectra (R_λ) for a two-stage detector at 78 and 100 K are shown in Figure 3-17. At 10 μm the responsivity was 0.35 A/W at 78 K under 300 mV bias. However, as stated above, the responsivity was low at zero bias for all tested devices made from the three wafers. As shown in inset (a) to Figure 3-17, for the zero-bias responsivity at $\lambda = 10$ μm, the single-stage device with the thickest absorber had the lowest photo-response, while the three-stage device, with the second thickest absorber (in its third stage), had the second lowest value. Their zero-bias responsivity increased with raising the device temperature up to 143 K. Such a temperature dependence characteristic was observed for all tested devices from the three wafers. At higher device temperatures, photogenerated carriers have larger thermal energy and have better chance to surmount the electrostatic barrier. This observation supports the existence of an unwanted electrostatic barrier that blocks the collection of photogenerated carriers. At 78 and 100 K, the photoresponse of these detectors increased significantly with reverse bias. For example, the responsivity at 10 μm increased from 4.0 mA/W at zero bias to 352 mA/W at 300 mV for a two-stage ICIP at 78 K. At 100 K, the responsivities were reduced compared to the values for the three devices at 78 K and at the same bias voltage. For instance, under 150 mV the one-stage device exhibited a significant (~46%) reduction in its photo-response as the temperature was increased from 78 to 100 K. However, the responsivities for the two- and three-stage devices at the same bias (150 mV) were moderately decreased (6% for two-stage and 13% for three-stage) compared to their values at 78 K. This is indicative of a poorer collection of photo generated carriers in thick-absorber detectors at higher temperatures. The responsivity for temperatures above 100 K for the two-stage detector (under zero-bias) is shown in inset (b) to Figure 3-17. We attempted to identify the maximum operating temperature at which a meaningful response spectrum could be obtained using the FTIR

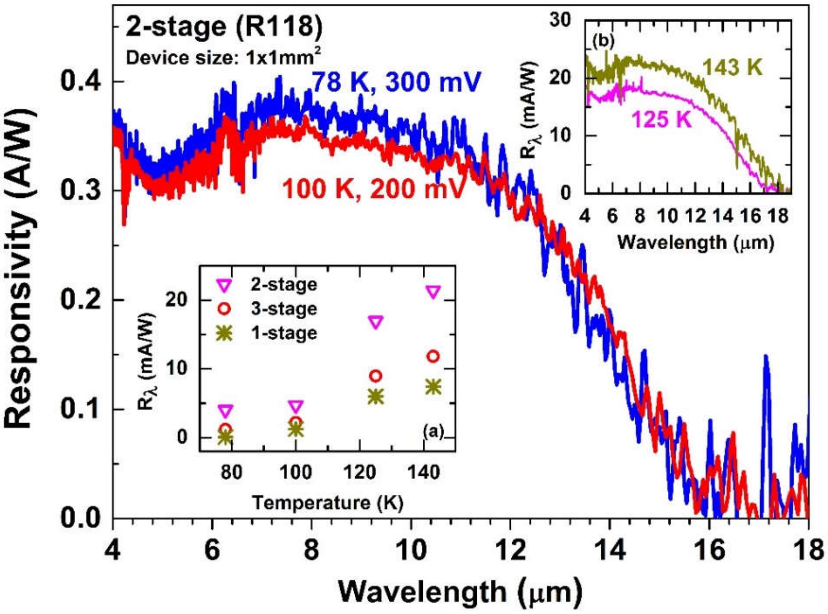

Figure 3-17: Responsivity spectra (R_λ) for a two-stage VLWIR detector at 78 and 100 K under reverse bias. Indicated voltages are the bias at which the maximum response was acquired. Inset (a): zero-bias R_λ at λ =10 µm for one-, two- and three-stage ICIPs at different temperatures. Inset (b): Zero-bias R_λ at 125 and 143 K for the two-stage VLWIR photodetector.

spectrometer. Although the response spectra were noisy, both two- and three-stage detectors were able to operate up to 185 K, which is higher than the maximum operating temperature of 167 K for the single absorber detector.

3.4.3.2 Detectivity

To further compare the performance of these ICIPs, the normalized detectivity, D^*, was calculated (see Figure 3-18). Since the maximum photoresponse was obtained under a reverse bias, the dark current shot noise was considered for the D^* calculations (Equation 2-8). As shown in Figure 3-18, D^* for the two-stage detector was comparable to that of the one-stage detector, while it was significantly lower in the three-stage detectors. The unexpectedly lower D^* in three-stage devices was attributed to their low responsivity and high dark current. In the one-stage device, the responsivity is substantially higher because of the thicker absorber (1.96 μm). For example, at a bias of 150 mV and λ=10 μm the responsivity was 0.68 A/W for one-stage detector; while it was 0.29 and 0.12 A/W for two- and three-stage detectors. Because the two- and three-stage detectors were designed to be photocurrent-matched, equal responsivities were projected for these photodetectors. However, the three–stage detectors had lower responsivity, which could be associated with the imperfect implementation of photocurrent matching and the requirement of a higher bias voltage for reaching the maximum photocurrent with an additional stage.

Under a 150 mV bias, the D^* for the single-absorber detector at T=78 K and λ=10 μm was 1.5×10^9 cm.Hz$^{1/2}$/W, which is lower than 4×10^{10} cm.Hz$^{1/2}$/W reported for a 14-μm-cutoff-wavelength detector with a similar absorber thickness (1.9 μm) [12]. The peak responsivity of 0.81 A/W obtained for the single-stage detectors was somewhat lower than the peak responsivity of 1.4 A/W at similar wavelengths reported

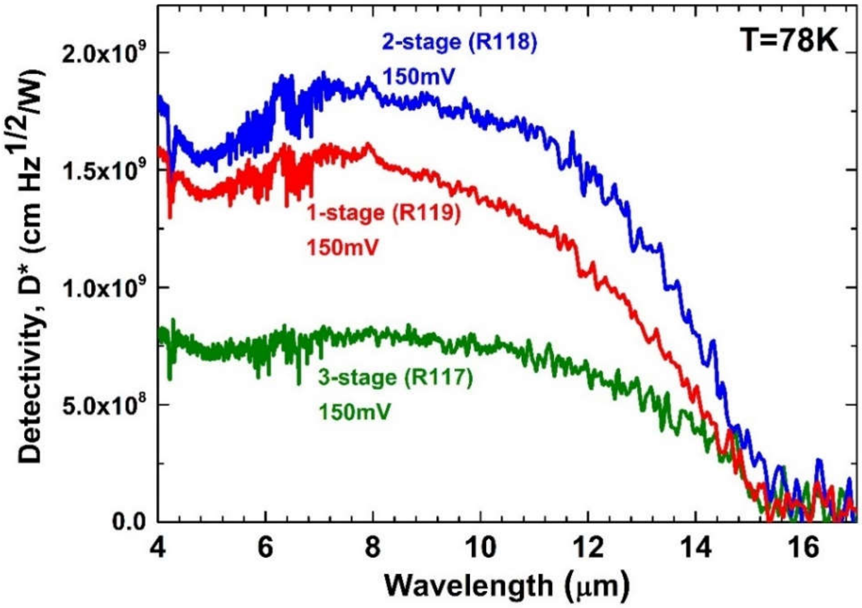

Figure 3-18: Detectivity D^* for representative one-, two- and three-stage VLWIR ICIPs at 78 K. Since the device response was obtained under reverse bias, both Johnson and shot noise terms were included in D^* determination.

in [12]. This implies that the lower D^* in our detectors was related to both the lower signal (R_λ) and higher levels of noise (*i.e.*, dark current shot noise). If the maximum photo-response was obtained under zero-bias condition, the corresponding Johnson-noise-limited D^* would be 9.5×10^9 cm.Hz$^{1/2}$/W, 8.3×10^9 cm.Hz$^{1/2}$/W, and 4.1×10^9 cm.Hz$^{1/2}$/W for the one-stage, two-stage, and three-stage detectors, which is more than ~5-7 times higher than the corresponding maximum values of D^* obtained for these detectors. Thus, much higher D^* can be achieved by merely optimizing the device structure for zero-bias operation.

As a final note, it should be mentioned that in an ideal case where the absorber thicknesses are shorter than the carriers diffusion length, the particle conversion efficiency (PCE) (PCE=N_s.EQE), is proportional to the total absorber thicknesses. Hence, the PCE is equal for both one- and three-stage detectors due to their similar total absorber thicknesses. However, the measured values for PCE (in three-stage ICIP) was significantly lower (about 70% at 10 μm) than PCE in the one-stage device. It is speculated that some levels of current mismatch exist in two- and three-stage ICIPs. Furthermore, we were unable to apply sufficient bias to reach the full response (where the device photoresponse does not further increase by increasing bias) in these detectors. Because the photoresponse exhibited a very strong bias dependency, higher levels of reverse bias might be required for a detector with more number of stages to reach maximum photoresponse. The high levels of dark current and instrument limitations precluded measurements outside a small range of applied voltages. Therefore, the reported D^* values may not be the maximum possible D^* that can be achieved with these detectors. At all the measurement temperatures (78-143 K), the highest D^* was obtained for the two-stage ICIP, however, this result may have been constrained by the limited bias voltage applied to these detectors.

3.5 Summary and concluding remarks

In summary, three sets of LWIR and VLWIR ICIPs were designed and grown to investigate the influence of number of stages and configuration on the device low and high temperature performance.

Devices from the first set were able to operate at room temperature and above (up to 340 K) with a cutoff wavelength beyond 8 μm. At temperatures above 125 K, better device performance was achieved for the three-stage ICIPs compared to the two-stage ICIPs, demonstrating the benefits of utilizing more stages. In the middle temperature range (125-200 K), the experimentally extracted R_0A ratios between the three- and two-stage ICIPs (regular illumination configuration) were in excellent agreement with the theoretical predictions for diffusion limited ICIPs. This suggests that the device performance could be mainly determined by intrinsic processes at such medium temperatures, and high temperatures with improved design. It is expected that with improvements in the growth and fabrication, enhanced performance for ICIPs with more stages will be observed at lower temperatures.

While detectors from the two LWIR (λ_c≈9 μm at 78 K) wafers had excellent carrier transport and response at low temperatures, both wafers exhibited bias dependent response at high temperatures (167 K and above), providing additional evidence on inefficient carrier transport at high temperatures in T2SL detectors. The activation energies obtained from the temperature dependence of the dark current imply that the device was limited neither by diffusion nor *g*-*r* processes.

Measurements for the VLWIR ICIPs show some non-idealities in the carrier transport that may arise from the presence of an unintentional electrostatic barrier and the *n*-type background doping of the SL absorber. The latter effect leads to lower collection efficiencies due to the inefficiency of hole transport in SL absorbers. We speculate that absorbers in these VLWIR and LWIR ICIPs are *n*-type, especially at high temperatures. In this case, holes would become the minority carriers with less efficient transport compared to the electrons. This is consistent with the observation that external bias was required to aid the collection of photocarriers. We have also observed high levels of dark current, which arise from a very narrow bandgap, high defect densities, and possible fabrication process issues. The finding that hole transport influences the VLWIR detector performance indicates that modifications in the ICIP structures are needed. Such modifications may include: shorter absorbers and better band-edge alignments between the absorbers and the unipolar barriers, as well as *p*-type doping in each layer of the SL absorber to make electrons as the minority carriers. These modifications should be investigated in the future works.

3.6 Bibliography

[1] M. Razeghi, A. Haddadi, A. Hoang, E. Huang, G. Chen, S. Bogdanov*, et al.*, "Advances in antimonide-based Type-II superlattices for infrared detection and imaging at center for quantum devices," *Infrared Physics & Technology,* vol. 59, pp. 41-52, 2013.

[2] Y. Wei, A. Hood, H. Yau, A. Gin, M. Razeghi, M. Z. Tidrow*, et al.*, "Uncooled operation of type-II InAs⁄GaSb superlattice photodiodes in the midwavelength infrared range," *Applied Physics Letters,* vol. 86, p. 233106, 2005.

[3] N. Gautam, S. Myers, A. Barve, B. Klein, E. Smith, D. Rhiger*, et al.*, "High operating temperature interband cascade midwave infrared detector based on type-II InAs/GaSb strained layer superlattice," *Applied Physics Letters,* vol. 101, p. 021106, 2012.

[4] R. Q. Yang, H. Lotfi, L. Li, R. T. Hinkey, H. Ye, J. F. Klem*, et al.*, "Quantum-engineered interband cascade photovoltaic devices," *in Proceedings of SPIE, Quantum Sensing and Nanophotonic Devices XI*, vol. 8893, p. 899310, 2013.

[5] Z. Tian, R. T. Hinkey, R. Q. Yang, D. Lubyshev, Y. Qiu, J. M. Fastenau*, et al.*, "Interband cascade infrared photodetectors with enhanced electron barriers and p-type superlattice absorbers," *Journal of Applied Physics,* vol. 111, p. 024510, 2012.

[6] R. T. Hinkey and R. Q. Yang, "Theory of multiple-stage interband photovoltaic devices and ultimate performance limit comparison of multiple-stage and single-stage interband infrared detectors," *Journal of Applied Physics,* vol. 114, p. 104506, 2013.

[7] R. Q. Yang, Z. Tian, Z. Cai, J. F. Klem, M. B. Johnson, and H. C. Liu, "Interband-cascade infrared photodetectors with superlattice absorbers," *Journal of Applied Physics,* vol. 107, p. 054514, 2010.

[8] H. Ye, L. Li, H. Lotfi, L. Lei, R. Q. Yang, J. C. Keay*, et al.*, "Molecular beam epitaxy of interband cascade structures with InAs/GaSb superlattice absorbers for long-wavelength infrared detection," *Semiconductor Science and Technology,* vol. 30, p. 105029, 2015.

[9] A. Khoshakhlagh, F. Jaeckel, C. Hains, J.-B. Rodriguez, L. Dawson, K. Malloy*, et al.*, "Background carrier concentration in midwave and longwave InAs/GaSb type II superlattices on GaAs substrate," *Applied Physics Letters,* vol. 97, p. 051109, 2010.

[10] L. Bürkle, F. Fuchs, J. Schmitz, and W. Pletschen, "Control of the residual doping of InAs/(GaIn) Sb infrared superlattices," *Applied Physics Letters,* vol. 77, pp. 1659-1661, 2000.

[11] C. Cervera, J. Rodriguez, J. Perez, H. Ait-Kaci, R. Chaghi, L. Konczewicz*, et al.*, "Unambiguous determination of carrier concentration and mobility for InAs/GaSb superlattice photodiode optimization," *Journal of Applied Physics,* vol. 106, p. 033709, 2009.

[12] B.-M. Nguyen, S. Bogdanov, S. A. Pour, and M. Razeghi, "Minority electron unipolar photodetectors based on type II InAs/GaSb/AlSb superlattices for very

long wavelength infrared detection," *Applied Physics Letters,* vol. 95, p. 183502, 2009.

Chapter 4: Short-wavelength interband cascade infrared photodetectors

4.1 Motivation and background

Short-wavelength infrared (SWIR) detectors have numerous military and civilian applications including low photon flux detection, medical diagnostics, optical communications, low-light night vision, security, produce inspection, and remote sensing. These detectors are also widely used in multicolor detectors as one of the colors [1]. Detecting multiple bands (colors) has advantages for more versatile detection and integrating detectors of different bands reduces the overall system size, cost, and complexity and enhances the accuracy of object temperature mapping. As discussed in Chapter 1 (see Table 1-2), for SWIR technologies, $In_xGa_{1-x}As$ is very mature, but cannot be extended to other IR colors. $Hg_{1-x}Cd_xTe$ (MCT) is mature and works over all IR colors, however, MCT has limitations associated with irregular substrates and their availability, the complexity of materials growth and fabrication. Similar to MCT alloy, type-II InAs/GaSb SL detectors can cover the SWIR to VLWIR wavelength range. While extensive research on the mid- to very-long-wave type-II SL IR detectors have shown some promising results, there has been limited research on the SWIR band operating at high temperatures [2-4]. A SWIR ICIP benefits from many of the aforementioned properties of ICIPs, such as high device resistance, reduced shot noise, feasibility to perform well at high temperatures, and high-speed operation without compromising sensitivity. A SWIR ICIP can be a stand-alone detector or can be integrated with MWIR, LWIR, and/or VLWIR detectors to realize multi-color ICIPs.

Thus ICIPs are viable for a multi-color detector implementation in a wide range of the IR spectrum. For example, ICIPs with regular and reverse configurations (photogenerated carriers travel in opposite directions) that have been discussed in Chapter 2 (see section 2.4.2.2) can be integrated to realize a bias selectable two-color ICIP. ICIPs for the MWIR to VLWIR ranges have been demonstrated in our previous works [5-7], but there has been no work on SWIR ICIPs. In this chapter, the first demonstration of SWIR ICIPs working in 250-340 K temperature range along with the future research for ICIPs in this band is discussed in details.

4.2 Device design, growth, and fabrication

4.2.1 Design of short-wavelength type-II superlattice absorber

Short cutoff wavelengths (<3 μm) can be directly achieved using thin InAs layers in a two-constituent InAs/GaSb SL. However, thin InAs layers add some complexity to the growth process in terms of interface mixing/roughness and make the device bandgap very sensitive to the thickness variations in time and space (uniformity) during growth. Difficulties such as lower material and interface quality have been reported in the literature[2, 3]. Furthermore, although thinning each InAs layer in the SL moves the electron-energy state up, at the same time the electron miniband widens due to the increased extension of electron wave function into barrier layers. Thus, trying to increase the SL bandgap by only thinning the InAs layers can be problematic. To address these problems a four-layer *M*-shape SL can be used [8], where each SL period is composed of InAs/GaSb/AlSb/GaSb constituent layers. Cutoff wavelengths of ~2.2 μm at 300 K have been reported in InAs/GaSb/AlSb/GaSb *M*-shape SL detectors [3]. In this work, each period of the SL absorber is composed of InAs/GaSb/$Al_{0.8}In_{0.2}Sb$/GaSb layers, where compressive strained $Al_{0.8}In_{0.2}Sb$ layers can provide flexibility to balance tensile strain of the InAs layers and to adjust the miniband width for carrier transport. Figure 4-1 contrasts the band structures for the simple two-layer and the four-layer *M*-shape SLs, in which the minibands and electron and hole wave functions for the ground states in the conduction and valence bands were calculated based on the two-band ***k·p*** [9, 10] for the two SLs. In this work, the ***k·p*** model was used mainly for illustrating the difference between the simple two-layer and the four-layer *M*-shape SLs. Because of the absence of common atoms in the interfaces of InAs/GaSb SLs, there could be some uncertainties between experimentally determined bandgaps and the calculated values regardless of using the ***k·p*** model or any other theoretical model. For this reason, one needs to work closely with experiments to track possible variations every time. Moreover, the uncertainty and variations are more of a concern for laser devices with a narrow emission spectral linewidth compared to photodetectors with broad response spectrum. To achieve a cutoff wavelength of ~2.8 μm in a two-component InAs/GaSb SL, the InAs thicknesses need to be 14 Å when the GaSb layer is chosen to be 30 Å thick (example is shown Figure 4-1(b)). A similar cutoff wavelength can be obtained by adding a thin $Al_{0.8}In_{0.2}Sb$ layer to the SL structure in which the InAs layer can be as thick as 20 Å, while the GaSb layer thickness is kept at 30 Å. As shown in Figure 4-1(a), the penetration of the wave functions into barrier layers decreases by inserting the $Al_{0.8}In_{0.2}Sb$ layer in each SL period, resulting in narrower minibands in both conduction and valence band.

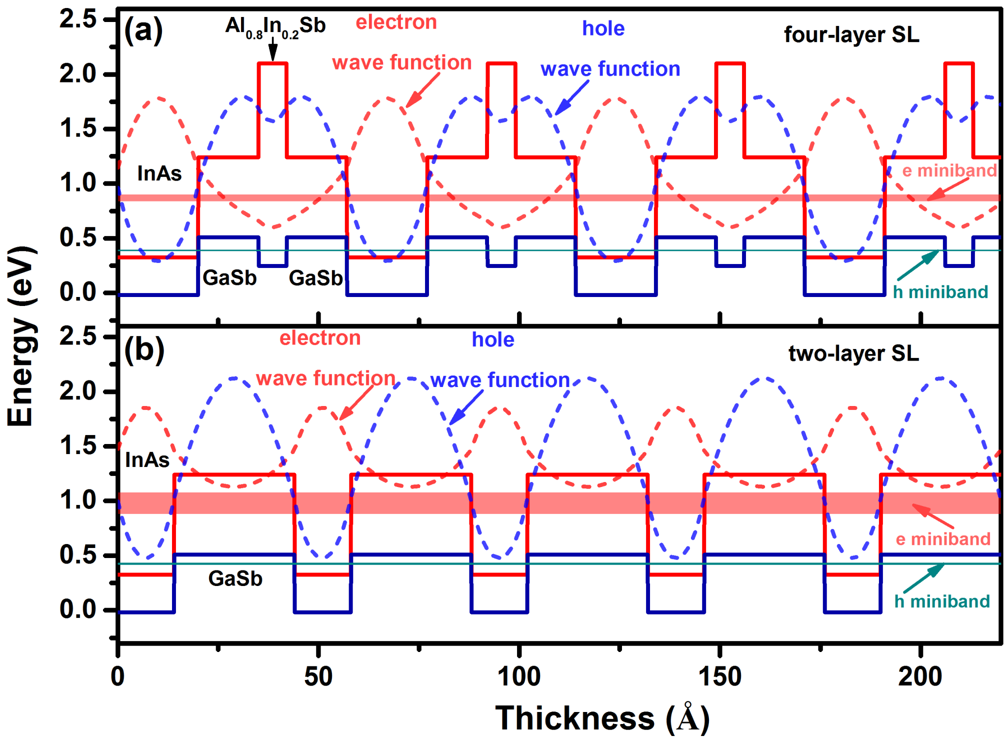

Figure 4-1: Electron and hole wave functions and the related minibands for (a) four-layer *M*-shape SL and (b) two-layer SL. In both designs, the thicknesses of the layers were tailored to achieve similar cutoff wavelengths (~2.8 µm) at 300 K.

4.2.2 Device design and band structure

The two- and three-stage ICIPs presented in this chapter were designed to target the SWIR band at room temperature. All the design parameters (electron and hole barriers, *etc*.) were the same for both ICIPs, only the number of stages were changed. To achieve a short cutoff wavelength (<3 µm) at room temperature, we used a SL period composed of InAs/GaSb/Al$_{0.8}$In$_{0.2}$Sb/GaSb with thicknesses of 20, 15, 7 and 15 Å, respectively.

The thin Al$_{0.8}$In$_{0.2}$Sb layer inserted in the middle of GaSb layers serves two main purposes. The larger lattice constant for Al$_{0.8}$In$_{0.2}$Sb layer (*cf.* the GaSb substrate) provides an extra degree of freedom to compensate the tensile strain induced by InAs layers. Also, the insertion of this layer reduces the wave function penetration into

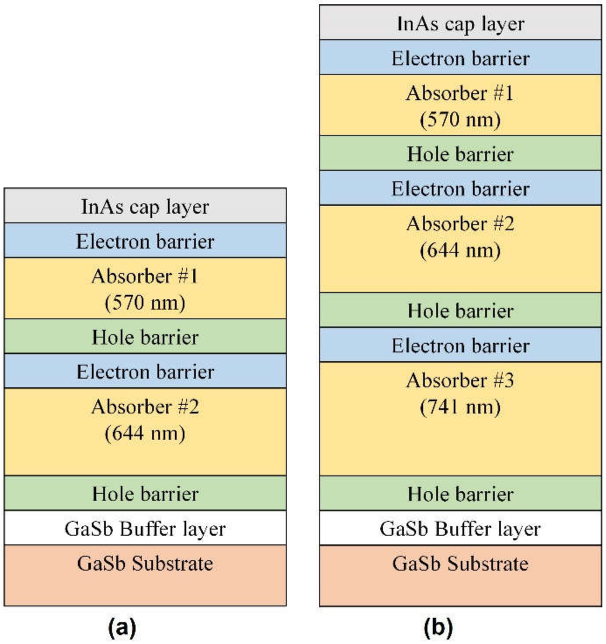

Figure 4-2: Schematic structure for (a) two- and (b) three-stage ICIPs.

barrier layers, resulting in narrower minibands than for a simple two-component InAs/GaSb SL. This makes the density of states (DOS) of the InAs/GaSb/AlSb/GaSb *M*-shape SL have more characteristics of two-dimensional (2D) DOS, which allows a sharper increase of the device absorption coefficient near its bandgap as compared to a 3D DOS.

Based on the reduction of quantum efficiency observed at high temperatures in T2SL detectors with absorber thicknesses in the range of 0.8-2 μm [11, 12], the high temperature diffusion length in superlattice structures is estimated to be on the order of 1 μm, which could vary with the material quality. Hence, we designed the thickness of individual absorbers in the ICIPs to be shorter than 1 μm. In the two-stage ICIP, the SL first (upper) and second absorbers were 570 and 644 nm thick, respectively, and in the three-stage ICIP, the additional third absorber was 741 nm thick, as indicated in Figure 4-2(a & b). The absorbers in the optically deeper stages were made thicker to achieve photocurrent matching across the stages. Electron barriers were made of three GaSb/AlSb quantum wells with 39, 53, 75 Å thick GaSb wells. Hole barriers were composed of seven InAs/Al(In)Sb quantum wells with 25, 31.5, 35, 39.5,46, 55, 69 Å thick InAs wells. Figure 4-3 shows the calculated band structure using the two-band ***k·p*** model. The ground states and their corresponding wave functions were calculated and plotted using a 2-band Kronig-Penny model. For clarity, only 10 SL periods of the absorber are shown; whereas the actual SL absorber consists of hundreds of periods.

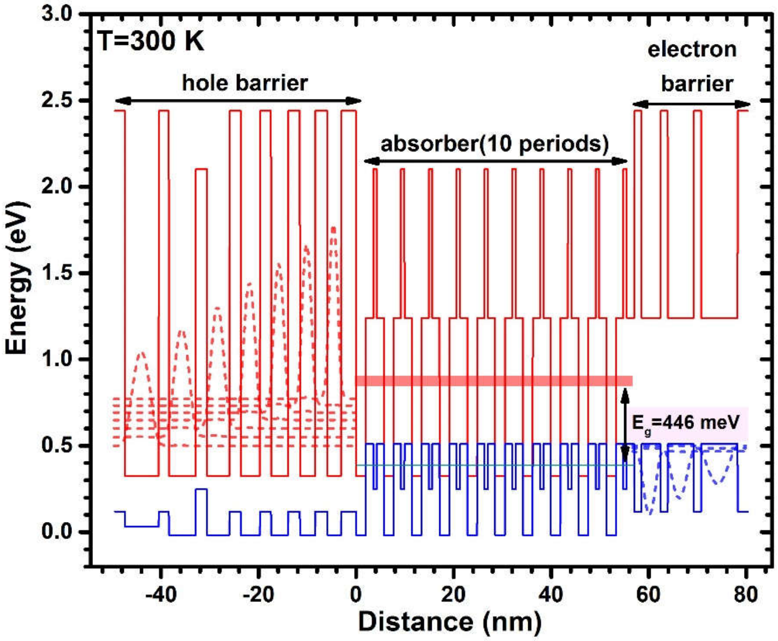

Figure 4-3: Band structure in one stage of the designed ICIPs: the ground states and their corresponding wave functions as calculated using a two-band *k·p* model.

4.2.3 Device growth and fabrication

The ICIP structures were grown by MBE on GaSb substrates at Sandia National Laboratories. Figure 4-4 shows the high-resolution X-ray diffraction (HRXRD) scans for the two detector structures. Both structures have compressive strain relative to the GaSb substrate. The lattice mismatch is 0.089% and 0.108% in the two- and three-stage

ICIPs, respectively. The FWHM for the 0th order peaks are 20 and 28 arc sec in the two- and three-stage ICIPs, respectively (see inset, Figure 4-4). These scans indicate that the two- and three-stage ICIP structures are comparable in terms of material quality.

The device fabrication followed the process that is described in Chapter 2 (see section 2.7). The grown wafers were processed into a series of square mesa detectors with edge lengths varying from 50 to 1000 µm. The two-layer passivation used for these detectors was consisted of 190 nm of SiN_x followed by 160 nm of SiO_2 deposited by RF-sputtering.

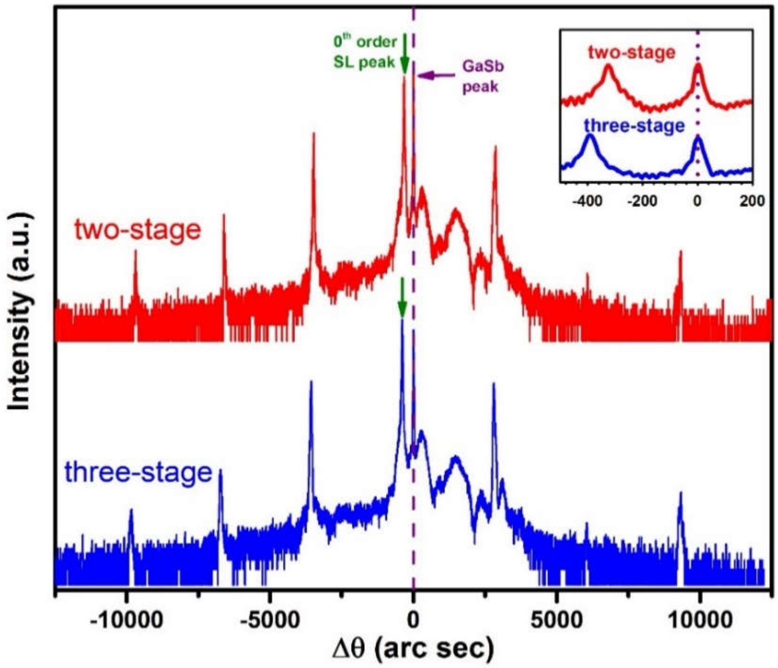

Figure 4-4: HRXRD scans for two- and three-stage ICIPs. Both ICIPs had compressive strain relative to the GaSb substrate.

4.3 Device performance and discussion

4.3.1 Electrical characteristics

4.3.1.1 Dark current

The dark current density (J_d)-voltage (V) characteristics of ICIPs were measured at 250 to 340 K (250 K can be achieved using one-stage thermoelectric coolers). For a representative 500×500 μm^2 detector from the two-stage (three-stage) wafer, dark current density at -50 mV was 4.7×10^{-4} A/cm^2 (2.7×10^{-4} A/cm^2) at 250 K. The dark current density increased to 1.0×10^{-2} A/cm^2 (0.68×10^{-2} A/cm^2) at 300 K, for the same bias. Figure 4-5 shows the dark current densities for three different size ICIPs made from both two- and three-stage wafers. As can be seen in this figure, dark current densities were larger in smaller size detectors for both two- and three-stage ICIPs throughout the temperature range. The size-dependent dark current densities were attributed to the imperfect passivation and related surface states. Another factor is the rough side walls associated with the wet etching process, caused by the different etch rates in different layers of the structure. Rough side wall surfaces make reliable and consistent passivation difficult. Such mesa-size dependence has also been reported for the mature $In_xGa_{1-x}As$ SWIR detectors and other III-V based SWIR photodetectors at room temperature [13, 14]. While there has been some progress in this area, the surface leakage issue has not been fully resolved in these materials and has remained as one of the major technological issues for III-V based, specifically type-II SL, IR detectors [15].

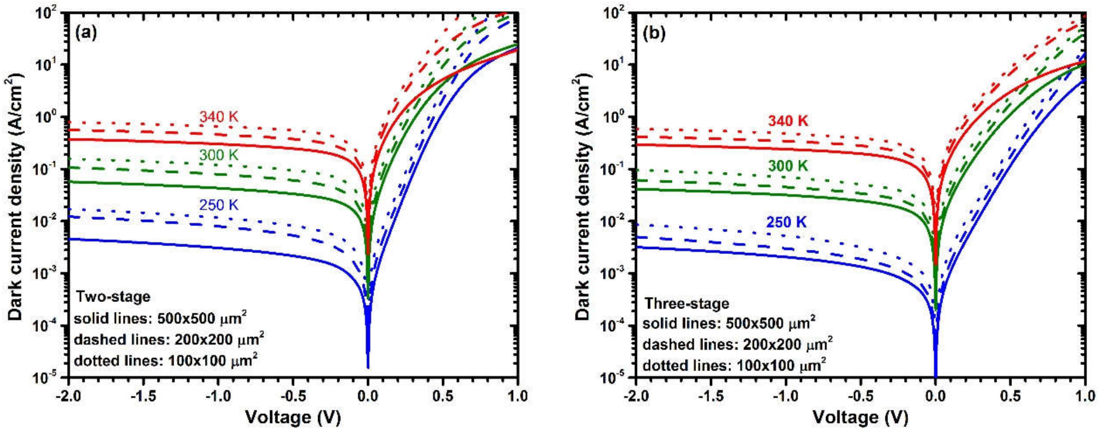

Figure 4-5: Dark current densities for 250-340 K for (a) two- and (b) three-stage SWIR ICIPs. The densities were larger for smaller size detectors indicating the side walls and the device passivation need to be improved.

4.3.1.2 Size dependency of device dark current and activation energy

To investigate the size-dependent behavior of the dark current density, the product of zero-bias resistance and device area (R_0A) for the different sized ICIPs are plotted as a function of the perimeter (P) to area (A) ratio. The contribution of bulk and surface currents on the device R_0A can be separated by fitting the device R_0A to the equation [16]:

$$\frac{1}{R_0A} = \left(\frac{1}{R_0A}\right)_{Bulk} + \frac{1}{\rho_{sw}}\left(\frac{P}{A}\right) \tag{4-1}$$

where ρ_{sw} is the device sidewall resistivity. Figure 4-6 (a) shows the size dependent R_0A for two- and three-stage ICIPs at 300 K. The extracted $(R_0A)_{\text{Bulk}}$ and sidewall resistivities (ρ_{sw}) were larger in three-stage ICIPs compared to the two-stage ICIPs in this temperature range. Table 4-1 summarizes these fitting parameters for the different operating temperatures.

An Arrhenius plot of device R_0A over the temperature range for the different size ICIPs allows us to determine the activation energy of the dominant dark current mechanism that give rise to the observed temperature variation. This amounts to fitting the device R_0A to:

$$\frac{1}{(R_0A)} = Ce^{-\frac{E_a}{k_BT}} \tag{4-2}$$

where E_a, T, k_B and C are the activation energy, temperature (K), Boltzmann constant, and fitting prefactor, respectively. Figure 4-6(b) shows the Arrhenius plots of the different detector sizes. These Arrhenius plots show the expected linear behavior. Table 4-2 summarizes these activation energies. The activation energies are slightly larger for the three-stage in comparison with those for the two-stage ICIPs, for all different sizes. Also, activation energies were lower in ICIPs with smaller sizes for the two- and three-stage devices. In order to specifically investigate the effect of surface leakage on the device activation energy, $(R_0A)_{\text{Bulk}}$ and sidewall resistivities (ρ_{sw}) obtained from size dependent analysis of R_0A were fitted to Equation 4-2. Bulk activation energies were

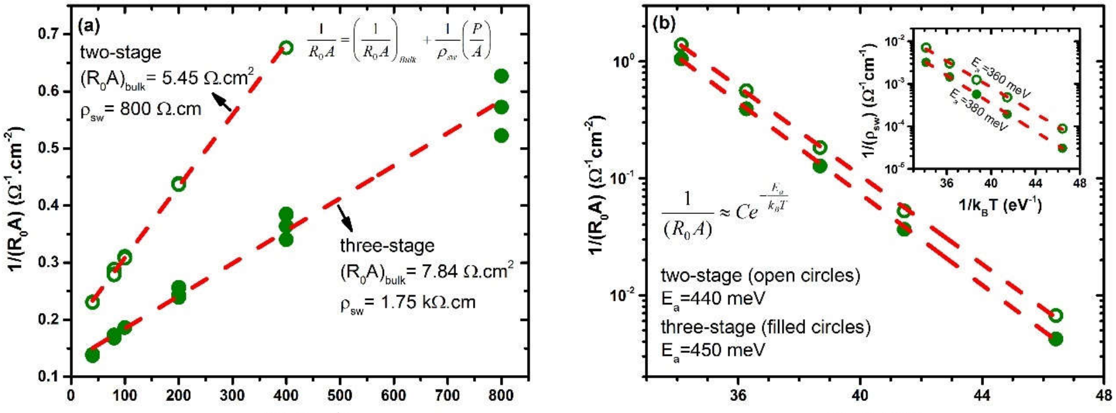

Figure 4-6: Size-dependent R_0A for two- and three-stage SWIR ICIPs at 300 K. Sidewall resistivity and bulk R_0A were larger in three-stage detectors compared to the two-stage detectors. (b) Arrhenius plot of bulk and surface (inset) activation energies for two- and three-stage ICIPs.

Table 4-1: Summary of the bulk and surface contributions to the device R_0A for 250-340 K in two- and three-stage ICIPs.

Temperature (K)	Two-stage		Three-stage		$\frac{R_0A_{3-stage}}{R_0A_{2-stage}}$
	$(R_0A)_{bulk}$ (Ω.cm^2)	ρ_{sw} (kΩ.cm)	$(R_0A)_{bulk}$ (Ω.cm^2)	ρ_{sw} (kΩ.cm)	
250	150	11.3	237	32.6	1.59
280	19.1	2.07	27.3	5.19	1.43
300	5.45	0.80	7.84	1.75	1.44
320	1.78	0.33	2.54	0.69	1.43
340	0.72	0.14	0.95	0.31	1.32

close to the device bandgap.

The extracted activation energies for the side wall resistivity was 360 meV (380 meV) in two-stage (three-stage) ICIPs. These numbers were larger than the half of the bandgap (~240 meV) and were about 75% and 80% of the bandgap energy in two- and three-stage ICIPs, respectively. Because surface states were more influential on small size ICIPs, the device activation energy had a larger reduction from the bulk activation energy and approached the side wall activation energy for small size ICIPs. This observed reduction in activation energy for smaller size ICIPs suggests a degree of sidewall leakage current through surface states. Activation energies close to the bulk limit can be achieved with improved sidewall passivation.

Table 4-2: Activation energies for different detector sizes of the two- and three-stage detectors for 250-340 K. Bulk and sidewall activation energies refer to the Arrhenius fit for $(R_0A)_{Bulk}$ and ρ_{sw} extracted from Equation 4-2.

Detector	E_g(0 K) (meV)	Activation energy (meV)					
		200×200 μm^2	400×400 μm^2	500×500 μm^2	1000×1000 μm^2	Bulk	Sidewall
Two-stage	480	390	410	410	420	440	360
Three-stage	480	430	420	430	450	450	380

4.3.2 Diffusion length in SWIR ICIPs

At high temperatures, most of the material parameters (*e.g.*, diffusion length and carrier lifetime) are unknown for the type-II SL material system. Often, diffusion length is inferred from the measurements of other parameters such as carrier mobility and lifetime. These techniques require precise setups and complicated optics [17-19]. An easier approach to extract the material parameters is to fit the dark current *I*-*V* curves to the detailed mathematical equations used for carrier transport in photodetectors [20]. In these models, a large number of fitting parameters could result in some uncertainties in the extracted parameters.

In this section a simple, yet effective, technique to extract the diffusion length and its temperature dependency in ICIPs are discussed. Although this technique was applied to ICIPs at high temperatures, it can be used with any type of semiconductor devices and at any temperature, provided that the device dark current is dominated by diffusion. This technique requires, at least, two photodetectors with similar designs but different absorber thicknesses and/or number of stages. Having a larger set of similar detectors results in a more accurate determination of diffusion length.

As described in Chapter 2, the device zero-bias resistance and area product (R_0A) in a diffusion-limited ICIP, with electrons as the minority carriers follows the below equation [21]:

$$R_0A = \frac{k_B T}{q^2 g_{th} L_e} \sum_m \frac{1}{\tanh\left(\frac{t_m}{L_e}\right)} \tag{4-3}$$

where k_B, T, t_m, L_e, g_{th} and q are Boltzmann constant, absolute temperature, absorber thickness in the m^{th} stage, electron diffusion length, thermal generation rate and electronic charge, respectively. Note that this equation is also applicable to single-stage photodetectors. Once the diffusion-limited behavior of the device dark current is assured (this can be examined by the device activation energy or observance of a flat region in the device dark *I-V*), the above equation can be used to extract the device diffusion length. There are two unknowns, namely diffusion length and thermal generation rate in Equation 4-3. By using the R_0A ratio between two photodetectors with different absorber thicknesses or number of stages, we can eliminate the thermal generation rate (g_{th}) and only one unknown will remain. For example, the R_0A ratio for the two SWIR ICIPs reported in this chapter is:

$$\frac{(R_0A)_{three-stage}}{(R_0A)_{two-stage}} = \frac{\frac{1}{\tanh\left({t_1}/{L_e}\right)}+\frac{1}{\tanh\left({t_2}/{L_e}\right)}+\frac{1}{\tanh\left({t_3}/{L_e}\right)}}{\frac{1}{\tanh\left({t_1}/{L_e}\right)}+\frac{1}{\tanh\left({t_2}/{L_e}\right)}} \tag{4-4}$$

where, t_1 and t_2 are the absorber thickness in the first and second stage of the two ICIPs and t_3 denotes the absorber thickness in the third stage of the three-stage ICIP. Because the R_0A ratio in Equation 4-4 is known from the measurements, the minority carriers diffusion length (L_e), as the only unknown, can be readily found at each temperature.

Note that care must be taken to use this approach as there are four requirements related to this approach:

(1) Surface leakage currents are neglected in Equations 4-3 & 4-4. These currents are often present in type-II SL detectors, thus, $(R_0A)_{bulk}$, which can be extracted from the plots of different sized detectors R_0A, should be used for more accurate determination of the diffusion length.

(2) The device series resistance and the parasitic resistances from the measurement setup should be excluded from the device measured resistance. In narrow bandgap photodetectors, these parasitic resistances are in the same order of the device resistance for certain device sizes at high temperatures and may result in uncertainties in the diffusion length estimation.

(3) Equation 4-4 is only valid for detectors with similar material and processing quality.

(4) The carriers transport should be controlled by minority carriers. Depending on the device bandgap, temperature, and the absorber doping level, ambipolar effects *(i.e.*, both electrons and holes) could start to control the transport dynamics.

To ensure these assumptions, these two SWIR ICIPs were grown by the same MBE system and in two consecutive growth runs with similar growth conditions. Also, because the surface leakage currents were present in these SWIR ICIPs, the $(R_0A)_{\text{bulk}}$ extracted from the size-dependent plot of different-sized ICIPs was used for the R_0A ratios. However, some levels of uncertainty may exist in the extracted values for diffusion length. Figure 4-7 shows the theoretical R_0A ratio for the two- and three-stage ICIPs versus diffusion length. The single points on this curve represent the calculated

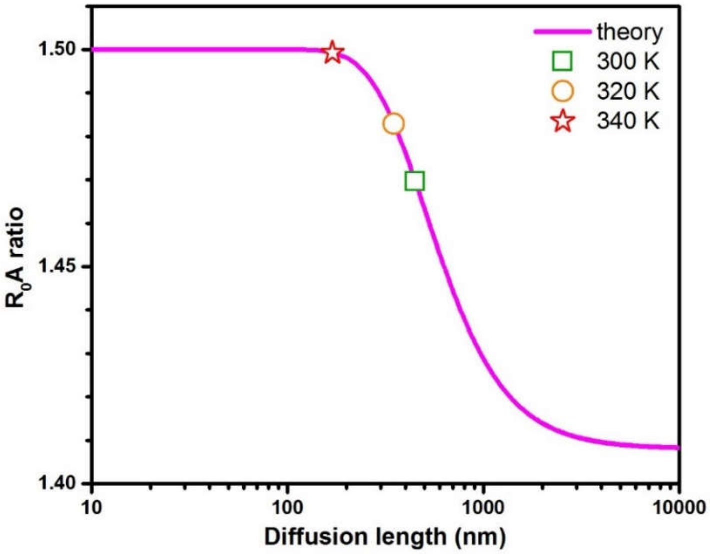

Figure 4-7: The theoretical curve and the measured R_0A ratios (single points on the curve) for T=300-340 K. The device dark current was dominated by the diffusion process in this temperature range.

ratios of the measured R_0A values for T=300-340 K. The minority carrier diffusion length was estimated to be 450 nm at 300 K. The extracted diffusion lengths at different temperatures along with the R_0A ratios are summarized in Table 4-3. Diffusion lengths were well below 1 µm at high temperatures. Typically, type-II SL detectors have absorber thickness of 1 to 3 µm. While thick absorbers are required for sufficient photon absorption, short diffusion lengths limit the device quantum efficiency and only photogenerated carriers generated within a diffusion length of the collection point(s) will contribute to the device quantum efficiency and the rest of carries are wasted. Therefore, multiple-stage devices with each individual absorber shorter than the minority carriers diffusion length will enhance the collection efficiency and the overall device performance at high temperatures.

Table 4-3: Summary of the measured and extracted parameters for two- and three-stage SWIR ICIPs at room temperature and above.

Temperature (K)	**$(R_0A)_{bulk}$ (Ω.cm^2)**		$\frac{(R_0A)_{Three-stage}}{(R_0A)_{Two-stage}}$	**Diffusion length (nm)**
	Two-stage	**Three-stage**		
300	5.446	8.006	1.470	450
320	1.738	2.578	1.483	350
340	0.612	0.918	1.500	≤170

4.3.3 Optical characteristics

4.3.3.1 Responsivity

Following the procedure that was described in Chapter 2, the optical response spectra of these ICIPs were collected using an IR glow-bar source within an FTIR spectrometer and calibrated using an 800 K blackbody source (aperture diameter: 1.52 cm). Figure 4-8(a) shows the calibrated responsivity for the two- and three-stage ICIPs for 250-340 K. The zero-bias response did not show an appreciable decrease for an increase in the device temperature at 2.1 μm for both two- and three-stage ICIPs.

The zero-bias response at 2.1 μm and 300 K was 0.44 and 0.37 A/W for two- and three-stage ICIPs, respectively. While the two ICIPs were designed to be photo-current matched, photo-response was ~16% lower in the three-stage ICIP at this wavelength. This suggests the possible imperfect photocurrent matching between individual stages and perhaps larger photocurrent mismatch in the three-stage ICIP. The current mismatch can be minimized by adjusting thicknesses of the absorbers so that the photoresponse can be improved in both ICIPs.

The detectors photoresponse was also measured under different reverse bias (see Figure 4-8(b)). At λ=2.1 μm and 300 K, the device maximum photo-response increased by 18% and 24% under reverse bias in two- and three-stage ICIPs, respectively. This small dependence of photoresponse on bias voltage may be caused by the combination of imperfect metal contact to semiconductor surfaces (non-ideal Ohmic contacts) and some degree of misalignments of energy levels between quantum wells and absorber in adjacent stages. When the contacts and alignments of energy levels in every region are optimized, such a bias-voltage dependence of the photoresponse can be eliminated and the maximum photoresponse can be obtained under zero-bias condition.

4.3.3.2 Detectivity

The performance of the ICIPs can further be examined by comparing their specific detectivities (D^*). By considering Johnson and shot noise as the only noise sources and neglecting the surface currents, the specific detectivity for ICIPs can be calculated using Equation 2-8. Based on the theory of ideal ICIPs, larger resistance and

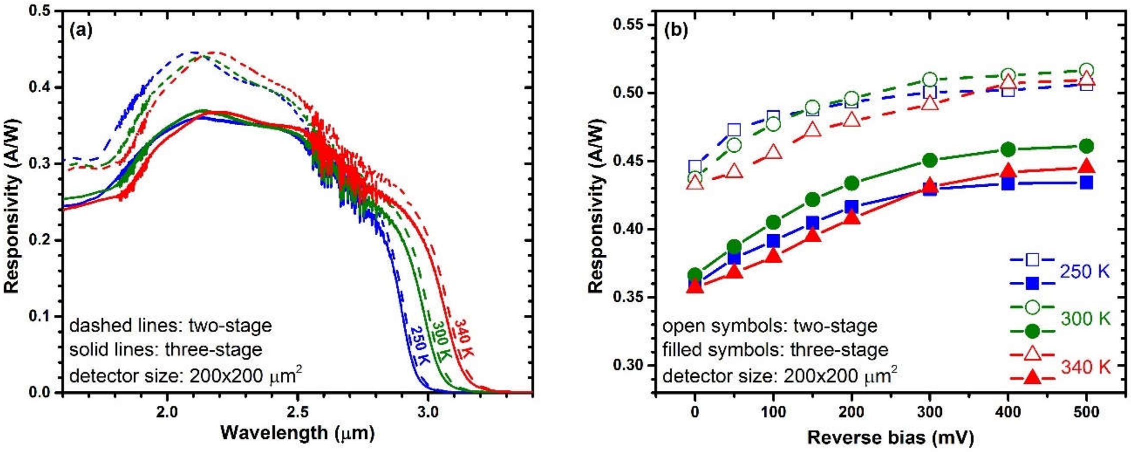

Figure 4-8: Zero- bias responsivity for representative two- and three-stage ICIPs at 250-340 K. (b) Photo-response (at 2.1 µm) *vs*. reverse bias in two- and three-stage ICIPs for 250-340 K.

area product (*RA)* and lower (dark currents (J_d) are expected in a three-stage device compared to a similar two-stage device. Also, the shot noise term ($2qJ_d/N_s$) in Equation (2-8) is inversely proportional to the number of stages.

Because of the size dependent dark current density, the device D^* was also size dependent. For instance, at 250 K D^*, was 4.1×10^{10} and 3.1×10^{10} cm.Hz$^{1/2}$/W for representative 1,000×1,000 µm^2 and 200×200 µm^2 three-stage ICIPs, respectively. Figure 4-9 compares the specific detectivity under zero-bias for two- and three-stage ICIPs (200×200 µm^2) at different temperatures. Calculated Johnson-limited D^* (for λ=2.1 µm) was 3.1×10^{10} (2.5×10^{10}) and 5.8×10^9 (5.1×10^9) cm.Hz$^{1/2}$/W for the three-stage (two-stage) ICIP at 250 and 300 K, respectively.

If diffusion current controls the device dark current, the device resistance will exponentially increase with reverse bias within a certain range. This means even if the device signal does not increase with reverse bias, D^* could increase under reverse bias condition. The maximum calculated D^* at 300 K was 7.5×10^9 (5.6×10^9) cm.Hz$^{1/2}$/W for

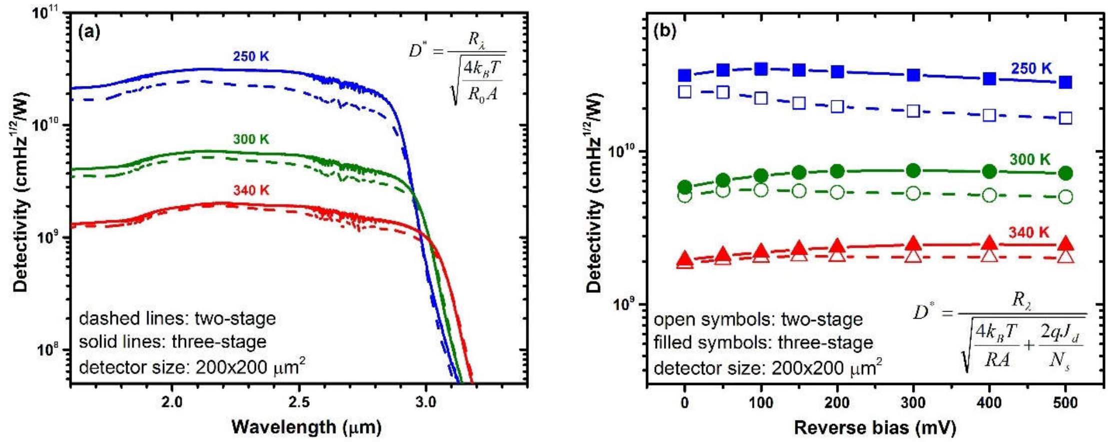

Figure 4-9: (a) Specific detectivity (FOV=2π sr) for two- and three-stage ICIPs under the zero-bias condition for 250-340 K. (b) Specific detectivity *vs.* reverse bias for the same ICIPs. Detectors were covered with a copper shield (at the device temperature) during dark current measurements.

the three-stage (two-stage) ICIP and was obtained under -300 mV (-100 mV) reverse bias. However, other sources of noise, such as 1/*f* noise, usually increase rapidly under reverse bias and often negates the benefits of the larger device resistance obtained under a reverse bias condition [23]. This D^* is close to 2.8×10^{10} cm.Hz$^{1/2}$/W, the value claimed by Judson Technologies for a commercial 2.8 μm cutoff $Hg_{1-x}Cd_xTe$ detector at 295 K [24]. The device specific detectivity was larger in the three–stage ICIP at all temperatures, demonstrating the benefits of the three-stage detector over the two-stage detector. Because D^* is directly proportional to the device responsivity, D^* in the three-stage ICIP can be increased by improving the photocurrent matching. Considering that the total thickness (1.96 μm) of absorbers in the three-stage ICIP structure is less than 2 μm, ICIPs with more stages should further increase absorption efficiency and suppress noise, resulting in improved device performance. More stages will present challenges including device design for better current matching, material quality for longer growth times, and device fabrication/passivation for more interfaces. However, such advancement is possible with improved understanding and knowledge of the material properties, MBE growth technology, as well as device fabrication techniques.

4.4 Summary and concluding remarks

The first demonstration of high-temperature two- and three-stage SWIR ICIPs was discussed in this chapter. The photo-response of these ICIPs showed no decrease at high temperatures. This implies that ICIPs can circumvent the diffusion length limitation on carrier transport at high temperatures (at least up to 340 K). Values of Johnson-noise-limited detectivity D^* exceeding 10^9 cm.Hz$^{1/2}$/W were obtained at temperatures up to 340 K. The value of D^* was larger in the three-stage ICIP for all measured temperatures compared to the two-stage ICIP, confirming the benefits of ICIPs with more stages. Size-dependent analysis of the R_0A for devices indicates that the surface current was significant in small size ICIPs, which contributed to the dependence of the activation energies for these ICIPs. Better device performance is expected by improving the device fabrication/passivation and optimizing the device structure for better photocurrent matching in ICIPs with more stages.

4.5 Bibliography

[1] A. M. Hoang, A. Dehzangi, S. Adhikary, and M. Razeghi, "High performance bias-selectable three-color short-wave/mid-wave/long-wave infrared photodetectors based on type-II InAs/GaSb/AlSb superlattices," *Scientific Reports,* vol. 6, p. 24144, 2016.

[2] T. Bao, X. Ying-Qiang, Z. Zhi-Qiang, H. Rui-Ting, W. Guo-Wei, R. Zheng-Wei*, et al.*, "GaAs based InAs/GaSb superlattice short wavelength infrared detectors grown by molecular beam epitaxy," *Chinese Physics Letters,* vol. 26, p. 028102, 2009.

[3] A. M. Hoang, G. Chen, A. Haddadi, S. Abdollahi Pour, and M. Razeghi, "Demonstration of shortwavelength infrared photodiodes based on type-II InAs/GaSb/AlSb superlattices," *Applied Physics Letters,* vol. 100, p. 211101, 2012.

[4] A. Haddadi, X. V. Suo, S. Adhikary, P. Dianat, R. Chevallier, A. M. Hoang*, et al.*, "High-performance short-wavelength infrared photodetectors based on type-II InAs/$\mathrm{InAs_{1-x}Sb_x}$/$\mathrm{AlAs_{1-x}Sb_x}$ superlattices," *Applied Physics Letters,* vol. 107, p. 141104, 2015.

[5] R. Q. Yang, Z. Tian, Z. Cai, J. F. Klem, M. B. Johnson, and H. C. Liu, "Interband-cascade infrared photodetectors with superlattice absorbers," *Journal of Applied Physics,* vol. 107, p. 054514, 2010.

[6] H. Lotfi, L. Li, H. Ye, R. T. Hinkey, L. Lei, R. Q. Yang*, et al.*, "Interband cascade infrared photodetectors with long and very-long cutoff wavelengths," *Infrared Physics & Technology,* vol. 70, pp. 162-167, 2015.

[7] R. T. Hinkey, H. Lotfi, L. Li, R. Q. Yang, J. F. Klem, J. C. Keay*, et al.*, "Interband casade thermophotovoltaic devices with type-II superlattice absorbers of ~0.4 eV bandgap," *IEEE 39th Photovoltaic Specialists Conference,* pp. 1013-1016, 2013.

[8] B.-M. Nguyen, D. Hoffman, P.-Y. Delaunay, and M. Razeghi, "Dark current suppression in type II InAs⁄GaSb superlattice long wavelength infrared photodiodes with M-structure barrier," *Applied Physics Letters,* vol. 91, p. 163511, 2007.

[9] E. O. Kane, "Zener tunneling in semiconductors," *Journal of Physics and Chemistry of Solids,* vol. 12, pp. 181-188, 1960.

[10] R. Q. Yang and J. M. Xu, "Bound and quasibound states in leaky quantum wells," *Physical Review B,* vol. 46, pp. 6969-6974, 1992.

[11] Y. Wei, A. Hood, H. Yau, A. Gin, M. Razeghi, M. Z. Tidrow*, et al.*, "Uncooled operation of type-II InAs⁄GaSb superlattice photodiodes in the midwavelength infrared range," *Applied Physics Letters,* vol. 86, p. 233106, 2005.

[12] J. V. Li, C. J. Hill, J. Mumolo, S. Gunapala, S. Mou, and S.-L. Chuang, "Midinfrared type-II InAs⁄GaSb superlattice photodiodes toward room temperature operation," *Applied Physics Letters,* vol. 93, p. 163505, 2008.

[13] J. P. Prineas, J. Yager, S. Seyedmohamadi, and J. T. Olesberg, "Leakage mechanisms and potential performance of molecular-beam epitaxially grown GaInAsSb 2.4 μm photodiode detectors," *Journal of Applied Physics,* vol. 103, p. 104511, 2008.

[14] M. Razeghi, E. Tournié, G. J. Brown, F. Rutz, P. Kleinow, M. Walther*, et al.*, "Infrared photodetector development at Fraunhofer IAF," in *Proceedings of SPIE, Quantum Sensing and Nanophotonic Devices XI*, vol. 8993, p. 89930W, 2013.

[15] M. A. Kinch, *State-of-the-Art Infrared Detector Technology*, SPIE press, Bellingham, 2014.

[16] H. K. Chung, "Origin of 1/f noise observed in $Hg_{0.7}Cd_{0.3}Te$ variable area photodiode arrays," *Journal of Vacuum Science & Technology A: Vacuum, Surfaces, and Films,* vol. 3, p. 189, 1985.

[17] B. C. Connelly, G. D. Metcalfe, H. Shen, and M. Wraback, "Direct minority carrier lifetime measurements and recombination mechanisms in long-wave infrared type II superlattices using time-resolved photoluminescence," *Applied Physics Letters,* vol. 97, p. 251117, 2010.

[18] L. Höglund, A. Soibel, D. Z. Ting, A. Khoshakhlagh, C. J. Hill, and S. D. Gunapala, "Minority carrier lifetime and photoluminescence studies of antimony-based superlattices," in *Proceedings of SPIE, Infrared Remote Sensing and Instrumentation XX*, vol. 8511, p. 851106, 2013.

[19] B. Klein, N. Gautam, E. Plis, T. Schuler-Sandy, T. J. Rotter, S. Krishna*, et al.*, "Carrier lifetime studies in midwave infrared type-II InAs/GaSb strained layer superlattice," *Journal of Vacuum Science & Technology B: Microelectronics and Nanometer Structures,* vol. 32, p. 02C101, 2014.

[20] Q. K. Yang, F. Fuchs, J. Schmitz, and W. Pletschen, "Investigation of trap-assisted tunneling current in InAs/(GaIn)Sb superlattice long-wavelength photodiodes," *Applied Physics Letters,* vol. 81, p. 4757, 2002.

[21] R. T. Hinkey and R. Q. Yang, "Theory of multiple-stage interband photovoltaic devices and ultimate performance limit comparison of multiple-stage and single-stage interband infrared detectors," *Journal of Applied Physics,* vol. 114, p. 104506, 2013.

[22] L. Lei, L. Li, H. Lotfi, Y. Jiang, R. Q. Yang, M. B. Johnson*, et al.*, "Mid-wave interband cascade infrared photodetectors based on GaInAsSb absorbers," *Semiconductor Science and Technology,* vol. 31, p. 105014, 2016.

[23] P. Capper and C. Elliott, *Infrared detectors and emitters: materials and devices*, Springer Science & Business Media, 2013.

[24] Teledyne Judson Technologies catalogue, *Photovoltaic mercury cadmium telluride detectors*.

Chapter 5: High-frequency mid-IR interband cascade lasers and photodetectors

5.1 Motivation and background

ICLs can be combined with ICIPs or ICTPVs to build a functional interband cascade system with devices either on closely packaged units or on a single chip. The system will be compact and portable because IC devices can operate efficiently with high-performance characteristics and low power consumption [1] (*e.g.*, low threshold current density for ICLs and high detectivity for ICIPs) at room temperature and above. These features are important in many applications such as chemical sensing, free space optical (FSO) communication, and power beaming. Additionally, some specific applications, such as heterodyne detection and high-bandwidth FSO communication, require devices capable of high-frequency operation.

Generally, semiconductor lasers with appropriate packaging are able to operate at high frequencies (with bandwidths in the GHz range), as was demonstrated for ICLs at low temperatures with operation up to 3.2 GHz [2, 3]. However, it is difficult for conventional photodetectors to achieve high-frequency operation without sacrificing the device sensitivity. The 3-dB bandwidth for a conventional photodetector with a single absorber, in which the diffusion process controls the carrier transport, is $f_{3-dB} = \frac{2.43D}{2\pi t^2}$ [4, 5], where D and t are the diffusion coefficient and the absorber thickness, respectively. Therefore, the device bandwidth will be increased by reducing the absorber thickness. However, this would also reduce the optical absorption and thus the device sensitivity (signal to noise ratio). For this reason, the product of the device sensitivity and bandwidth remains constant in single-stage photodetectors. The compromise between the device speed and QE can be avoided in ICIPs with a multiple-stage discrete absorber architecture. Since the photogenerated carriers recombine at the interface between the electron and hole barriers of adjacent cascade stages (See Figure 5-1), they travel only a short distance, at most one cascade stage, before being collected at the interfaces of adjacent stages or the contacts. Consequently, when individual absorbers are short, ICIPs can respond quickly to direct optical modulation at high frequencies while significant absorption of incident light is ensured by multiple absorbers in serially connected stages. As such, the total absorber thickness is sufficient to maintain a high absorption efficiency and a high sensitivity [6, 7].

While many properties of ICIPs including the high-temperature operation with large device resistance and detectivity, and short response time (on the order of ns) have been demonstrated in previous works [8-13], high-frequency operation of ICIPs has not been explored until this work. It is worth noting that intersubband based detectors have been previously studied for high-speed mid-IR detection. However, these intersubband

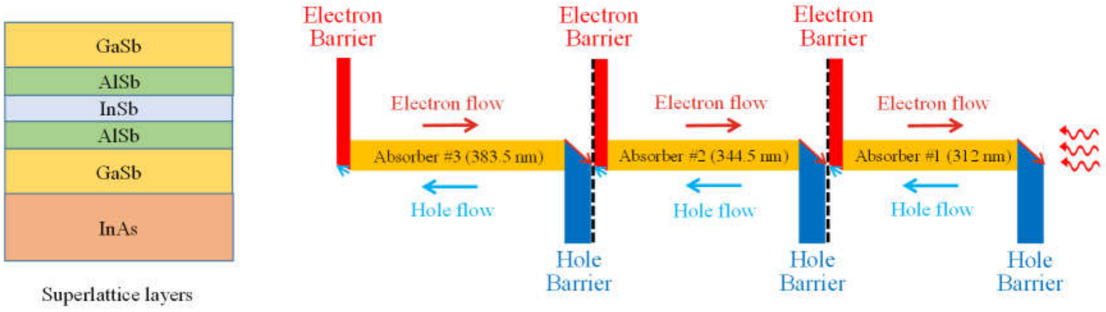

Figure 5-1: Schematic diagram of the three-stage ICIP. From right to left, the absorber thicknesses are 312.0, 344.5 and 383.5 nm. The left block is a schematic layer diagram for one period of the SL absorber.

photodetectors require gratings for normal incidence detection, usually work only at low temperatures and have a low photo-response (and a low detectivity) that decreases further at high temperatures [14-16]. These issues in intersubband photodetectors are circumvented in an appropriately designed ICIP.

5.2 Device design, growth, and fabrication

To investigate the high-speed performance of ICIPs at room temperature, mid-wavelength ICIPs (λ_c=4.3-4.6 μm) with a different number of stages and absorber thicknesses were designed and grown by MBE at OU. Table 5-1 Summarizes the performance of this set of MWIR ICIPs. At 300K, the highest D^* that was achieved under zero-bias operation was 1.7×10^9 cm.Hz$^{1/2}$/W (from wafer Y010D with three stages). Most of these wafers, except R146, R148, and R149, had a reverse configuration. Figure 5-2 shows the zero-bias responsivity and Johnson-noise-limited detectivity (D^*) spectra of a three-stage reverse-configuration ICIP (Y004D) at 300 K. The absorber thicknesses were 312.0, 344.5 and 383.5 nm in the first, second and the third stages, respectively. The device responsivity was 0.25 A/W and its D^* exceeded 10^9 cmHz$^{1/2}$/W at 3 μm. Each absorber was composed of a T2SL, in which each period consisted of InAs (27 Å)/GaSb (15 Å)/AlSb (2.7 Å)/InSb (2.6 Å)/AlSb (2.7 Å)/GaSb (15 Å) layers.

The schematic diagram of this ICIP and the device simulated band structure using a ***k.p*** model are shown in Figures 5-1 & 5-2. After MBE growth, square-mesa ICIPs with side lengths from 20 to 400 μm were defined using conventional contact UV

Table 5-1: Summary of the device structure and room temperature performance of MWIR ICIPs designed to study the high-frequency operation of ICIPs.

Wafer name	# of stages	λ_c (μm)	Zero-bias response (A/W)	Maximum response (A/W)	Zero-bias D^* (cm.Hz$^{1/2}$/W)	Maximum D^* (cm.Hz$^{1/2}$/W)
R146	8	4.3	0.127	-	9.67×10^{8}	-
R149	6	4.3	0.019	0.138 (at -1.79 V)	1.89×10^{8}	6.51×10^{8} (at -1.79 V)
R150	3	4.3	0.029	0.174 (at -1.0 V)	2.17×10^{8}	6.40×10^{8} (at -1 V)
R151	3	4.3	0.033	0.166 (at -1.5 V)	3.11×10^{8}	6.89×10^{8} (at -1 V)
Y004D	3	4.3	0.255	0.261 (at 0.05 V)	1.35×10^{9}	1.62×10^{9} (at 0.15 V)
Y005D	3	4.3	0.234	0.254 (at 0.1 V)	1.35×10^{9}	1.75×10^{9} (0.15 V)
Y008D	6	4.3	0.216	-	1.62×10^{9}	2.0×10^{9} (0.15 V)
Y009D	8	4.3	0.154	0.16 (at 0.3 V)	1.08×10^{9}	1.29×10^{9} (0.4 V)
Y010D	3	4.3	0.331	0.384 (at 0.5 V)	1.72×10^{9}	2.01×10^{9} (0.15 V)
Y007D	1	4.3	0.723	0.803 (at 0.3 V)	1.67×10^{9}	2.04×10^{9} (0.15 V)
Y011D	1	4.5	0.191	1.058 (at 1.0 V)	8.08×10^{8}	1.92×10^{9} (0.8 V)
Y011D	1	4.5	0.847	1.360 (at 0.1 V)	1.33×10^{9}	2.08×10^{9} (0.1 V)
Y012D	1	4.6	0.434	1.374 (at 0.4 V)	9.05×10^{8}	1.89×10^{9} (at 0.3 V)
Y012D	1	4.6	0.712 0.782	1.610 (at 0.1V) 1.465 (at 0.1 V)	1.02×10^{9} 9.16×10^{8}	2.01×10^{9} (at 0.1 V) 1.55×10^{9} (at 0.1 V)

photolithography and chemical wet etching. Note that the mask used for photolithography was specifically designed for high-frequency ICIPs. Smaller mesa sizes (down to 20×20 μm^2) and reduced bonding pad size (100×100 μm^2) were part of the design considerations for this mask. For passivation, 174-nm of Si_3N_4 and 224-nm of SiO_2 were deposited by RF sputtering to improve overall stress management and minimize pin holes compared to single-layer passivation. However, the significantly higher dielectric constant of Si_3N_4 (7.5) compared to SiO_2 (3.9) increases the bonding pad capacitance. Ti/Au top and bottom contacts were also sputter deposited. The top

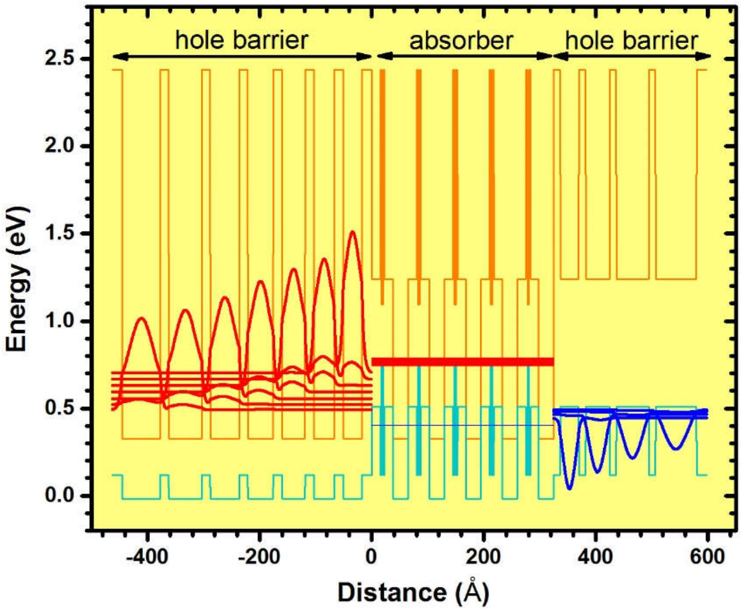

Figure 5-2: Band structure of one stage of Y004D ICIPs. For clarity, 5 periods of SL is shown in the absorber region. The simulated ICIP cutoff wavelength was ~3.7 µm at 300 K.

metallic contact of all ICIPs had finger patterns and the devices were wire bonded for characterization.

5.3 Low-frequency characterizations

5.3.1 Electrical and optical performance

The regular spectral response for a representative 200×200 µm^2 ICIP at 300 K was measured under zero bias using our optical setup and a calibrated 800 K blackbody source. As shown in Figure 5-3, the cutoff wavelength was 4.2 µm, corresponding to a bandgap of 0.295 eV and the device responsivity exceeded 0.2 A/W in a broad spectral range. The Johnson-noise-limited detectivity (D^*) reached a value higher than 1.0×10^9 cm·Hz$^{1/2}$/W soon after the photon energy exceeded the device bandgap. These values are more than an order of magnitude higher than what is reported for intersubband

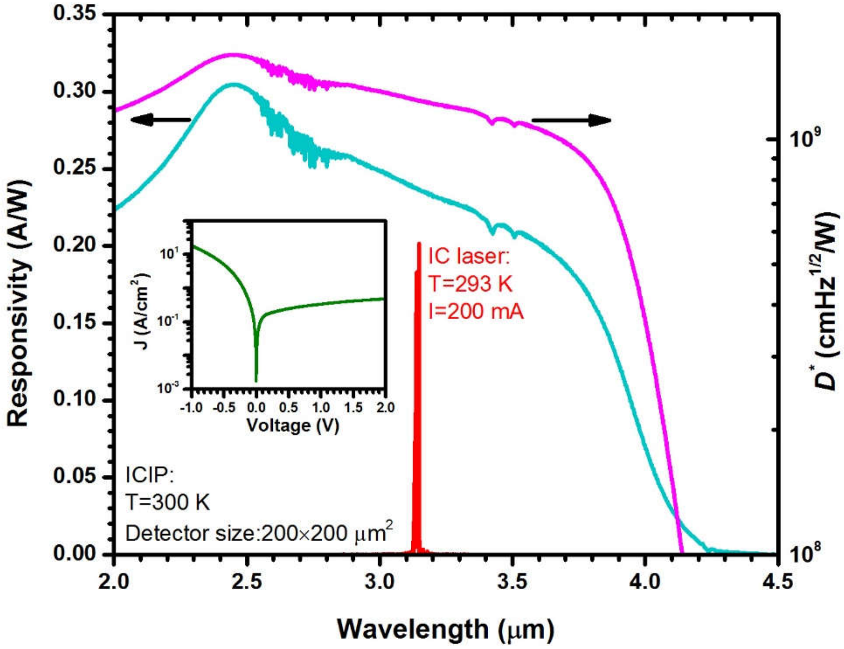

Figure 5-3: Zero-bias responsivity and Johnson-noise-limited detectivity for a 200×200 μm^2 ICIP at 300 K. The IC laser emission spectrum at *T*=293 K, under 200 mA injection, is also displayed. Inset, dark *J*-*V* curve for the same ICIP at 300 K.

photodetectors [16-18], suggesting the suitability of ICIPs for high-operating-temperature (HOT) detection. In the study of high-frequency characteristics, ICIPs with different sizes were used. Values for the zero-bias resistance and area product (R_0A) were extracted from current density (J) and voltage characteristics (*e.g.*, see inset of Figure 5-3). For ICIPs made from the same wafer, the average value of R_0A was 0.27 Ω·cm^2 and a typical 20×20 μm^2 ICIP had a resistance of ~35 kΩ at 300 K.

5.3.2 Gain in ICIPs

Since absorbers are thin in these ICIPs, we can reasonably assume that almost all of the photo-generated carriers are collected. As such, the absorption coefficient is estimated to be larger than 5,400 cm^{-1}. This number is significantly larger than the expected values for T2SL absorbers. To further investigate the large responsivities observed in these ICIPs, a one-stage ICIP with absorber thickness of 1,040 nm was grown (Y007D) to directly measure the absorption coefficient of the SL. The absorption coefficient spectrum obtained from the transmission measurement is shown in Figure 5-4. The measured absorption coefficient was ~3,300 cm^{-1} at 3 μm, which is significantly smaller than the number extracted from the response measurements. The large responsivities observed in these ICIPs are attributed to a possible gain mechanism in their structure. The short absorbers employed in these ICIPs could result in a gain mechanism similar to the gain in photoconductors. If the carriers transit time becomes shorter than their lifetime, it is possible to have gain in the device structure. Further investigations are needed to understand the source of gain in these ICIPs.

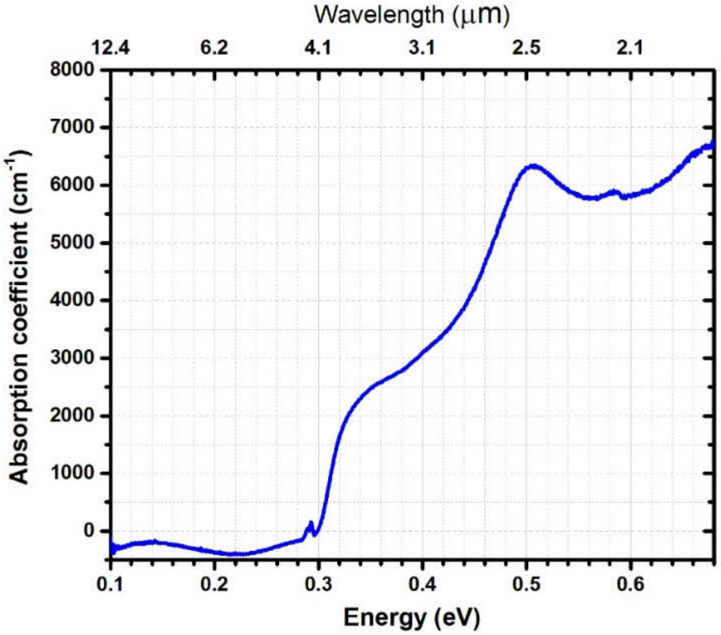

Figure 5-4: The absorption coefficient spectrum for the T2SL absorber measured at room temperature. The T2SL was made of InAs (27 Å)/GaSb (15 Å)/AlSb (2.7 Å)/InSb (2.6 Å)/AlSb (2.7 Å)/GaSb (15 Å) in each period.

5.4 High-frequency setup and measurements

The schematic diagram of the interband cascade system for high-frequency modulation is shown in Figure 5-5. A narrow ridge type-I ICL [19] (ridge width: 20 μm, cavity length: 2 mm) was used as the mid-IR light source for high-frequency modulation measurements. The laser temperature was maintained at *T*=293 K using a thermoelectric (TE) cooler. The emission wavelength was near 3.15 μm as shown in Figure 5-3, with a threshold current density of 405 A/cm^2 at *T*=293 K. At a DC current of 200 mA, the output power was 1.7 mW per facet. A constant-amplitude RF signal with frequency up to 1.2 GHz was sweep generated (with a 2 ms dwell time) by an analog signal generator and was applied to the IC laser using a bias-tee. The laser output beam was then collimated and focused on an uncooled ICIP. A second bias-tee was used to separate the DC and RF signals from the ICIP. The ICIP's RF output was then fed to a spectrum analyzer and the system frequency spectrum was collected at room temperature. At the laser's emission wavelength, the ICIP's responsivity was 0.24 A/W

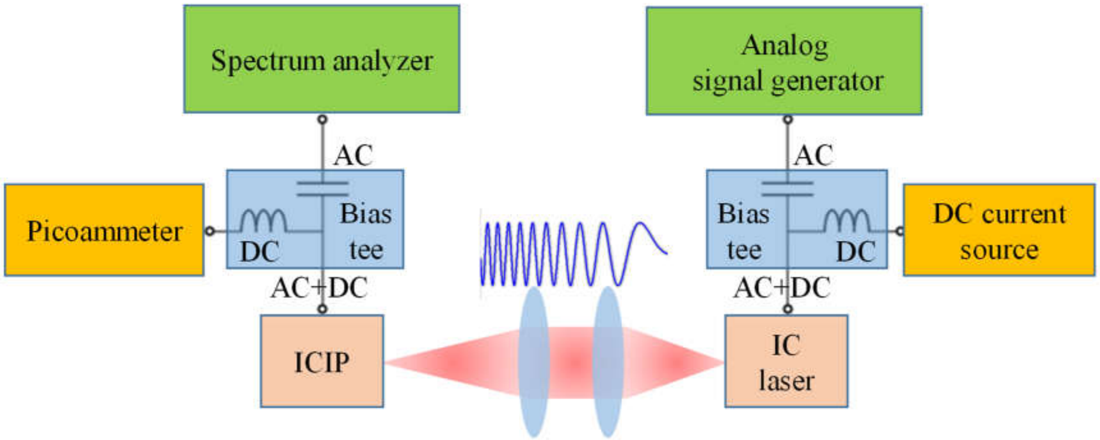

Figure 5-5: Schematic drawing of the high-frequency mid-IR interband cascade system.

with a specific detectivity of 1.2×10^{9} cm·Hz$^{1/2}$/W. Because of these large values for photo-response and D^{*}, no RF amplifier was required before the spectrum analyzer. Using the same IC laser, the RF response of the interband cascade system was investigated for ICIPs of different size.

The obtained frequency response of this system with uncooled ICIPs of different size (at zero-bias) is displayed in Figure 5-6. The frequency dependent attenuations of bias-tees and coaxial cables were excluded from the measurements. It is evident that the device frequency response was lower in larger mesa sizes at high frequencies. This means that the device frequency response was not limited by fundamental mechanisms such as carrier transport time and the device frequency response has room for improvement by refining the device packaging and fabrication. For the 20×20 μm^2 ICIP, the measured 3-dB bandwidth of the system was ~850 MHz at room temperature. Because the IC laser frequency response was not independently measured, the obtained

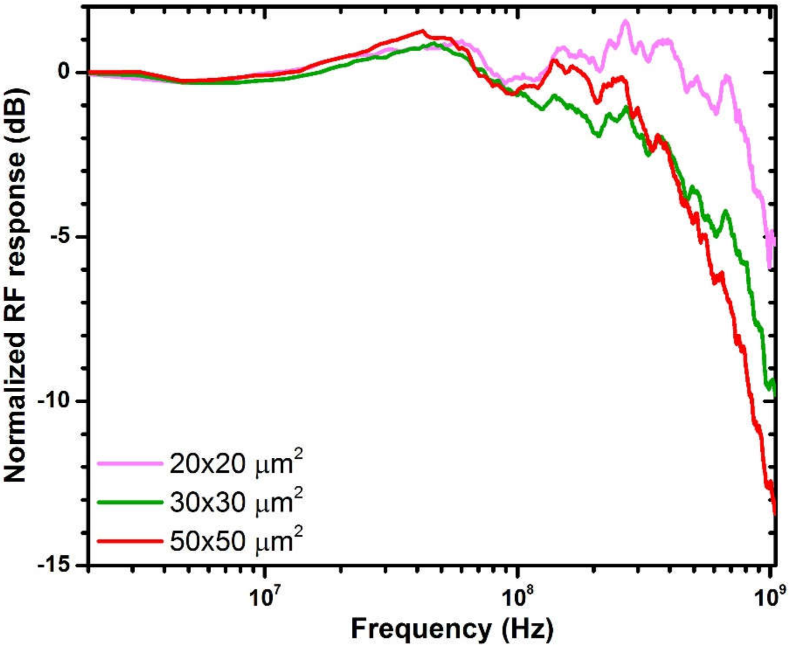

Figure 5-6: The measured frequency response for the MWIR interband cascade system using different-sized ICIPs.

spectra include the frequency response from both the IC laser and the ICIP. To extract their individual frequency responses, an equivalent circuit model was constructed as shown in Figure 5-7. All the circuit parameters for the IC laser were directly measured and are summarized in Table 5-2; thus its frequency response was independently simulated. The calculated frequency response (R_{ICL}) for the IC laser is shown in Figure 5-8 (middle panel). The 3-dB bandwidth of this IC laser was 760 MHz at T=293 K and was mainly limited by the bonding pad capacitance ($C_{\mathrm{bp}} \approx 77.4$ pF). From the R_{ICL} spectrum, the calibrated frequency response of the ICIP(s) can be extracted using $R_{ICIP} = \frac{R_{system}}{R_{ICL}}$, where R_{system} denotes the obtained system frequency response. The extracted frequency response for a 20×20 μm^2 ICIP is presented in Figure 5-8 (bottom panel), which indicates a 3-dB bandwidth of ~1.3 GHz and corresponds to a sub-nanosecond response time for this device. At room temperature, the ICIP's resistance R_{d} was large enough (in the kΩ range and in parallel to an equivalent current source) that it would not affect the modulation bandwidth, which could be considered to be infinite in the response simulations. Similar to the IC laser except for the device capacitance (C_{d}), all other parameters for the ICIP in the high-frequency circuit were directly measured. The series resistance (R_{s}) was estimated from the measured I-V curves at a large forward bias (5 V). The bonding pad capacitance (C_{bp}) related to the two-layer passivation was 1.1 pF for the ICIP. The another high-frequency parasitic element was the parasitic inductance from the gold bonding wires. Depending on the value of

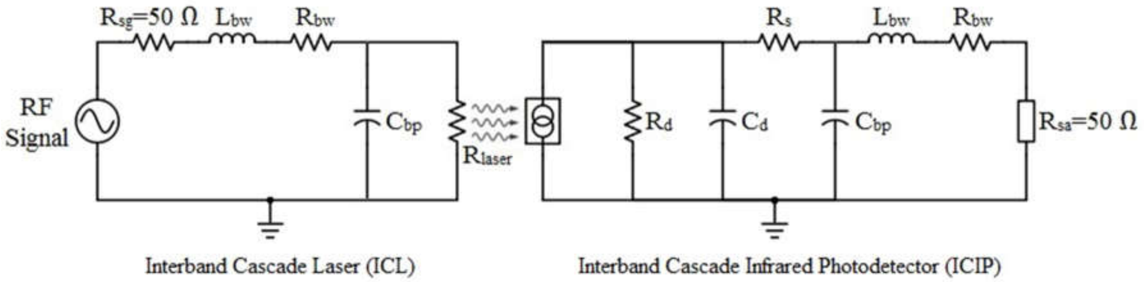

Figure 5-7: High-frequency circuit model constructed for the interband cascade mid-IR system. R_{sg} and R_{sa} are the output or input resistance of the analog signal generator and the spectrum analyzer, respectively. All the other circuit parameters are denoted in Tables 5-2 and 5-3.

parasitic capacitances, at some frequencies this inductance can counterbalance the capacitive behavior of the circuit and cause a response boost at a certain frequency range (as can been seen in Figure 5-8). However, this parasitic inductance will cause a sharp decrease in the RF signal at higher frequencies. The ICIP's capacitance (C_d), as the only unknown, was set as a fitting parameter. A curve based on the fitted capacitance is also shown in the top and bottom panels in Figure 5-8. The measured and extracted parameters are listed in Table 5-3 for two different ICIPs with 20×20 μm^2 and 30×30 μm^2 mesa sizes. The observed size dependence of the bandwidth suggests that the 3-dB bandwidth was not limited by the fundamental carrier transit time. This implies that the bandwidth of this interband cascade system can be increased further by reducing the parasitic capacitances and inductances, along with implementing impedance matching circuits.

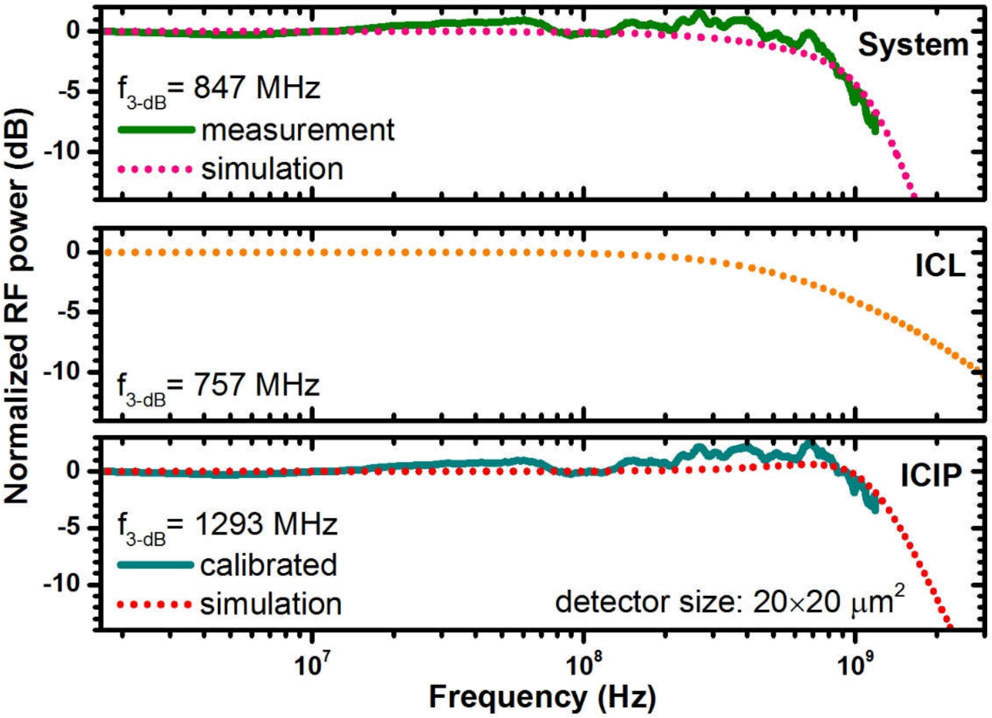

Figure 5-8: The measured and simulated frequency response of the interband cascade system with a 20×20 μm^2 ICIP (top). The calculated frequency response of the type-I IC laser (middle) and the calibrated and simulated frequency response for the ICIP (bottom).

It is worth noting that the frequency response of single-stage ICIPs with thick absorbers was also investigated experimentally. These single-stage ICIPs with thick absorbers had bandwidths more than an order of magnitude narrower than the three-stage ICIP with thin individual absorbers, which validates the advantage of the multiple discrete absorber architecture.

Table 5-2: The measured and simulated high-frequency circuit parameters for the IC laser working at *T*=293 K.

Laser size (μm×μm)	Laser resistance R_{laser} (Ω)	Bonding pad size (μm×μm)	Bonding pad capacitance C_{bp} (pF)	Bonding wire inductance L_{bw} (nH)	Bonding wire resistance R_{bw} (Ω)	ICL simulated bandwidth (MHz)
20×2000	4.9	300×2000	77.4	3.4	0.06	757

Table 5-3: Summary of the measured and simulated high-frequency circuit parameters for two different-sized ICIPs. The ICIP capacitance (C_d) was deduced from a fit to the measurement data.

Detector size (μm^2)	Device resistance R_d (kΩ)	Device capacitance C_d (pF)	Series resistance R_s (Ω)	Bonding pad size (μm×μm)	Bonding pad capacitance C_{bp} (pF)	Bonding wire inductance L_{bw} (nH)	Bonding wire resistance R_{bw} (Ω)	Simulated ICIP bandwidth (MHz)	Simulated system bandwidth (MHz)	Measured system bandwidth (MHz)
20×20	35.1	1.04	101	100×100	1.1	11.1	0.44	1293	847	848
30×30	19.3	2.83	73	100×100	1.1	11.1	0.44	604	430	431

5.5 Time domain characterizations

While the frequency domain measurements are an effective tool to examine the performance of an optical link, the time domain measurements (*e.g.*, eye diagrams) provide valuable information related to the signal integrity and the quality of the optical link. The time domain setup was very similar to our high-frequency domain setup (Figure 5-5). Instead of the analog signal generator, an arbitrary waveform generator (AWG) was used to generate pseudo-random bit sequences (PRBS). Each period of the PRBS had 16 random bits (zeros and ones). On the receiver end, a high-frequency oscilloscope was used to capture the received bits. Figure 5-9 shows the generated bits fed to the IC laser and the detected bits by an eight-stage ICIP at 32 Mb/s bit rate. Note that the bit inversion in the detector output was associated with the high-frequency

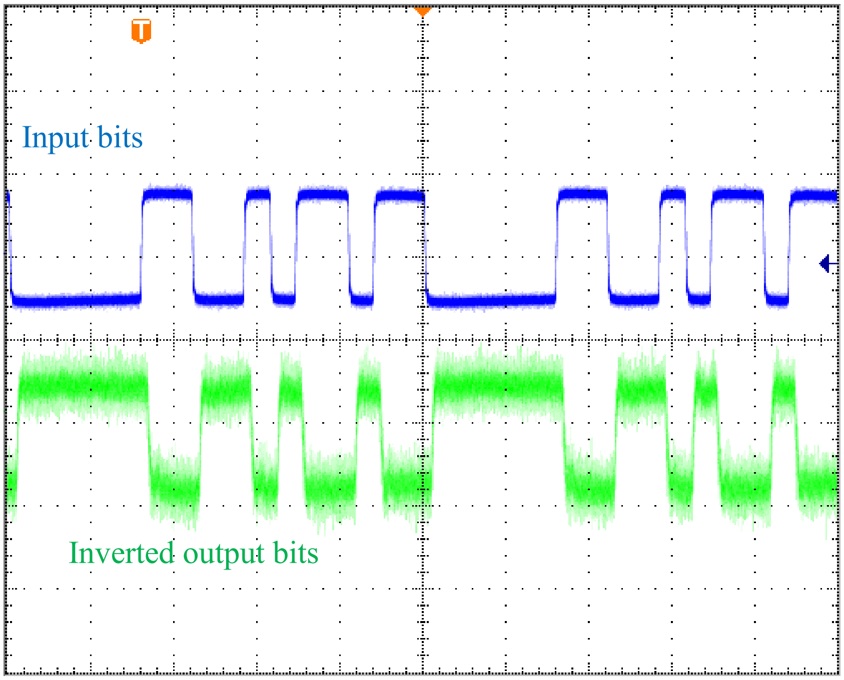

Figure 5-9: The input PRBS fed to the IC laser (top) and the detected bits by an eight-stage ICIP (mesa size: 50×50 μm^2). Output bits inversion is related to the high-frequency amplifier used before the oscilloscope. The bit rate was 32 Mb/s. Each horizontal division is 100 ns.

amplifier that was used to amplify the detector output before oscilloscope. The eye diagrams generated for three different ICIPs with a different number of stages and absorber thicknesses are displayed in Figure 5-10 for two bit rates (8 and 48 Mb/s). The absorber thickness was 1,040 nm in the one-stage ICIP, whereas the thickest absorbers were 383.5 and 591.5 nm in three- and eight-stage ICIPs, respectively. Note that the AWG was only able to generate PRBS with bit rates up to 50 Mb/s. Based on the frequency domain measurements of the interband cascade system, clear and open eyes at significantly higher bit rates are expected in three- and eight-stage ICIPs. The generated eyes show the limited rise and fall times in the one-stage ICIP at 48 Mb/s, while the other two ICIPs (three- and eight-stage ICIPs) with short absorbers and more stages did not exhibit any signal degradation up to this bit rate. Although all three ICIPs had similar detectivities ($\sim 10^9$ cm.Hz$^{1/2}$/W) at room temperature, the one-stage ICIP had degraded high-frequency performance compared to the other two ICIPs, showing that short absorbers and multiple stages are beneficial in high-speed applications. This behavior is a clear indication of the unique ability of ICIPs to maintain a high sensitivity, similar to that of a one-stage detector with thick absorber, while the device frequency response is significantly enhanced.

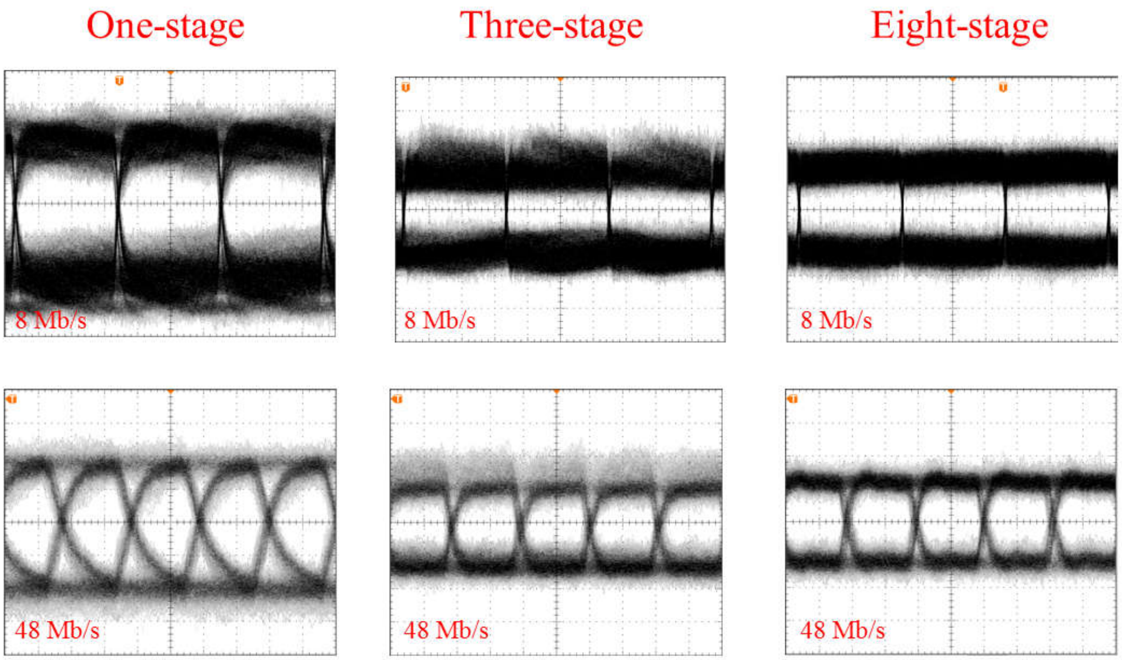

Figure 5-10: Eye diagrams for ICIPs with a different number of stages and absorber thicknesses. Each horizontal division is 40 ns (top row) and 10 ns (bottom row). Bit rate was 8 Mb/s (top row) and 48 Mb/s (bottom row).

5.6 Summary and concluding remarks

In summary, the high-frequency operation ($f_{3\text{-}dB}$≈850 MHz) of an interband cascade system that is composed of an IC laser and an uncooled three-stage ICIP has been demonstrated at room temperature. This initial study shows that ICIPs (at zero-bias) can achieve gigahertz bandwidth with detectivities higher than 10^9 cm·Hz$^{1/2}$/W at room temperature, suggesting great potential and the feasibility of compact systems for relevant applications. Nevertheless, many aspects such as carrier dynamics and transport mechanisms remain unexplored in interband cascade structures. Further research on the device physics, growth and fabrication are desirable to provide more perspectives on the ultimate performance of interband cascade systems.

5.7 Bibliography

[1] I. Vurgaftman, R. Weih, M. Kamp, J. Meyer, C. Canedy, C. Kim*, et al.*, "Interband cascade lasers," *Journal of Physics D: Applied Physics,* vol. 48, p. 123001, 2015.

[2] A. Soibel, M. Wright, W. Farr, S. Keo, C. Hill, R. Q. Yang*, et al.*, "High-speed operation of interband cascade lasers," *Electronics Letters,* vol. 45, p. 1, 2009.

[3] A. Soibel, M. W. Wright, W. H. Farr, S. A. Keo, C. J. Hill, R. Q. Yang*, et al.*, "Midinfrared interband cascade laser for free space optical communication," *IEEE Photonics Technology Letters,* vol. 22, pp. 121-123, 2010.

[4] D. E. Sawyer and R. H. Rediker, "Narrow base germanium photodiodes," *Proceedings of the IRE,* vol. 46, pp. 1122-1130, 1958.

[5] A. Rogalski, *Infrared detectors*, CRC press, 2010.

[6] R. Q. Yang, Z. Tian, Z. Cai, J. F. Klem, M. B. Johnson, and H. C. Liu, "Interband-cascade infrared photodetectors with superlattice absorbers," *Journal of Applied Physics,* vol. 107, p. 054514, 2010.

[7] R. T. Hinkey and R. Q. Yang, "Theory of multiple-stage interband photovoltaic devices and ultimate performance limit comparison of multiple-stage and single-stage interband infrared detectors," *Journal of Applied Physics,* vol. 114, p. 104506, 2013.

[8] Z. Tian, R. T. Hinkey, R. Q. Yang, D. Lubyshev, Y. Qiu, J. M. Fastenau*, et al.*, "Interband cascade infrared photodetectors with enhanced electron barriers and p-type superlattice absorbers," *Journal of Applied Physics,* vol. 111, p. 024510, 2012.

[9] N. Gautam, S. Myers, A. Barve, B. Klein, E. Smith, D. Rhiger*, et al.*, "High operating temperature interband cascade midwave infrared detector based on type-II InAs/GaSb strained layer superlattice," *Applied Physics Letters,* vol. 101, p. 021106, 2012.

[10] H. Lotfi, L. Lei, L. Li, R. Q. Yang, J. C. Keay, M. B. Johnson*, et al.*, "High-temperature operation of interband cascade infrared photodetectors with cutoff wavelengths near 8 µm," *Optical Engineering,* vol. 54, pp. 063103-063103, 2015.

[11] H. Lotfi, L. Li, L. Lei, R. Q. Yang, J. F. Klem, and M. B. Johnson, "Short-wavelength interband cascade infrared photodetectors operating above room temperature," *Journal of Applied Physics,* vol. 119, p. 023105, 2016.

[12] W. Pusz, A. Kowalewski, P. Martyniuk, W. Gawron, E. Plis, S. Krishna*, et al.*, "Mid-wavelength infrared type-II InAs/GaSb superlattice interband cascade photodetectors," *Optical Engineering,* vol. 53, pp. 043107-043107, 2014.

[13] Z.-B. Tian, S. Godoy, H. Kim, T. Schuler-Sandy, J. Montoya, and S. Krishna, "High operating temperature interband cascade focal plane arrays," *Applied Physics Letters,* vol. 105, p. 051109, 2014.

[14] D. Hofstetter, M. Graf, T. Aellen, J. Faist, L. Hvozdara, and S. Blaser, "23 GHz operation of a room temperature photovoltaic quantum cascade detector at 5.35 μm," *Applied Physic Letters,* vol. 89, pp. 1-3, 2006.

[15] A. Vardi, N. Kheirodin, L. Nevou, H. Machhadani, L. Vivien, P. Crozat*, et al.*, "High-speed operation of GaN/AlGaN quantum cascade detectors at λ= 1.55 μm," *Applied Physic Letters,* vol. 93, 2008.

[16] D. Hofstetter, F. R. Giorgetta, E. Baumann, Q. Yang, C. Manz, and K. Köhler, "Mid-infrared quantum cascade detectors for applications in spectroscopy and pyrometry," *Applied Physics B,* vol. 100, pp. 313-320, 2010.

[17] P. Reininger, T. Zederbauer, B. Schwarz, H. Detz, D. MacFarland, A. M. Andrews*, et al.*, "InAs/AlAsSb based quantum cascade detector," *Applied Physics Letters,* vol. 107, p. 081107, 2015.

[18] B. Schwarz, D. Ristanic, P. Reininger, T. Zederbauer, D. MacFarland, H. Detz*, et al.*, "High performance bi-functional quantum cascade laser and detector," *Applied Physics Letters,* vol. 107, p. 071104, 2015.

[19] Y. Jiang, L. Li, R. Q. Yang, J. A. Gupta, G. C. Aers, E. Dupont*, et al.*, "Type-I interband cascade lasers near 3.2 μm," *Applied Physics Letters,* vol. 106, pp. 2-6, 2015.

Chapter 6: Monolithically integrated mid-IR interband cascade lasers and detectors

6.1 Background and motivation

Over the last decades, photonic integrated circuits (PICs) that incorporate different optoelectronic devices including lasers, photodetectors, modulators and waveguides on a single chip have been extensively explored. Monolithic integration of optoelectronic devices results in compact, power efficient, and robust optical systems for applications such as miniaturized sensors, spectrometers, and on-chip optical communication and processing. Research on PICs has mainly focused on near-infrared (NIR) optoelectronic components and their on-chip integration on GaAs and InP platforms [1], whereas PICs in mid-IR (>3 μm) bands have remained largely unexplored until recent years. Advances in quantum engineered mid-IR lasers namely, quantum cascade lasers (QCLs) [2] and interband cascade lasers (ICLs) [3] with room temperature operation [4, 5] have stimulated research initiatives in PICs for mid-IR bands.

Of course, along with high-performance room-temperature mid-IR lasers, high-performance high-operating-temperature mid-IR photodetectors are also required for PICs. Although III-V based mid-IR ICLs and QCLs are able to work very well at room temperature and above, mid-IR photodetectors made of III-V semiconductors are not as mature as their II-VI $Hg_{1-x}Cd_xTe$ based counterparts [6] and usually require cryogenic cooling for high performance. As discussed in Chapter 2, among III-V based mid-IR photodetectors, type-II superlattice (T2SL) photodetectors are projected to outperform $Hg_{1-x}Cd_xTe$ photodetectors [7, 8].

Because interband transitions are much slower (order of ns) than intersubband relaxation involved in carrier transport (order of ps) within the same band, ICL structures operate well as an IR photodetector (*i.e.*, an ICIP) at zero and reverse bias condition, as demonstrated using early ICLs [9]. Hence, without any structure optimization for detector operation, ICL wafers can be used to realize both ICLs and ICIPs on a single chip, enabling high-performance functional units for PICs. Compared to monolithically integrated QCLs and quantum cascade detectors, referred as QCLDs [10-14], in which the fast intersubband transitions are comparable to transit times of carrier transport in the conduction band, monolithically integrated IC lasers and detectors (ICLDs) have significant advantages in terms of low power consumption, high sensitivity, and design flexibility owing to their broad absorption spectrum and a large difference in the time scales of interband transitions and intraband transport. Monolithic integration of lasers and detectors is also recently reported in quantum dot micropillar structures in NIR band [15]. However, these structures have very low specific detectivity (with an upper limit of ~1×10^5 cm.$Hz^{1/2}$/W) and operate at cryogenic temperatures.

In this chapter, we report on the first demonstration of a monolithically integrated mid-IR interband cascade laser and photodetector operating at room temperature. The laser/detector pair was defined using focused ion beam milling. The laser section lased in cw mode with an emission wavelength of ~3.1 µm at 20 °C and top-illuminated photodetectors fabricated from the same wafer had Johnson-noise-limited detectivity of 1.05×10^9 cm.Hz$^{1/2}$/W at this wavelength and temperature. Under the same condition, the detectivity for the edge illumination configuration for the monolithically integrated laser/photodetector pairs is projected to be as high as 1.85×10^{10} cm.Hz$^{1/2}$/W, as supported by experimentally observed high photocurrent and open-circuit voltage.

6.2 Device structure and method of forming

6.2.1 Base structure for ICLDs

To realize an ICLD, a six-stage type-I ICL, grown on a GaSb substrate, with quaternary $Ga_{0.45}In_{0.55}As_{0.22}Sb_{0.78}$ quantum well (QW) active regions was used as the base structure. Figure 6-1 shows the band profile and the layering sequence in one stage of this ICL. Each stage is composed of an 8.8 nm $Ga_{0.45}In_{0.55}As_{0.22}Sb_{0.78}$ active region

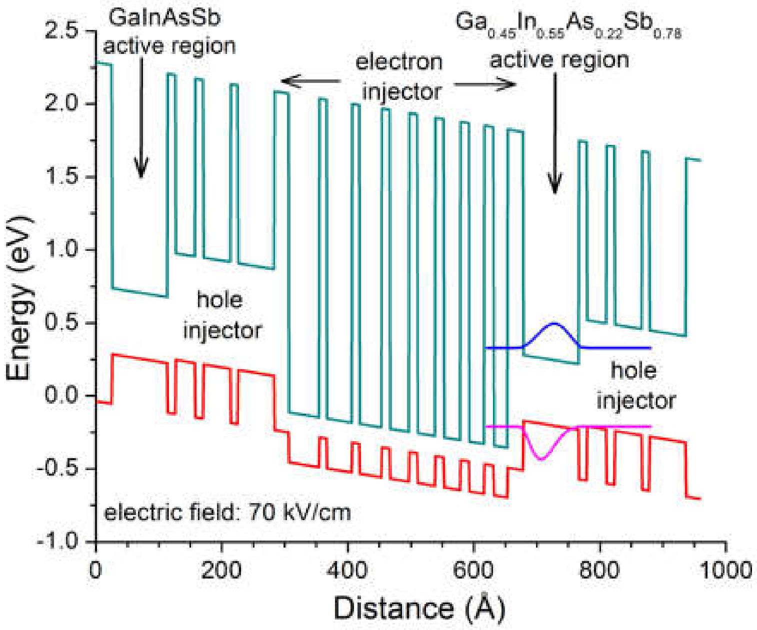

Figure 6-1: Band profile and the layering sequence (for one stage) of type-I ICLs used for fabrication of ICLDs [16].

sandwiched between electron injector (8 InAs/AlSb QWs) and hole injector (3 GaSb/AlSb QWs). ICLs made from this wafer lased in cw mode up to 306 K. Further details about the ICL structure and its performance have been reported in [16].

6.2.2 Device fabrication

6.2.2.1 Focused ion beam milling of III-V semiconductors

Focused ion beam (FIB) milling and deposition have been widely used in different areas of semiconductor research and development. Real-time imaging during nanoscale manipulations is possible in dual platform systems, which integrate an SEM with a FIB instrument. This system integration provides a large degree of accuracy and control over the milling or deposition process. FIB has been used in the fabrication of different electronic and optoelectronic devices such as coupled cavity lasers (CCLs), infrared detectors, and manipulation of nanostructures [17-22]. Moreover, the tedious job of sample preparation for TEM is greatly simplified by FIB, and TEM samples can be prepared sometimes within an hour [23].

Various physical and chemical reactions take place during FIB process. The nature and dynamics of these reactions are sensitive to the material that is milled. Therefore, a successful recipe for a material system may not necessarily work for the others. Parameters such as gas flow rate, FIB current, energy, and angle need careful calibration and optimization for different materials and structures. FIB fundamentals and instrumentation are beyond the scope of this dissertation. Further discussion and details on different aspects of FIB and its instrumentation can be found in [24, 25].

A Zeiss Neon-40 SEM-FIB system with gallium ions as the liquid metal ion source (LMIS) was used to define each laser/detector unit. This system allows milling currents of 5 pA-16 nA with acceleration energies of 5-30 keV. Figure 6-2 (a & b) compares the FIB milled side walls when high (16 nA) and low milling currents (100 pA) are used. While higher FIB currents increase the milling rate, they also result in rough side walls and significant redeposition. FIB milling of III-V semiconductors has further difficulties compared to that of other material systems such as silicon [26]. These difficulties are associated with Ga^+ ions, often used in FIB. Ga-rich droplets are prevalent when gallium is used as LMIS for milling of III-V compounds. Since these droplets and the redeposited materials are electrically conductive the electrical resistance of milled structures suffers. To circumvent this issue, gas injection system (GIS) can be used during FIB milling. Figure 6-2 (c & d) compares the side will quality with and without using GIS. By introducing a reactive gas such as XeF_2 the milling rate increases and the formation of droplets and redeposited materials are reduced. When XeF_2 is flashed during milling, the chemical reactions between gallium and fluorine result in the formation of GaF_3, which is a solid material with high melting point. Consequently, the formation of Ga-rich droplets is reduced and the quality of FIB milled side walls are considerably enhanced.

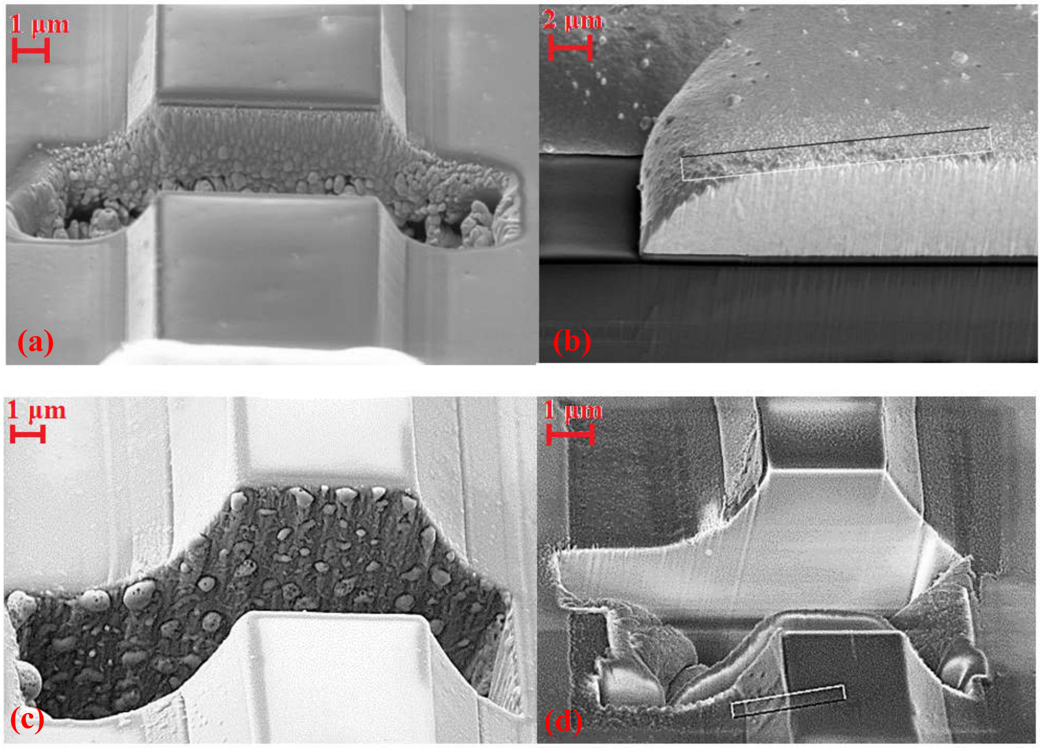

Figure 6-2: SEM images of the fabricated slots in type-I ICLs under different FIB conditions: (a) 30 keV and 16 nA, GIS: OFF (b) 30 keV and 200 pA, GIS: OFF (c) 30 keV and 200 pA, GIS: OFF. (d): 10 keV and 100 pA, GIS: ON. Lower FIB currents and GIS reduce the amount of droplets and redeposition on side walls.

6.2.2.2 Fabrication of ICLD devices using focused ion beam milling

The ICL used as the base structure had a nominal ridge width of 12 µm and a cavity length of 1.5 mm. The base ICL structure was fabricated into an ICLD pair, as shown in Figure 6-3 using FIB milling. Along the longitudinal cavity direction of this ICL, there was a ~50 µm-wide stripe without a gold layer as shown by a scanning electron microscope (SEM) image (see Figure 6-3). This stripe was originally designed to allow cleaving the structure into 1.0-mm or 0.5-mm-long lasers.

The FIB current was ~250 pA and XeF_2 gas was periodically (10 ms for each 30 s) injected into the milling area during all the five milling steps. As stated in the previous section, the purpose of using XeF_2 gas was to reduce the redeposition and formation of gallium-rich droplets. It is worth to mention that long exposure times to XeF_2 resulted in undesired chemical reactions between the insulator layers (SiN_x+SiO_2) and fluorine. Therefore, the gas injection was limited to short time intervals. Five sequential milling steps, marked as 1 to 5, in Figure 6-3(c), were carried out to electrically and optically isolate laser and detector sections from each other. The gap cavity between the laser and detector inner facets (see Figure 6-3(a)) was defined by milling a 10 μm ×10 μm hole to form the laser and detector sections. Typically, the sputter redeposition onto previously cleaned FIB-milled facets could significantly reduce the resistance of the device and consequently degrade the device performance. To alleviate this problem, after milling the 10 μm square hole both facets were further polished by milling narrow slotted areas on each facet (steps 2 and 3 in Figure 6-3(c)), resulting in a final gap cavity of ~12 μm between the laser and detector inner facets. Finally, two separate slots (40 μm×2 μm) were milled (steps 4 and 5) in the gold bridge to electrically isolate the laser and detector sections. The two separate slots in the gold bridge area were to reduce the redeposition on the freshly milled facets.

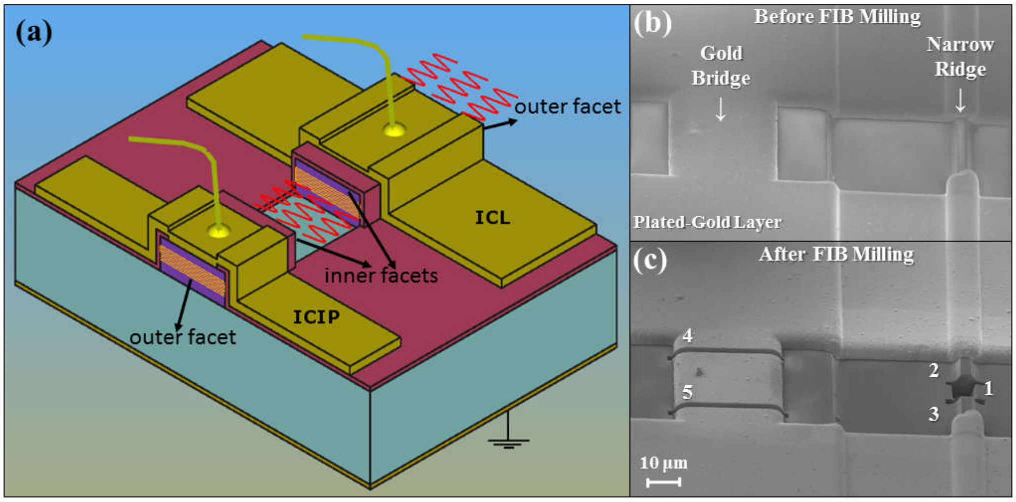

Figure 6-3: (a) Schematic drawing of an ICLD. SEM images of (b) the base ICL before FIB milling and (c) the fabricated ICLD after FIB milling.

6.3 Device performance characteristics and discussion

Before FIB milling, the base ICL (cavity length: 1.5 mm, ridge width: 12 μm) with as cleaved facets lased at ~3.1 μm in cw mode with a threshold current density of 370 A/cm^2 at 20 ˚C. After FIB milling, the laser section of ICLD unit (cavity length: 1 mm) lased in cw mode with an increased threshold current density of 490 A/cm^2 at 20 ˚C. This increase of threshold current density is mainly attributed to the larger mirror loss for a shortened cavity (from 1.5 to 1.0 mm) rather than the possibly degraded FIB-milled mirror. As shown by the current-voltage-light (*I*-*V*-*L*) plots in Figure 6-4, we observed similar threshold current densities for the ICLD laser section compared with two other 1-mm long ICLs with cleaved facet mirrors fabricated from the same wafer. Thus, the quality of the FIB milled facets on GaSb-based structures was comparable to cleaved facets.

The ICLD was in such a way that the laser emission spectrum and output power could be collected from the laser's outer facet. At 20 ˚C, the output power from the outer facet of the laser section of the ICLD (corrected for the window's transmission but not for beam divergence) was 2.6 mW at 95 mA, as shown in Figure 6-4. Considering the power loss (~40%) associated with the beam divergence, the ICLD's actual output power is estimated to be 4.3 mW.

To characterize the performance of the ICLD, the laser section was biased at injection currents from 0 to 100 mA, while the *I*-*V* characteristics of the detector section were collected at each injection current. The short-circuit current (I_{sc}) of the detector section of the ICLD is shown in Figure 6-4 as a function of the injection current applied to the laser section. I_{sc} exhibits similar characteristics as the output power obtained from

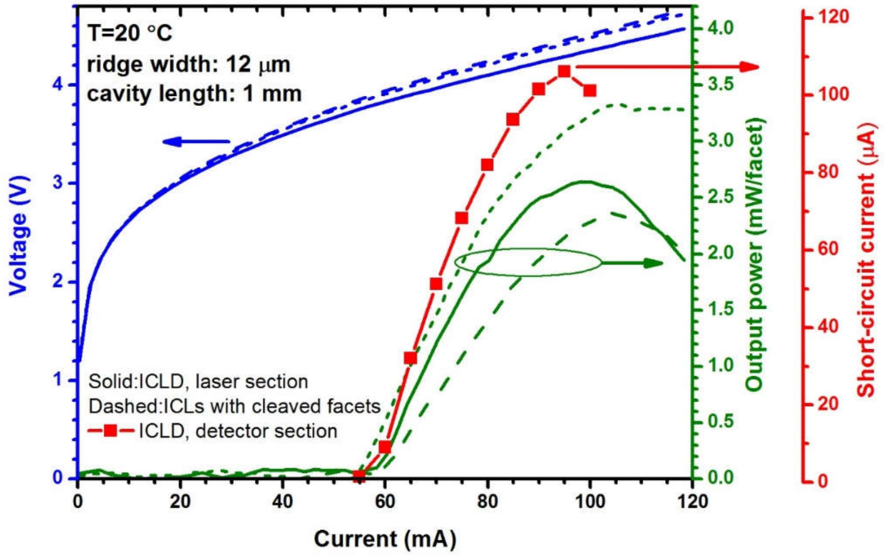

Figure 6-4: The *I-V-L* characteristics of the laser section of the ICLD (solid lines) compared with that of two ICLs (dash and short dash lines) with as-cleaved facets. Also shown is the I_{sc} of the detector section of the ICLD as a function of the injection current that was applied to the laser section.

the outer facet of the laser section (*e.g.*, a rollover at high injection currents). When 95 mA of current was injected to the laser section, the detector section showed strong photovoltaic characteristics with I_{sc} of 106 μA and an open-circuit voltage (V_{oc}) of 1.06 V. Figure 6-5 shows the *I-V* curves of the detector section without illumination from the laser (no current through the laser) and with the illumination from the laser at 95 mA injection current and lasing wavelength of 3.12 μm (inset Figure 6-5). The non-flat *I-V* characteristics under reverse bias was attributed to the device shunt and series resistances, which can be improved with advances in device design and fabrication. The two cladding regions in the device structure, which are required for the laser operation, but unnecessary for the detector, may contribute extra series resistance. The open-circuit voltage (1.06 V) significantly exceeds the single bandgap determined value (E_g/e=0.38 V) indicating the cascade action is highly effective [27, 28]. Here the bandgap E_g is determined from the device photoresponse spectrum (Figure 6-6). Such a high value of V_{oc} (~1.1 V) with a voltage efficiency of ~48% (from $qV_{oc}/(6 \cdot E_g)$, taking into account the six cascade stages) is an unambiguous indication of strong photoresponse to the laser illumination, implying the high sensitivity of the detector section (discussed more below).

Note that in contrast to conventional ICIPs with the top illumination configuration (*i.e.*, light incident in the normal or growth direction), the detector section in ICLDs is edge illuminated. For edge-illumination, the detector's optically active area (six discrete thin (8.8 nm) QW active absorption layers) is extremely small compared to that for the usual top illumination and it is difficult to accurately determine the absolute responsivity for edge illumination using our standard photoresponse calibration with a blackbody source. To circumvent this difficulty and for comparison purposes, square-mesa ICIPs were fabricated from this wafer for the top illumination measurements. Figure 6-6 shows the calibrated responsivity and Johnson-noise-limited detectivity of a

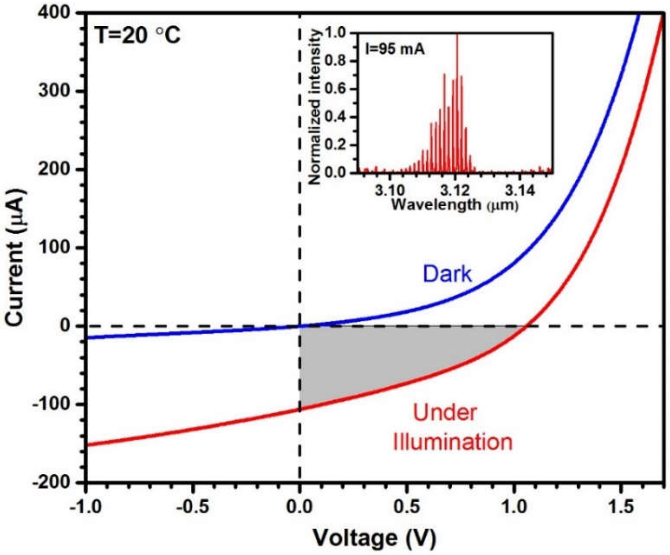

Figure 6-5: The *I-V* characteristics of the detector section of ICLD under dark and laser illumination. The shaded area shows the photovoltaic performance of this detector. Inset is the laser emission spectrum collected from its outer facet.

representative (1.0 mm × 1.0 mm) ICIP at 20 ˚C under top illumination from a calibrated 800 K blackbody source. As shown, the 100% cutoff wavelength of this ICIP was 3.4 μm at 20 ˚C. Two Fabry-Perot oscillations are observed in the top illuminated ICIPs. These oscillations result from interference between reflections from the back surface of the *n*-type GaSb substrate and the vertical cavity of the laser.

Relative photoresponse spectrum for edge illumination was measured using a broadband IR source and was compared with that for top illumination (inset of Figure 6-6). Because of the extremely small optical area in edge illumination, the relative response spectrum was somewhat noisy. Note that the edge illumination response did not exhibit Fabry-Perot oscillations because the IR light propagated along the longitudinal direction of the laser waveguide in contrast to the vertical direction for

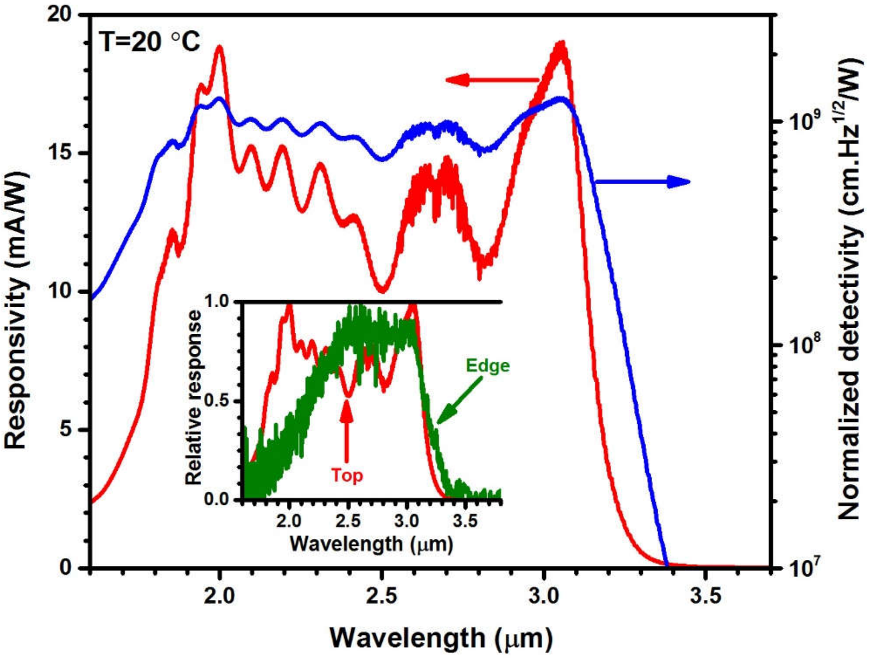

Figure 6-6: Responsivity and Johnson-noise-limited detectivity spectra for a representative top illuminated photodetector. The inset displays the relative response spectra for the top and edge illumination configurations.

normal illumination. In edge illumination configuration, the light propagation is mainly confined in the guiding layers with narrow bandgaps and less penetrates into other regions made of wider bandgap materials (*e.g.*, cladding layers), hence the response was substantially reduced at the short wavelengths compared to that for normal illumination. However, both the top and edge illumination configurations had similar cutoff wavelengths (~3.4 um), which ensures appreciable photon absorption at the laser's emission wavelength. For the top illumination, the detector responsivity and specific detectivity (D^*) were 15.6 mA/W and 1.05×10^9 cm.Hz$^{1/2}$/W at the laser emission wavelength (3.1 µm), respectively. Because of the very thin absorbers, the device responsivity increased by raising the device temperature up to 340 K (our highest temperature measured), which is due to the bandgap narrowing effects. Since the carrier transport is in the vertical (growth) direction for both edge and top illumination, the device dark current (and electrical resistance) is identical for both configurations. Meanwhile, because of very long absorbers in the longitudinal direction (~500 µm for the detector section of ICLD, reported here), the device photoresponse was expected to be significantly larger for the edge illumination configuration.

Due to a short distance for the vertical transport of photogenerated carriers and a long propagation path along the longitudinal direction for optical absorption of incident photons, a full collection of photogenerated carriers is expected with a high external quantum efficiency. Considering the series connection of the six stages in this structure and a reflection loss of 32% for the incident IR beam, the projected external quantum efficiency would be $68\div6\approx 11\%$, corresponding to a responsivity of 275 mA/W and D^* of 1.85×10^{10} cm.Hz$^{1/2}$/W at 20 ˚C and 3.1 µm. This value of D^* is more than an order of magnitude larger than that extracted for the top illumination configuration. Based on the projected responsivity for edge illumination, the incident power on the detector's inner facet of ICLD can be estimated using $P_{\mathrm{Inc}} = I_{\mathrm{sc}} / R_{\lambda}$, where P_{Inc}, I_{sc}, and R_{λ} are the received power, short-circuit current and the device responsivity, respectively. As stated earlier, at 95 mA injection current, the short-circuit current of the detector section of the ICLD was 106 μA, which indicates that ~0.385 mW of the total output power/facet of the laser section was collected (~9% of the total output power/facet). Due to the high detectivity (sensitivity) that can be achieved in IC detectors (also demonstrated in this work), this level of received power is more than sufficient for the ICLD unit to work effectively. Compared with intersubband-based quantum cascade lasers and detectors, the ICLD reported here has orders of magnitude larger detectivity. The large sensitivity of ICIPs along with the inherently low power consumption of ICLs makes ICLDs a promising structure for practical on-chip integration of IR lasers and photodetectors.

6.4 Summary and concluding remarks

The first demonstration of high-performance monolithically integrated IC lasers and interband cascade IR photodetectors was discussed in this chapter. This ICLD was able to operate at room temperature with high open-circuit voltage and sensitivity. Compared to the conventional top-illuminated ICIPs, the edge illumination configuration used in ICLDs could result in more than an order of magnitude enhancement in device sensitivity. These initial results validate the potential of interband cascade-based compact IR devices for applications including on-chip miniaturized sensors, spectrometers, optical communication and processing.

6.5 Bibliography

[1] L. A. Coldren, S. W. Corzine, and M. Mashanovitch, *Diode lasers and photonic integrated circuits*, Wiley series in microwave and optical engineering, 2012.

[2] J. Faist, F. Capasso, D. L. Sivco, C. Sirtori, A. L. Hutchinson, and A. Y. Cho, "Quantum cascade laser," *Science,* vol. 264, pp. 553-556, 1994.

[3] R. Q. Yang, "Infrared laser based on intersubband transitions in quantum wells," *Superlattices and Microstructures,* vol. 17, p. 77, 1995.

[4] M. S. Vitiello, G. Scalari, B. Williams, and P. D. Natale, "Quantum cascade lasers : 20 years of challenges," *Optics Express,* vol. 23, pp. 5167-5182, 2015.

[5] I. Vurgaftman, R. Weih, M. Kamp, J. R. Meyer, C. L. Canedy, C. S. Kim*, et al.*, "Interband cascade lasers," *Journal of Physics D: Applied Physics,* vol. 48, p. 123001, 2015.

[6] W. E. Tennant, "“Rule 07” Revisited: Still a Good Heuristic Predictor of p/n HgCdTe Photodiode Performance?," *Journal of Electronic Materials,* vol. 39, pp. 1030-1035, 2010.

[7] D. L. Smith and C. Mailhiot, "Proposal for strained type II superlattice infrared detectors," *Journal of Applied Physics,* vol. 62, pp. 2545-2548, 1987.

[8] C. H. Grein, P. M. Young, and H. Ehrenreich, "Minority carrier lifetimes in ideal InGaSb/InAs superlattices," *Applied Physics Letters,* vol. 61, p. 2905, 1992.

[9] J. V. Li, R. Q. Yang, C. J. Hill, and S. L. Chuang, "Interband cascade detectors with room temperature photovoltaic operation," *Applied Physics Letters,* vol. 86, p. 101102, 2005.

[10] A. Harrer, R. Szedlak, B. Schwarz, H. Moser, T. Zederbauer, D. MacFarland*, et al.*, "Mid-infrared surface transmitting and detecting quantum cascade device for gas-sensing," *Scientific Reports,* vol. 6, p. 21795, 2016.

[11] B. Schwarz, P. Reininger, H. Detz, T. Zederbauer, A. M. Andrews, W. Schrenk*, et al.*, "Monolithically integrated mid-infrared quantum cascade laser and detector," *Sensors,* vol. 13, pp. 2196-2205, 2013.

[12] B. Schwarz, P. Reininger, H. Detz, T. Zederbauer, A. Maxwell Andrews, S. Kalchmair*, et al.*, "A bi-functional quantum cascade device for same-frequency lasing and detection," *Applied Physics Letters,* vol. 101, 2012.

[13] B. Schwarz, P. Reininger, D. Ristanić, H. Detz, A. M. Andrews, W. Schrenk*, et al.*, "Monolithically integrated mid-infrared lab-on-a-chip using plasmonics and quantum cascade structures.," *Nature Communications,* vol. 5, p. 4085, 2014.

[14] B. Schwarz, D. Ristanic, P. Reininger, T. Zederbauer, D. MacFarland, H. Detz*, et al.*, "High performance bi-functional quantum cascade laser and detector," *Applied Physics Letters,* vol. 107, p. 071104, 2015.

[15] M. M. Karow, P. Munnelly, T. Heindel, M. Kamp, S. Höfling, C. Schneider*, et al.*, "On-chip light detection using monolithically integrated quantum dot micropillars," *Applied Physics Letters,* vol. 108, p. 081110, 2016.

[16] Y. Jiang, L. Li, R. Q. Yang, J. A. Gupta, G. C. Aers, E. Dupont*, et al.*, "Type-I interband cascade lasers near 3.2 μm," *Applied Physics Letters,* vol. 106, pp. 2-6, 2015.

[17] N. Antoniou, "Failure analysis of electronic material using cryogenic FIB-SEM," *Electronic Device Failure Analysis,* vol. 15, pp. 12-19, 2013.

[18] M. C. Dolph and C. Santeufemio, "Exploring cryogenic focused ion beam milling as a Group III-V device fabrication tool," *Nuclear Instruments and Methods in Physics Research, Section B: Beam Interactions with Materials and Atoms,* vol. 328, pp. 33-41, 2014.

[19] R. DeFreez, J. Puretz, R. Elliott, J. Orloff, and L. Swanson, "CW operation of widely and continuously tunable micromachined-coupled-cavity diode lasers," *Electronics Letters,* vol. 17, pp. 919-921, 1986.

[20] J. Puretz, R. DeFreez, R. Elliott, and J. Orloff, "Focused-ion-beam micromachined AlGaAs semiconductor laser mirrors," *Electronics Letters,* vol. 13, pp. 700-702, 1986.

[21] M. Mack, G. Via, A. Abare, M. Hansen, P. Kozodoy, S. Keller*, et al.*, "Improvement of GaN-based laser diode facets by FIB polishing," *Electronics Letters,* vol. 34, pp. 1315-1316, 1998.

[22] H. Cai, B. Liu, X. Zhang, A. Liu, J. Tamil, T. Bourouina*, et al.*, "A micromachined tunable coupled-cavity laser for wide tuning range and high spectral purity," *Optics Express,* vol. 16, pp. 16670-16679, 2008.

[23] L. A. Giannuzzi, *Introduction to focused ion beams: instrumentation, theory, techniques and practice*, Springer Science & Business Media, 2006.

[24] I. Utke, P. Hoffmann, and J. Melngailis, "Gas-assisted focused electron beam and ion beam processing and fabrication," *Journal of Vacuum Science &*

Technology B: Microelectronics and Nanometer Structures, vol. 26, p. 1197, 2008.

[25] J. Orloff, L. Swanson, and M. Utlaut, *High resolution focused ion beams: FIB and its applications*, Springer Science & Business Media, 2003.

[26] J. Huang, *Applications of XeF_2 chemistry on Ga-beam sensitive materials*, Carl Zeiss Microscopy, USA, 2011.

[27] R. Q. Yang, Z. Tian, J. Klem, T. D. Mishima, M. B. Santos, and M. B. Johnson, "Interband cascade photovoltaic devices," *Applied Physics Letters,* vol. 96, p. 063504, 2010.

[28] H. Lotfi, R. T. Hinkey, L. Li, R. Q. Yang, J. F. Klem, and M. B. Johnson, "Narrow-bandgap photovoltaic devices operating at room temperature and above with high open-circuit voltage," *Applied Physics Letters,* vol. 102, p. 211103, 2013.

Chapter 7: Interband cascade thermophotovoltaic devices

7.1 Motivation and background

As discussed in section 1.4.2, the optimum cell bandgap in a thermophotovoltaic (TPV) system with a broadband heat source (*i.e.*, a TPV system without selective emitter and filter) with a temperature of 1,000-2,000 K falls between 0.2-0.4 eV. However, narrow bandgap TPV cells (E_g<0.5 eV) are in their early stage of development and have inferior performance compared to the larger bandgap cells [1, 2]. Multiple-stage ICTPVs with engineered structures can be used to address issues such as low open-circuit voltage and series resistance losses in narrow bandgap TPV cells. In this chapter, the development and characterization of two sets of ICTPV devices with cutoff wavelengths of ~3 μm and >5 μm along with the possible routes to enhance the performance of ICTPVs are discussed.

7.2 Interband cascade thermophotovoltaic devices with bandgap of 0.41 eV

7.2.1 Device structure, growth, and fabrication

Two structures, one with two the other with three stages, were designed to study the influence of number of stages and absorber thickness on the performance of ICTPVs with 3 μm cutoff wavelength. Both structures had identical electron and hole barriers, and SL composition. The thickness of the individual absorbers was thicker in the optically deeper absorbers to achieve photocurrent matching between stages. As shown in Figure 7-1, the absorbers in the two-stage devices were 570 nm and 644 nm thick, respectively. The additional stage in the three-stage device had a 741-nm-thick absorber. The electron barriers consisted of three GaSb/AlSb QWs and the hole barriers were made of seven InAs/AlSb QWs in both structures. In these two structures, each period of the SL absorber consisted of four layers: InAs (20 Å), GaSb (15 Å),

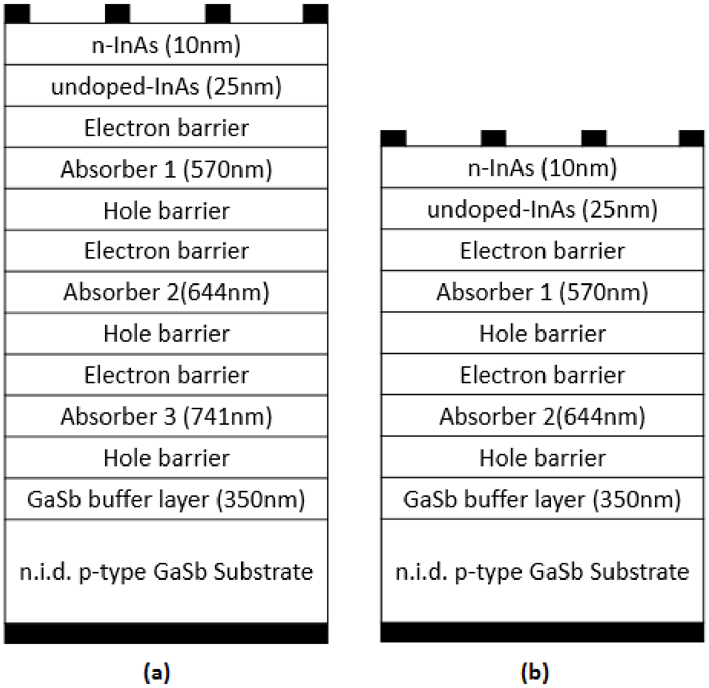

Figure 7-1: Schematic structure of (a) three- and (b) two-stage (b) ICTPV devices.

$Al_{0.2}In_{0.8}Sb$ (7 Å) and GaSb (15 Å). Further details on the device structure, growth and fabrication for the ICTPVs presented in this section are discussed in Chapter 4, where these wafers were used to realize SWIR ICIPs.

7.2.2 Device external quantum efficiency

External quantum efficiency (EQE) was measured using the optical setup described in Chapter 2. The blackbody temperature was set to 800 K with the device to blackbody (aperture radius:0.76 cm) distance as 30 cm. Figure 7-2 shows the EQE for representative devices from the two- and three-stage ICTPVs for 300-340 K. While the cutoff wavelength was slightly shorter in three-stage devices, the device 90% cutoff wavelength was 3 µm at 300 K and extended to 3.1 µm at 340 K. At the wavelength of 2.1 µm, where the maximum EQE was obtained, the EQE was 25.8% and 21.7% in two- and three-stage ICTPVs, respectively. Lower EQE in the three-stage devices is attributed to photocurrent mismatch among different stages. Because no antireflection coating was applied to these devices, the maximum possible particle conversion efficiency (PCE) is:

$$Max(PCE) = \left[1 - \left(\frac{n_{InAs} - n_{air}}{n_{InAs} + n_{air}}\right)^2\right] = 69\% \qquad (7-1)$$

where n_{InAs} and n_{air} are the refractive index of InAs (3.5) and air (1) in infrared, respectively. If the two- and three-stage devices were photocurrent matched, the maximum achievable EQE for two- and three-stage devices would be 34.5% and 23%, respectively. However, due to relatively thin individual absorbers, the EQE at wavelengths longer than 2.5 µm was significantly lower than the maximum values of theoretical projection. For instance, at 2.81 µm, the EQE was 11.7% and 10.8 % in two- and three-stage devices, respectively. Therefore, extra stages are required to fully absorb incident photons at these long wavelengths. As shown in Figure 7-2, the EQE did not decrease with raising the device temperature up to 340 K in both two- and three-stage devices. This implies that the device diffusion length could be comparable to or longer than the thickest absorber (741 nm) in three-stage devices up to this temperature. Thus, increasing the total absorber thickness by incorporating more stages in the device structure with improved current matching is a feasible approach to enhance the device PCE at the wavelengths close to the bandgap.

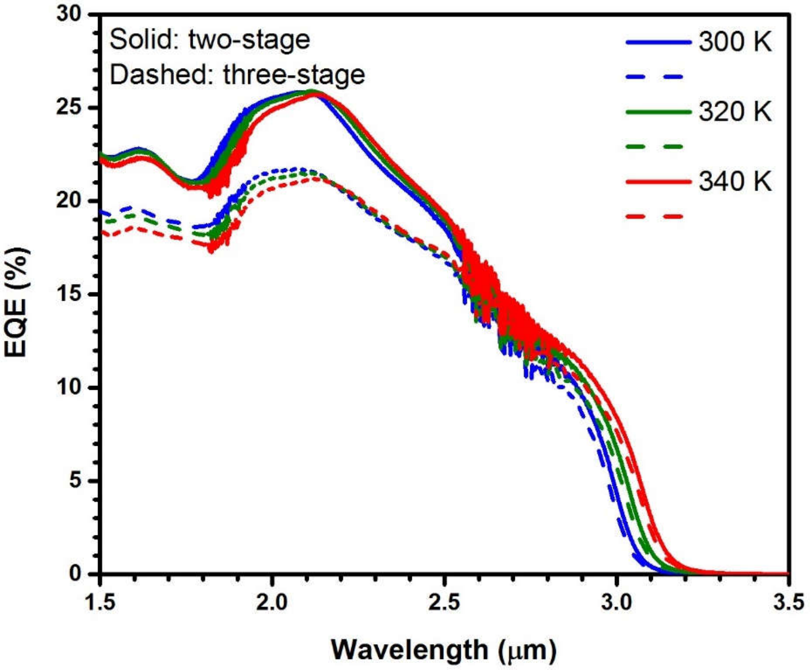

Figure 7-2: EQE for two- and three-stage ICTPV devices at 300-340 K. EQE was lower in three-stage TPV cells compared to that of two-stage devices.

7.2.3 Photovoltaic characteristics

7.2.3.1 Measurement setup

The experimental setup arranged for laser illumination of ICTPVs is depicted in Figure 7-3. In order to exclude the influence of parasitic resistances of test cables and wirings inside the cryostat, a four-wire setup was used to collect the device *I-V* under different levels of laser illumination. Figure 7-4 compares two- and four-wire setups. To implement four-wire tests, two extra bonding wires (one at the top and one at the bottom contact) were bonded to each device. In contrast to a two-wire setup, where the current and voltage are measured through the same terminals, separate circuits are used to measure them in a four-wire setup. The negligible current (in pA range) that flows in the voltage measurement circuit ensures that the measured voltage closely follows the device voltage.

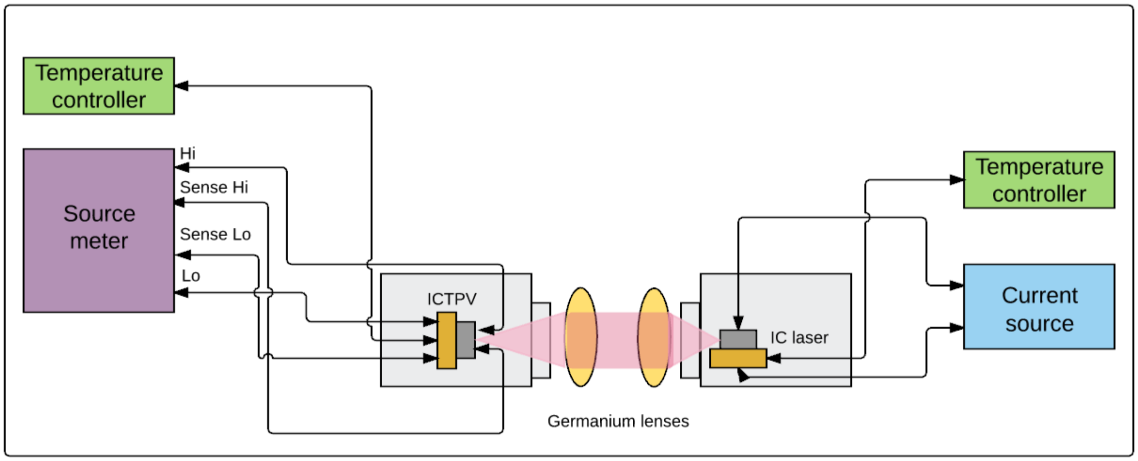

Figure 7-3: Schematic drawing of the measurement setup used in laser illumination of ICTPV devices.

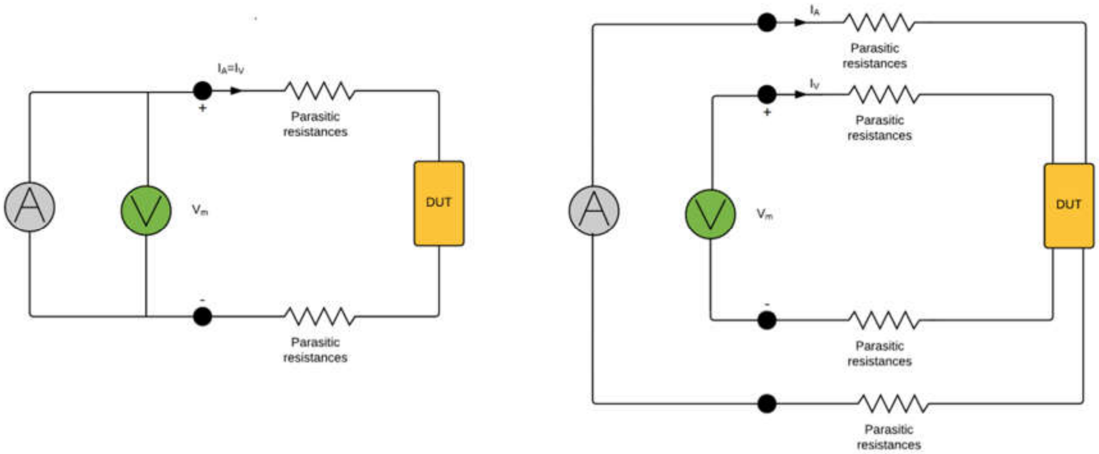

Figure 7-4: Schematics of (a) two- and (b) four-wire setups. In contrast to a two-wire setup, where the current and voltage have the same path, separate circuits are utilized for current and voltage measurements in a four-wire setup.

As discussed in Chapter 1, thermalization and below-bandgap losses are significantly lower in TPV systems with selective emitters with radiation spectrum that is matched to the TPV cell bandgap. To minimize the influence of these two loss mechanisms on the device efficiency, a type-I IC laser [3] (Figure 6-1) was employed to mimic the characteristics of a selective emitter with narrow emission spectrum closely matched to the TPV cell bandgap. The type-I IC laser (V146-BA-1-E) was a broad area laser (ridge width: 150 μm, cavity length: 1.6 mm) that was cooled down to LN_2 temperature (~78 K). Figure 7-5 shows the laser output power as a function of the injection current. The measured output power was not corrected for the diffraction and transmission losses associated with the laser geometry and the cryostats' window. At 78 K, the maximum output power (per facet) was 350 mW. The emission spectrum of this laser was centered at 2.81 μm which was closely matched to the TPV cell cutoff wavelength at 300-340 K. Consequently, the below bandgap and thermalization losses were minimal in this configuration.

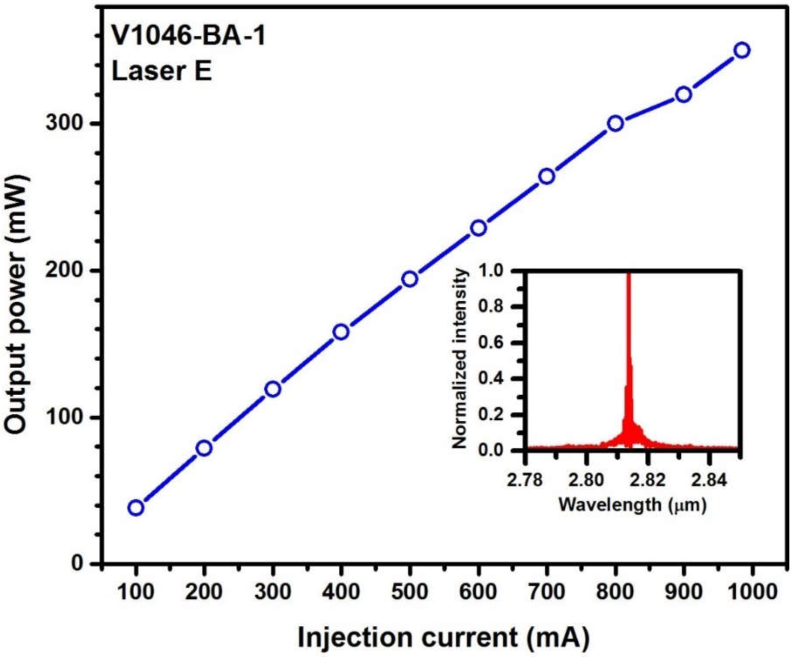

Figure 7-5: The measured output power (per facet) for the broad area laser used in laser illumination measurements. This laser was cooled down to LN2 temperature to achieve higher output power and match the emission wavelength with the bandgap of TPV cells. The inset shows the emission spectrum of this laser at 80 K.

7.2.3.2 J-V characteristics of ICTPVs under laser illumination

The performance of ICTPV devices was investigated under different illumination levels from the IC laser. Figure 7-6 shows the *J-V* characteristics of representative devices from both ICTPV wafers under different illumination levels. At 300 K, the maximum short-circuit current density (J_{sc}) and open-circuit voltage (V_{oc}) for two-stage (three-stage) devices were 50 A/cm^2 (43.5 A/cm^2) and 529 mV (799 mV), respectively and the voltage efficiency ($\frac{q.V_{oc}}{N_s E_g}$) was 64% in both ICTPV devices. A summary of photovoltaic performance of these wafers is provided in Tables 7-1 and 7-2. The device J_{sc} was increased by raising the device temperature (up to 340 K) in both wafers, which validates the efficient collection of photo-generated carriers at high temperatures. Larger J_{sc} at higher device temperatures is related to bandgap narrowing in III-V semiconductors by increasing the device temperature. Note that the device

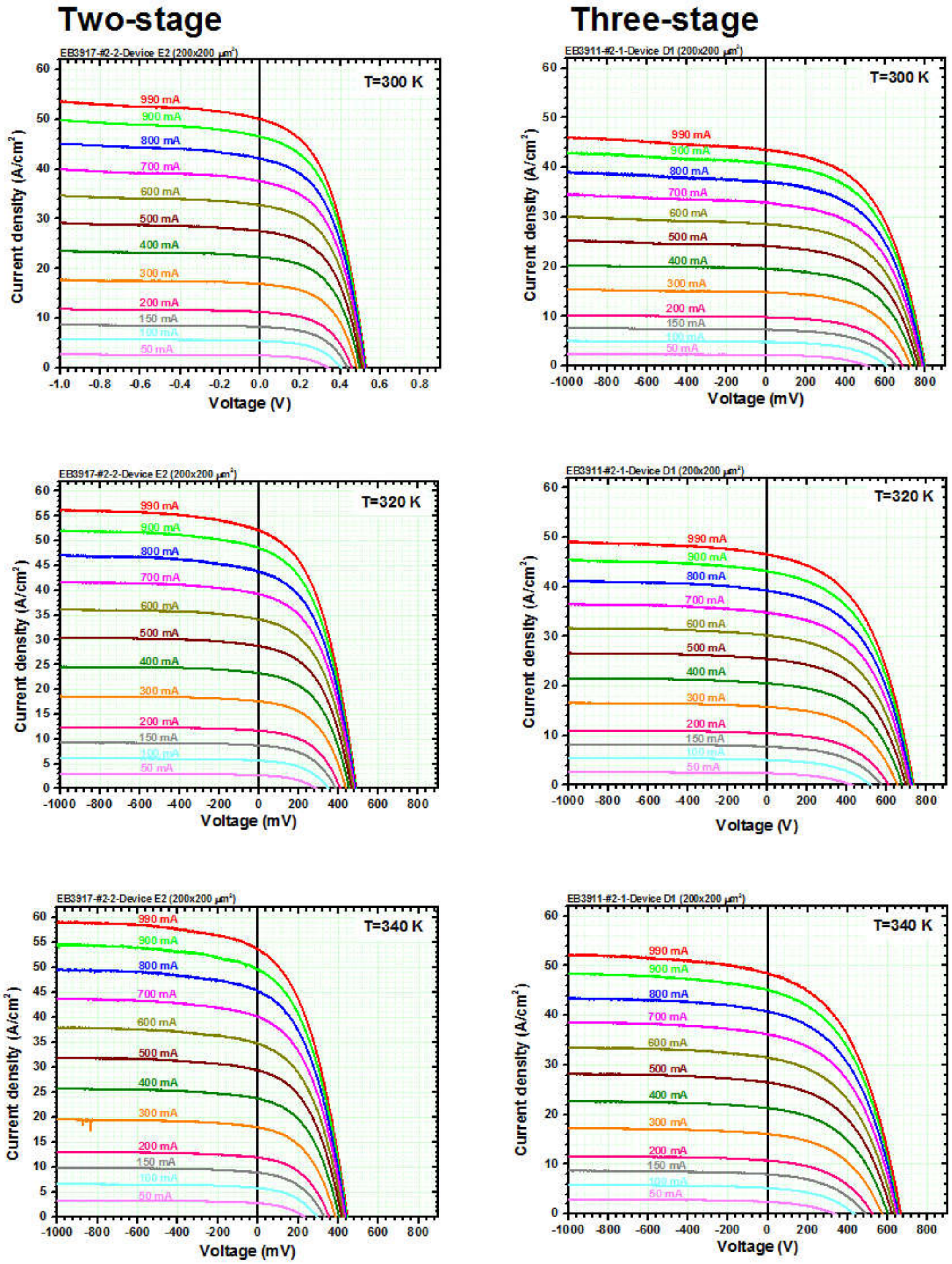

Figure 7-6: ***J-V*** **curves for representative devices from two- and three-stage ICTPV wafers under different laser illumination levels. The legend above each curve shows the injection current applied to the IC laser. Higher injection currents correspond to higher levels of laser illumination that was incident on TPV cells.**

Table 7-1: Summary of the photovoltaic performance and the related parameters of a 200×200 μm^2 two-stage ICTPV device.

Temperature (K)	J_{sc} (A/cm^2)	I_{ph} (mA)	V_{oc} (mV)	R_s (Ω)	R_{sh} (kΩ)	FF (%)	Maximum efficiency (%)
300	50.0	21.0	529	9.27	5.04	47.5	6.5
320	52.1	22.4	489	8.87	1.91	44.4	5.8
340	53.6	23.5	445	8.67	0.85	40.7	4.8

Table 7-2: Summary of the photovoltaic performance and the related parameters of a 200×200 μm^2 three-stage ICTPV device.

Temperature (K)	J_{sc} (A/cm^2)	I_{ph} (mA)	V_{oc} (mV)	R_s (Ω)	R_{sh} (kΩ)	FF (%)	Maximum efficiency (%)
300	43.5	17.9	799	12.14	9.04	51.4	9.6
320	46.6	19.4	736	11.20	3.26	48.2	8.5
340	48.4	20.8	666	11.09	1.38	44.9	7.3

open-circuit voltage was reduced to 445 mV (666 mV) in two-stage (three-stage) ICTPV devices at 340 K owing to increased dark currents at higher temperatures.

7.2.3.3 Fill factor and efficiency

7.2.3.3.1 Fill factor

It is instructive to compare the influence of number of stages and the device J_{sc} on the fill factor (FF) and efficiency of two- and three-stage ICTPV cells. Fill factor for selected devices from both wafers were calculated under different laser illumination levels for 300-340 K. Overall, fill factors were higher in three-stage devices at various temperatures compared to that of two-stage devices. The device FF *vs*. J_{sc} for two- and three-stage devices are plotted in Figure 7-7. At T=300K, the peak fill factor was 51.8% and 53.3% in two- and three-stage devices, respectively. The higher fill factors in three-stage devices could be related to the photocurrent mismatch that has been observed between different stages. Higher fill factors in photocurrent mismatched multi-junction solar cells has been reported in [4, 5]. The higher FF in a photocurrent mismatched multi-junction photovoltaic cell can partially mitigate the power loss associated with the photocurrent mismatch. Because of the ambiguity in determination of the main factor behind larger FF in three-stage devices, the percentage change in the FF ($\Delta\mathrm{FF} = \frac{\mathrm{FF}-\max(\mathrm{FF})}{\max(\mathrm{FF})}$) *vs*. J_{sc} was evaluated for both wafers. ΔFF exhibited a roll off at high short-circuit currents in both wafers, however the device fill factor decreased more rapidly by increasing the illumination level in two-stage devices for 300-340 K (inset in Figure 7-7). Sharper decrease of the device fill factor at high illumination levels could be related to the larger J_{sc} and consequently higher Ohmic losses in two-stage devices.

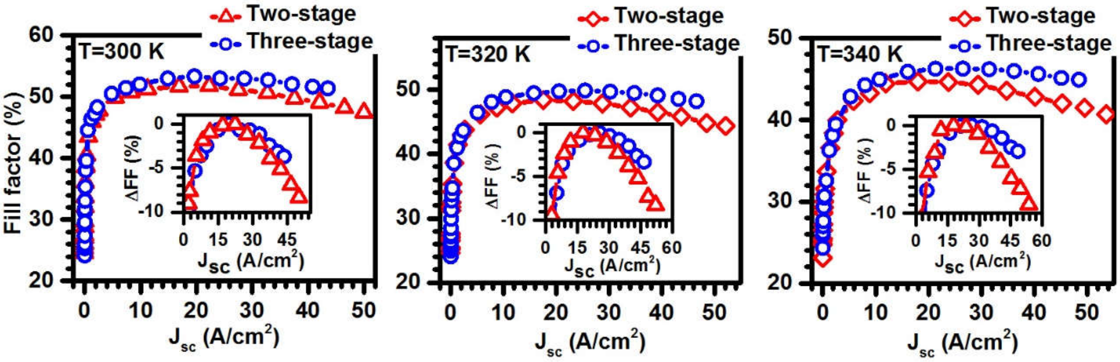

Figure 7-7: Device fill factor *vs*. J_{sc} for representative 200×200 μm² devices from two- and three-stage wafers at T=300-340 K. Insets show ΔFF for the same devices at different short-circuit currents. Two- stage device exhibited sharper decrease (compared to the three-stage device) in fill factor at high illumination levels.

7.2.3.3.2 Efficiency

The most useful metric to compare the ultimate performance of different ICTPV structures is the device conversion efficiency. Conversion efficiency is defined as the ratio of the maximum photovoltaic power (*MPP*) ($V_{oc}.I_{sc}$.FF) to the total input power received by the TPV cell. The main difficulty in assessment of the device conversion efficiency in our setup was the accurate determination of the radiant power received by the TPV cell. These difficulties are associated with the non-uniform and divergent beam of an edge-emitting laser. A simple approach to estimate the received optical power is to incorporate the relation between the device EQE (at the laser emission wavelength) and measured photocurrent to estimate the incident power on the device surface. The received optical power by a TPV cell can be estimated by:

$$P_{inc} = \frac{1.24\, I_{ph}}{\lambda_{laser}\, EQE} \qquad (7-2)$$

where P_{inc}, I_{ph}, λ_{laser} are the received incident power, device photocurrent and the laser emission wavelength (in μm), respectively. Therefore, the device efficiency can be formulated as:

$$\eta = \frac{MPP}{P_{inc}} = \frac{\lambda_{laser}\, EQE.I_{sc}.V_{oc}.FF}{1.24\, I_{ph}} \qquad (7-3)$$

The plots of the device V_{oc}, maximum output power density, and efficiency *vs.* J_{sc} are presented in Figure 7-8 for both two- and three-stage devices at 300 K. The maximum conversion efficiency was 6.5% (9.6%) in two-stage (three-stage) ICTPV cells. These values are the highest conversion efficiencies so far obtained for ICTPVs at room temperature. Note that the conversion efficiency was ~48% higher in the three-stage devices compared to that of two-stage ICTPVs, which confirms the benefits of having more stages and a multiple-stage architecture in narrow bandgap TPV cells. Similar to the device FF, the device efficiency exhibited a slight roll over at higher illumination levels in both two- and three-stage devices. However, the efficiency decrease was lower in three-stage ICTPVs (1.1%) compared to that of two-stage devices (4.6%). Because the thermalization and below-bandgap losses are minimal when a closely matched laser (to TPV cell cutoff wavelength) is used for illumination, larger conversion efficiencies are expected by reducing the parasitic losses associated with the device shunt and series resistances in these TPV cells.

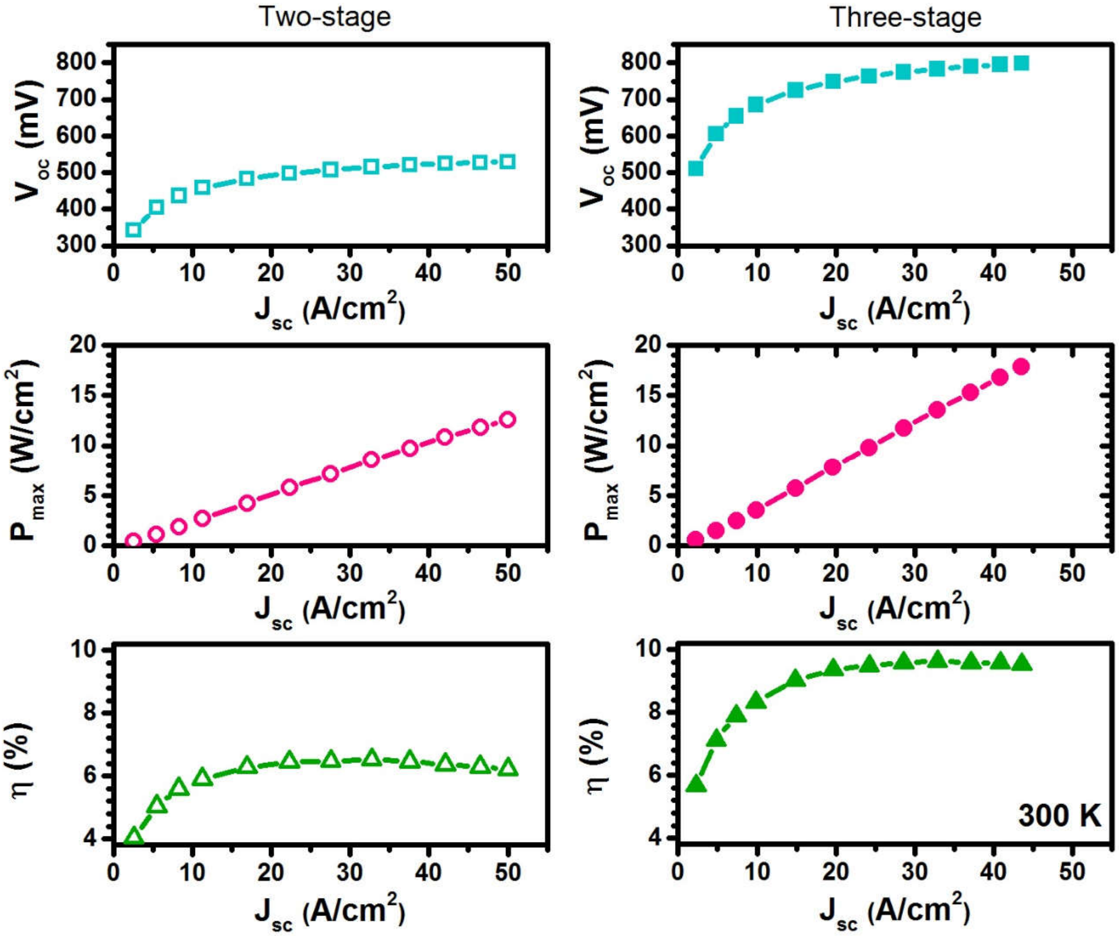

Figure 7-8: Open-circuit voltage (top panels), maximum output power density (middle panels), and conversion efficiency (bottom panels) as a function of short-circuit current density for representative 200×200 μm^2 devices from the two- and three-stage ICTPV wafers at 300 K.

7.2.3.4 Shunt and series resistance

7.2.3.4.1 Series resistance

Parasitic resistances, especially series resistance, are a detrimental factor on the performance of concentrated photovoltaic cells and TPVs. This is mainly associated with Ohmic losses that are proportional to the square of the device current. As such, high currents (which are typical in TPV cells) exacerbate the Ohmic losses and reduce the device efficiency. Various numerical and empirical techniques have been developed to extract the device shunt and series resistance in solar cells [6]. Among all, the method of *Suns*-V_{oc} [7, 8] is the most versatile, convenient and yet reliable approach. This method is applicable to any type of photovoltaic cells regardless of their series resistance value. The *Suns*-V_{oc} technique is a refined version of an earlier approach that was first proposed by Swanson in 1960 and was later published by Wolf and Rauschenbach in 1963 [9].

Under open-circuit condition, the device *I*-*V* is written as:

$$I_{ph} = I_o\left(exp\left[{}^{qV_{oc}}/_{nk_BT}\right] - 1\right) + \frac{V_{oc}}{R_{sh}} \qquad (7-4)$$

where I_0, q, V_{oc}, n, k_{B}, T and R_{sh} are saturation current, electronic charge, open-circuit voltage, ideality factor, Boltzmann constant, device absolute temperature and shunt resistance, respectively. As can be seen in the above equation, the device V_{oc} is not affected by the series resistance. A plot of I_{ph}-V_{oc} that has been constructed using different light illumination levels represents the device *I*-*V* if the series resistance was removed. Moreover, a comparative analysis of the device measured *I*-*V* versus the constructed I_{ph}-V_{oc} curve reveals the device series resistance. Albeit, this method is only applicable to cells with sufficiently large shunt resistance or at high illumination levels where the shunt resistance influence is minimal. Since the influence of the device series resistance on its J_{sc} becomes substantial at high illumination levels, the device J_{sc} is not an accurate measure of the device photocurrent under this condition and significantly underestimates the device photocurrent. For this reason, care must be taken in use of

Wolf and Rauschenbach method in cells with large series resistance or at high illumination conditions. This issue has been resolved in *Suns*-V_{oc} technique, where a calibrated solar cell with low series resistance is utilized to calibrate the incident power falling on the device under test. Figure 7-9 shows a commercial *Suns*-V_{oc} apparatus made by Sinton instruments. In this apparatus, a halogen lamp is used as the light source and the light intensity from this lamp exponentially decays with a time constant which is long enough to ensure a semi-equilibrium condition in the solar cell under test. At each power level (measured by the calibrated cell) the device V_{oc} is recorded and a plot of V_{oc} versus illumination power is generated. It is assumed that the device photocurrent is linearly proportional to the incident power and superposition theorem is applicable. This curve can be further processed to generate a so-called implied *I-V* curve.

Figure 7-9: A commercial *Suns*-V_{oc} apparatus manufactured by Sinton instruments. Image from: http://sintoninstruments.com

According to the superposition theorem, as long as a linear relation between the device photocurrent and the incident power is ensured, an implied *I-V* curve can be formed using the following equation [8]:

$$I_t = I_{sc}(1 - P_n) \qquad (7-5)$$

Here, I_t denotes the implied terminal current at each V_{oc} and P_n is the incident power normalized to one sun. The concept of *Suns*-V_{oc} and the overlaid implied and measured *I-V* curves are shown in Figure 7-10. The main drawback of this method is the difficulty in determination of the device I_{sc}. Typically, I_{sc} is assumed or calculated from the theoretical modeling of the cell. Because of the voltage drop on the device series resistance (R_s), the diffusion current term, $I_o\left(exp\left[{q(V - R_s I)}/{nk_B T}\right] - 1\right)$, in diode equation equals to zero at a negative terminal voltage rather than zero voltage. This is the reason behind the discrepancy between the device I_{sc} and I_{ph}, however the device *I-V* eventually exhibits a flat region, where the terminal current is equal to the device I_{ph}. As

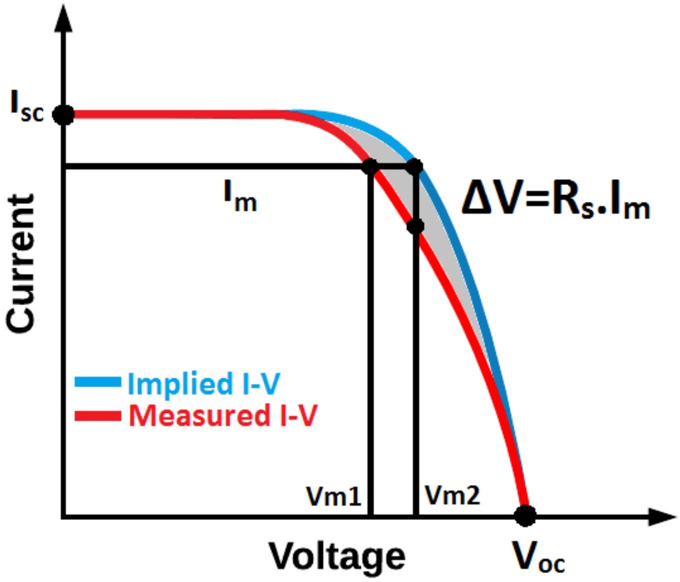

Figure 7-10: Schematic drawing of the overlaid plot of the device measured *I-V* to the implied *I-V* curve. The difference between the two curves is caused by the device series resistance.

can be inferred from Equation 7-4, the terminal voltage equals to the voltage drop on the series resistance (V_m=R_s.I) and the device voltage (V_D) approaches zero at a certain reverse bias. At this point, the exponential term in the diode equation vanishes and the diffusion current approaches the saturation value (I_0) with further reverse bias. Because I_{ph} is orders of magnitude larger than I_0 in a practical cell, the device *I-V* curve exhibits a negligible change with further reverse bias of the device and the terminal current represents the device I_{ph}.

From Figure 7-6, it is evident that the device series resistance has affected its *I-V* at high illumination levels in both two- and three-stage ICTPV cells. Therefore, J_{sc} is not an appropriate measure of the device photocurrent. The device I_{ph} was extracted from its *I-V* at reverse bias, where the *I-V* curve exhibited a saturated current. Additionally, Equation 7-5 was modified to incorporate the extracted photocurrents in the implied *I-V* curve:

$$I_t = I_{ph,max}\left(1 - \frac{I_{ph}}{I_{ph,max}}\right) \qquad (7-6)$$

here $I_{ph,max}$ is the maximum photocurrent achieved under different laser illumination levels and I_{ph} denotes the corresponding photocurrent at each illumination level. The implied terminal current from this equation along with the measured V_{oc} at different illuminations was used to construct the implied *I-V* curve. As such the influence of the device series resistance on its *I-V* characteristics is not present in the implied *I-V* curve.

Figure 7-11 shows the implied and measured *I-V* curves for representative devices from the two- and three-stage wafers at 300 K. The device series resistance decreased by raising the device temperature in both two- and three-stage ICTPV cells. For example, R_s was 9.27 Ω (12.14 Ω) in two-stage (three-stage device) at 300 K and decreased to 8.67 Ω (11.09 Ω) at 340 K. The extracted series resistances are also provided in Tables 7-1 and 7-2 for 300-340 K. Note that R_s was larger for devices from the three-stage wafer compared to two-stage devices at all temperatures. This observation was attributed to larger bulk series resistance (originated from the extra absorber in the three-stage device) and possible resistivity (due to energy level

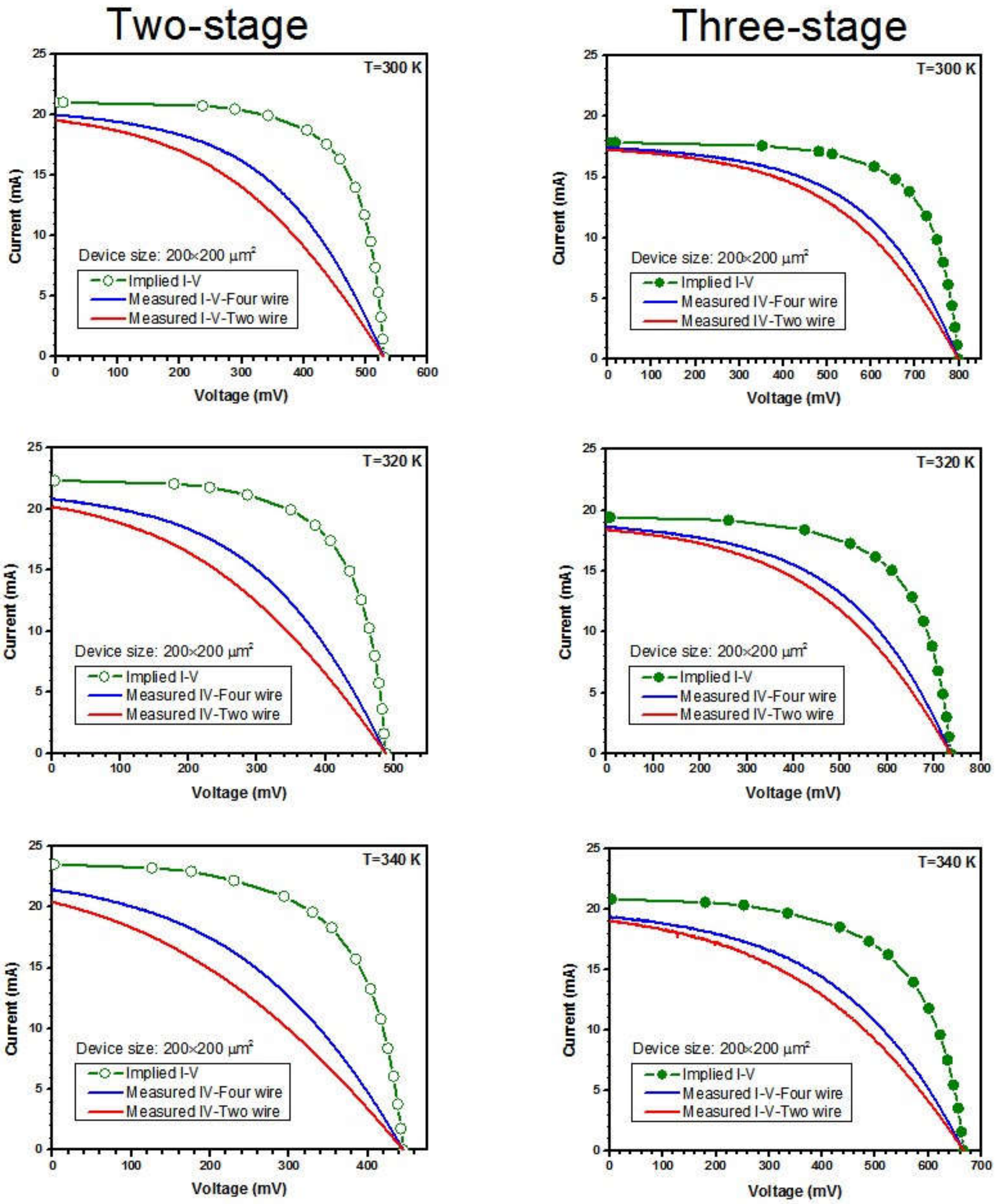

Figure 7-11: The implied and measured *I-V* curves for two- and three-stage ICTPV devices for 300-340 K. The device *I-V* curves were measured using both two- and four-wire setups.

misalignments in the device band structure) in carrier transport across stages as was also speculated from the bias dependent response in both wafers (see Figure 4-8).

7.2.3.4.2 Shunt resistance

Similar to the device series resistance, various fitting and experimental methods have been reported [6] to extract the device shunt resistance. However, the uncertainty involved in the fitting of various parameters of the device *I-V* may produce misleading fitting results and requires careful consideration. Here, we follow a simple approach presented in [6] for the extraction of the device shunt resistance.

As stated in the previous section, the device *I-V* can be modeled by equation 7-4 under open-circuit condition. The exponential term in this equation becomes negligible at very low light illumination levels and the device *I-V* is simplified to:

$$I_{ph} = \frac{V_{oc}}{R_{sh}} \qquad (7-7)$$

From this equation, a linear relation exists between the device photocurrent and the open-circuit voltage at low light intensities. Therefore, the slope of the linear fit represents the device shunt resistance. Moreover, because of low illumination levels the device series resistance has negligible influence on the device *I-V* and it is safe to assume I_{ph}=I_{sc}. Figure 7-12 shows the plots of V_{oc} *vs*. I_{sc} for representative devices from the two- and three-stage ICTPV cells under low illumination levels at 300 K. As can be seen from these curves, a linear relation exists between the device I_{sc} and V_{oc}, where the slope of the linear curve is the device shunt resistance. Shunt resistance for representative devices from the two wafers is also presented in Tables 7-1 and 7-2. For a 200×200 μm^2 device, the R_{sh} was 5.0 kΩ and 9.0 kΩ in two- and three-stage devices at

300 K, respectively. The device shunt resistance decreased by increasing the device temperature in both wafers, however, R_{sh} was larger in three-stage devices compared to two-stage TPV cells at all the measurement temperature and for all different mesa sizes. A detailed study of the influence of the device size and temperature on its bulk resistance and sidewall resistivity was provided in Chapter 4.

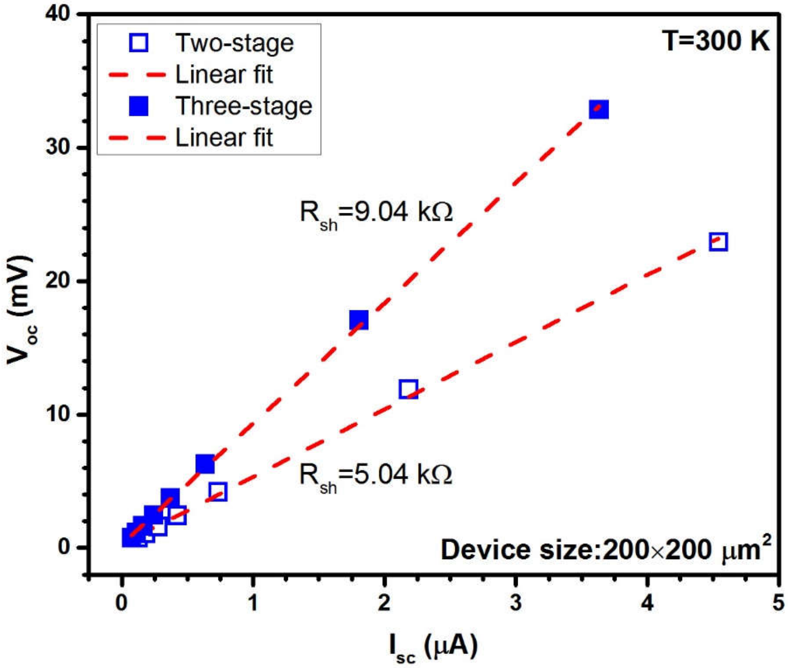

Figure 7-12: Plots of I_{sc}-V_{oc} for representative two- and three-stage ICTPV devices at 300K. The slope of the linear fit lines represents the device shunt resistance. R_{sh} was larger in three-stage devices compared to two-stage devices at all the measurement temperatures.

7.3 Narrow-bandgap interband cascade thermophotovoltaic devices with bandgap of 0.25 eV

7.3.1 Motivation and background

As discussed in Chapter 1, most of the research on TPV cells and systems has been devoted to GaInAsSb/GaSb and InGaAsP/InP material systems [10-17] with cell bandgaps of >0.5 eV. Because of the device bandgap, the radiant photons with energies less than 0.5 eV contribute to the below bandgap losses and their energy cannot be harvested. When the heat source temperature, with a blackbody-type radiation pattern, falls in 1000-2000 K range, based on the theory of detailed balance limit [18, 19] the optimum device bandgap for energy conversion lies between 0.2-0.4 eV (see section 1.4.2). This temperature range is important from a practical point of view because heaters and selective emitters will have simpler design and fabrication process, extended lifetime and lower gas emission compared to TPV systems operating with higher heat source temperatures. In fact, it is beneficial to hold the emitter at as low a temperature as possible to avoid overheating of the TPV cell when it is placed in close proximity to the emitter. This is of particular importance for micron-gap configurations [20, 21], where the enhanced radiative transfer between hot and cold surfaces is achieved by a micron-gap (about the radiation wavelength) distance.

To convert the long-wavelength IR radiation narrow-bandgap InAsSbP alloys have been explored for TPV cells with limited success [10]. The longest cutoff wavelengths reported in the literature are in the range 4.0-4.5 µm (E_g~0.3 eV) with an open-circuit voltage of 28 mV at room temperature [2]. Most recently, an open-circuit voltage of 60 mV was achieved in InAs-based TPV cells with a cutoff wavelength of ~3.9 μm at room temperature [22].

The main challenges associated with narrow bandgap TPV cells are related to the high carrier concentration and defect density in these semiconductors. These issues result in a significantly reduced diffusion lengths and poor collection of photo-generated carriers, as well as large dark and leakage currents. These factors lead to a very low open-circuit voltage for narrow-bandgap TPV devices. However, the limited collection of photo-generated carriers due to short diffusion lengths can be mitigated by utilizing interband cascade (IC) structures [23]. The next sections of this chapter discuss narrow-bandgap ICTPV cells (with >5 μm cutoff wavelength) that operate at room temperature and above with a high open-circuit voltage (~0.65 V at 300 K).

7.3.2 Device structure, growth, and fabrication

The ICTPV structure presented in this section had seven identical cascade stages. Each stage was composed of a 33-period InAs/GaSb (19/27 Å) type-II superlattice (SL) sandwiched between an AlSb/GaSb quantum well (QW) electron barrier and an InAs/Al(In)Sb QW hole barrier, as shown in Figure 7-13. These ICTPV devices were grown by MBE on a (001) GaSb substrate at Sandia National Laboratories. The detailed layer structure and low operating temperature (*e.g.*, 80 K) performance characteristics of circular mesa devices made from this wafer were reported in [24] . Here, we focus on the high operating temperature (300 and 340 K) performance of square mesa devices with mesa side dimensions ranging from 0.2 to 1.0 mm.

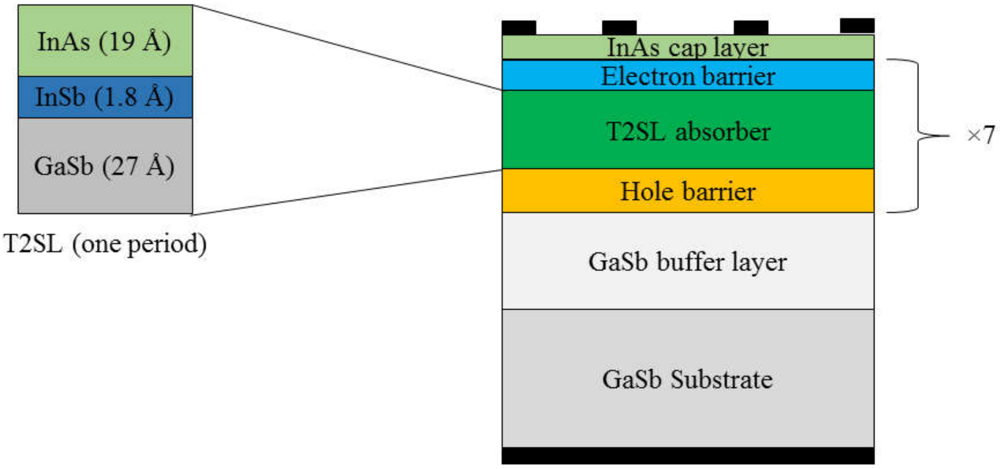

Figure 7-13: Schematic structure of the seven-stage narrow-bandgap ICTPV cells. Absorbers were identical in all stages and had similar absorber thickness of ~158 nm.

7.3.3 Device performance

7.3.3.1 Quantum efficiency

The zero-bias particle conversion efficiency (PCE) for a representative ICTPV device from this wafer at 300 and 340 K is shown in Figure. 7-14. Here, PCE is defined as the total number of electrons generated and collected in any stage per incident photon. The cutoff wavelength for this device was ~5 µm at 300 K and ~5.2 µm at 340 K, corresponding to bandgaps of 0.25 eV and 0.24 eV, respectively. The inset of Figure. 7-14 shows the electroluminescence (EL) spectra at these temperatures. The device bandgap obtained from EL spectra was in good agreement with the cutoff wavelength determined from PCE measurements. The observe dips in the EL and PCE spectra near 4.25 µm are caused by CO_2 absorption. The value of PCE is relatively low due to the ~31% reflection loss from the air/semiconductor interface (estimated based on their refractive indexes) and the rather short overall absorber thickness (~1.1 µm total from

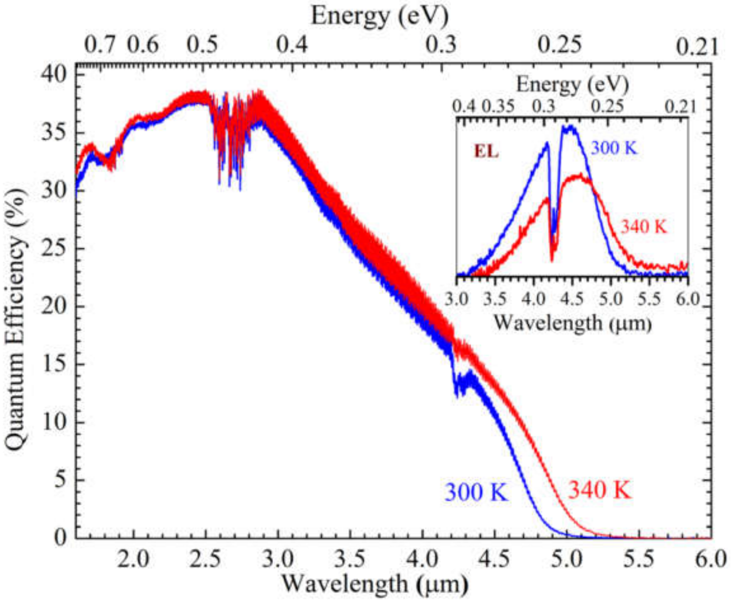

Figure 7-14: Particle conversion efficiency (PCE) of an ICTPV device at 300 and 340 K. The inset is the electroluminescence (EL) spectrum of an ICTPV device at 300 and 340 K.

the seven stages), which only absorbs part of incident light. These thin absorbers allowed a significant amount of incident light to be transmitted to and absorbed in the ~150 μm-thick substrate. A portion of that light is reflected back from the interface between the substrate and metal sub-mount as evidenced by the somewhat strong, high-frequency interference oscillations observed in PCE curves. The peak value of PCE was unchanged at different device temperatures, confirming the efficient photocarrier collection associated with the use of the short-discrete-absorber architecture in these ICTPV cells.

7.3.3.2 J-V characteristics of TPV devices under laser illumination

Similar to the setup used for shorter wavelength ICTPVs presented in section 7.2.3.1, two IC lasers with emission wavelengths of 3.3 μm and 4.3 μm were used to mimic a selective emitter. Under illumination of a 4.3 μm laser with the emission photon energy of ~0.29 eV slightly higher than the absorber bandgap, these ICTPV devices were able to achieve a high open-circuit voltage at RT and above. The intensity level from the laser on the TPV devices was similar to a concentrated solar source (up to ~190 suns) with a bandwidth of 20 to 100 nm depending on the laser injection current. Under the laser illumination (emission spectrum is shown in the inset of Figure 7-15) of 19 W/cm^2, the measured current density-voltage (*J*-*V*) curves for a 0.2×0.2 mm^2 device at 300 K and 340 K are shown in Figure 7-15. The open-circuit voltage was as high as 0.65 V (with J_{sc}=1.4 A/cm^2), which is larger than a single bandgap value (E_g/e~0.25 V), validating the successful operation of series-connected multiple stages with large output voltage. At 340 K, the open-circuit voltage was near 0.4 V with a cutoff wavelength ~5.2 μm (corresponding to a bandgap of 0.24 eV). Under the same illumination, the short-circuit current density J_{sc} was higher at 340 K due to the higher absorption coefficient at the same wavelength (4.3 μm) associated with bandgap narrowing effect.

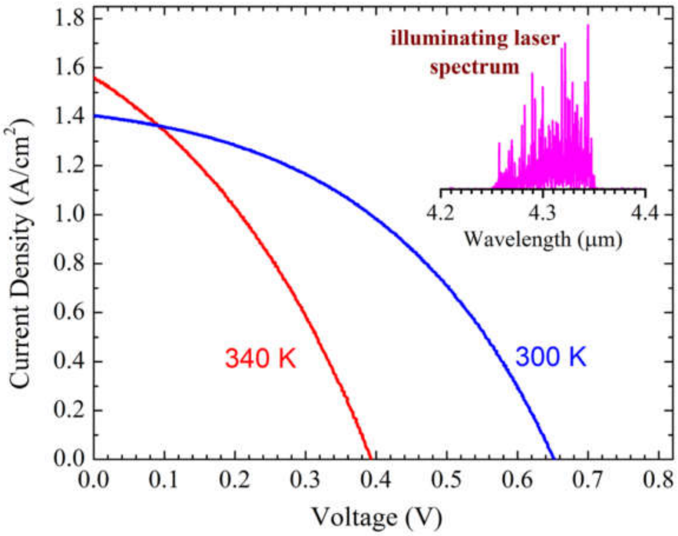

Figure 7-15: Current density–voltage (*J*-*V*) characteristics of a 200×200 μm^2 device at 300 and 340 K under illumination by an IC laser with emission wavelength near 4.3 μm (inset).

By varying the laser output power, we also obtained the relationship between J_{sc} and V_{oc} for devices with different mesa sizes at 300 and 340 K with different illumination wavelengths. The lasing wavelength of the 4.3 μm IC laser was tuned from 4.2 to 4.6 μm by changing its operating temperature. Results were compared with J_{sc}-V_{oc} relationship obtained under illumination by another IC laser with a higher emission energy (near 3.33 μm). We found that the J_{sc}-V_{oc} relationship (Figure 7-16) mainly depended on the TPV device operating temperature and was independent of the laser emission wavelength. The observed variations in the J_{sc}-V_{oc} curve for different size devices was attributed to variations in the surface recombination velocity (passivation quality and sidewall profile) and bulk defect density for different devices introduced by the non-uniformities in wafer and device fabrication. Since the measured J_{sc}-V_{oc} curves are essentially a reflection of intrinsic properties of ICTPV devices, overall, all the devices showed consistent quality and performance. For the ideal diffusion-limited case, a diode-like equation can be used to describe the device J-V [25]:

$$J = J_0(exp(qV/N_s k_B T) - 1) \tag{7-8}$$

where q is the electron charge, $k_B T$ is the thermal energy at temperature T, N_s is the number of cascade stages, and J_0 is the saturation current density related to carrier concentration and diffusion length [25]. Considering approximately equal voltage and the same J_0 across each stage and adding an empirical ideality factor n for possible deviations from the ideal diffusion-limited case that is described by Equation (7-8), the open-circuit voltage can be expressed as:

$$V_{oc} = n\frac{N_c kT}{e}\ln\left(\frac{J_{sc}}{J_0}+1\right). \tag{7-9}$$

Applying Equation (7-9) to fit the data presented in Figure 7-16 for a 0.2×0.2-mm^2 device, we found an excellent agreement for J_0=88.5 mA/cm^2, n=1.28, and J_0= 410 mA/cm^2, n=1.22 for 300 and 340 K, respectively. The fit results verify the expected increase of J_0 at higher temperatures attributed to the increased carriers, while the ideality factor n is close to the value for the ideal case (n=1) and is nearly unchanged with the temperature. How the values of J_0 and n are related to the intrinsic material and structural properties of ICIPs requires further investigations and research.

The device fill factor and the maximum output power density $P_{\max}$ are shown in Figure 7-17 for two ICTPV devices with side dimensions of 0.2 mm and 0.5 mm at 300 and 340 K for laser illumination near 4.3 and 3.3 μm. Both FF and $P_{\max}$ increased with the short-circuit current density. The highest FF was 43% at 300 K under laser

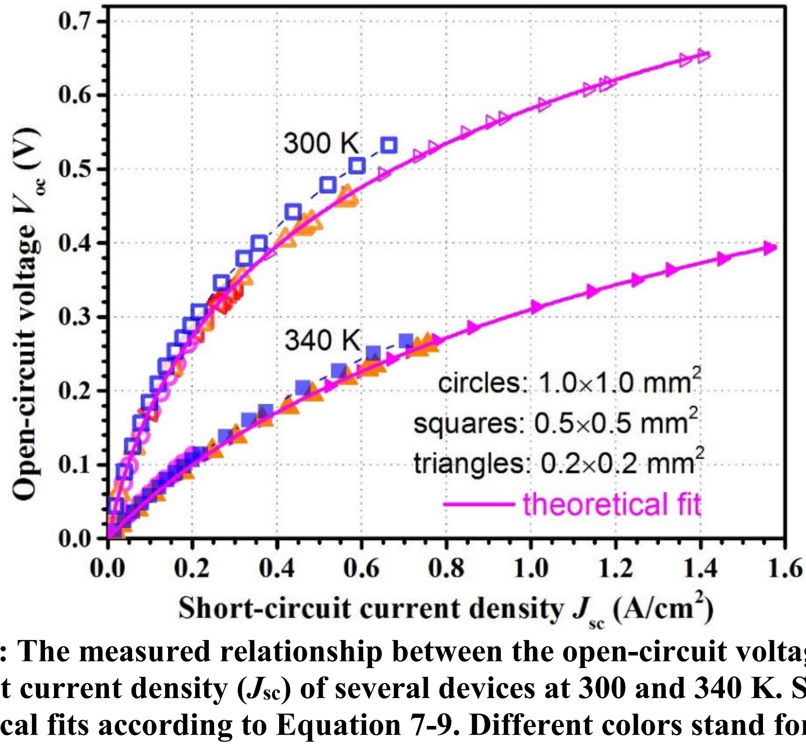

Figure 7-16: The measured relationship between the open-circuit voltage V_{oc} and short-circuit current density (J_{sc}) of several devices at 300 and 340 K. Solid lines are theoretical fits according to Equation 7-9. Different colors stand for different illumination wavelengths from the two IC lasers.

illumination near 4.3 μm, which is smaller than a typical value (60-70%) for TPV cells with bandgaps of 0.5-0.6 eV [10-16]. This relatively low FF is partially due to the much narrower bandgap (<0.25 eV) and low PCE (~15% at 4.3 μm) with a thin total absorber layer (~1.1 μm). For the same reasons, P_{max} was limited to 395 mW/cm^2 at an incident laser power density of 18.9 W/cm^2 (extracted from J_{sc} and EQE at 4.3 μm), resulting in a power conversion efficiency of 2.1%. The conversion efficiencies as a function of the incident power density are plotted in the inset of Figure 7-17 for the 0.2 mm device at 300 K and 340 K. The PCE, FF, and power conversion efficiency should be much higher once an antireflection coating is used, and more stages are incorporated into ICTPV devices along with photocurrent matching between the cascade stages. The current matching can be achieved by adjusting the thicknesses of individual absorbers based on either estimated or measured absorption coefficients. Thus a power efficiency

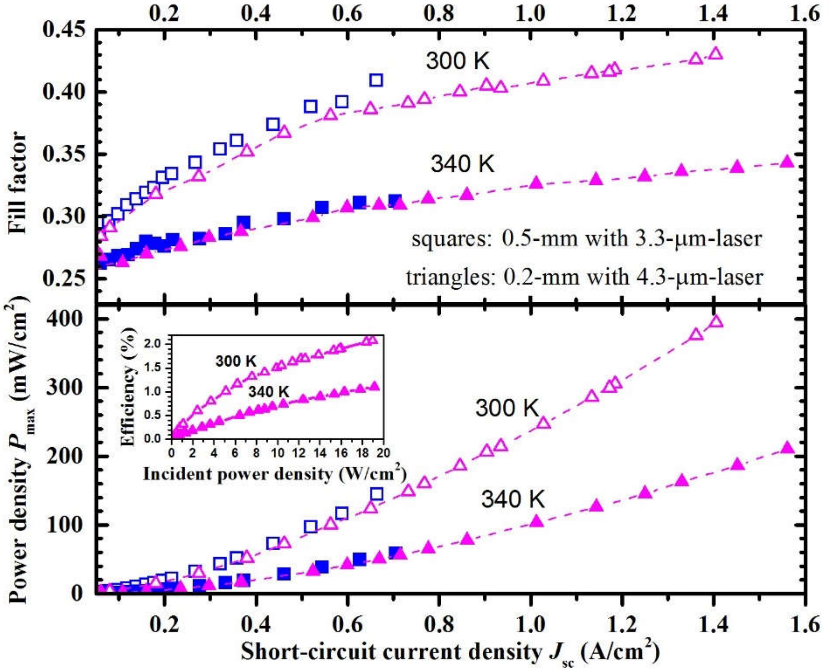

Figure 7-17: Fill factor and maximum output power density P_{max} *vs*. short-circuit current density J_{sc} for two square mesa ICTPV devices with side dimensions of 0.2 and 0.5 mm at 300 and 340 K illuminated by IC lasers near 4.3 and 3.3 μm. The inset is the power conversion efficiency of the 0.2 mm device at 300 and 340 K.

exceeding 10% could be reached with these improvements (*e.g.*, PCE is raised from 15% to 80%), which would be remarkable for low source temperature TPV systems at this level of maturity, operating at such a long wavelength and with modest light intensities. Nevertheless, to achieve higher than 10% power efficiencies advances in other aspects such as the reduction of contact resistance and dark current with improved material quality, device fabrication, as well as the optimization of device structure are required.

7.4 Summary and concluding remarks

In summary, two sets of narrow-bandgap (<0.5 eV) ICTPV devices were demonstrated at room temperature and above. The two- and three-stage TPV devices from the first set had a bandgap of ~0.4 eV at 300 K. The higher conversion efficiencies (up to 48%) in three-stage ICTPV devices for 300-340 K validates the advantages of a multiple-stage architecture with more stages at high temperatures. The other set had a bandgap of <0.25 eV at room temperature. The high open-circuit voltage (~0.65 V at 300 K) that exceeds the bandgap of an individual absorber also validates the advantages of ICTPV structures as the base for conversion cells in long-wavelength (low temperature heat sources) TPV systems. ICTPV devices are in their early stage of development and thus, with continued effort, significant advancements are expected in the future.

7.5 Bibliography

[1] M. G. Mauk and V. M. Andreev, "GaSb-related materials for TPV cells," *Semiconductor Science and Technology,* vol. 18, p. S191, 2003.

[2] K. J. Cheetham, P. J. Carrington, N. B. Cook, and A. Krier, "Low bandgap GaInAsSbP pentanary thermophotovoltaic diodes," *Solar Energy Materials and Solar Cells,* vol. 95, pp. 534-537, 2011.

[3] Y. Jiang, L. Li, R. Q. Yang, J. A. Gupta, G. C. Aers, E. Dupont*, et al.*, "Type-I interband cascade lasers near 3.2 μm," *Applied Physics Letters,* vol. 106, pp. 2-6, 2015.

[4] M. Meusel, R. Adelhelm, F. Dimroth, A. W. Bett, and W. Warta, "Spectral mismatch correction and spectrometric characterization of monolithic III–V multi-junction solar cells," *Progress in Photovoltaics: Research and Applications,* vol. 10, pp. 243-255, 2002.

[5] W. E. McMahon, K. E. Emery, D. J. Friedman, L. Ottoson, M. S. Young, J. S. Ward*, et al.*, "Fill factor as a probe of current-matching for GaInP2/GaAs tandem cells in a concentrator system during outdoor operation," *Progress in Photovoltaics: Research and Applications,* vol. 16, pp. 213-224, 2008.

[6] D. K. Schroder, *Semiconductor material and device characterization*, John Wiley & Sons, 2006.

[7] R. A. Sinton, "Possibilities for process-control monitoring of electronic material properties during solar-cell manufacture," in *Proceedings of 9th Workshop on Crystalline Silicon Solar Cell Materials and Processes*, pp. 67-73, 1999.

[8] R. Sinton and A. Cuevas, "A quasi-steady-state open-circuit voltage method for solar cell characterization," in *Proceedings of the 16th European Photovoltaic Solar Energy Conference*, 2000.

[9] M. Wolf and H. Rauschenbach, "Series resistance effects on solar cell measurements," *Advanced Energy Conversion,* vol. 3, pp. 455-479, 1963.

[10] M. G. Mauk, "Survey of thermophotovoltaic (TPV) devices," in *Mid-infrared Semiconductor Optoelectronics*, Springer, pp. 673-738, 2006.

[11] T. Bauer, *Thermophotovoltaics: basic principles and critical aspects of system design*, Springer Science & Business Media, 2011.

[12] A. Datas and C. Algora, "Global optimization of solar thermophotovoltaic systems," *Progress in Photovoltaics: Research and Applications,* vol. 21, pp. 1040-1055, 2013.

[13] T. Coutts, "A review of progress in thermophotovoltaic generation of electricity," *Renewable and Sustainable Energy Reviews,* vol. 3, pp. 77-184, 1999.

[14] C. Wang, H. Choi, S. Ransom, G. Charache, L. Danielson, and D. DePoy, "High-quantum-efficiency 0.5 eV GaInAsSb/GaSb thermophotovoltaic devices," *Applied Physics Letters,* vol. 75, pp. 1305-1307, 1999.

[15] C. Wang, R. Huang, D. Shiau, M. Connors, P. Murphy, P. O'BRIEN*, et al.*, "Monolithically series-interconnected GalnAsSb/AlGaAsSb/GaSb thermophotovoltaic devices with an internal backsurface reflector formed by wafer bonding," *Applied Physics Letters,* vol. 83, pp. 1286-1288, 2003.

[16] R. K. Huang, R. J. Ram, M. J. Manfra, M. K. Connors, L. J. Missaggia, and G. W. Turner, "Heterojunction thermophotovoltaic devices with high voltage factor," *Journal of Applied Physics,* vol. 101, p. 6102, 2007.

[17] R. Tuley and R. Nicholas, "Band gap dependent thermophotovoltaic device performance using the InGaAs and InGaAsP material system," *Journal of Applied Physics,* vol. 108, p. 084516, 2010.

[18] W. Shockley and H. J. Queisser, "Detailed balance limit of efficiency of p-n junction solar cells," *Journal of Applied Physics,* vol. 32, pp. 510-519, 1961.

[19] T. J. Coutts and J. S. Ward, "Thermophotovoltaic and photovoltaic conversion at high-flux densities," *IEEE Transactions on Electron Devices,* vol. 46, pp. 2145-2153, 1999.

[20] R. DiMatteo, P. Greiff, S. Finberg, K. Young-Waithe, H. Choy, M. Masaki*, et al.*, "Micron-gap thermophotovoltaics (MTPV)," in *AIP Conference Proceedings*, pp. 232-240, 2003.

[21] W. R. Chan, P. Bermel, R. C. Pilawa-Podgurski, C. H. Marton, K. F. Jensen, J. J. Senkevich*, et al.*, "Toward high-energy-density, high-efficiency, and moderate-temperature chip-scale thermophotovoltaics," *Proceedings of the National Academy of Sciences USA,* vol. 110, pp. 5309-14, Apr 2 2013.

[22] A. Krier, M. Yin, A. R. J. Marshall, and S. E. Krier, "Low Bandgap InAs-Based Thermophotovoltaic Cells for Heat-Electricity Conversion," *Journal of Electronic Materials,* vol. 45, pp. 2826-2830, 2016.

[23] R. Q. Yang, Z. Tian, J. Klem, T. D. Mishima, M. B. Santos, and M. B. Johnson, "Interband cascade photovoltaic devices," *Applied Physics Letters,* vol. 96, p. 063504, 2010.

[24] R. T. Hinkey, Z.-B. Tian, S. S. S. Rassel, R. Q. Yang, J. F. Klem, and M. B. Johnson, "Interband cascade photovoltaic devices for conversion of mid-IR radiation," *IEEE Journal of Photovoltaics,* vol. 3, pp. 745-752, 2013.

[25] R. T. Hinkey and R. Q. Yang, "Theory of multiple-stage interband photovoltaic devices and ultimate performance limit comparison of multiple-stage and single-stage interband infrared detectors," *Journal of Applied Physics,* vol. 114, p. 104506, 2013.

Chapter 8: Concluding remarks and research perspective for interband cascade devices

8.1 Summary

Interband cascade (IC) optoelectronic devices include IC lasers (ICLs), IC infrared photodetectors (ICIPs), and IC thermophotovoltaic (ICTPV) devices. In this family of infrared devices, a multiple-stage architecture is employed to enhance the device performance over that of conventional single-stage devices. It is through this unique multiple-stage structure and type-II broken-gap band alignments that ICLs have the record low threshold current density [1] among different types of mid-IR lasers at room temperature. Moreover, ICIPs, owing to their cascade structure and reliance on interband transitions, have shown great promise to become the technology of choice for high-operating-temperature (HOT) and high-speed detectors. Similarly, ICTPV devices, with multiple absorbers that are individually shorter than the minority carrier diffusion length, result in enhanced collection efficiencies, high open-circuit voltages and conversion efficiencies over single-stage TPV cells with thick absorbers.

While ICLs have been investigated for the past 20 years, ICIPs and ICTPV devices are in their early phase of research. The main purpose of the current work was to investigate the projected enhancements such as higher detectivities, higher operating temperature, and high-frequency response for these devices over conventional single-stage IR detectors and TPV cells.

In this dissertation, after a detailed overview on the current status of different technologies for IR detectors and TPV systems, the theory of IC devices, their operation principles and design guidelines, are discussed. As well, detailed discussions on the conditions under which a multiple-stage device has superior performance over conventional designs are presented. The other chapters are devoted to the design and characterization of ICIPs for different IR bands, monolithically integrated mid-IR ICLs and ICIPs, and ICTPV devices.

To investigate the performance of long-wavelength and very long-wavelength ICIPs, three sets of devices with type-II InAs/GaSb superlattice absorbers were designed and grown by MBE. For the first set, the 100% cutoff wavelength of detectors was 6.2 μm at 78 K, extending to 8 μm at 300 K. At T=125 K and higher temperatures we were able to observe the benefits of the three-stage detector over the two-stage device in terms of lower dark current and higher detectivity. We conjecture that imperfections associated with device growth and fabrication had a substantial effect on the low-temperature device performance and were responsible for unexpected behavior at these temperatures. It is also found that the zero-bias photo-response increased with temperatures up to 200 K, which was indicative of an efficient collection of photogenerated carriers at high temperatures. These detectors were able to operate at temperatures up to 340 K with a cutoff wavelength longer than 8 μm. A second set of detectors included two-stage LWIR ICIPs with engineered interfaces in the SL absorbers. These detectors were able to operate at high temperatures (up to 250 K) with an extended cutoff wavelength of ~12 μm. At 78 K, these LWIR detectors have a bias-independent photocurrent, with an R_0A of 115 Ω.cm^2. This corresponds to a Johnson-noise-limited D^* of 3.7×10^{10} cm.Hz$^{1/2}$/W at 8.0 μm. Finally, the last set had 100% cutoff wavelengths of 16.0 μm at 78 K. The very-long-wavelength infrared (VLWIR) detectors were able to operate at temperatures up to 143 K. Relatively high dark current densities were observed from these VLWIR detectors. This was attributed to the very narrow bandgap and possibly to defects in the materials. In addition, the photo-response of these detectors was strongly dependent on the bias, indicating that further research and device optimization are necessary. Overall, these results demonstrate the advantage of the interband cascade structures to achieve high-temperature operation for long-wave infrared photodetectors.

In Chapter 4, high temperature operation (250-340 K) of short-wavelength ICIPs with InAs/GaSb/$Al_{0.2}In_{0.8}Sb$/GaSb superlattice absorbers has been demonstrated with a 50% cutoff wavelength of 2.9 μm at 300 K. Two ICIP structures, one with two and the other with three stages, were designed and grown to explore this multiple-stage architecture. At λ=2.1 μm, the two- and three-stage ICIPs had Johnson-noise-limited detectivities of 5.1×10^9 and 5.8×10^9 cm·$Hz^{1/2}$/W, respectively at 300 K. The better device performance of the three-stage ICIP over the two-stage ICIP confirmed the advantage of more stages for the cascade architecture. An Arrhenius activation energy of 450 meV is extracted for the bulk resistance-area product, which indicates the dominance of the diffusion current at these high temperatures.

The high-frequency operation of a mid-IR interband cascade system is discussed in Chapter 5. This IC optoelectronic system consists of a type-I ICL and an uncooled ICIP. The 3-dB bandwidth of this system under direct frequency modulation was ~850 MHz. A circuit model was developed to analyze the high-frequency characteristics. The extracted 3-dB bandwidth for an uncooled ICIP was ~1.3 GHz, signifying the great potential of interband cascade structures for high-speed applications. The Johnson-noise-limited detectivity of these ICIPs exceeded 10^9 cm·Hz$^{1/2}$/W at 300 K. These results validate the advantage of ICIPs to achieve both high speed and sensitivity at high temperatures.

Next, in Chapter 6, the first demonstration of a monolithically integrated mid-IR interband cascade (IC) laser and photodetector operating at room temperature is reported. The base structure for the integrated laser and detector is a six-stage type-I IC laser with GaInAsSb quantum well active regions. The laser/detector pair was defined using focused ion beam milling. The laser section lased in cw mode with an emission wavelength of ~3.1 µm at 20 ˚C and top-illuminated photodetectors fabricated from the same wafer had Johnson-noise-limited detectivity of 1.05×10^9 cm.Hz$^{1/2}$/W at this wavelength and temperature. Under the same conditions, the detectivity for the edge illumination configuration for the monolithically integrated laser/photodetector pairs is projected to be as high as 1.85×10^{10} cm.Hz$^{1/2}$/W, as supported by experimentally observed high photocurrent and open-circuit voltage. These high-performance characteristics for monolithically integrated IC devices show great promise for on-chip integration of mid-IR photonic devices for miniaturized sensors and on-chip optical communication systems.

Two sets of ICTPV devices were designed and grown to investigate the influence of the number of stages and thickness of absorbers on device performance. The devices from a first batch of TPV cells had a cutoff wavelength of ~2.9 µm at room temperature. Two-stage (three-stage) photocurrent matched devices from this set had open-circuit voltage of 530 mV (800 mV) and efficiency of 6.5% (9.6%) at 300 K. These experimental results reveal that the three-stage devices had higher efficiencies and open-circuit voltage over the two-stage TPV devices and validate the benefits of more stages for this IC device architecture. A second batch consisted of narrower bandgap (<0.25 eV) TPV devices. These TPV devices can achieve a high open-circuit voltage (~0.65 V at 300 K), which significantly exceeds the single bandgap limited value. This work demonstrates the capabilities and advantages of ICTPV devices designed to effectively convert long wavelength (>5 μm) infrared photons from relatively low-temperature radiation sources (<1,000 K) into electricity. Detailed characteristics of these TPV devices were presented and discussed in Chapter 7.

8.2 Future works

Since ICIPs and ICTPV devices are in their early stage of development, some of their properties are not fully understood and require further investigation. Below, some possible future research routes are briefly discussed in the hope that better understanding of the device physics will lead to an enhanced device performance.

As discussed in Chapter 2, when αL_e is small (*e.g.,* <0.5), multiple-stage detectors have a significant enhancement of the detectivity over single-stage detectors. This means that an accurate knowledge of the absorption coefficient and diffusion length is critical for optimization of the ICIPs and ICTPV devices structure (*e.g.*, optimum number of stages and absorber thicknesses). While there has been some work on the measurement and modeling of the absorption coefficient of type-II SL structures [2-4] most of these works are not comprehensive and do not cover a wide range of temperatures. Furthermore, because the device absorption coefficient is sensitive to the SL structure and its constituent layers [4], the data for a specific SL structure does not represent the absorption coefficient for all structures. Direct measurements of the absorption spectrum for specific type-II SL structures, similar to the study presented in section 5.3.2, are crucial for evaluation of the absorption coefficient for type-II SL structures in different IR bands.

Similarly, there has been limited work on the study of the diffusion length and carrier lifetime in T2SLs and it has mainly been carried out at low temperatures [5-9]. Similar studies to those presented in section 4.3.2 are required to extract the device diffusion length in the different IR bands and for different SL configurations. As an alternative to this approach, the measured quantum efficiencies can be used to fit the related equation(s) to find the device diffusion length.

The experimental investigation of high-frequency operation of ICIPs shows gigahertz bandwidth for these devices. It is expected that by better device packaging the device frequency response can be further enhanced for demanding applications such as free-space optical (FSO) communications and heterodyne detection. While a preliminary FSO link (detector-to-laser distance of 1 m) has been demonstrated with current ICIPs and ICLs, because of high detectivity of ICIPs at room temperature, further enhancements in the system packaging will result in long-distance (*e.g.*, building to building) FSO communication systems in mid- and long-wave IR bands. Also, the measured 3-dB bandwidths of ICIPs can be used to extract the device diffusion length at different temperatures. How the frequency response of ICIPs changes with bias and temperature remains unexplored and is worth investigation.

In ICLDs, parameters such as the coupling efficiency between the laser and the detector sections require further investigation. Direct measurement of the device responsivity and the possible enhancement of the device detectivity compared to a top illumination configuration is of particular importance for future developments of ICLDs. Because the ICLD structure is similar to that of coupled-cavity lasers, single mode operation of ICLDs is expected by the incorporation of another slot in the device structure to control the mode selection.

The series and shunt resistance in ICTPV devices are far from optimum. Further work is required to improve the device fabrication and thereby reduce the sidewall leakage and series resistance. Direct measurements of the device contact resistance by methods such as transmission line method (TLM) and the post-fabrication annealing of the devices and its influence on the contact resistance need further investigation. Also, the nearly lattice-matched constant of 6.1-Å-material family provides great flexibility in realizing a multi-bandgap tandem TPV cell to achieve higher conversion efficiency.

The current theoretical model for ICIPs only considers diffusion processes, this model can be further improved by the introduction of other terms such as *g*-*r* and tunneling, which are usually important in narrow bandgap III-V semiconductors. These modifications can enhance the accuracy of the model to predict the device performance, particularly at low temperatures, where diffusion is not the dominant transport mechanism. Moreover, high intrinsic carrier concentrations at high temperatures in narrow bandgap semiconductors could counter the device doping. It is possible that holes start to become an important factor in the carrier transport. Therefore, a refined model that includes the hole transport in the device equations could enhance the accuracy of the theoretical models for ICIPs and ICTPV devices.

8.3 Bibliography

[1] L. Li, Y. Jiang, H. Ye, R. Q. Yang, T. D. Mishima, M. B. Santos*, et al.*, "Low-threshold InAs-based interband cascade lasers operating at high temperatures," *Applied Physics Letters,* vol. 106, p. 251102, 2015.

[2] B. Satpati, J. Rodriguez, A. Trampert, E. Tournié, A. Joullié, and P. Christol, "Interface analysis of InAs/GaSb superlattice grown by MBE," *Journal of Crystal Growth,* vol. 301, pp. 889-892, 2007.

[3] Y. Livneh, P. Klipstein, O. Klin, N. Snapi, S. Grossman, A. Glozman*, et al.*, "k·p model for the energy dispersions and absorption spectra of InAs/GaSb type-II superlattices," *Physical Review B,* vol. 86, p. 235311, 2012.

[4] Z. B. Tian, E. A. Plis, R. T. Hinkey, and S. Krishna, "Influence of composition in InAs/GaSb type-II superlattices on their optical properties," *Electronics Letters,* vol. 50, pp. 1733-1734, 2014.

[5] E. Aifer, J. Tischler, J. Warner, I. Vurgaftman, W. Bewley, J. Meyer*, et al.*, "W-structured type-II superlattice long-wave infrared photodiodes with high quantum efficiency," *Applied Physics Letters*, vol. 89, p. 053519, 2006.

[6] S. Mou, J. V. Li, and S. L. Chuang, "Quantum efficiency analysis of InAs–GaSb type-II superlattice photodiodes," *IEEE Journal of Quantum Electronics,* vol. 45, pp. 737-743, 2009.

[7] D. Donetsky, G. Belenky, S. Svensson, and S. Suchalkin, "Minority carrier lifetime in type-2 InAs-GaSb strained-layer superlattices and bulk HgCdTe materials," *Applied Physics Letters,* vol. 97, 2010.

[8] D. Wang, D. Donetsky, S. Jung, and G. Belenky, "Carrier lifetime measurements in long-wave infrared InAs/GaSb superlattices under low excitation conditions," *Journal of Electronic Materials,* vol. 41, pp. 3027-3030, 2012.

[9] L. Höglund, A. Soibel, D. Z. Ting, A. Khoshakhlagh, C. J. Hill, and S. D. Gunapala, "Minority carrier lifetime and photoluminescence studies of antimony-based superlattices," *in Proceedings of SPIE, Infrared Remote Sensing and Instrumentation XX*, vol. 8511, p. 851106, 2013.

Appendix A: List of publications

Refereed journal articles

1. L. Lei, L. Li, H. Ye, **H. Lotfi**, R. Q. Yang, M. B. Johnson, J. A. Massengale, T. D. Mishima, and M. B. Santos, "Long wavelength interband cascade infrared photodetectors operating at high temperatures," J. Appl. Phys, 120, 193102 (2016). http://dx.doi.org/10.1063/1.4967915

2. **H. Lotfi**, L. Li, S. M. S. Rassel, R. Q. Yang, C. J. Corrége, M. B. Johnson, P. R. Larson, and J. A. Gupta, "Monolithically integrated mid-IR interband cascade laser and photodetector operating at room temperature," Appl. Phys. Lett, 109, 151111 (2016). http://dx.doi.org/10.1063/1.4964837

3. L. Lei, L. Li, **H. Lotfi**, Y. Jiang, R. Q. Yang, M. B. Johnson, D. Lubyshev, Y. Qiu, J. M. Fastenau, and A. W. K. Liu, "Mid-wave interband cascade infrared photodetectors based on GaInAsSb absorbers," Semicond. Sci. Technol., 105014, 31 (2016). http://iopscience.iop.org/article/10.1088/0268-1242/31/10/105014/meta

4. **H. Lotfi**, L. Li, L. Lei, H. Ye, S. M. S. Rassel, Y. Jiang, R. Q. Yang, T. D. Mishima, M. B. Santos, J. A. Gupta, and M. B. Johnson, "High-frequency operation of a mid-infrared interband cascade system at room temperature," Appl. Phys. Lett, 108, 201101 (2016). http://dx.doi.org/10.1063/1.4950700

5. **H. Lotfi**, L. Li, L. Lei, R. Q. Yang, J. F. Klem, and M. B. Johnson, "Short-wavelength interband cascade infrared photodetectors operating above room temperature," J. Appl. Phys. 119, 023105 (2016). http://dx.doi.org/10.1063/1.4939961

6. H. Ye, L. Li, **H. Lotfi**, L. Lei, R. Q. Yang, J. C. Keay, T. D. Mishima, M. B. Santos, and M. B. Johnson, "Molecular beam epitaxy of interband cascade structures with InAs/GaSb superlattice absorbers for long-wavelength infrared detection," Semicond. Sci. Technol. 30, 105029 (2015). http://dx.doi.org/10.1088/0268-1242/30/10/105029

7. **H. Lotfi**, L. Lei, L. Li, R. Q. Yang, J. C. Keay, M. B. Johnson, Y. Qiu, D. Lubyshev, J. M. Fastenau, and A. W. K. Liu, "High-temperature operation of interband cascade infrared photodetectors with cutoff wavelengths near 8 μm," Opt. Eng. 54(6), 063103 (2015). http://opticalengineering.spiedigitallibrary.org/article.aspx?articleid=2330668

8. **H. Lotfi**, L. Li, H. Ye, R. T. Hinkey, L. Lei, R. Q. Yang, J. C. Keay, T. D. Mishima, M. B. Santos, and M. B. Johnson, "Interband cascade infrared photodetectors with long and very long cutoff wavelengths," Infrared Phys. Technol. 70, 162-167 (2015). http://dx.doi.org/10.1016/j.infrared.2014.08.017

9. H. Ye, **H. Lotfi**, L. Li, R. T. Hinkey, R. Q. Yang, L. Lei, J. C. Keay, M. B. Johnson, T. D. Mishima, and M. B. Santos, "Multistage interband cascade photovoltaic devices with a bandgap of 0.23 eV operating above room temperature," Chin. Sci. Bull., 59, 950-955 (2013). http://link.springer.com/article/10.1007/s11434-014-0144-6

10. **H. Lotfi**, R. T. Hinkey, L. Li, R. Q. Yang, J. F. Klem, and M. B. Johnson, "Narrow-bandgap photovoltaic devices operating at room temperature and above with high open-circuit voltage," Appl. Phys. Lett, 102, 211103 (2013). http://dx.doi.org/10.1063/1.4807938

Conference proceedings and presentations

1. **H. Lotfi**, S. M. S. Rassel, L. Li, C. J. Corrége, R. Q. Yang, P. R. Larson, J. A. Gupta, and M. B. Johnson, “Monolithically integrated mid-infrared interband cascade lasers and photodetectors,” Quantum Sensing and Nano Electronics and Photonics XIV, Photonics West, 2017, ***invited talk***.

2. L. Lei, L. Li, H. Ye, **H. Lotfi**, R. Q. Yang, M. B. Johnson, J. A. Massengale, T. D. Mishima, and M. B. Santos, “Long wavelength interband cascade infrared photodetectors towards high temperature operation,” Quantum Sensing and Nano Electronics and Photonics XIV, Photonics West, 2017.

3. **H. Lotfi**, L. Li, L. Lei, H. Ye, S. M. S. Rassel, Y. Jiang, R. Q. Yang, T. D. Mishima, M. B. Santos, J. A. Gupta, and M. B. Johnson, “High-speed operation of a mid-infrared optical system at room temperature,” paper JW2A.121 at The Conference on Lasers and Electro-Optics (CLEO) and the Quantum Electronics and Laser Science Conference (QELS), San Jose, CA, Jun. 5-10, 2016.

4. **H. Lotfi**, L. Li, L. Lei, H. Ye, S. M. S. Rassel, Y. Jiang, R. Q. Yang, J. F. Klem, T. D. Mishima, M. B. Santos, M. B. Johnson, and J. A. Gupta, “Recent developments in interband cascade infrared photodetectors,” Infrared Technology and Applications XLII at SPIE Defense + Commercial Sensing, Baltimore, MD, Apr. 18-21, 2016 (in Proc. SPIE. 9819, paper 98190Q).

5. R. Q. Yang, **H. Lotfi**, L. Li, L. Lei, H. Ye, S. M. S. Rassel, Y. Jiang, T. D. Mishima, M. B. Santos, and M. B. Johnson, “Recent progress in interband cascade IR photodetectors,” talk 9755-36 at Quantum Sensing and Nanophotonic Devices XIII at Photonics West, San Francisco, CA, Feb. 13-18, 2016, ***invited talk***.

6. **H. Lotfi**, L. Lei, L. Li, R. Q. Yang, J. C. Keay, M. B. Johnson, Y. Qiu, D. Lubyshev, J. M. Fastenau, and A. W. K. Liu, “Long-wavelength interband cascade infrared photodetectors operating above room temperature,” Quantum Sensing and Nanophotonic Devices XII at Photonics West, San Francisco, CA, Feb. 8-12, 2015 (in Proc. SPIE. 9370, paper 937032).

7. H. Ye, L. Li, **H. Lotfi**, L. Lei, S. M. S. Rassel, R. Q. Yang, J. C. Keay, T. D. Mishima, M.B. Santos, and M. B. Johnson, “MBE growth of long-wavelength interband cascade infrared photodetectors with InAs/GaSb superlattice absorbers,” 18th International Conference on Molecular Beam Epitaxy, Flagstaff, AZ, Sep. 7-12, 2014.

8. **H. Lotfi**, L. Li, H. Ye, R. T. Hinkey, L. Lei, R. Q. Yang, J. C. Keay, T. D. Mishima, M. B. Santos, and M. B. Johnson, "Interband cascade infrared photodetectors with long and very long cutoff wavelengths," at The Quantum Structured Infrared Photodetector International Conference, Santa Fe, NM, Jun. 29- Jul. 3, 2014.

9. **H. Lotfi**, R. T. Hinkey, L. Li, R. Q. Yang, J. F. Klem, J. C. Keay, and M. B. Johnson, “Multi-stage photovoltaic devices with a cutoff wavelength of ~3 µm,” at The 40th IEEE Photovoltaic Specialists Conference, Denver, CO, Jun. 8-13, 2014.

10. Rui Q. Yang, **H. Lotfi**, L. Li, R. T. Hinkey, H. Ye, J. F. Klem, L. Lei; T. D. Mishima, J. C. Keay, M. B. Santos, and M. B. Johnson, “Quantum-engineered interband cascade photovoltaic devices,” Quantum Sensing and Nanophotonic Devices XI at Photonics West, San Francisco, CA, Feb. 2-6, 2014 (in Proc. SPIE. 8993, paper 899310), ***invited talk***.

11. R. T. Hinkey, **H. Lotfi**, L. Li, H. Ye, L. Lei, R. Q. Yang, J. C. Keay, T. D. Mishima, M. B. Johnson, and M. B. Santos, “Interband cascade infrared photodetectors with InAs/GaSb superlattice absorbers,” Paper 8868-3 at Infrared Sensors, Devices, and Applications III, SPIE Optics + Photonics 2013, San Diego, CA, Aug. 25-29, 2013 (in Proc. SPIE 8868, paper 886805).

12. H. Ye, **H. Lotfi**, L. Li, R. T. Hinkey, R. Q. Yang, L. Lei, J. C. Keay, M. B. Johnson, and M. B. Santos, "Interband cascade photovoltaic devices operating at room temperature and above with a bandgap of ~0.23 eV," The 16th International Conference on Narrow Gap Semiconductors, Hangzhou, China, Aug. 2-5, 2013.

13. M. B. Santos, T. D. Mishima, J. C. Keay, M. B. Johnson, L. Li, R. T. Hinkey, H. Ye, Y. Jiang, **H. Lotfi**, L. Zhao, L. Lei, and R. Q. Yang, "Mid-infrared interband cascade lasers and related optoelectronic devices," The 4th International Workshop on Bismuth-Containing Semiconductors, Fayetteville, Arkansas, Jul. 14-17, 2013, ***invited talk***.

14. R. T. Hinkey, **H. Lotfi**, L. Li, R. Q. Yang, J. F. Klem, J. C. Keay, and M. B. Johnson, "Interband cascade thermophotovoltaic devices with type-II superlattice absorbers of ~0.4 eV bandgap," The 39th IEEE Photovoltaic Specialists Conference, Tampa, FL, Jun. 16-21, 2013.